14/9/76

INTERPLANETARY SCINTILLATION AND SOLAR ACTIVITY

by

Michael Wiseman, B.Sc. (Hons)

A Dissertation for the Degree of Doctor of Philosophy, in the University of Adelaide.

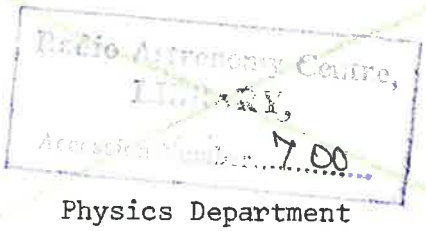

Physics Department

June 1972

523.24
WIS

TABLE OF CONTENTS

RADIO PHYSICS LIBRARY

SUMMARY

This thesis contains a study of the origin and development of the large-scale features which occur in the solar wind. Two types of disturbance have been studied; well defined streams of disturbed plasma which corotate with the sun, and blasts of turbulent plasma travelling out from active regions on the solar surface.

The work was carried out using the 80 MHz C.S.I.R.O. radioheliograph situated at Culgoora, N.S.W., and involved the observation of the interplanetary scintillation of a grid of discrete radio sources, selected to be spaced as evenly as possible over the celestial sphere.

It has proved possible to relate the observation of corotating streams in the interplanetary plasma with the presence of active regions existing on the sun. The streams are also shown to be directly associated with the presence of sector boundaries in the interplanetary magnetic field. Comparison of the present results with geomagnetic activity, has shown that both propagating plasma blast waves, and corotating streams in the ambient plasma are primary agents in the onset of geomagnetic storms.

In parallel with this investigation, the author has been involved in the construction of a three-station radio-astronomy aerial array, designed to operate simultaneously at two frequencies. It is intended

that future work using this array will extend the observations presented in this thesis, and provide more detailed information on the structure of the solar wind.

PREFACE

To the best of the author's knowledge and belief this thesis contains no material previously published or written by another person, except where due reference is made in the text. This thesis contains no material which has been accepted for the award of any other degree or diploma in any University.

M. Wiseman

University of Adelaide
26/5/72

ACKNOWLEDGEMENTS

The work described in this thesis was carried out in the Physics Department of the University of Adelaide under the supervision of Dr P. A. Dennison. The author is indebted to Dr Dennison for many helpful discussions and for his general encouragement throughout the course of the work.

The observations described in the text were made using the C.S.I.R.O. radioheliograph situated at Culgoora, N.S.W. The author wishes to express his gratitude to Dr J. P. Wild for providing access to these facilities, and to the staff at Culgoora for their helpful cooperation in maintaining the equipment during the observations.

The author has benefited from numerous discussions with his colleagues in the Radiophysics Group, and in particular with Dr R. Buckley, a visiting Research Fellow. The observations at Culgoora were made jointly with Mr R. G. Blesing during 1969 and 1970, and the computer program for the analysis of these results was written in collaboration with him.

Assistance with the preparation of data was given by Mrs Anne McLean, and the author is grateful to her for completing this tedious task.

Dr P. A. Dennison was responsible for the overall design of the

radio-astronomy aerial arrays which have been constructed at Buckland Park, Kadina and Burra. Much of the construction was carried out by Mr R. E. Lomax, whose technical knowledge and practical experience has been invaluable in the implementation of this design.

The outstation sites at Burra and Kadina were on the properties of Mr D. White and Mr C. Marsh respectively, and the author wishes to thank them for provision of these facilities.

During the course of the present research the author was the holder of a University Research Grant from the University of Adelaide for one year, and the holder of a Commonwealth Postgraduate Award for three years.

CHAPTER 1

THE SOLAR WIND

Introduction

This chapter is intended as an introduction to the solar wind, and as a brief survey of the theoretical models which have been proposed to account for its observed properties. The material reviewed here is derived mainly from optical observations of the sun and from direct sampling of the interplanetary plasma by experiments aboard deep space probes.

The main body of the thesis will be concerned with those large-scale properties of the solar wind which can be determined from the interplanetary scintillation of small diameter radio sources, and a review of this method and the associated theory will be presented in Chapter 2.

1.1 The Solar Wind Plasma

The solar wind, which is formed by the continuous expansion of the solar corona into interplanetary space, reflects the properties of its source. Any disturbance at the surface of the sun due to solar activity is convected outwards into interplanetary space by the solar wind. The expanding plasma also determines the configuration of the interplanetary magnetic field, and hence controls the propagation of cosmic rays of both solar and galactic origin. Irregularities and discontinuities in

the field or plasma flow are convected out to the orbit of the earth and provide the link between solar and geomagnetic activity. The properties of the solar wind plasma will be discussed under a number of headings.

(a) Chemical Composition

Our knowledge of the chemical composition of the solar wind is based mainly upon observations of just two ions, H^+ and He^{++}. The long term average helium abundance has been derived from spacecraft observations aboard Mariner 2, Vela 3 and Explorer 34. Results from the three craft agree very closely, giving a helium-hydrogen abundance ratio, ξ, of $\sim$ 4.5% (Hundhausen et al., 1967a; Neugebauer and Snyder, 1966; Robbins et al., 1970; Ogilvie and Wilkerson, 1969).

The establishment of a solar origin of the interplanetary plasma suggests that a relationship should exist between the relative chemical composition in the interplanetary medium and that in the surface layers of the sun. Unfortunately the abundance of helium in the sun is not easily determined since very little helium is ionized at the solar photospheric temperature of 6000° K. However, nearly all indirectly derived values of the solar helium-hydrogen ratio are larger than the 4.5% value for the solar wind plasma. Thus helium appears to be less abundant in the interplanetary medium than in the solar photosphere. This suggests that hydrogen escapes from the sun in coronal expansion more efficiently than helium.

Parker (1963a) suggested a mechanism to explain such a separation.

The unequal ratio of gravitational and pressure-gradient forces on electrons and ions in the solar corona produces, and is counteracted by, an electric field. The basic interplay between the charge separation field and gravity in separating ions of differing charge-to-mass ratios can thus account for the settling of heavy ions in the corona. Hundhausen (1970) discussed the solutions presented by Parker (1963b) for three cases, (1) a static corona, (2) a steady expansion of the corona, and (3) a transient coronal expansion. He concluded that a difference between the helium abundances in the sun and the solar wind is clearly possibly by such a mechanism.

Large time variations in the ratio, ξ, have been observed (Robbins et al., 1970) even when averaged over a full solar rotation. Sudden increases in the solar wind helium content were observed to follow simultaneous occurrences of Forbush decreases and sudden-commencement geomagnetic storms. The magnitude of the ratio ξ however, was not correlated with the geomagnetic activity index, K_p. From 1965-1967, averages over 27 days of the ratio ξ showed a small trend (Robbins et al., 1970) which might have been related to the rise in the general level of solar activity moving towards sunspot maximum (Figure 1.1(a)). The appearance of plasma with an extremely high ξ ratio about 10 hours after an interplanetary shock or geomagnetic storm sudden-commencement, has been reported by a number of authors (Gosling et al., 1967; Bame et al., 1968a; Hirshberg et al., 1970), and these all appear to confirm a connection between an enhanced helium content of the interplanetary

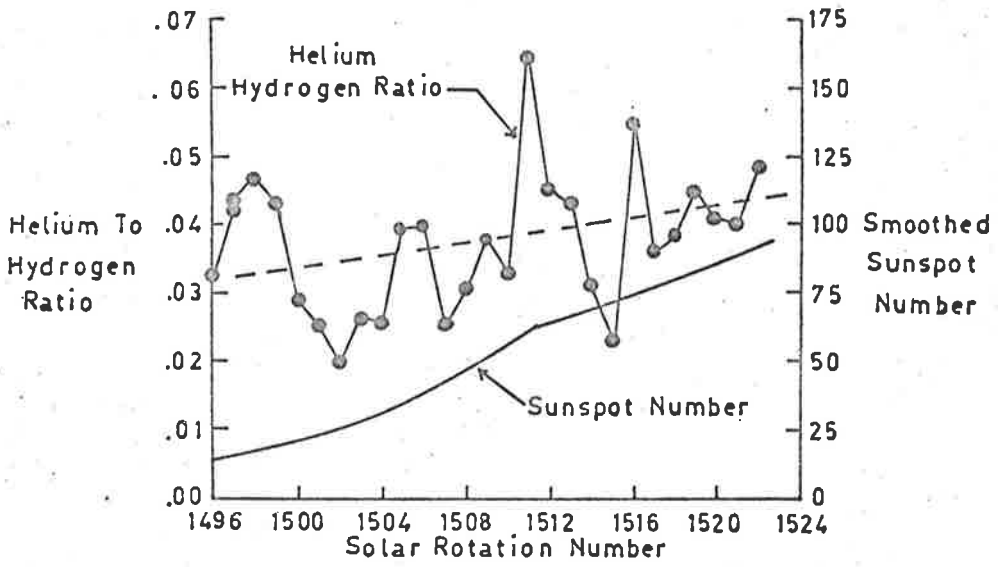

Figure 1.1(a) The helium-hydrogen density ratio observed by Vela 3 between 1965 and 1967 (after Robbins et al., 1970).

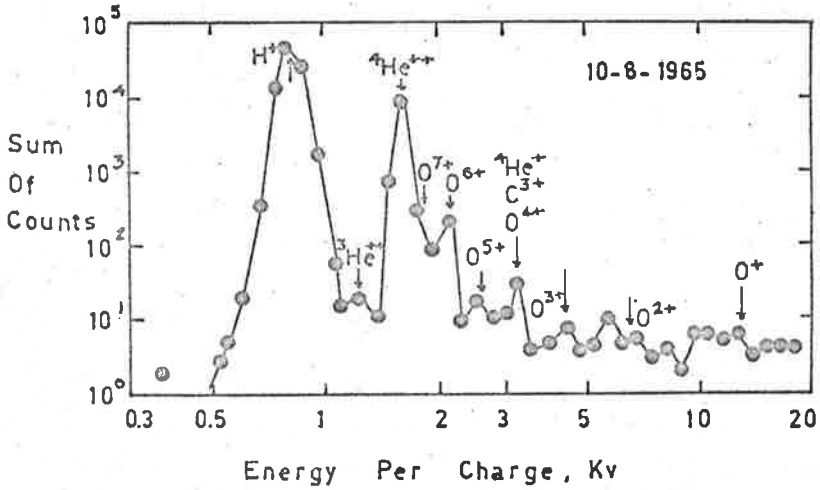

Figure 1.1(b) Energy-per-charge spectra observed with low pulse threshold by Vela 3A (after Bame et al., 1968a).

plasma and flare associated interplanetary disturbances.

The presence of other ions beside helium and hydrogen results in additional flux peaks in the solar wind spectra (Figure 1.1(b)), which have been observed in ideal low ion temperature - high flux conditions aboard Vela 3 (Bame et al., 1968b). The ions detected were $^{4}He^{+}$, $^{3}He^{++}$, $^{16}O^{+5}$, $^{16}O^{+6}$ and $^{16}O^{+7}$, although the spectral peaks were small for most ions because of their low abundances. The presence of the $^{3}He^{++}$ ion in the solar wind has been confirmed by the Apollo 11 and 12 composition experiments, (Büler et al., 1969). The significance of these heavy-ion abundance measurements is apparent when it is realised that the observed ionization states in the solar wind are also those occurring in the corona itself. Because of the very low density of the plasma in interplanetary space, the rate of ionization and recombination will be very small during the transit of the plasma from the sun to the earth. Thus the ionization states observed in the plasma will be essentially those occurring in the coronal source of the wind, and we have the possibility (Hundhausen, 1970) of using the measured ionization temperature to trace the coronal source of particular regions of the solar wind. Also, the comparison of coronal ion abundances with those of the photosphere should provide further insight into the dynamical interaction of the two regions.

(b) Flow Speed, Direction and Density

The first accurate measurements of the solar wind velocity were made

using the Mariner 2 spacecraft in 1962. Individual velocities as low as 306 km/sec and as high as 842 km/sec were recorded (Neugebauer and Snyder, 1966), and the daily average velocity from these observations was 504 km/sec. Later observations have yielded similar variations in flow velocity (Pai et al., 1967; Wolfe et al., 1966a; Hundhausen et al., 1967b), and Figure 1.2 shows Vela 2 and Vela 3 measurements of the average solar wind velocity and temperature for 14 solar rotations from July 1964 to July 1965 (Strong et al., 1967). The gradual decline in these average values was probably due to the decrease in solar activity as sunspot minimum was approached. The average solar wind velocity at solar minimum was 320 km/sec (Hundhausen, 1968).

From Mariner 2 data (Neugebauer and Snyder, 1966), the direction of the solar plasma flow was determined to be radial within an accuracy of 10°, and further data from Imp 1 and Vela 2 spacecraft showed that deviations from the radial flow directions of $\pm 6^{\circ}$ commonly occur (Wolfe et al., 1966a; Coon, 1966). Measurements from Vela 2 (Strong et al., 1967) during 1964-1965 gave an rms deviation in flow direction of $\sim 3^{\circ}$ about the mean direction, and deviations of more than 10° were shown to be relatively rare. The mean flow direction was observed to be $\sim 1\frac{1}{2}^{\circ}$ from the east, corresponding to the slight corotation of the interplanetary plasma with the sun. This corresponds to a mean azimuthal velocity of $\sim$ 10 km/sec at the orbit of the earth.

Measurements of the proton density of the solar wind (Neugebauer and

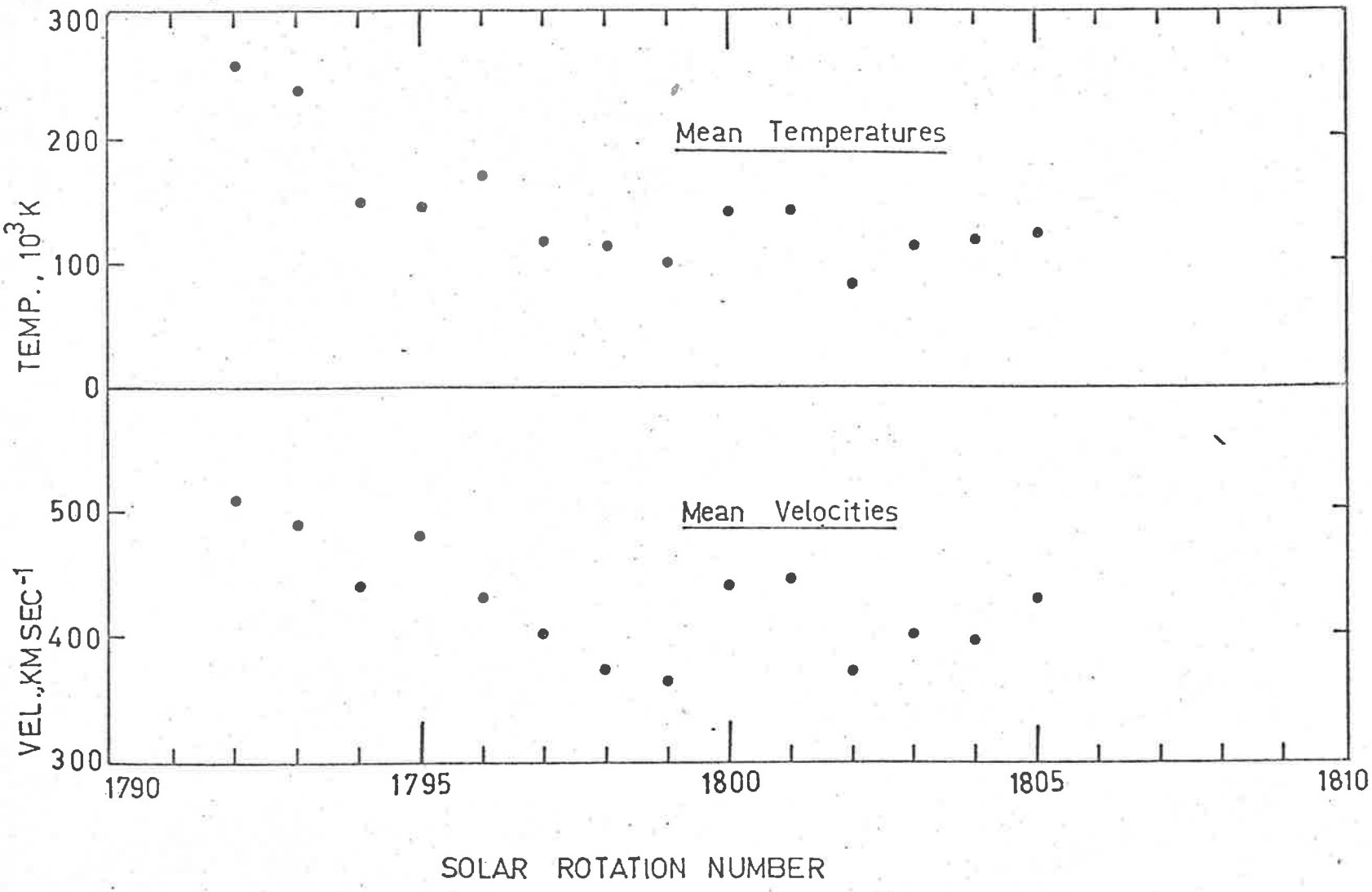

Figure 1.2 Average solar wind flow speed and proton temperature observed on Vela 3 from 1964 to 1965 (after Strong et al., 1967).

Snyder, 1966; Wolfe et al., 1966a, 1966b; Coon, 1966; Gringauz et al., 1966; Lazarus et al., 1966) have shown that large variations can occur over time scales of the order of hours. The density is generally highest on the leading edge of a high velocity plasma stream and low in the centre of the stream. The measured average proton density was 5 cm^{-3}, with variations from 0.1 to 100 cm^{-3} at 1 A.U. An increase in density as Mariner 2 approached perihelion was consistent with a $1/r^2$ dependence on heliocentric radius, within the range 0.7 to 1 A.U.

(c) Thermal Properties

The proton temperature of the solar wind is derived from the width of the particle energy-per-charge spectrum measured aboard solar plasma probes, and the lower limit of temperature resolution is determined by the spacing of the energy-per-charge channels. Early measurements aboard Mariner 2 had a low temperature limit of 6×10^4 ^{o}K (Neugebauer and Snyder, 1966), and as detectors with higher resolving powers were developed, lower proton temperatures were observed. More extensive observations have confirmed the existence of these lower temperatures, and shown that a value of $\sim 5 \times 10^4$ ^{o}K is typical for quiet solar wind conditions (Burlaga and Ogilvie, 1970). Figure 1.3 shows the hourly average temperature distribution derived from Explorer 34 proton spectra between June 1967 and December 1968 (Burlaga and Ogilvie, 1970).

A qualitative expression relating the proton flow speed and proton temperature was reported by Strong et al. (1966) and Hundhausen et al.

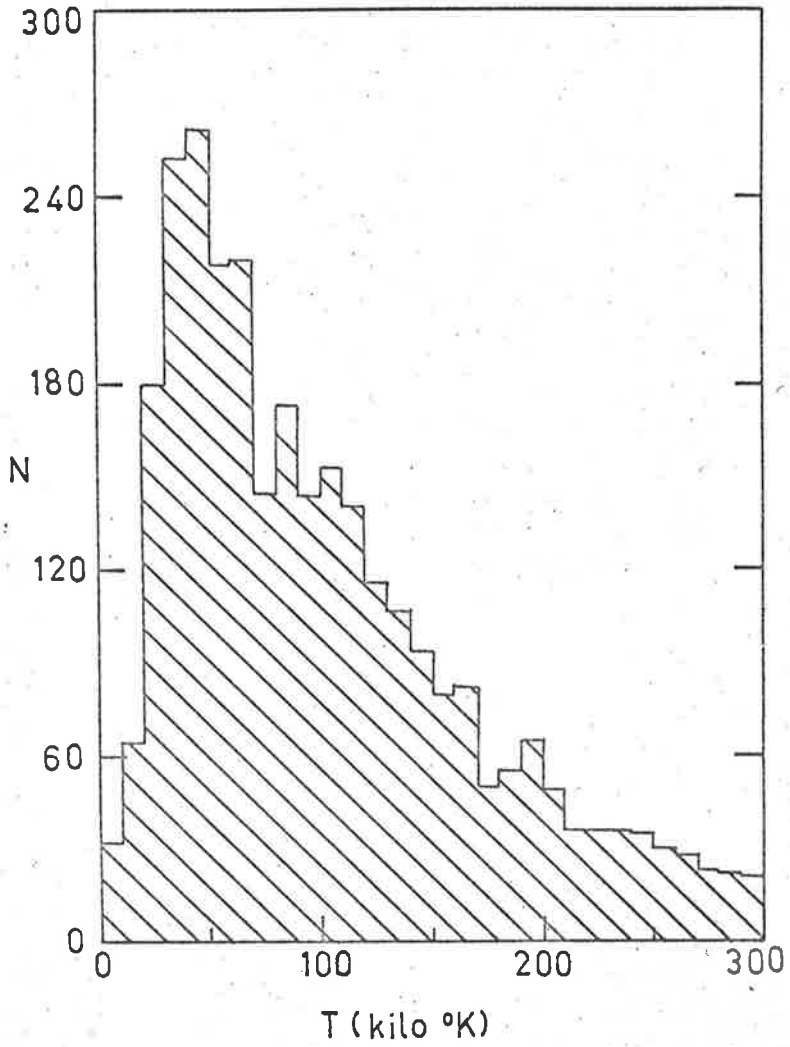

Figure 1.3 The distribution of solar wind proton temperatures observed on Explorer 34 from 1967 to 1968 (after Burlaga and Ogilvie, 1970).

(1967). It was observed that variations in the proton temperature followed the variations in bulk speed as a function of time; i.e. high velocity streams were "hotter" than the ambient plasma. Burlaga and Ogilvie (1970) have represented this effect by an empirical relationship,

$$T_p^{\frac{1}{2}} = (0.036 \pm 0.003)V - (5.54 \pm 1.50),$$

where T_p is the proton temperature in units of 10^3 $^{\circ}$K, and V is the flow speed in km/sec. For flow speeds near 300 km/sec, the average temperature is only 2.7×10^4 $^{\circ}$K (quiet-sun conditions).

Figure 1.4 shows a contour map of a typical proton velocity distribution derived from Vela 3 data (Hundhausen et al., 1967a, 1967c), where v_1 is the radial velocity away from the sun, and v_2 is the azimuthal velocity perpendicular to v_1. If the random motions of the protons were isotropic, then the contours would be circles centred on the measured mean bulk velocity (denoted by a triangle in Figure 1.4). The vector B_p is the direction of the average interplanetary magnetic field observed aboard the Imp 3 spacecraft simultaneously with the proton measurements.

A distinct anisotropy is evident in Figure 1.4. The proton velocity distribution is asymmetric along the magnetic field direction, and a tail of high energy protons appears in the high v_1 - low v_2 region, which implies (Hundhausen et al., 1967a) a transport of heat energy along the magnetic lines of force. Hundhausen et al. (1967c) derived a proton energy transport rate of $\sim 10^{-5}$ ergs cm^{-2} sec^{-1}, which is several orders of magnitude smaller than the conduction by the electron component of

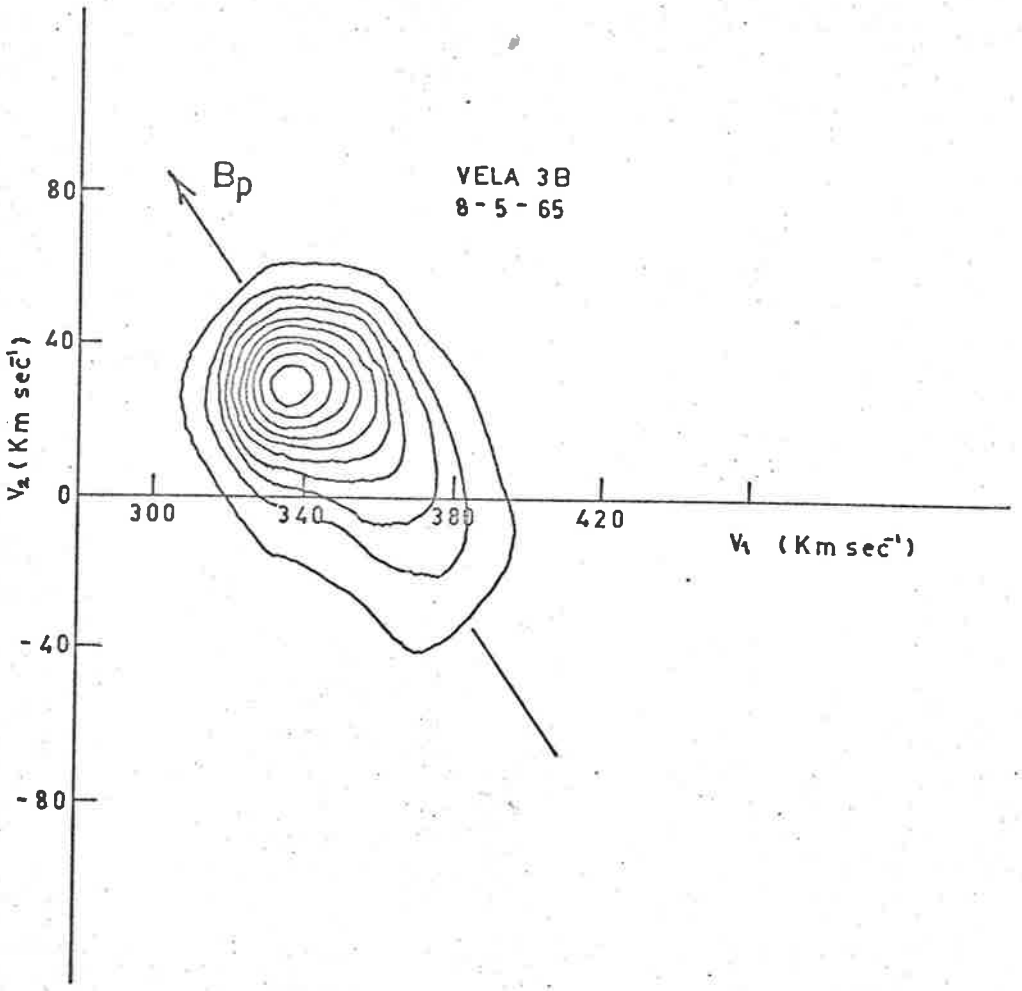

Figure 1.4 A contour map of a typical proton-distribution function (after Hundhausen et al., 1967c).

the plasma.

(d) Solar Wind Electrons

A complete understanding of the interplanetary plasma must include a knowledge of the electron distribution function, however, observations of the solar wind electrons are difficult because of the low average energies of the particles. Early measurements (Serbu and Maier, 1966) from Imp 2 were unreliable due to perturbations caused by the spacecraft potential and possible confusion with photo-electrons. The improved techniques in later spacecraft produced more reliable results (Pioneer 6 - Wolfe and McKibbin, 1968, and Vela 4B - Montgomery et al., 1968a, b). Figure 1.5 shows the flow velocity, particle density and temperature obtained from six hours of Vela 4B data (Montgomery et al., 1968b). The bulk speed of the electron population agrees, within reasonable limits, with that of the proton population, and was measured to be radial within the error limits of the electron detectors ($\pm 15^{\circ}$). Electron and proton density plots show excellent agreement, whereas the electron temperatures are consistently higher than the proton temperatures and show much less variation with time. The electron temperature anisotropy was found to be smaller than that of the proton distribution (1.2 compared with 2.0), and the energy flux due to electron heat conduction (10^{-2} ergs cm^{-2} sec^{-1}) was considerably greater than that due to proton heat conduction (10^{-5} ergs cm^{-2} sec^{-1}). The electron anisotropy was aligned with the direction of the proton anisotropy and hence with the direction of the magnetic field. Both the electrons and

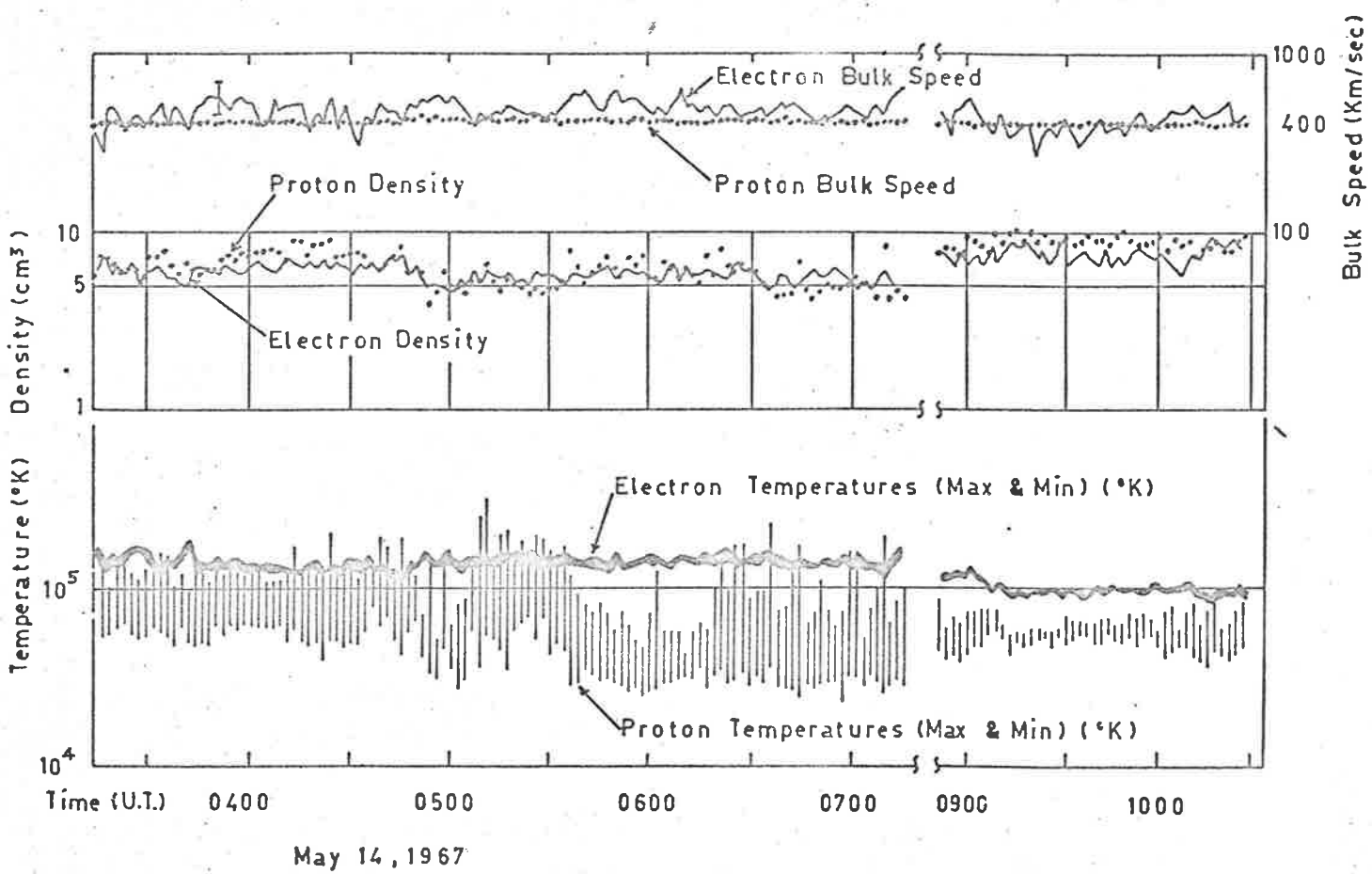

Figure 1.5 Electron-proton temperature, density, and bulk speed in the solar wind (after Montgomery et al., 1968).

the protons therefore appear to conduct heat away from the sun along the interplanetary magnetic field lines.

1.2 The Interplanetary Magnetic Field

Following Biermann's suggestion (1951) of an outward streaming solar plasma to account for the observed motion of comet tails, Parker (1958) developed a theory for the hydrodynamic expansion of the solar corona and successfully predicted several properties of the interplanetary medium. In particular he predicted the subsonic-supersonic transition of the solar wind flow radially away from the sun, and pointed out that the effect of solar rotation and radial plasma flow on the interplanetary magnetic field would be to stretch the field lines out into an Archimedes-spiral configuration.

For a mean solar wind velocity of 400 km/sec in the radial direction, the interplanetary magnetic field at the orbit of the earth will be directed $\sim 45^{\circ}$ to the earth-sun line and either towards or away from the sun according to the polarity of the line of force leaving the solar surface. Thus, a direct relation might be expected between the polarity of the interplanetary field and that of the underlying photospheric field. Observations from the Imp 1 satellite during 1963 are reproduced in Figure 1.6 (Wilcox and Ness, 1965). The histograms show the distribution of the measured interplanetary magnetic field direction in the plane of the ecliptic and normal to the ecliptic, averaged over 5 minute intervals (Figure 1.6(a)), and again over 3 hour

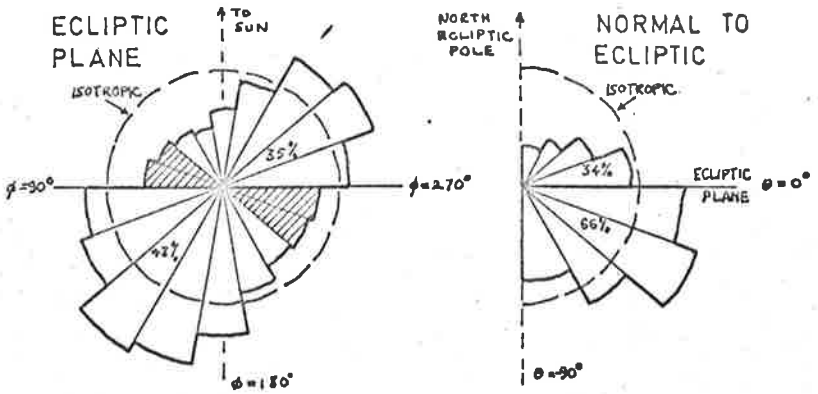

(a) 5.46 MIN AVERAGES

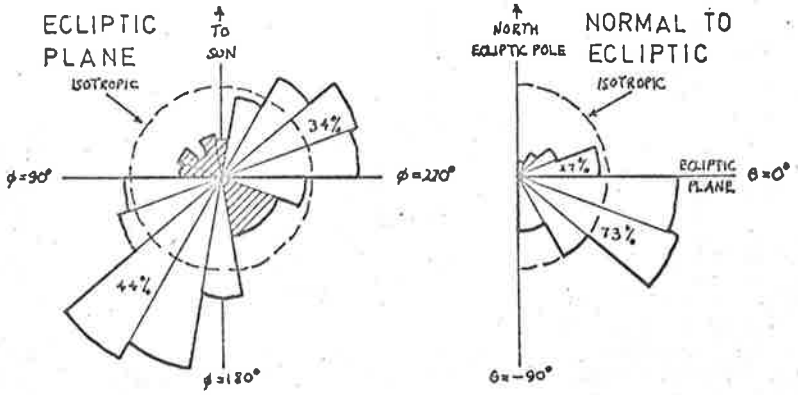

(b) 3 HOUR AVERAGES

Figure 1.6 Distribution of the measured interplanetary magnetic field direction in the plane of the ecliptic and normal to it (after Wilcox and Ness, 1965).

intervals (Figure 1.6(b)).

The distribution is peaked in the direction corresponding to the spiral streaming angle, and with polarity away from the sun for 48% of the time and towards the sun for 35% of the time. The marked asymmetry in the north-south direction produced a serious discrepancy between theory and experimental observations (Dessler, 1967), and it has been suggested that the strong southern predominance observed by Imp 1 may be due to experimental error. Later observations aboard Explorer 33 from 1966-1967 appeared to confirm this interpretation (Hirshberg, 1969). The field direction lay close to the equatorial plane and pointed southward during only 45% of the time, in marked contrast to the 73% from the Imp 1 results.

When the 3 hour averages (from Imp 1) were plotted as a function of time in the ecliptic plane, the interplanetary magnetic field exhibited a simple sector structure consisting of four distinct regions (Figure 1.7), with the average field in consecutive sectors being alternately toward and away from the sun. The data from Mariner 2 also showed a quasi-stationary structure with a strong 27 day periodicity (Davis et al., 1966). If the interplanetary magnetic field corotates with the sun, then particular features of the field would be expected to reappear with a 27 day recurrence period. An autocorrelation of the magnetic field direction calculated from Imp 1 data (Wilcox and Ness, 1965) displayed a distinct 27 day periodicity, and also a sub-periodicity of 13½ days,

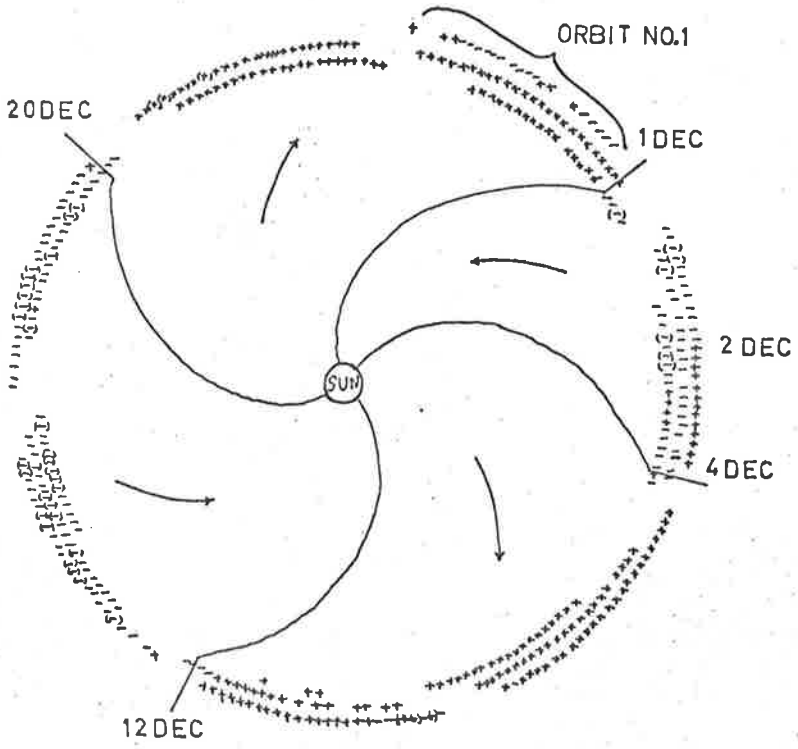

Figure 1.7 The direction of the measured interplanetary magnetic field during successive 3 hour intervals (after Wilcox and Ness, 1965).

which is further evidence for the validity of the sector structure description. (Representing four sectors by (+1, -2, +3, -4) a rotation of 180° or 13½ days will produce a secondary correlation with (+3, -4, +1, -2), which is not as large as the 27 day correlation due to the different sizes of the four sectors). Further observations from two spacecraft (Imp 3 and Pioneer 6), having an appreciable separation in azimuth,have clearly established (Ness, 1966) that most of the structure in the interplanetary magnetic field corotates with the sun, with an azimuthal velocity $\sim$ 400 km/sec at 1 A.U.

The magnetic field also exhibits a well defined structure within each sector. Figure 1.8 shows the variations of plasma velocity, proton density and magnetic field strength during the passage of a sector observed by Imp 1 (Wilcox and Ness, 1965). The average magnitude of the field rose to nearly 7 γ (1 γ = 10^{-5} gauss) two days after the sector boundary had passed and then decreased to a minimum value of about 3 - 5 γ over the next three days, with a minor peak $\sim$ 4.5 γ in the trailing edge. The solar wind velocity showed a similar variation within the sector but without a second peak. The proton density distribution on the other hand showed a variation almost in antiphase with the velocity distribution; low values of density being recorded during periods of high velocity, with the maximum density occurring in the leading edge of the sector.

Since the sector structure is developing continually, with more

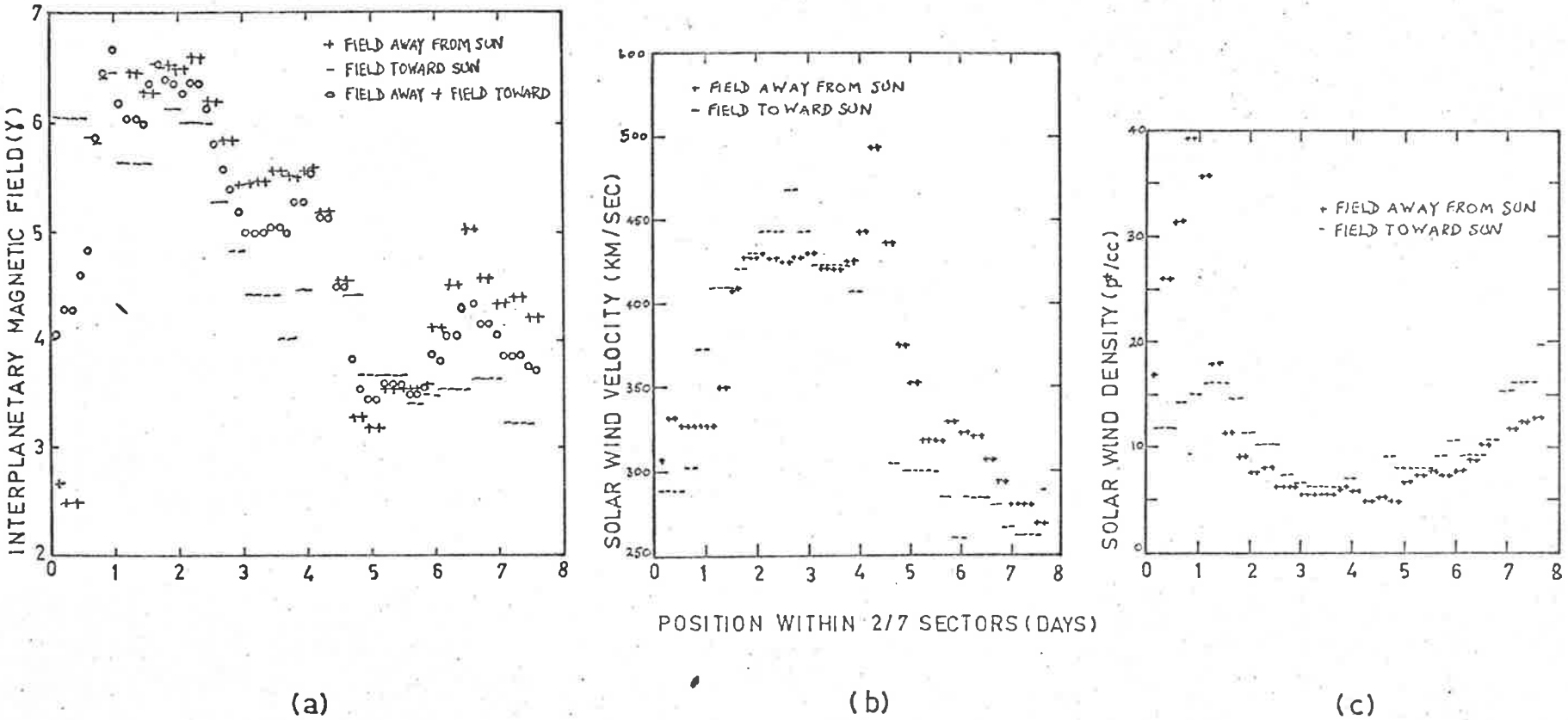

Figure 1.8 Superposed epoch analysis of the magnitude of the interplanetary magnetic field, solar wind velocity, and solar wind density as a function of position within a sector (after Wilcox and Ness, 1965).

dominant sectors expanding into their neighbouring sectors, one would expect the sharp increase in density which is observed at the sector boundaries, due to the compression of the plasma by the relative movement of the two sectors. Thus the solar wind plasma appears to be well organized by the magnetic field sector structure, which can be regarded as a fundamental property of the interplanetary medium. The boundaries separating adjacent sectors are relatively thin ($\sim 10^5$ km), with no apparent magnetic connection between them (Wilcox and Ness, 1965).

Severny et al. (1970), have obtained measurements of the mean photospheric magnetic field during the period March - June 1968 and compared its polarity with the direction of the interplanetary magnetic field (Wilcox et al., 1969 and Wilcox, 1969). A very close correspondence between the two magnetic fields was observed, after the interplanetary observations had been adjusted to allow for an average 5 day transit time of the solar wind plasma from sun to earth (Wilcox, 1968). This indicates that the interplanetary field was part of a field pattern which 'was ordered over an appreciable portion of the solar disc' (Wilcox, 1969). Bumba and Howard (1965) and Severny et al. (1970) have studied the distribution of these weak photospheric magnetic fields over the solar disc, and shown that a solar sector (in the photosphere) extends over a large area on both sides of the heliographic equator out to $\sim \pm 40^{\circ}$ latitude (Figure 1.9).

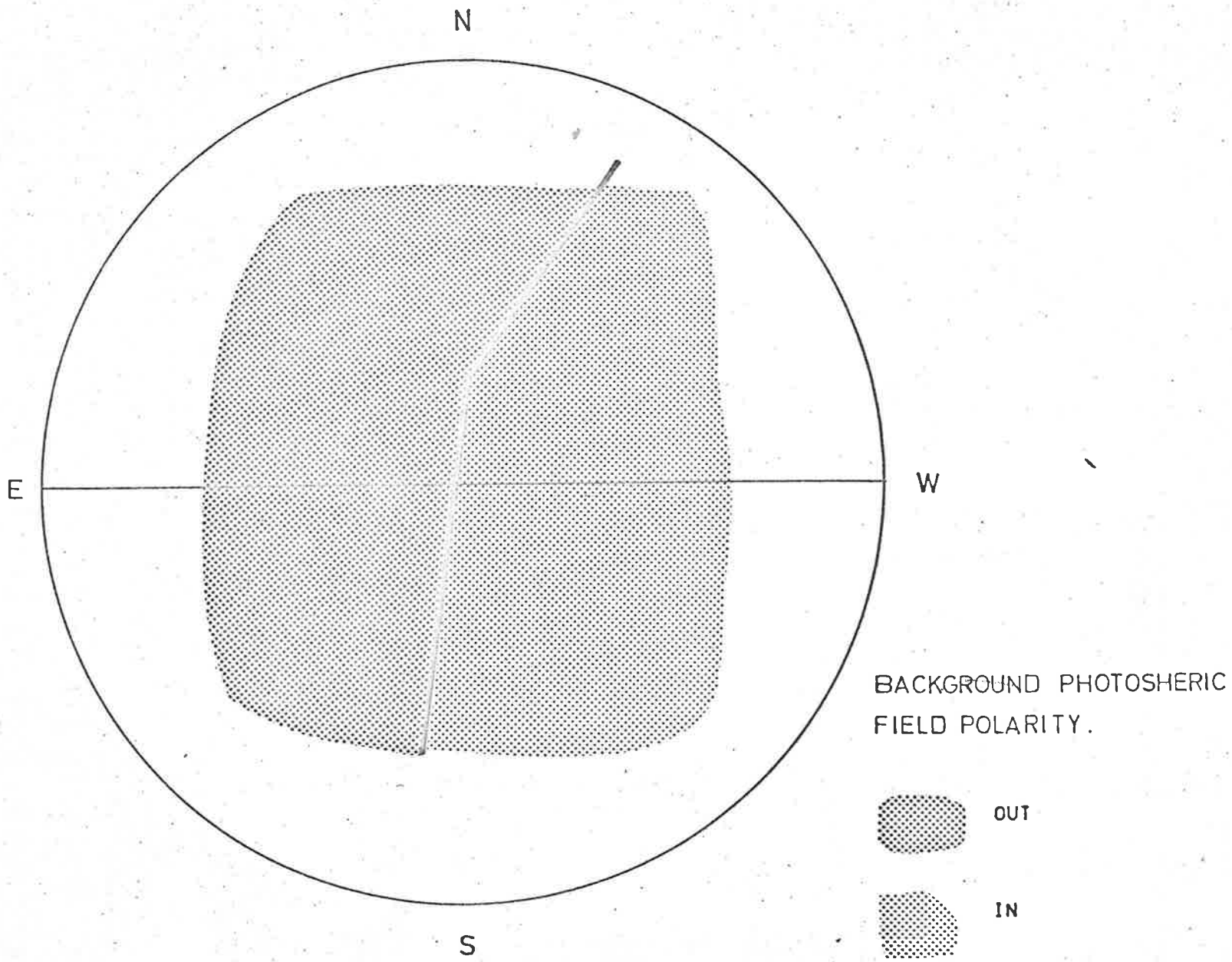

Figure 1.9 The distribution of weak photospheric magnetic fields over the solar disc

Interplanetary sectors observed during the rising portion of the sunspot cycle do not necessarily have the same properties as those observed near sunspot minimum. The latitudinal extent of the source at solar minimum has been observed to be large ($\pm 40^{\circ}$), whereas a newly formed sector observed during the rising portion of the sunspot cycle has been related to a photospheric bipolar magnetic region (Schatten et al., 1968), indicating that the extent in latitude of such young sectors may be much more limited.

Howard (1959) showed that photospheric magnetic regions have a close relationship to calcium plage regions, often the seat of developing active centres on the sun, such that plages are very nearly outlined by a 10 gauss contour line. Wilcox and Ness (1967) carried out a superposition of calcium plage areas on the sun for days when a large sector was believed to be approximately centred on the central meridian. They found that the trailing edge of the sector was relatively free of plages, whilst the densest concentration of plages occurred within the first quarter of the sector. This distribution of plage density is similar to the distribution of solar wind velocity and interplanetary magnetic field intensity shown earlier in Figure 1.8.

When considering the solar source of the interplanetary sector structure, an important consideration is its longitudinal extent. Davis (1965), from Mariner 2 observations in 1962, postulated that the interplanetary sectors arose from small regions on the sun, essentially

"nozzles," in which the field was unidirectional. Davis suggested that the plasma does not expand out from the corona uniformly over the sun's surface, but that its flow is restricted in most regions by irregular magnetic fields. Those regions of weak but regular magnetic fields might then feed the upper corona with material to fill an entire sector in the solar wind. Thus all the solar wind plasma would come from a few relatively "smooth" regions in the photosphere.

Wilcox (1968) supports a contrary opinion in which the sectors originate from large well ordered magnetic structures on the sun, so that each longitude near the sun is connected by magnetic field lines to a longitude at the orbit of the earth, i.e. a direct longitudinal mapping. High cross-correlation coefficients observed between the interplanetary magnetic field direction and the photospheric magnetic field direction (Ness and Wilcox, 1966) favour the mapping hypothesis, but the possibility of a localised source of unidirectional photospheric fields cannot be excluded.

The origin of the sector patterns in the interplanetary medium can be investigated by considering the magnetic field patterns in the inner corona. Newkirk (1967) suggested that a potential dipole model was capable of yielding a crude representation of the magnetic field above active regions and the more quiet portions of the sun. This model implies that below a height of $\sim 3\ R_o$ (R_o = 1 solar radius) the coronal material is controlled by the magnetic field, and above this height the

coronal magnetic fields are drawn out into interplanetary space by the solar wind. This conclusion is supported by the observations of Bugoslavskaya (1949) from 1887 to 1945, that the highest closed arches visible in the data from eclipses have a mean height of only 0.6 R_o above the limb.

Schatten et al. (1969) have developed a physical model that is consistent with many of the properties observed in the corona and in interplanetary space. In this model they distinguish three main regions. In region 1, the photosphere, the magnetic field configuration is governed by the motion of the plasma. Above the photosphere the plasma density decreases rapidly, accompanied by moderate decreases in the magnetic energy density. This is region 2, where the magnetic energy density is greater than the plasma energy density, and hence the field controls the plasma configuration. Much further out in the corona the magnetic energy density diminishes to a value less than the plasma energy density, so that near 20 solar radii the solar wind completely dominates the flow. However, before the total magnetic energy density falls below the plasma energy density, there occurs a region where the transverse magnetic energy does so, the boundary of region 3. In this region the transverse magnetic fields are transported out by the radially flowing plasma. It is this transverse magnetic field that interacts with the coronal plasma, since a radial field would not affect or be affected by a radially flowing plasma. The magnetic field existing at the boundary between regions 2 and 3, is thus orientated

approximately in the radial direction, and serves as a source for the interplanetary magnetic field. This boundary occurs at a different radial distance to that defined by Pneuman (1966) at which the energy density of the solar wind flow becomes greater than the total magnetic energy density.

Schatten et al. (1969) have used a Green's function to provide a solution of Laplace's equation between a photospheric distribution of monopoles and an outer source surface at which the field becomes radial. In region 2, closed magnetic loops will form above photospheric regions of opposite polarity. For a theoretical source surface at $R_s = R_o$, the magnetic field on the source surface will be almost identical to the photospheric field. As surfaces at larger distances are considered, fewer loops of magnetic field reach the source surface. Hence the source surface tends to smooth out the photospheric field, and explains why the interplanetary field is unidirectional for several days at a time, while the photospheric field is more filamentary in nature. Numerical calculations of the magnetic field on a source surface 0.6 R_o above the photosphere agree reasonably well with the observed interplanetary magnetic field.

Altschuler and Newkirk (1969) have considered several different mathematical methods to determine the magnetic field of the solar corona in the current-free (or potential-field) approximation. They conclude that the field obtained from the monopole method is not consistent with

the magnetic data because of non-local effects produced by monopoles on a curved surface. The model of Schatten et al. (1969) does, however, provide an insight into the possible source regions of the interplanetary magnetic field, even if the method is not rigorous, as claimed by Altschuler and Newkirk. The latter have used a Legendre polynomial fitted to the measured line of sight (photospheric) magnetic field and show that it is a self consistent solution with respect to the available data. Computer generated maps of the magnetic field in the corona have been produced (Newkirk et al., 1968), which compare favourably with a white light photograph of the sun at total eclipse. Comparison of the density structure of the corona - as evidenced by rays, arches and plumes - with the shape of the calculated magnetic field lines shows very satisfactory agreement. This agreement indicates that the potential magnetic field model is reasonably valid in the lower corona ($r < 2.5\ R_o$) and that the density structure of the lower corona correlates with magnetic tubes containing varying amounts of coronal plasma (Newkirk and Altschuler, 1970).

The stable configuration of the magnetic sector structure, with a corotation period of 27 days, showed little change during the early observations of 1963 and 1964. The change from the old to the new solar cycle appeared to start near the beginning of 1965 (Ness and Wilcox, 1967) during the flight of Mariner 4. The recurrence period early in 1965 was observed to increase from 27 to 28 days, and this increase was probably related to the high-latitude activity at the onset of the new

sunspot cycle. Near the end of an old cycle there is little activity to break up the large scale patterns in the photosphere, but as the new cycle progresses the patterns are interrupted by new activity and the sectors begin to evolve more rapidly.

Within a sector there exist smaller distinct magnetic structures which take approximately one hour to rotate past the earth (Ness, 1966). These may be related to the often quite marked anisotropy of solar generated cosmic radiation (McCracken and Ness, 1966). The direction of the maximum cosmic ray flux is parallel to the interplanetary magnetic field, and follows it even in the presence of major changes in the field direction. Bartley et al. (1966) proposed that filaments of the interplanetary magnetic field are able to constrain cosmic rays to move through the interplanetary medium in well defined paths, and estimated filamentary diameters of between 0.5×10^6 and 4×10^6 km. Step-wise changes in the solar wind velocity and temperature have been associated with interplanetary filaments observed by Vela 2 (Hundhausen et al., 1967b), and in later observations from the Vela satellites, the observed spacing of the filament boundaries suggested that the widths of the filaments were of $\sim 2 \times 10^6$ km (Strong et al., 1967).

Wilcox and Ness (1965) performed a superposed epoch analysis of the Deep River neutron monitor counting rate as a function of position within an average magnetic field sector observed by Imp 1. The count rate increased throughout most of the sector, being smallest where the

interplanetary field magnitude was largest, and vice versa. These observations are consistent with the idea that galactic cosmic rays can be excluded from the solar system by irregularities in the interplanetary magnetic field.

Rao et al. (1967), have pointed out that sectors which produce large Forbush decreases in cosmic ray intensity also tend to produce recurring geomagnetic storms, and are able to contain recurring proton streams. Fairfield and Ness (1967) have investigated the variation in geomagnetic activity as interplanetary sector structures rotate past the earth, and they conclude that the average field direction in the magnetosheath differs by 180° for sectors with polarity toward and away from the sun. The average response of the geomagnetic activity index, K_p, as a function of position within a sector is shown in Figure 1.10 (Wildox and Colburn, 1971). The solid line represents similar results obtained near solar minimum (Wilcox and Ness, 1965), the dots represent the results of Wilcox and Colburn (1969), the crosses the results of Wilcox and Colburn (1970), and the triangles are the results of Wilcox and Colburn (1971). The tendency for a decline in geomagnetic activity during the trailing portion of a sector, and a rapid increase near and after a sector boundary passes the earth are clearly evident. We note, however, that the peak of geomagnetic activity is reached approximately one day earlier in the sector during the rising portion of the sunspot cycle, compared with that at solar minimum.

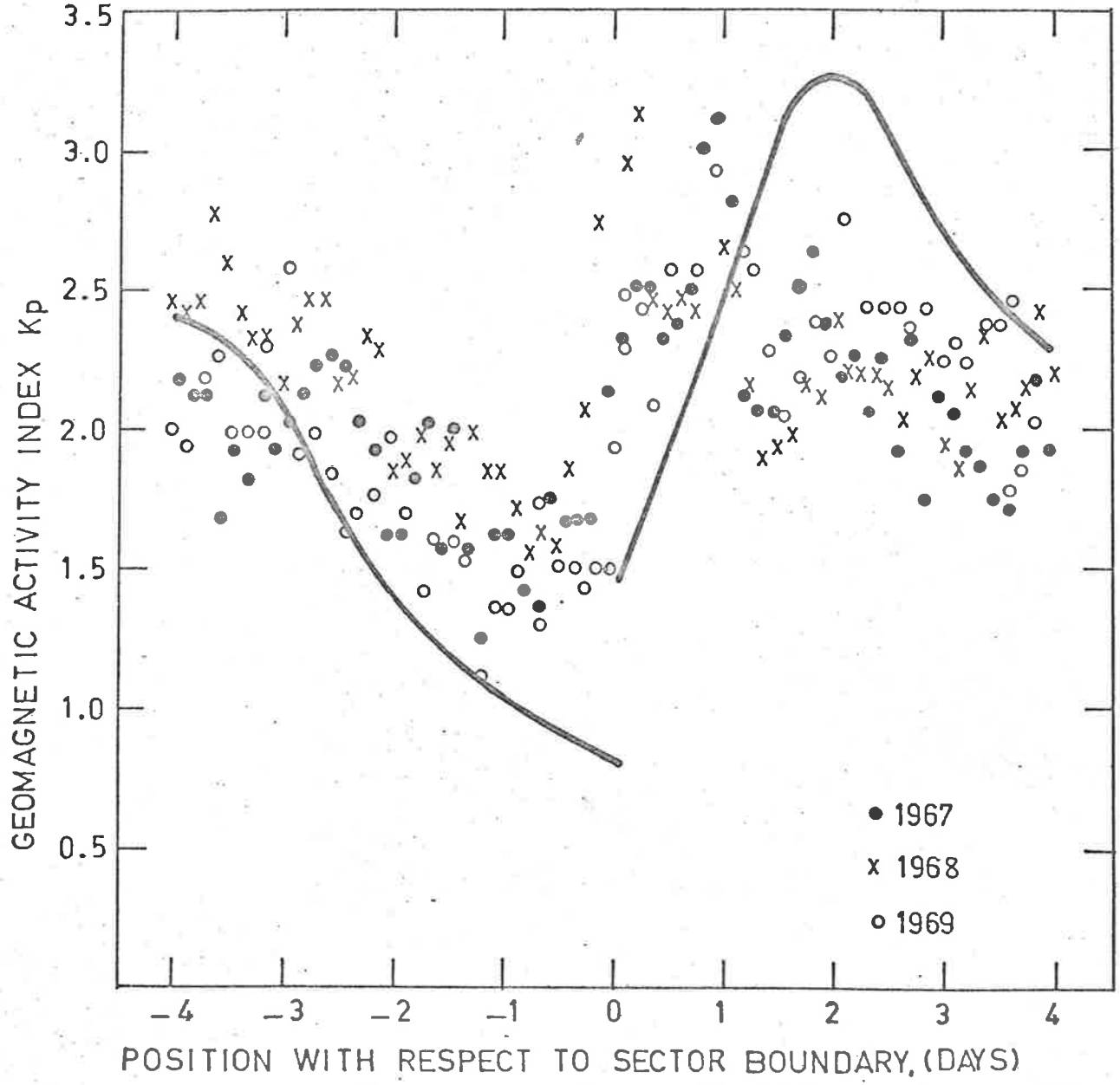

Figure 1.10 Average response of the geomagnetic activity index as a function of position within a sector of the interplanetary magnetic field (after Wilcox and Colburn, 1971).

Figure 1.11 is a possible magnetic field configuration associated with a sector boundary (Wilcox, 1968), which is modified to include the asymmetry between the preceding and following portions of sectors. The isothermal surfaces are depressed at the sector boundary since the thermal conductivity normal to the field is small compared to that along the lines of force. However, more observations are required to delineate the real, and probably complex, structure associated with sector boundaries.

1.3 Theoretical Models of the Solar Wind

The initial work of Parker (1958) describing the expansion of the solar corona into interplanetary space has led to a number of models based on the equations of hydrodynamics. Parker (1958, 1963b) considered the coronal expansion in terms of a one-fluid model with a known variation of temperature with distance from the sun. For a spherically-symmetric steady-state system with a coronal temperature of 3×10^6 ^{o}K, the hydrodynamic equations imply a subsonic-supersonic transition in the plasma flow. Chauser (1960) was the first to recognise that the hydrodynamic equations describing the solar corona are similar to those describing the flow of gas through a de Laval nozzle, the constriction of the nozzle being supplied by the gravitational field of the sun.

In Parker's model (1958, 1963b) the energy equation plays no part because of the assumed functional dependence of the temperature on radial

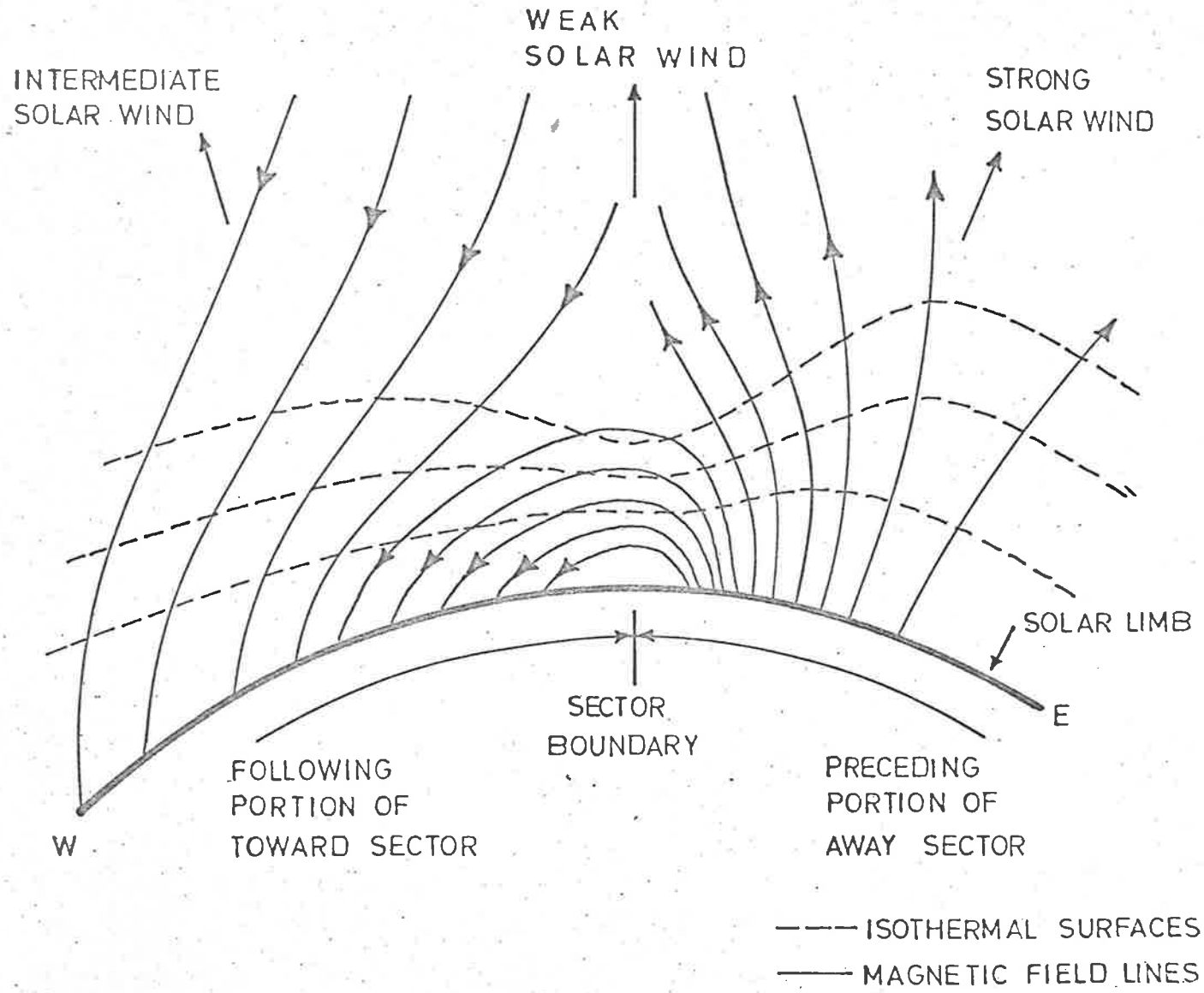

Figure 1.11 A possible magnetic field configuration associated with a sector boundary (after Wilcox, 1968).

distance. For an isothermal corona at a temperature of 1.22×10^6 °K, the model predicts a solar wind velocity and density at the orbit of the earth of 550 km/sec and 24 cm^{-3} respectively. These values are much higher than the observed quiet solar wind values of 320 km/sec and 5 cm^{-3}.

Noble and Scarf (1963) have included the heat (i.e. energy) equation explicitly in their treatment of the one-fluid model, and assuming a thin-shell heat source at the base of the corona they were able to show that the presence of heat conduction leads to supersonic coronal expansion. Their model predicted a velocity V = 352 km/sec, density D = 6.75 cm^{-3}, and temperature $T = 2.8 \times 10^5$ °K at the orbit of the earth. The velocity and particle density are in much better agreement with the observed values, but the predicted temperature is considerably greater than that observed for protons and electrons, $T_p = 4 \times 10^4$ °K and $T_e = 10^5$ °K. Scarf and Noble (1965) further developed this model to include the effect of viscosity.

Whang and Chang (1965) also obtained solutions for the inviscid, one-fluid hydrodynamic equations, but with the additional boundary condition that the total energy flux at large distances from the sun is convective; i.e. negligible transport by conduction. Whang et al. (1966) extended this treatment to include the effects of viscosity. However, both of these approaches yielded solar wind velocities much lower than the observed values.

Sturrock and Hartle (1966) and Hartle and Sturrock (1968) developed a two-fluid solar wind model of electrons and protons. Separate energy equations were used for the two components of the wind, and the only heat transport was via classical heat conduction, with energy transfer due to collisions between the electrons and protons. This model predicted a proton temperature of $\sim 4 \times 10^3$ $^{\circ}$K at the orbit of the earth, and a flow velocity of 250 km/sec, both of which are lower than the typically observed values of $\sim 5 \times 10^4$ $^{\circ}$K and 350 km/sec (Neugebauer and Snyder, 1966; Axford, 1968; and Hundhausen, 1968). The two fluid model also predicts an electron temperature of 3.4×10^5 $^{\circ}$K, which is very roughly in agreement with direct observations (Montgomery et al., 1968b). One way to explain these discrepancies is to insist that predictions of the two-fluid model should only be compared with observations made during quiet sun conditions, when the solar wind speed is near the actual value predicted by the model (Burlaga and Ogilvie, 1970). The implication is then that during non-quiet solar wind conditions, a non-thermal (i.e. non-conductive) heating term must be included in the proton energy equation.

The coronal plasma is strongly held by the sun's gravitational field, and so there must exist a source of heat which is strong enough to drive the plasma through the gravitational nozzle. This heating must extend out from the sun at least as far as the subsonic-supersonic transition. Heat transport in the wind by thermal conduction alone was found to be insufficient to match the observed velocities and densities

with the predicted values. Parker (1964) suggested that non-conductive heating due to wave dissipation in the upper corona could play an important role in the energy dynamics of the solar wind.

Heating below the subsonic-supersonic transition level will largely go into increasing the flow speed and will also thereby decrease the density at large distances (conservation of flux). Energy added beyond the point of transition will raise the proton temperature, with little change in the other parameters. In fact all the changes produced by adding a heating term in the energy equation would improve the agreement between observation and theory. Hartle and Barnes (1970) therefore extended the two-fluid model by including an external energy source in the proton heat equation and then varying its strength and spatial distribution to determine the general requirements of such a source. They concluded that 'by depositing heat over the extended range $2\ R_o < r < 25\ R_o$, solar wind speeds and proton temperatures can be brought into direct correspondence with the empirical results of Burlaga and Ogilvie (1970).' On the basis of this model, they concluded that primary energy deposition should take place inside $r = 25\ R_o$.

In connection with the nature of the energy source, Barnes (1968, 1969) has examined the role of collisionless heating in the solar wind caused by damping of fast-mode hydromagnetic waves emitted from the sun. He shows that this mechanism enhances the component of kinetic temperature parallel to the average magnetic field direction, but does

not affect the transverse temperatures, thus accounting for the observed temperature anisotropy. It also explains the discrepancy between the average solar wind velocities and proton temperatures, and those predicted by the Sturrock and Hartle two-fluid model.

However, these developments of the basic Parker model still do not explain why the electron temperature $T_e = 3.5 \times 10^5\ ^{o}K$ predicted at 1 A.U. by the two-fluid model is considerably larger than the observed value of $1.5 \times 10^5\ ^{o}K$. The problem becomes more serious in the light of the point recently made by Hundhausen (1969), that the high electron temperature from the two-fluid model implies a large transport of energy by conduction, and hence a much larger discrepancy between the observed and predicted total energy flux at 1 A.U. The energy equations in the two-fluid model are normally coupled by an exchange term ν due entirely to Coulomb collisions between the two components. However, Cuperman and Harten (1970) have reworked the equations for the two-fluid model and included a term to allow for an enhanced (non-collisional) interparticle coupling via wave-particle interactions. A choice of ν 30 times higher than the Coulomb collision exchange rate yields a solution in which all the predicted parameters are in better agreement with the observed values than in models using only the Coulomb collision rate.

Parker (1964) has suggested that the situation can also be improved by modifying the rate of conduction with distance from the sun. Physically an inhibition of conduction could be caused by the restraint

of the spiral pattern of the interplanetary magnetic field, or by the development of plasma instabilities (Forslund, 1970) caused by the large heat conduction itself. A number of plasma instabilities have been proposed to limit the ion-temperature anisotropy (Barnes, 1968; Kennel and Scarf, 1968; Griffel and Davis, 1969; Hollweg and Volk, 1970; Eviatar and Shulz, 1970).

A complete agreement between observation and theory, however, can only be finally attained by taking into account all the physical processes which are neglected in the simple two-fluid model; i.e. real (non-spherical) symmetry, rotation, viscosity, magnetic field strength and variations, solar variability and all the non-thermal heating mechanisms (plasma instabilities, non-collisional damping of hydromagnetic waves, etc), and of course considerably more detailed observational data.

This section is intended as only a brief summary of theoretical models of the solar wind, and for fully detailed accounts the reader is referred to the papers noted in the text. A number of reviews of the present state of our knowledge of the whole solar wind process are available as follows: Dessler (1967), Ness (1967), Axford (1968), Hundhausen (1968), Wilcox (1968), Cowling (1969), Parker (1969), Wilcox (1969), Holzer and Axford (1970, Hundhausen (1970), Scarf (1970), Wolfe and Intriligator (1970).

CHAPTER 2

THEORY OF INTERPLANETARY SCINTILLATION

Introduction

In 1964, Hewish, Scott and Wills reported that small diameter radio sources exhibited random fluctuations in intensity on occasions when the line of sight to the source was within 90° of the sun. The characteristic time scale of the fluctuations ($\sim$ 1-2 seconds) was shown to be incompatible with an origin in the terrestrial ionosphere, but could be explained by the scattering of radio waves from irregularities of electron density situated in the interplanetary medium. The strong heliocentric dependence of the relative intensity of the fluctuations for a given source confirmed this interpretation and the phenomenon is now known as interplanetary scintillation (IPS).

The problem of radio wave scattering from randomly distributed phase-changing irregularities has been treated theoretically by a number of authors (Ratcliffe, 1956; Pisareva, 1959; Mercier, 1961; Budden, 1965; Uscinski, 1966; Bramley, 1967; Salpeter, 1967; Buckley, 1971a; 1971b) and we shall only present here a summary of the main results from these various accounts.

2.1 The Diffraction Screen

The geometry of the situation is sketched in Figure 2.1. Radiation from a point source passing along the line of sight to the

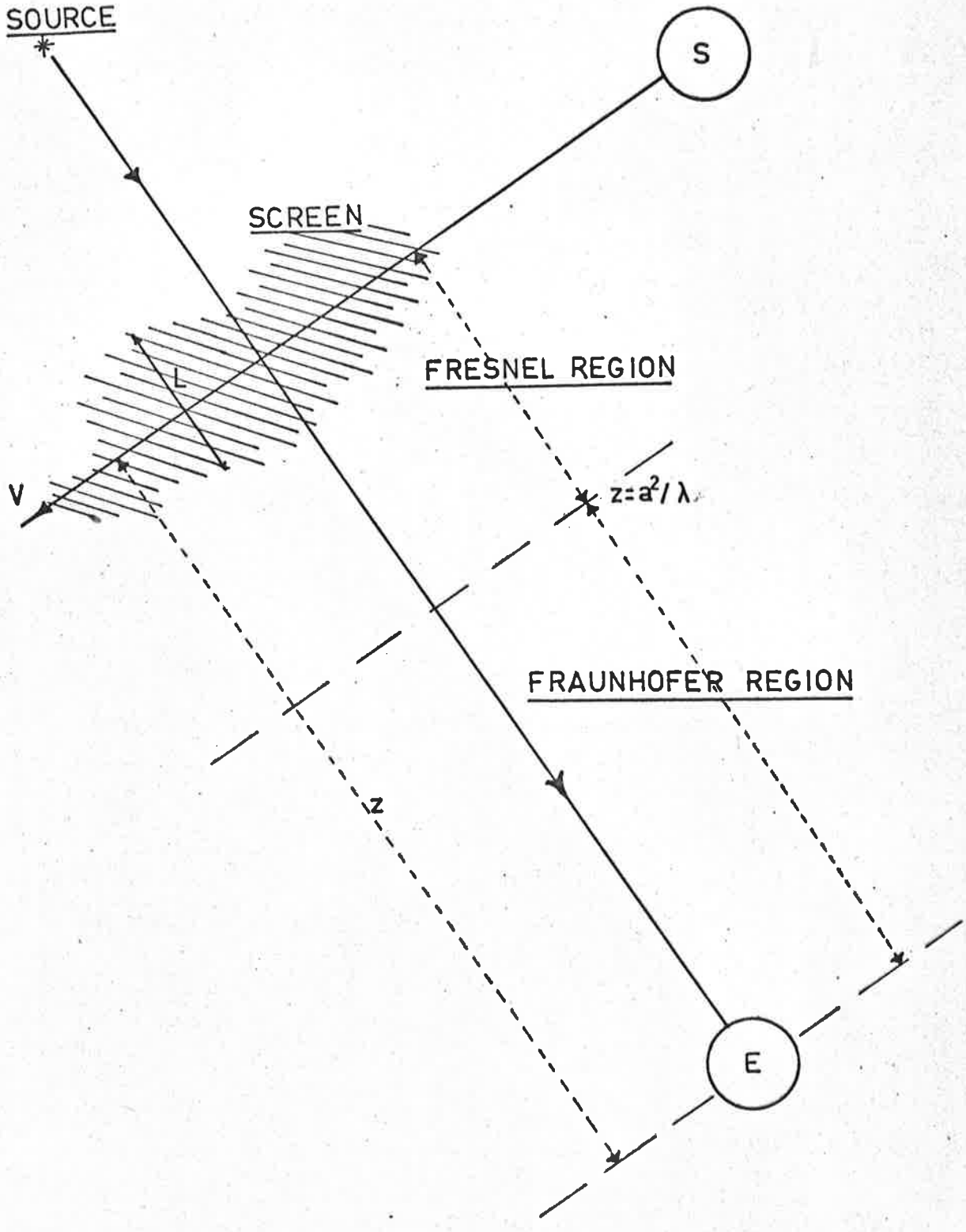

Figure 2.1 The geometry of the diffraction process (see text).

earth encounters irregularities in refractive index caused by fluctuations in electron density within the solar wind. Since the density of the interplanetary medium (and presumably also the fluctuation in the density) falls off rapidly with distance from the sun ($\sim r^{-2}$), it is reasonable to assume that the predominant phase fluctuations in the wave will be introduced in a region of plasma of limited thickness, L, around the point of closest approach to the sun, along the line of sight. This region will be referred to as 'the screen.'

We define the autocorrelation function of the electron density fluctuations in the screen, $\rho_s(\xi, \eta)$ as,

$$\rho_s(\xi, \eta) = \frac{< f(x, y)\, f(x + \xi, y + \eta) >}{< f^2(x, y) >} \qquad (2.1)$$

where $< >$ denotes spatial averaging, and the normalising factor $< f^2(x, y) >$ is simply the variance of the fluctuations. A convenient measure of the scale of the irregularities, a, is the point at which the autocorrelation function ρ_s falls to the value e^{-1}, and is called the correlation length. The rms phase fluctuation, ϕ_o, imposed on the incident wave by the screen depends upon the radio wavelength, λ, the scale, a, and the thickness, L, of the "phase screen",

$$\phi_o \propto \lambda\, (a\, L)^{\frac{1}{2}} < \delta N_e^{\,2} >^{\frac{1}{2}} \qquad (2.2)$$

where $< \delta N_e^{\,2} >^{\frac{1}{2}}$ is the rms fluctuation in electron density. That is, ϕ_o is independent of the mean background electron density and depends only on the variations from the mean. For the weak scattering case ($\phi_o < 1$ radian), we shall assume that the amplitude fluctuations across

the wavefront emerging from the screen are negligible compared with the fluctuations in phase. This is certainly not true for the strong scattering case ($\phi_o > 1$), and is only true for $\phi_o < 1$ when L is sufficiently small ($L < a^2/\lambda$).

2.2 Weak Scattering ($\phi_o < 1$)

In this case the incident plane wave will emerge from the phase screen with undiminished amplitude and random fluctuations of phase across its wavefront. We can represent this wave as the sum of an unscattered wave, E_o, and an angular spectrum of plane waves travelling at various angles to E_o (Ratcliffe, 1956). The specular component, E_o, and the waves of the angular spectrum are in phase quadrature at the screen. As the distance, z, from the screen increases, the wide angle components of the angular spectrum progressively lose their phase relationship with E_o and produce variations in amplitude across the wavefront. Thus as z increases, E_o and any particular side wave E_x will progressively move in and out of phase coherence, alternately producing fluctuations in the amplitude and phase of the wave.

For $z < a^2/\lambda$ (the Fresnel region), the energy in the phase and amplitude fluctuations is approximately equal, and the amplitude probability distribution is Gaussian. In this region the radius of the first Fresnel zone ($\sqrt{\lambda z}$) is less than the spatial scale, a, and the amplitude at any point is primarily determined by scattering from only one irregularity. As z increases, the number of irregularities enclosed

by each Fresnel zone increases and so the amplitude at any point on the wavefront is built up of waves scattered from many irregularities. Thus for $z > a^2/\lambda$ (Fraunhofer region), the amplitude fluctuations saturate and exhibit a Rice distribution.

A convenient measure of the degree of scintillation of a source is the scintillation index, F, which is defined as the rms intensity fluctuation relative to the intensity of the steady (unscattered) component,

$$F = \frac{< (I - I_o)^2 >^{\frac{1}{2}}}{I_o} \tag{2.3}$$

where I is the fluctuating intensity and I_o is the mean value, $< I >$. In the Fraunhofer region the index is proportional to ϕ_o,

$$F = \sqrt{2}\ \phi_o, \tag{2.4}$$

and thus from relation 2.2, $F \propto \lambda$. If $\phi_o < 1$ the spatial scale, ℓ, of the diffraction pattern is equal to the scale within the screen; that is, the pattern and screen autocorrelation functions are identical. Very close to the screen however (Fresnel region), the scale ℓ is less than a, since the amplitude fluctuations due to large spatial scales in the screen are not fully developed. Here the index F is proportional to λ^2.

2.3 Strong Scattering ($\phi_o > 1$)

In this case the thin phase screen approximation is no longer valid. The unscattered component E_o is small, and the amplitude at any point on the wave-front is determined by the relative phases and

amplitudes of the scattered waves in the angular spectrum. If the thickness of the scattering layer, L, is not sufficiently small, multiple scattering must also be taken into account. Mercier (1962) has considered the problem of diffraction in the far zone due to large random phase fluctuations ($\phi_o > 1$), and has deduced exact analytic expressions for all the even-order moments of the amplitude fluctuations, and hence proved that the amplitude in the far zone has a Rice probability distribution. At smaller distances (the Fresnel region), the variance of the intensity (i.e. the second moment) can be calculated numerically for $\phi_o \sim 1$. For $\phi_o > 1$ the normalized variance (or scintillation index F) is greater than unity, and approaches a maximum near the point where focussing of rays by individual irregularities occurs. Bramley and Young (1967) have extended the numerical results of Mercier up to rms phase deviations $\sim$ 3 radians. More recently Buckley (1971a) has considered the problem analytically for very large phase deviations in a one-dimensional screen. A companion paper extends the analysis to two-dimensional screens (Buckley, 1971b). He shows that the scintillation index, F, increases with distance, z, from the screen as z^2, reaching a maximum value of

$$F = 1 + \tfrac{1}{2} \ln \phi_o, \qquad (2.5)$$

due to focussing by individual irregularities at a distance approximately equal to that predicted by geometrical optics ($z_m = 2 \pi a^2/\phi_o \lambda$). At large distances the index approaches unity.

The scale of the diffraction pattern is independent of ϕ_o close to

the screen, and depends on the smaller scales within the screen. It approaches a minimum value, $\ell \sim a\sqrt{\ln \phi_o}/\phi_o$ just in front of the focussing region, and at large distances (the far zone) approaches the value $\ell \sim a/\phi_o$. These results also apply qualitatively in the more realistic two-dimensional screen situation (Buckley, 1971b).

2.4 The Effect of Source Size

In the discussion so far we have assumed that the radiation incident upon the screen is emitted from a point source. We must now take into account the effect of finite source size on the results we have described. Consider a source of finite angular diameter ψ. The image of this source on an observing plane, 0, at distance z from the screen, has a width $z\psi$. If this width becomes greater than the scale, a, of the plasma irregularities, the diffraction images at 0 begin to overlap, thus blurring out the fine detail in the diffraction pattern, (Briggs, 1966). Thus the conditions for which diameter blurring occurs can be written,

$$\psi > \frac{\ell}{z} \qquad (\phi_o < 1) \tag{2.6}$$

and

$$\psi > \frac{\ell}{z\,\phi_o} \qquad (\phi_o > 1)$$

Little and Hewish (1966) have derived quantitative measures of this effect for various source models. For the case of a circular Gaussian source, for example, they show that the observed pattern scale, ℓ', and scintillation index, F', are given by,

$$\ell' = \ell \left[1 + 2 \left(\frac{z\psi}{\ell}\right)^2\right]^{\frac{1}{2}},$$

and

$$F' = F \left[1 + 2 \left(\frac{z\psi}{\ell}\right)^2\right]^{-\frac{1}{2}}. \qquad (2.7)$$

Thus the observed pattern scale increases and the scintillation index is reduced as a result of the blurring. This effect has also been used to place useful upper limits on the angular diameters of scintillating radio sources (Little and Hewish, 1966, 1968). For a distance z = 1 A.U. and scale size ℓ = 200 km, diameter blurring occurs for sources with angular diameters greater than $0.5''$ arc.

2.5 Scintillation Bandwidth

The range of frequencies over which the amplitude scintillations show a correlation coefficient greater than 0.5 is defined as the scintillation bandwidth. For the weak scattering case ($\phi_o < 1$), Budden (1965) has calculated an expression for the normalized correlation coefficient of signal amplitudes received simultaneously on two frequencies at a single receiving point. The final expression is mathematically complex but can be readily simplified for the general case of vertical incidence and isotropic irregularities (see Appendix A), yielding

$$\frac{\Delta f}{f} = \frac{2\sqrt{1 - C}\, X}{(X^2 + 4c/\pi^2)^{\frac{1}{2}}}, \qquad (2.8)$$

where C is the correlation coefficient, Δf is the bandwidth about frequency f, and X is the dimensionless parameter $\ell^2/\lambda z$. Briggs (1966) has deduced an order of magnitude result from the diffraction approach,

$$\frac{\Delta f}{f} \sim \frac{\ell^2}{\lambda z} , \qquad (2.9)$$

which is the bandwidth limit below which the scintillations will be highly correlated. It is shown in Appendix A that expression (2.8) reduces to

$$\frac{\Delta f}{f} \sim \frac{\pi \ell^2}{\lambda z} , \qquad (2.10)$$

for a correlation C = 0.5, which agrees with the approximate result of Briggs. For the strong scattering case ($\phi_o > 1$), ℓ is replaced by ℓ/ϕ_o in the preceding expressions. A radio star is effectively a wide-band noise source and so the experimental bandwidth is usually determined by the receiver response. The scintillations will be seriously decorrelated over the receiver bandwidth, and hence significantly reduced if,

$$\frac{\Delta f}{f} > \frac{\pi \ell^2}{\lambda z} \qquad (2.11)$$

2.6 The Physical Reality of IPS Parameters

From observations of IPS the scale of the density fluctuations in the interplanetary medium can be inferred. Typical values for a, the correlation length, are 100 - 200 km (Dennison and Hewish, 1967). However, Jokipii and Hollweg (1970) have suggested that the plasma density irregularities will have a dominant structure comparable in size to the observed magnetic field variations. Direct measurements of the magnetic field correlation length (Holzer et al., 1966; Jokipii and Coleman, 1968) from OGO 1 and Mariner 4 spacecraft yield values of

$\sim 10^6$ km which are several orders of magnitude larger than the plasma density scales inferred from IPS and angular broadening observations.

The magnetic field variations have a power spectrum which exhibits an approximate power law decrease ($f^{-1.5}$) between 10^{-4} and 10^{-2} Hz and then falls rapidly ($f^{-3.8}$) in the region between 10^{-1} and 1.0 Hz (Coleman, 1968). Since the Alfvén velocity at 1 A.U. is much less than the solar wind velocity, the observed temporal variations are the result of magnetic spatial variations being swept past the spacecraft. In this case the frequency range 10^{-1} to 1.0 Hz corresponds to length scales of the order of 100 km. If, as Jokipii and Hollweg (1970) suggest, the magnetic field and plasma density fluctuations are strongly coupled throughout the above frequency spectrum, it would appear that radio scintillation estimates of the spatial scale of the density irregularities ($\sim$ 100 km) do not represent a dominant scale in the medium itself, but in fact correspond to the "inner scale" or dissipation length of the turbulence. Recent spacecraft observations of the solar wind plasma (Intriligator and Wolfe, 1970), yield power spectra with an average frequency dependence of $f^{-1.3}$ in the range 10^{-4} to 10^{-3} Hz and imply a plasma density correlation length of 10^6 km.

It is possible however that the frequency spectrum may contain two separate regimes (Hewish, 1971). A low frequency regime corresponding to large-scale plasma variations directly coupled to magnetic field fluctuations, and a smaller scale plasma regime which is decoupled from

the magnetic field. The results of Intriligator and Wolfe (1970) are consistent with the idea of large-scale coupling, but do not prohibit the existence of an uncoupled plasma regime above 10^{-3} Hz. Hewish (1971) has plotted the scintillation observations of a number of authors over a 30 to 1 wavelength range, and shown that the line of best fit to the data corresponds to F (scintillation index) $\propto \lambda$, which disagrees with the relation $F \propto \lambda^2$ implied by the model of Jokipii and Hollweg derived from geometrical optics. Buckley (1971) has shown that the method of geometrical optics is in any case not applicable to the particular situation under consideration, and has used a more rigorous approach to show that the scintillation data imply the existence of a quite distinct microstructure within the solar wind with scale $\sim 10^2$ km. He also suggests that such small-scale density fluctuations may be the result of electrostatic waves propagating at right angles to the average magnetic field. Such a situation would give rise to an enhanced level of small-scale density fluctuations not accompanied by comparable magnetic variations, and Buckley shows that this proposal of a two-component spatial power spectrum for the density fluctuations is in agreement with the radio scintillation and angular broadening observations.

Thus the general trend at this time appears to be towards justifying the IPS observations as being genuinely related to a distinct microstructure in the solar wind with scale $\sim 10^2$ km, not much larger than the ion gyro-radius in the medium, and certainly much smaller than

the scale $\sim 10^6$ km of the dominant magnetic structure detected by space probes. However, complete confirmation of this situation must await direct measurements by space vehicles of the small-scale electron density structures of the interplanetary plasma.

CHAPTER 3

COROTATING STREAMS AND PLASMA BLAST WAVES

Introduction

In Chapter 1 we described the properties and features of the solar wind and discussed a number of theoretical models which attempt to rationalize those properties. Some large-scale features of the interplanetary plasma were described briefly in the discussion of the sector structure in the interplanetary magnetic field.

This chapter will review our present knowledge of the movement and geometry of such large-scale features, especially in relation to corotating streams and plasma blast-waves associated with active regions on the sun.

3.1 Corotating Features in the Solar Wind

Plasma measurements made aboard Mariner 2 during 1962 (Neugebauer and Snyder, 1966) revealed a continuous variation in the velocity of the solar wind, which implied the existence of numerous regions on the solar surface from which plasma is ejected with velocity much higher than that of the ambient plasma flow. Identifiable structures of this kind were observed to persist for extended periods, sometimes over several solar rotations. Thus the rotation of the sun can provide a source of temporal variation at a fixed observation point even when solar wind conditions are steady, but varying with position. Solar wind features

related to such spatial variations can be identified by a recurrence period close to 27 days.

Neugebauer and Snyder (1966) observed recurrent high velocity regions in the Mariner 2 data for 1962 and attributed them to long-lived centres of activity on the sun. These high velocity streams were shown to be associated with the sector-like structure of the interplanetary magnetic field, which has been described in Chapter 1 (Ness and Wilcox, 1964; Wilcox and Ness, 1965). One of the sectors observed by Imp 1 late in 1963 was associated with a recurrent series of geomagnetic disturbances lasting for more than 20 solar rotations. These were correlated with a recurring proton stream (Fan et al., 1966) existing within the sector, but were not associated with any distinct feature on the surface of the sun.

A survey of the northern sky by interplanetary scintillation during 1967 (Burnell, 1969), revealed large increases in the scintillation of many of the radio sources observed. It was reported that most of the enhancements tended to recur with a period of 27 days, and that some enhancements also correlated with decreases in cosmic ray intensity at the earth. These anomalous scintillation enhancements were attributed to streams of disturbed plasma corotating with the sun.

Croft (1971) has also observed corotating regions in the solar wind, evident in the interplanetary electron number density measured by radio propagation techniques. These patterns of increased number density

revealed the existence of corotating regions in which a recognizable character was maintained during several solar rotations. The life-times of these regions were all shorter than those observed by Neugebauer and Snyder (1966), but it should be noted that the latter observations referred to regions of high velocity where the density was low, but relatively chaotic. The difference in the observed life-times of such streams may simply be an indication that the electron density in the interplanetary medium is more variable than the velocity, and hence long-term density trends would be more difficult to detect. However, the difference may also be due to the fact that the observations of electron density were made during a much later phase of the solar cycle.

Croft (1971) also noted a degree of randomness within the repeating patterns, such that transient density increases did not reliably reappear with a predictable period. These small variations in arrival time ($\sim$ 1 day) were almost certainly related to variations in the velocity of the solar wind. Such variations would change the spiral angle of the stream and hence its arrival time at any fixed observing point.

Following our preliminary report (Dennison and Wiseman, 1968) of a corotating feature in the solar wind using IPS, Houminer (1971) reported daily observations of four radio sources over a period of two months, and concluded that variations in the scintillation index which were not obviously associated with other activity, could be explained in terms of

plasma streams corotating with the sun. It was suggested that the observed increases in scintillation index might be associated with the sector structure of the interplanetary magnetic field. This relationship is confirmed by the experimental results to be described in the following chapters. Houminer found no obvious correlation between the scintillation enhancements and the presence of active regions on the surface of the sun, whereas our observations, in some cases, demonstrate the existence of such a relationship (see Chapter 6).

An increase in density within the leading edge of a fast stream was suggested by Neugebauer and Snyder (1967) to account for the observed features of the plasma data from Mariner 2, and similarly a decrease in density within the trailing edge of a fast stream was postulated by Sarabhai (1963). Dessler (1967) has pointed out that one effect of the solar rotation on the interaction of adjacent streams of different velocity would be to produce east-west deflections of the flow. Siscoe et al. (1969) have described this east-west velocity asymmetry within the framework of fluid mechanics. Their suggested mechanism predicts that fast streams will tend to come from the west and slow ones from the east with respect to the average solar wind direction, and experimental data from Pioneer 6 indicate that about 50% of the east-west variations in flow direction with a period $\sim$ 4 days may be due to this fast stream-slow stream interaction.

A theoretical model of recurrent solar wind streams has been

developed by Carovillano and Siscoe (1969). They begin with the hydrodynamic solutions of a spherically symmetric solar wind model, and consider corotating perturbations on a boundary fairly close to the sun to represent the effects of stationary features on the solar surface, such as hot and cool regions. They have then considered solutions of the perturbation equations which are time-stationary in the corotating frame of reference. The solutions are valid over the range 0.1 - 1.0 A.U. and are restricted to large-scale features of the medium. In this perturbation model the interaction between fast and slow corotating streams is treated in detail, and its predictions agree with the qualitative ideas of Siscoe et al. (1969).

The perturbation analysis of non-spherically symmetric solar wind flows has been extended by Siscoe and Finley (1969) to include both variations in the latitude of the velocity source, and also any flows across the solar equatorial plane due to north-south asymmetries. A further paper (Siscoe and Finley, 1970) has extended the treatment of Carovillano and Siscoe (1969) to include arbitrary distributions of coronal inhomogeneities. If the radial flow speed alone is perturbed at 0.1 A.U., the flow resulting at 1 A.U. is shown in Figure 3.1 as a function of solar longitude. The density, ρ, reaches a maximum during the rise in radial speed V_r, and then a minimum on the downward slope of V_r. Since the fast streams push against slow preceding ones, and slow streams lag behind fast preceding ones, the intervening gas is either compressed or rarefied depending on the configuration. The azimuthal

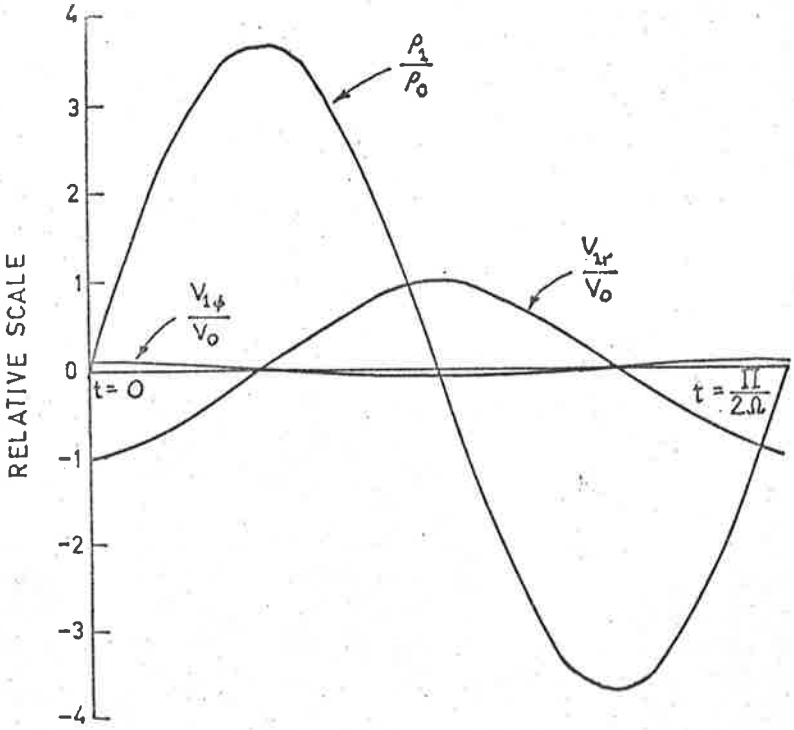

Figure 3.1 The perturbations in density and radial and azimuthal components of the flow speed produced at 1 AU by a perturbation of radial velocity only (after Carovillano and Siscoe, 1969).

component of the velocity V_ϕ indicates a flow from east of the sun for low flow speed, and from west of the sun for high flow speed. However, experimental data (Neugebauer and Snyder, 1966) indicate that there is a tendency for variations in V_r and ρ to be anti-correlated (i.e. 180 degrees out of phase) rather than 90° out of phase as suggested by the present model. Siscoe and Finley suggested that this difference is due to the choice of boundary conditions, and that future calculations must allow for variations in the polytropic index relating pressure and density in the solar wind.

A later paper (Siscoe and Finley, 1972) approaches this problem by extending the solutions of the linearized hydrodynamic equations to allow perturbations in all the hydrodynamic parameters (density, velocity and temperature), whereas the previous solutions (Carovillano and Siscoe, 1969 and Siscoe and Finley, 1969, 1970) were restricted to constant entropy perturbations, for which density and temperature variations were constrained to be in phase. This later study also resulted in the development of a convenient matrix method for obtaining solar wind perturbations at some particular radial distance, given the perturbations at some other radial distance. The solutions thus give a complete description of the linearized hydrodynamic problem for corotating time-stationary inhomogeneities, if the solar wind parameters are known accurately at a particular radial distance.

However, the model does not incorporate several effects which occur

in the solar wind which might modify the conclusions. For example, the time variations in a corotating frame were restricted in the model to a time-scale long compared to the flow time of the plasma from the sun to the point of observation ($\sim$ 4 days to the earth). Also the model entirely neglected the magnetic field, though a model of Weber and Davis (1967) suggests that the results with and without the field would be qualitatively similar.

A significant result of the model of Siscoe and Finley (1972) was the difference in the radial dependence of the amplitudes for the three cases of independent initial conditions, pure velocity perturbation, density perturbation, and temperature perturbation. The amplitudes at 1 A.U. were predicted to be $\sim$ 10% of the initial amplitudes for the first two cases, but of the order of 100% for the pure temperature perturbation. Hence if the perturbation amplitudes of all three were of similar magnitude at the critical point, the structure at the earth would largely reflect just the initial temperature perturbation. The relative phases between the various solar wind parameters for a pure temperature variation were very different from those resulting from a pure velocity or density perturbation.

The observations of Hundhausen et al. (1970) showed that density and azimuthal velocity were generally anti-correlated with the radial velocity, and that temperature was generally correlated with the radial velocity. The predicted relative phases of the parameters for the pure

temperature case were found to be consistent with these observations. Thus the different radial dependences of the three pure initial states at the critical point considerably improve our understanding of the solar wind fluctuations at the earth.

3.2 Discontinuities and Shock Waves in the Solar Wind

The large-scale structure of the interplanetary magnetic field is characterized by sectors having appreciable angular extent (Wilcox and Ness, 1965). These sectors exhibit a well-defined variation in density, velocity and the strength of the magnetic field. At the sector boundary there occurs a discontinuous jump in the direction of the interplanetary magnetic field, and sometimes in the other solar wind parameters. It is therefore important to consider this structured nature of the interplanetary medium when attempting to associate a particular disturbance in the medium with a particular solar flare. Many disturbances which appear to be abrupt, actually corotate with the sun and are not associated with a particular flare, but rather with some quasi-stationary feature on the solar surface.

It has been established that many of the most important solar flares are followed by geomagnetic storms at the earth (Akasofu and Yoshida, 1967a, 1967b; Hirshberg, 1968). The occurrence of geomagnetic storms at these times is attributed to the arrival at the earth of a plasma shell containing the gas ejected from the flare at the solar surface. The existence of an ambient plasma in interplanetary space

implies that the flare-ejected material will be preceded by a collision-free supersonic shock (Gold, 1959).

Associations of observed solar flares with particular geomagnetic storms yield sun-earth transit times of between 20 and 70 hours, which imply mean shock velocities of 600 - 2000 km/sec. Direct observations of shock waves in interplanetary space by spacecraft tend to confirm the solar flare-interplanetary shock-geomagnetic storm concept (Sonnet et al., 1964; Taylor, 1969; Gosling et al., 1968; Ogilvie et al., 1968).

Hirshberg (1968) has examined the intensities of geomagnetic storm sudden-commencements as a function of the central meridian position of the associated flares, and concluded that there is a considerable departure from sun-centred symmetry, with shocks expanding on much broader fronts. A typical shock front at the earth could be approximated by a sphere of radius 0.6 A.U. centred 0.4 A.U. from the sun.

Direct measurements of the magnetic field vector on both sides of the shock front can be used to compute the normal vector of the shock (Ogilvie and Burlaga, 1969). Shock normals determined from direct space-probe measurements tend to be grouped about the radial direction, although the deviations from the radial imply non-spherical symmetry about the sun in some cases. Taylor (1969) arrived at similar conclusions from magnetometer observations aboard Imp 3. Shock normals which are strongly inclined to the ecliptic plane have been reported by several observers (Bame et al., 1968; Hirshberg et al., 1970;

Greenstadt et al., 1970) and it has been suggested that the shock front may be tongue-shaped (i.e. a flattened disc) rather than an axially symmetric body of rotation.

Hundhausen (1970) has listed 27 shock observations which have been reported in the literature, and deduced the average characteristics of this statistical sample. The mean shock propagation speed was 500 km/sec, or about 100 km/sec higher than the mean solar wind velocity, and the normals to shock-fronts deviated from the radial direction by an average angle of 30°. The mean transit time of the shock to 1 A.U. was 55 hours, yielding a calculated mean propagation speed of 730 km/sec. This value is considerably larger than the average propagation speed measured by spacecraft at 1 A.U., and suggests a deceleration of the shocks in interplanetary space (Ogilvie and Burlaga, 1969).

The theoretical treatment of the propagation of solar wind disturbances involves the integration of time-independent conservation equations for mass, momentum and energy, which even in the one-fluid equations are complicated and require additional simplifications. Dryer (1967) made a first approximation for the case of a simple blast by assuming the ambient plasma density to be invariant with distance from the sun, and the solar wind to have zero velocity. The shock velocity relative to the earth, and the energy released, were then readily found from classical blast wave theory, with values of 450 km/sec and 10^{32} ergs respectively.

Models based on the similarity solutions of the hydrodynamic equations have been developed by Simon and Axford (1966) and Lee and Chen (1968). Similarity theory can be used together with satellite data to estimate limits for the energy in the solar wind disturbance following the shock, and hence for the energy released by the solar flares. Dryer and Jones (1968) obtained energy values in the range 10^{30} to 10^{32} ergs for such disturbances.

The hydrodynamic equations have also been integrated numerically without any simplifying assumptions by Hundhausen and Gentry (1969). The entire range of time-scales for energy deposition in the disturbance at the sun, from sharp impulsive blast waves to continuous deposition, have been considered. A shock of arbitrary strength was introduced into the ambient solar wind by changing the fluid parameters at 0.1 A.U.; the post-shock values were maintained for a duration T, and then the ambient conditions were resumed. For values of T very much less than the shock transit time from sun to earth, the properties of the wave were shown to be functions only of the total energy, W, in the blast. The ambient solar wind conditions assumed at 1 A.U. were, a velocity of 395 km/sec, a proton density of 12 cm^{-3} and a temperature of 5×10^4 ^{o}K. The inner boundary for the calculation was set at 18 solar radii.

In a particular case computed by Hundhausen and Gentry, the blast wave was initiated with a density jump of 4 and a shock velocity of

2000 km/sec at the inner boundary. The plasma parameters were returned to their ambient levels 2.1 hours after initiation, giving a total energy input of 1.6×10^{33} ergs. Figure 3.2 shows the velocity and density profiles as functions of heliocentric distance for periods of 2, 4 and 20 hours after initiation. It can be seen that the shock has not decreased in strength nor been significantly decelerated in transit. This solution, though in poor agreement with the observed properties of interplanetary shocks, illustrates the basic shock propagation characteristics. When disturbances with lower energies were considered, the solutions indicated much greater deceleration of the blast. Figure 3.3 shows the relationship between the total energy, W, and the transit time to 1 A.U. for the numerical blast wave solutions, using the same ambient solar wind conditions given above. The blast is seen to be significantly retarded at the lower energies typically observed in the medium ($\sim 3 \times 10^{31}$ ergs).

The theoretical models described up to this point have been based on the assumption that the flare-produced disturbance is spherically symmetric. However, as we have noted earlier, there is considerable evidence that shock normals deviate from the radial direction in many observations. Numerical solutions for non-spherical shock waves have been recently derived by De Young and Hundhausen (1971). Figure 3.4(a) shows the shock-front geometry as a function of the time after initiation of a disturbance initially occupying a cone of half-angle 15°. The initial disturbance velocity was 1000 km/sec at 0.1 A.U. with a total

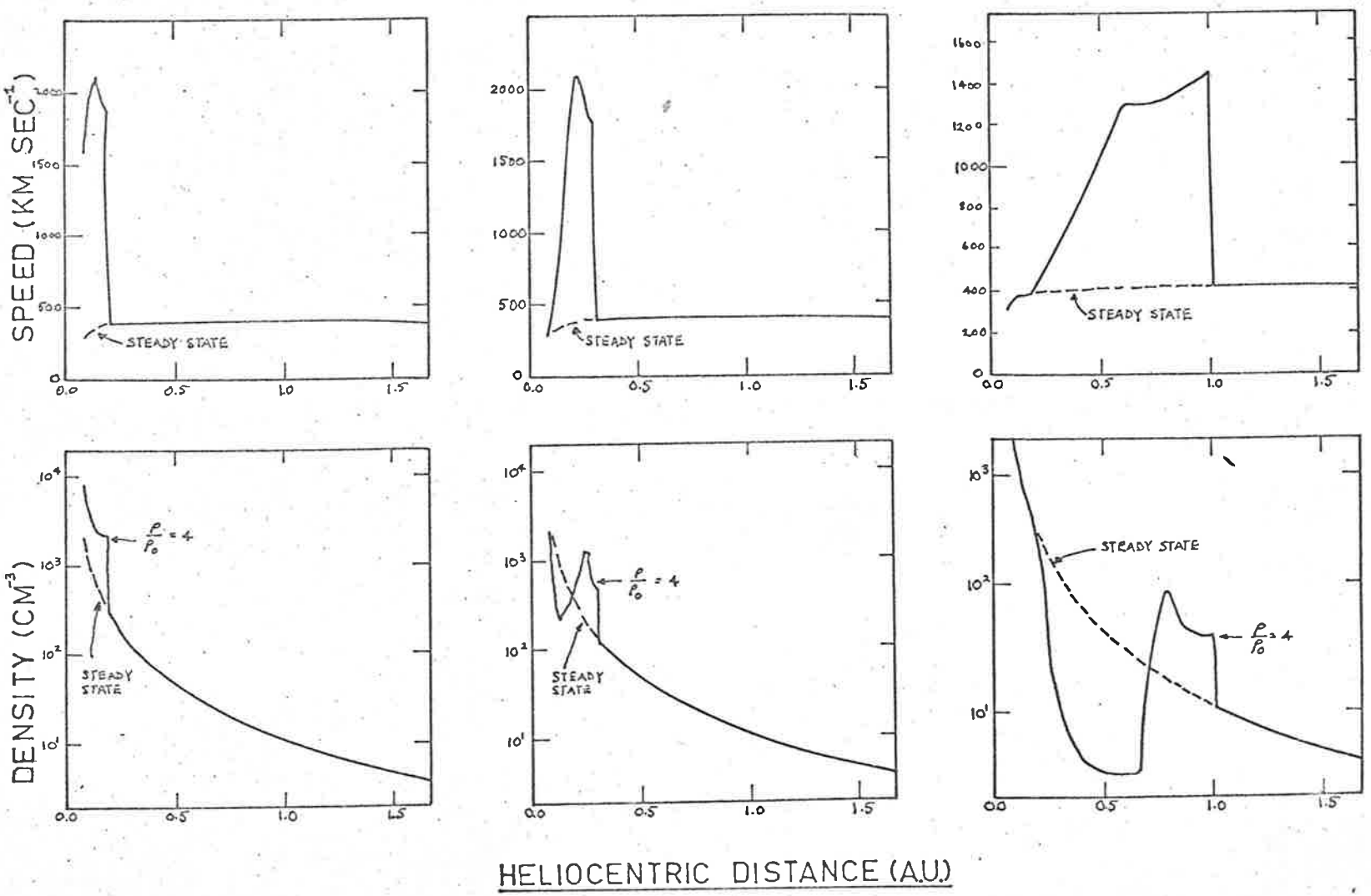

Figure 3.2 Solar wind flow speed and density as functions of heliocentric distance 2, 4.3 and 20.1 hours after shock initialization (after Hundhausen and Gentry, 1969).

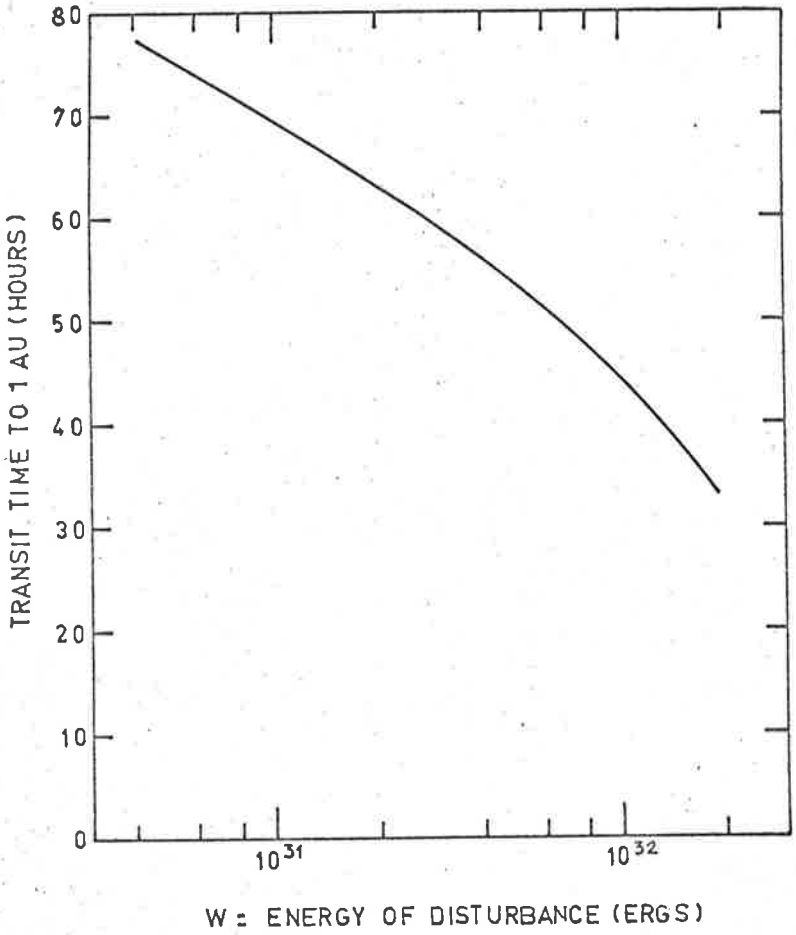

Figure 3.3 The transit time to 1 AU for blast waves with energy W in a 400 km/sec solar wind with a density of 12 protons/cc at 1 AU.

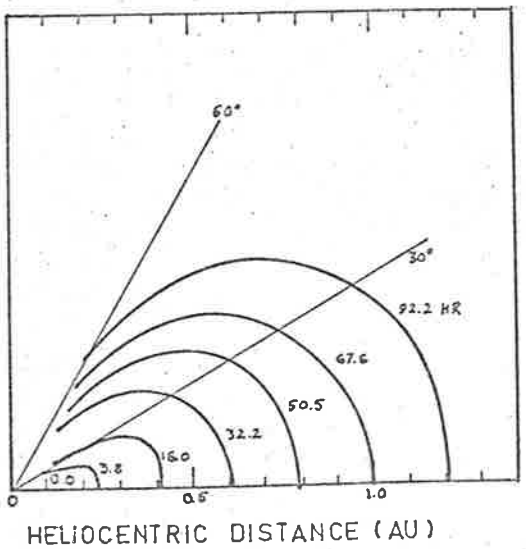

(a)

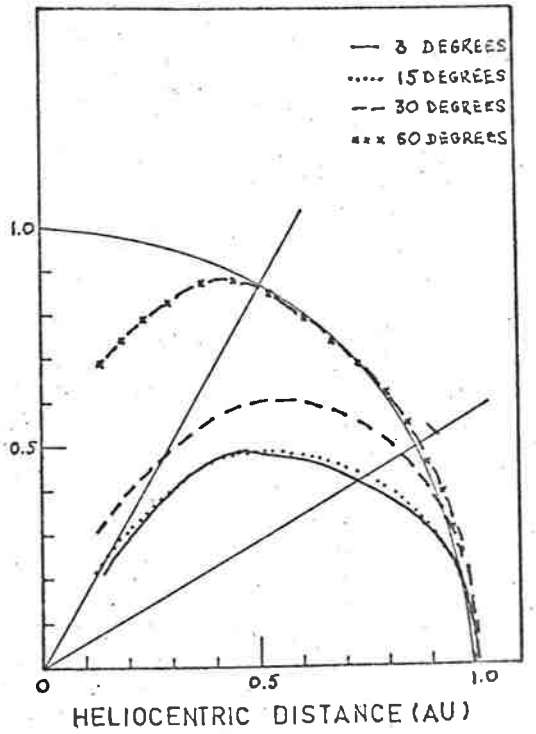

(b)

Figure 3.4 Shock front shape (a) as a function of elapsed time for an initial cone half angle of 15°, (b) at 1 AU for constant energy as a function of the initial cone half angle. The symmetry axis is along the bottom of the figures.

energy of 2.8 x 10^{30} ergs. Figure 3.4(b) indicates the computed shock-front shapes at 1 A.U. for a constant energy disturbance having varying initial cone half-angles at 0.1 A.U. These solutions indicate that the disturbance geometry is relatively insensitive to the initial angular extent for half-angles up to about 15°. In this range the shock-front shows a roughly spherical geometry at 1 A.U. with a centre of curvature near 0.5 A.U. This result was found to be generally independent of the initial disturbance energy for energies in the range 10^{29} to 10^{31} ergs, provided that a constant mass was maintained. The predicted shock profiles at 1 A.U. for cone half-angles less than 15° agree reasonably well with those inferred by Hirshberg (1968) from the observed intensities of geomagnetic storms, and are also roughly in agreement with the distribution of shock normals observed by Ogilvie and Burlaga (1969). The average energy of the disturbances (3 x 10^{31} ergs) predicted by De Young and Hundhausen is in good agreement with the values obtained from the integration of observed energy fluxes.

Although the non-spherical solutions of De Young and Hundhausen can account for the deviations from spherical symmetry suggested by Hirshberg (1968) and Taylor (1969), the observation of several shocks strongly tilted out of the ecliptic plane (Bame et al., 1968; Hirshberg et al., 1970; Greenstadt et al., 1970) cannot be accounted for in this model. Hundhausen (1970) has suggested that one possible means of producing such highly non-spherical shock configurations, would be a high degree of asymmetry in the ambient solar wind as a function of solar latitude.

However, further observational data outside the ecliptic plane are required to evaluate this hypothesis.

3.5 Geomagnetic Activity

The generally accepted relationship between solar and geomagnetic activity via interplanetary blast waves has been challenged by Ballif and Jones (1967, 1969a, b). These authors suggest that individual flares are not the cause of either Forbush decreases or geomagnetic storms. They claim that both of these effects can be accounted for entirely by corotating interplanetary streams. Bell (1961) observed that 'there is no one-to-one correlation between major flares and geomagnetic storms,' and that a large percentage ($\sim$ 50%) of even bright and optically impressive flares are not followed by any significant effect in the earth's magnetic field.

Ballif et al., (1971) have analysed solar flare data and cosmic ray count-rates for a 10 year period from 1958-1968 and conclude that it is possible to account for all of the observed cosmic ray decreases by assuming the existence of corotating interplanetary structures associated with flare-producing regions on the sun. An epoch analysis of 76 cosmic ray decreases and of the occurrence of solar flares at the same time (Ballif et al., 1971) indicated that flare producing regions tend to pass central meridian just before ($\sim$ 3 days) the cosmic ray events were observed at the earth. Thus if flares are observed in active regions which are near central meridian, they may appear to be the cause of

geomagnetic storms, which are in fact caused by the interaction of the earth's magnetic field with the irregular magnetic field structures of the associated stream. There must, of course, be a wide range in the intensity, duration and dimensions of such streams to account for the large variations in the observed geomagnetic events.

To determine the relative importance of blast waves and streams in the initiation of geomagnetic events would ideally require a number of space-probes arranged at various distances and elongations from the sun to map the course of such disturbances through the interplanetary medium. This is not possible at present with existing space-probes.

Sharp and Harris (1967) have suggested that large increases in the interplanetary scintillation of radio sources observed after substantial solar activity, can be used to resolve such questions. Careful monitoring of a grid of radio sources which are known to scintillate would be a powerful method in determining the geometry and movement of such disturbances in the interplanetary medium.

The author adopted this suggestion as the basis for the present study of the large-scale movements of the interplanetary plasma, and the development of this technique and the results obtained will be presented in the following chapters.

CHAPTER 4

RESULTS I - MAY 1968

Introduction

In this chapter we present the results of some preliminary observations made in May 1968, together with a description of the equipment used and a summary of the observing procedure.

The interpretation of the present observations is based on the discussion of large-scale structures in the solar wind, given in the previous chapter.

4.1 The Culgoora Radioheliograph

The observations to be described in this, and the following chapters, were carried out using the 80 MHz radioheliograph (Wild, 1967) at the C.S.I.R.O. Solar Observatory, Culgoora, New South Wales. A description of the instrument and of the particular mode of operation employed for our observations will facilitate the discussion of the experimental results.

The radioheliograph consists of 96 steerable parabolic reflectors each 13 metres in diameter with crossed dipole feeds. The aerials are equally spaced around the perimeter of a circle 3 km in diameter (Figure 4.1), the signals received at each aerial being returned to a central control room along open wire transmission lines for processing by a special-purpose computer. By the addition of suitable phase delays

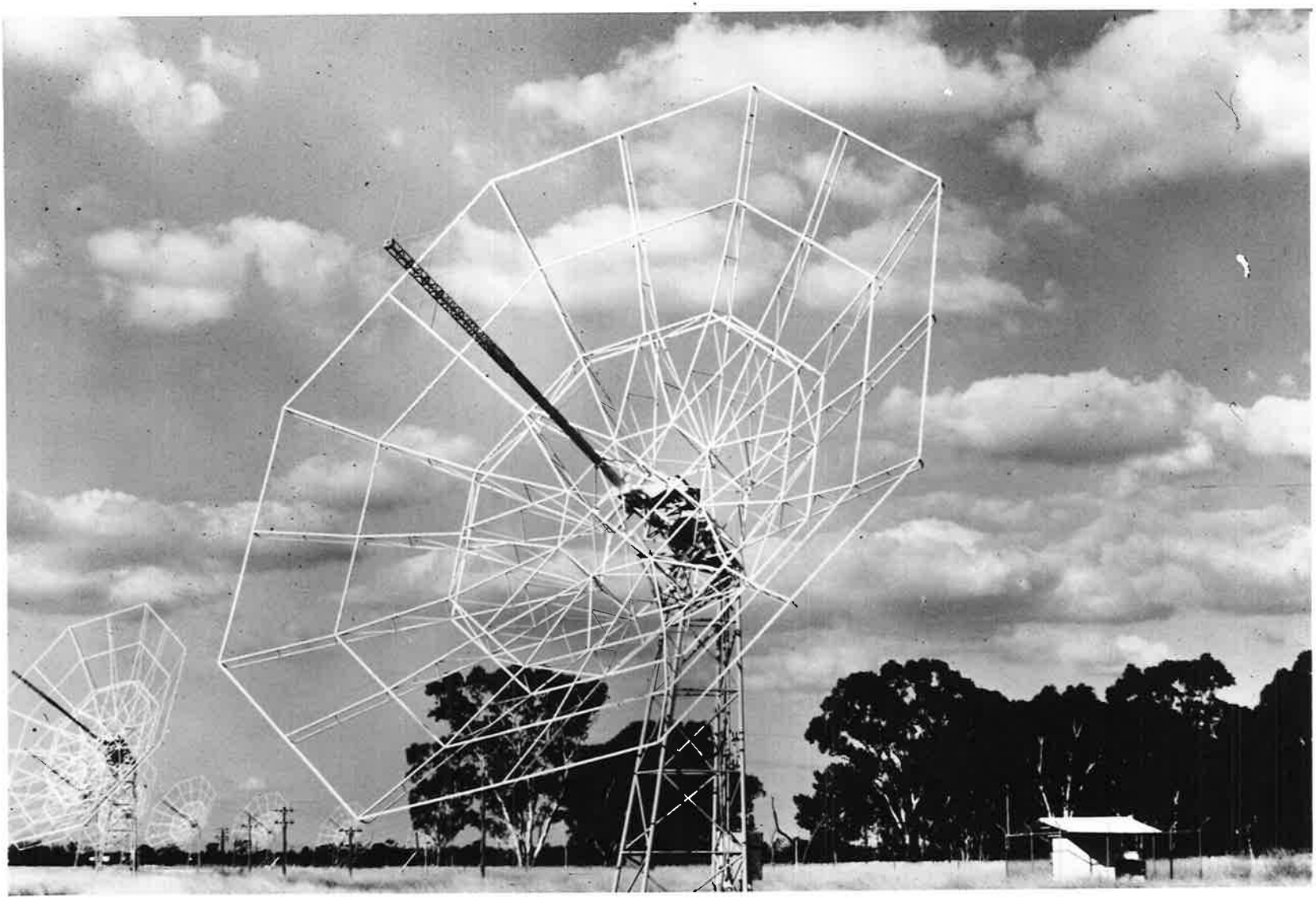

Figure 4.1

in the appropriate aerial feed lines the computer synthesizes 48 simultaneous receiving beams equally spaced in declination along a north-south line.

The 2^{o} field of view is scanned incrementally by the 48 beams in an east-west direction to produce radio pictures of the sun, 60 points wide in right ascension and 48 points wide in declination. Each beam has a width of 3.5 minutes of arc to half-power points, with adjacent beams separated by 2.1 minutes of arc at the zenith. Two pictures, one in each sense of circular polarization, are formed every second and displayed on cathode ray tube monitors for photographic recording. The pictures are also recorded digitally on magnetic tape for later computer averaging and analysis.

The bandwidth of the heliograph receiving system is limited to a rectangular 1 MHz response in the IF (intermediate frequency, 7 MHz) stages. These are followed by detectors which have a square-law characteristic thus producing an intensity (power) output display.

When the 96 elements of the array are connected together in phase the radial profile of the resulting power polar diagram has the form (Wild, 1967),

$$I(r) = J_{o}^{2} (2 \pi a r) \qquad (4.1)$$

where J_{o} is a Bessel function of zero order, r is the angular displacement from the centre of the pattern and a is the radius of the annulus. Because the receiving annulus is made up of discrete aerials,

the central field pattern is surrounded by unwanted grating responses at an angular distance λ/d, where d is the spacing between aerial elements and λ is the radio wavelength. These responses were made to lie outside the 2° picture field by a suitable choice of aerial spacing, d. The central field pattern is normally corrected by the process of J^2-synthesis (Wild, 1967), which involves the addition of higher order Bessel functions with appropriate weights to the J_o^2 (uncorrected) beam to suppress unwanted side-lobe responses. This is achieved at the expense of some loss of main beam resolution. The two beams, J_o^2 and J_n^2 are shown in Figure 4.2 for comparison. The J_n^2-synthesis technique is important in the observation of active regions on the sun where large side-lobes would sample neighbouring 'hot' regions on the solar disc. However, for the observation of extra-galactic radio sources of small angular diameter, side-lobe responses are less critical, except perhaps where sources lie in close proximity.

4.2 The Observing Procedure

For the present observations the heliograph was operated in the J_o^2 mode with the uncorrected beam. A stationary line of beams in the north-south direction was formed by inhibiting the computed scanning function, which normally traverses the 2° field of view. The position of these beams could then be set automatically by appropriate phasing of the 96 incoming signals. The six central beams of the north-south line were recorded on two 3-channel pen recorders together with time reference markers. A recording speed of 160 mm/minute was used for

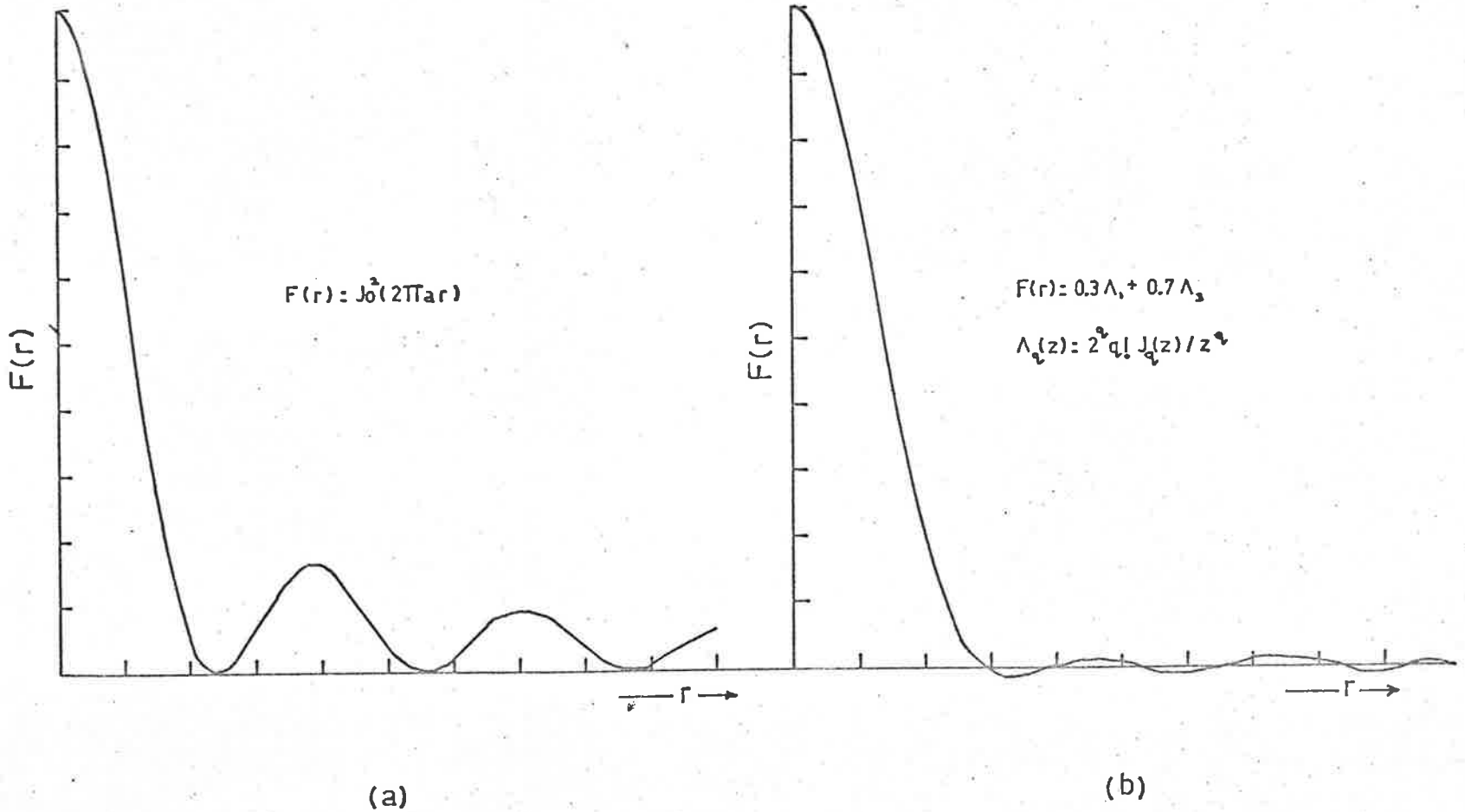

Figure 4.2 The in-phase, J_o^2, beam and the computer synthesized J_n^2 beam.

recording the scintillation. The procedure adopted was to first allow a source to transit the six central declination beams, and in the absence of ionospheric refraction the main source response would occur on the central beam, which in this case was a specially synthesized beam midway between beams 24 and 25. Thus beam '24½' was separated from beams 24 and 25 by 1' arc in declination, and for a point source a reduced signal would be recorded on the two adjacent beams due to the overlap of their responses. After the first transit, the beams were moved west of the source by computer-controlled phase manipulation, and the transit was repeated. This allowed accurate measurement of the relative source strength for future calculation of the scintillation index. The beams were moved west of the source once again and then computer directed tracking was initiated at source transit. Each source was tracked and recorded for 10 minutes to obtain a representative sample of its scintillation, followed by a shorter section of noise from a neighbouring region of the sky. On and off-source data were also recorded digitally on magnetic tape at a sampling rate of 32 sec^{-1}, and with a time constant of 0.05 second. The pen recorder time constants were 0.1 second.

It should be noted that the simultaneous monitoring of six declination beams around the actual source position provided certain very useful advantages. Firstly, it enabled scintillation to be followed in the presence of declination drifts of the source caused by ionospheric refraction, and secondly, the continuous recording both on

and off-source allowed the effects of solar noise bursts to be recognised. The few records affected by solar noise were generally discarded because of the difficulty in separating the solar and scintillation effects, which tend to have overlapping frequency power spectra.

4.3 Analysis of Scintillation Records

The paper chart records were analysed by hand to determine the scintillation index, F, defined in Chapter 2 as,

$$F = \frac{< (I(t) - I_o)^2 >^{\frac{1}{2}}}{I_o} \qquad (4.2)$$

where < > denotes a temporal average, I(t) is the intensity of the signal at time t and I_o the mean intensity < I(t) >. The pen recordings were direct intensity records and so the index, F, could be calculated directly from the chart. Dennison (1967) has shown that the index can be represented with little loss of accuracy by the relative half-width of the intensity probability distribution (P.D.) of the scintillation. The procedure for determining the intensity P.D. of a non-regular function of time is a tedious one however, and a convenient short-cut has been described by Orhaug (1965).

If we consider the random time-varying signal shown in Figure 4.3, the probability density p(A) is defined as,

$$p(A1) = \lim_{\Delta A \to 0} \left\{ \frac{1}{T} \sum \Delta t_i \right\},$$

for a particular level, A1, where T is the total length of data and $\Sigma\, t_i$

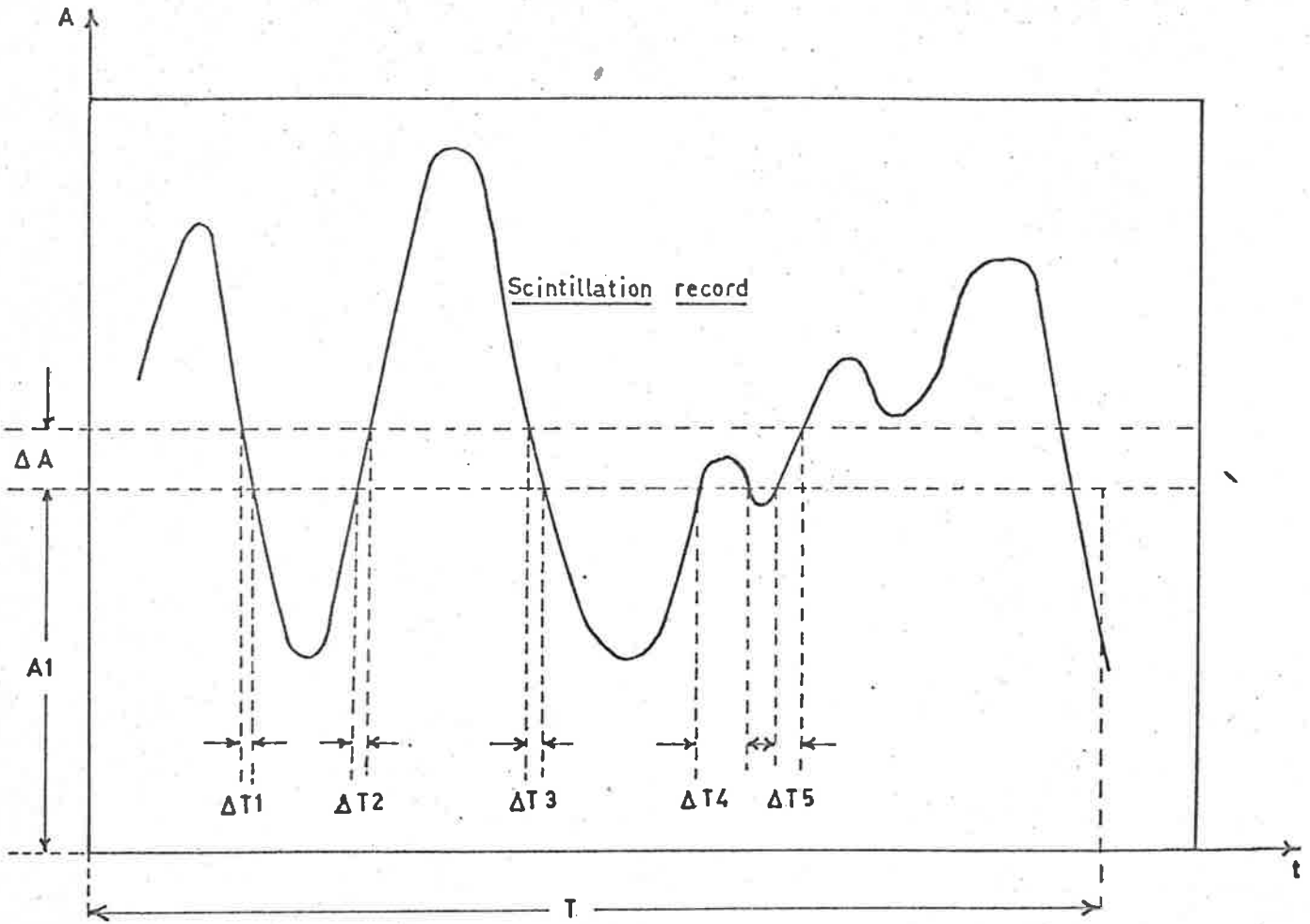

Figure 4.3 Calculation of the probability density of a random time varying signal.

is the total portion of time for which the amplitude A(t) is within the range ΔA. Rice (1944) has shown that the expected frequency with which the envelope passes through the amplitude level A with positive slope is,

$$N_A = \text{const} \cdot p(A) . \qquad (4.4)$$

This equation gives a convenient method for determining the probability density function of a scintillation record. The density function p(Al) is simply proportional to the number of times the scintillation signal crosses the amplitude level Al. The scintillation index, F, approximated by the relative half-width of the distribution was calculated in this way for each source on each day of observation. A typical index calculation is shown in Figure 4.4.

Scintillations of the nine sources listed in Table I were recorded each day, together with representative sections of noise from neighbouring regions of the sky. The scintillation indices for on-source records were corrected for the effects of noise using the relation,

$$F = \frac{(I_{S\frac{1}{2}}^2 - I_{N\frac{1}{2}}^2)^{\frac{1}{2}}}{< I >} , \qquad (4.5)$$

where $I_{S\frac{1}{2}}$ and $I_{N\frac{1}{2}}$ are the half-widths of the signal and noise intensity probability distributions.

4.4 Discussion of Results

The observations to be described in this chapter were carried out during the period May 24-29, 1968. In our analysis of these results we have assumed that the dominant region of scattering for a particular radio source, was normally at the point of closest approach to the sun of

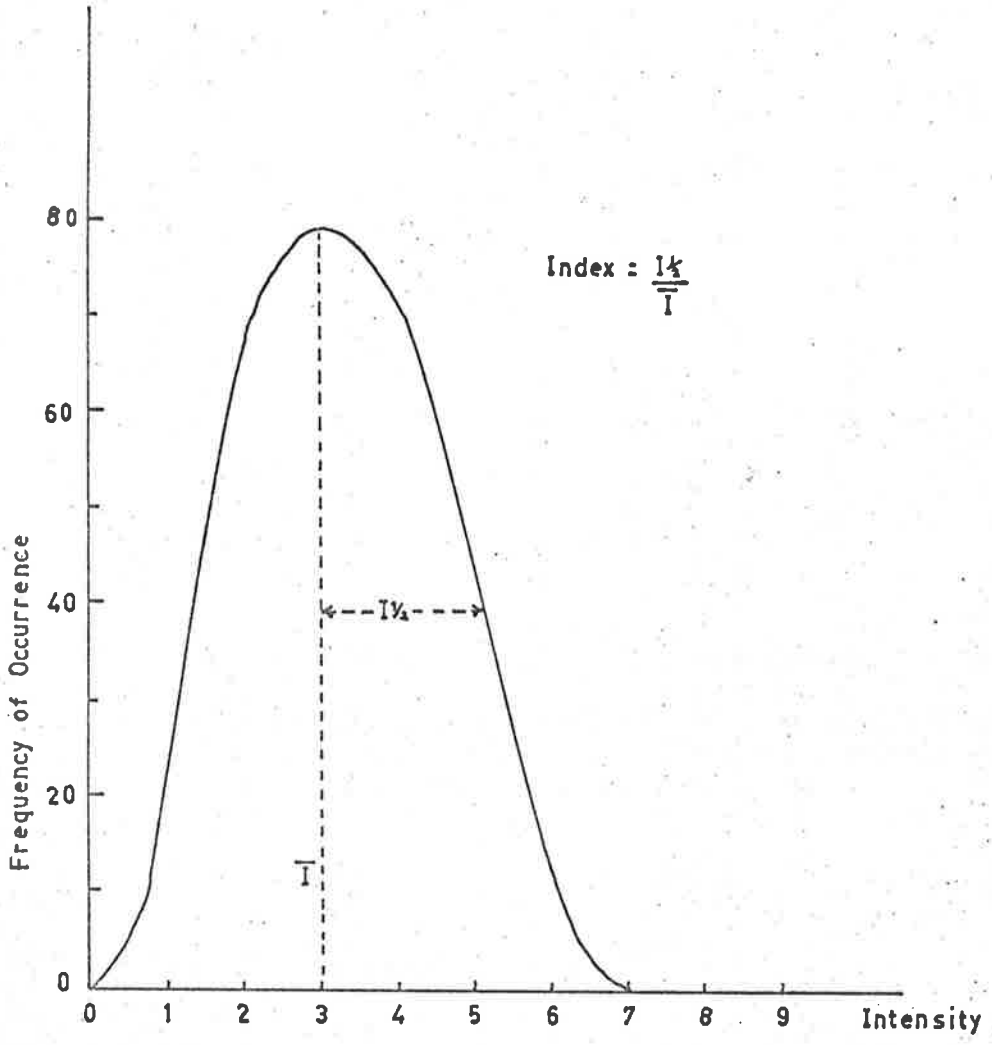

Figure 4.4 Calculation of the scintillation index from the probability density distribution.

Source	β	P(AU)	∅
0003-00	-01°	0.92	-02°
0134+32	+22°	0.60	+31°
0624-05	-28°	0.68	-39°
0758+14	-06°	0.82	-11
0933+04	-09°	0.99	-07°
1226+02	+04°	1.0	00°
1309-22	-15°	1.0	00°
1416+06	+19°	1.0	00°
2313+03	+08°	0.98	00°

TABLE I

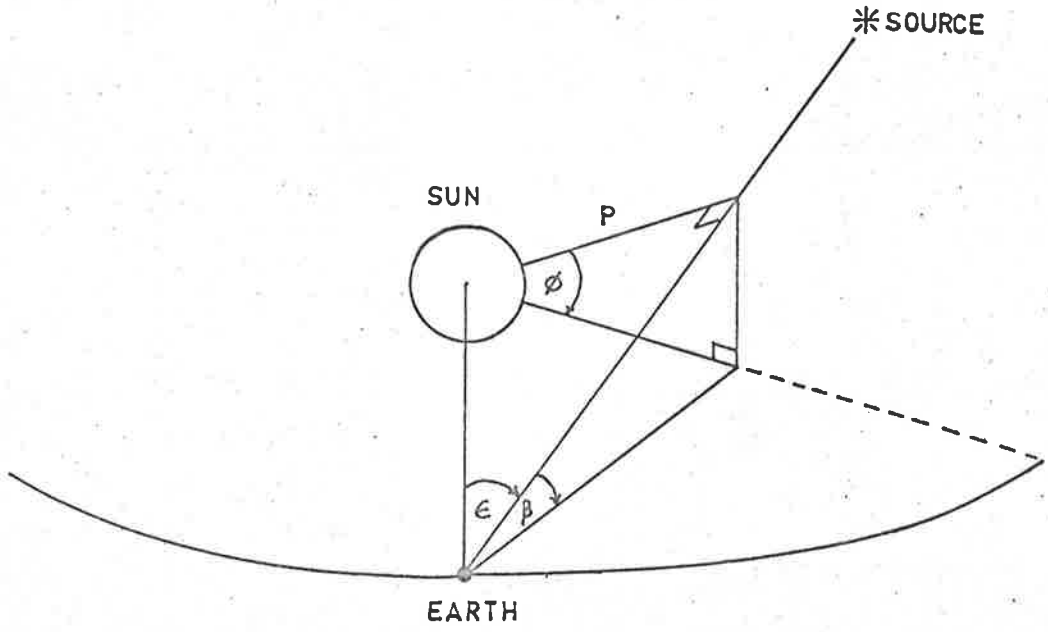

Table I Heliocentric coordinates of the line of sight to a radio source.

its line of sight to the earth. This appears to be a reasonable assumption since the density of the plasma (and presumably the fluctuations in density also) decreases with radial distance from the sun approximately as r^{-2}.

Significant changes in the scintillation indices were observed from day to day, and in Figure 4.5 sections of a record for one of these sources (0134+32) are shown, where the index increased by a factor of 2 from May 27-28. In Figure 4.6 the indices for the nine sources from May 24-29 are plotted. Unfortunately the observing session was interrupted on several days by strong solar noise storms and consequently there were gaps in the data for some sources. It can be seen from Figures 4.6 and 4.7 that enhancements in scintillation index tended to occur sequentially across sources whose lines of sight were spaced in order from the sun's eastern limb. Figure 4.7 shows the line of sight to each source projected onto the plane of the ecliptic. The ecliptic latitude is listed in Table I and shown beside each source number in Figure 4.7. It is difficult to explain the observed changes in scintillation indices in terms of a radially expanding blast of plasma from the solar surface, when the time sequence of the enhancements are considered. However, the observations did appear to be consistent with the movement of a radial stream of plasma corotating with the sun, and the variations in the indices will be discussed in terms of such a model.

In Figure 4.8 the source positions of Figure 4.7 are redrawn with

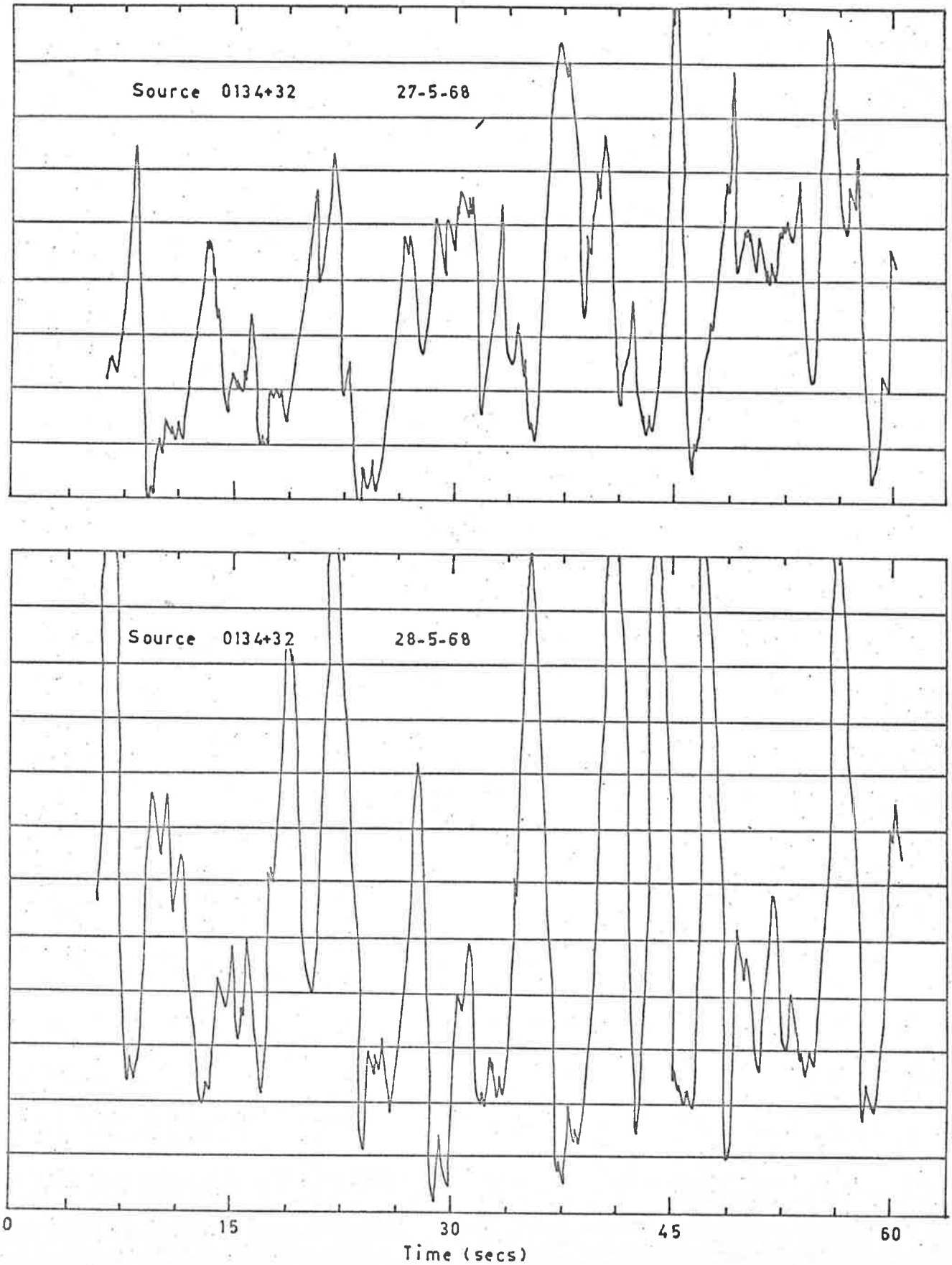

Figure 4.5 A significant change in the scintillation of source 0134+32 from May 27 to May 28.

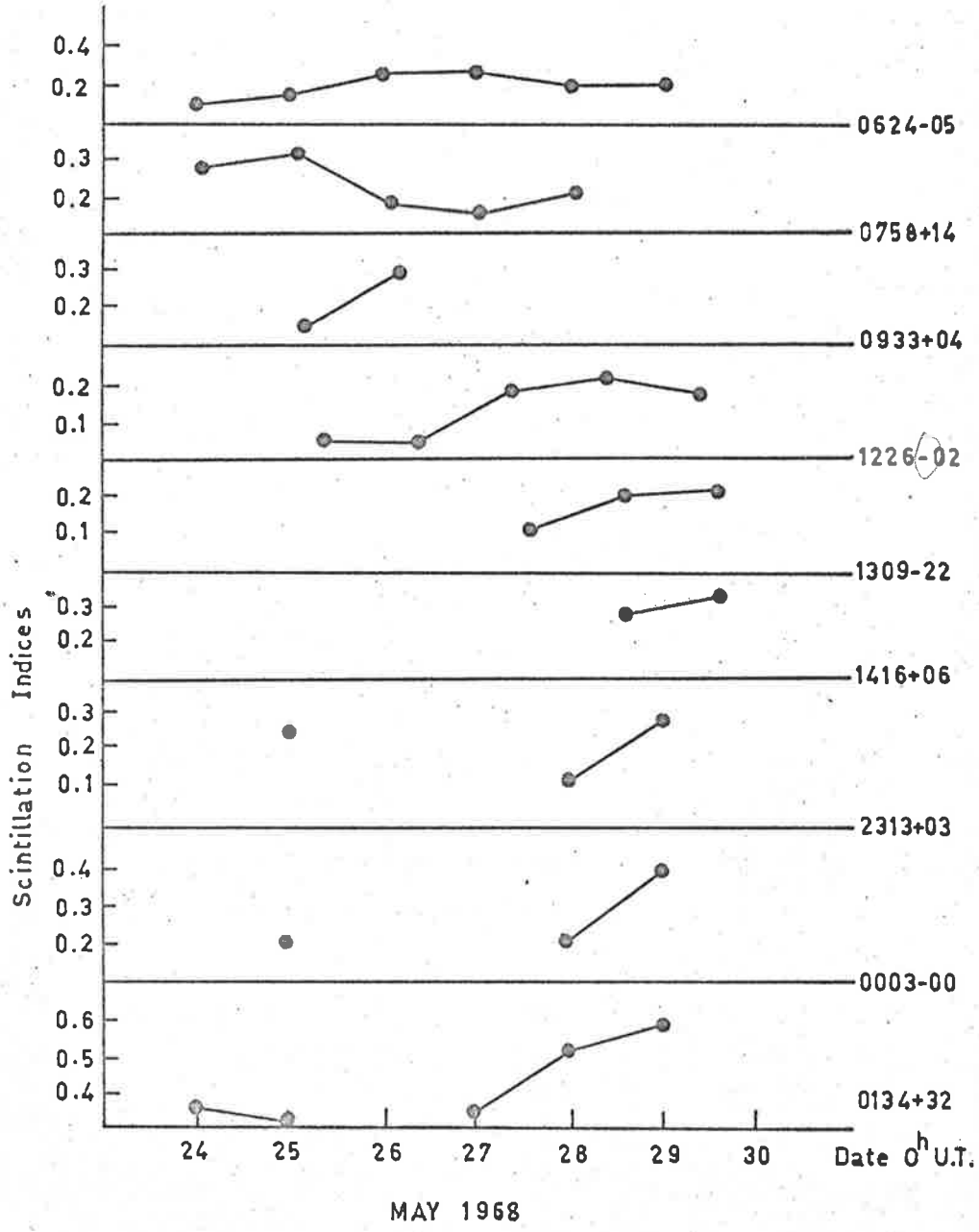

Figure 4.6 Scintillation indices for nine sources in May 1968.

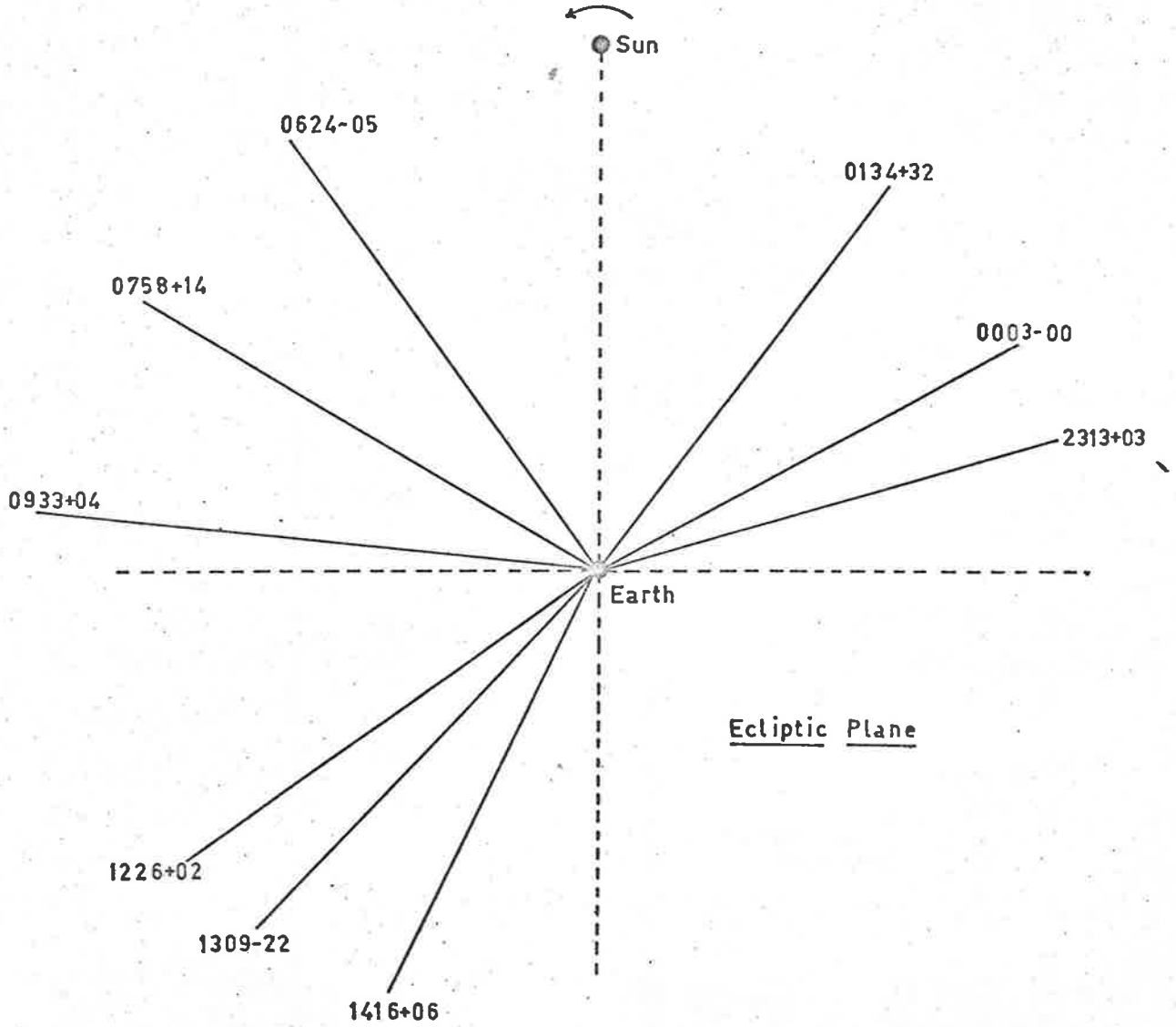

Figure 4.7 The line of sight to each radio source projected onto the ecliptic plane.

the positions of the leading edge of the proposed stream on consecutive days superimposed. The spiral geometry is drawn assuming a solar rotation period of 27 days with a constant solar wind velocity of 400 km/sec. To estimate the position of the stream, the time at which it intercepted the earth was determined from its effects on sources 1226+02, 1309-22 and 0134+32. Since the lines of sight to these sources lie nearly parallel to the leading edge of the stream a sudden increase in scintillation activity will determine the position of the stream boundary. As can be seen from Figure 4.8 the line of sight to 1226+02 should be affected first, followed after a short period by 1309-22 and 0134+32, all of which in fact showed an increase late on May 27. The earth became embedded in the stream by May 28 and the indices for 2313+03 and 0003-00 increased by 200% between May 28 and 29. Other solar and geomagnetic activity indices tended to confirm the time of interception of the stream by the earth and will be considered later in the chapter. It should be realised that the suggested sequence of events is completely dependent upon the spiral geometry of the stream and hence on the solar wind velocity. A stream velocity in the range 300 - 500 km/sec was inferred from the data on this basis. A lower velocity stream for example would have a more tightly wound spiral and would therefore have affected 0134+32 before 1226+02, while a higher velocity stream would sweep through the lines of sight producing time delays between sources again considerably different from those observed.

The extent of the stream in the ecliptic plane is not indicated in

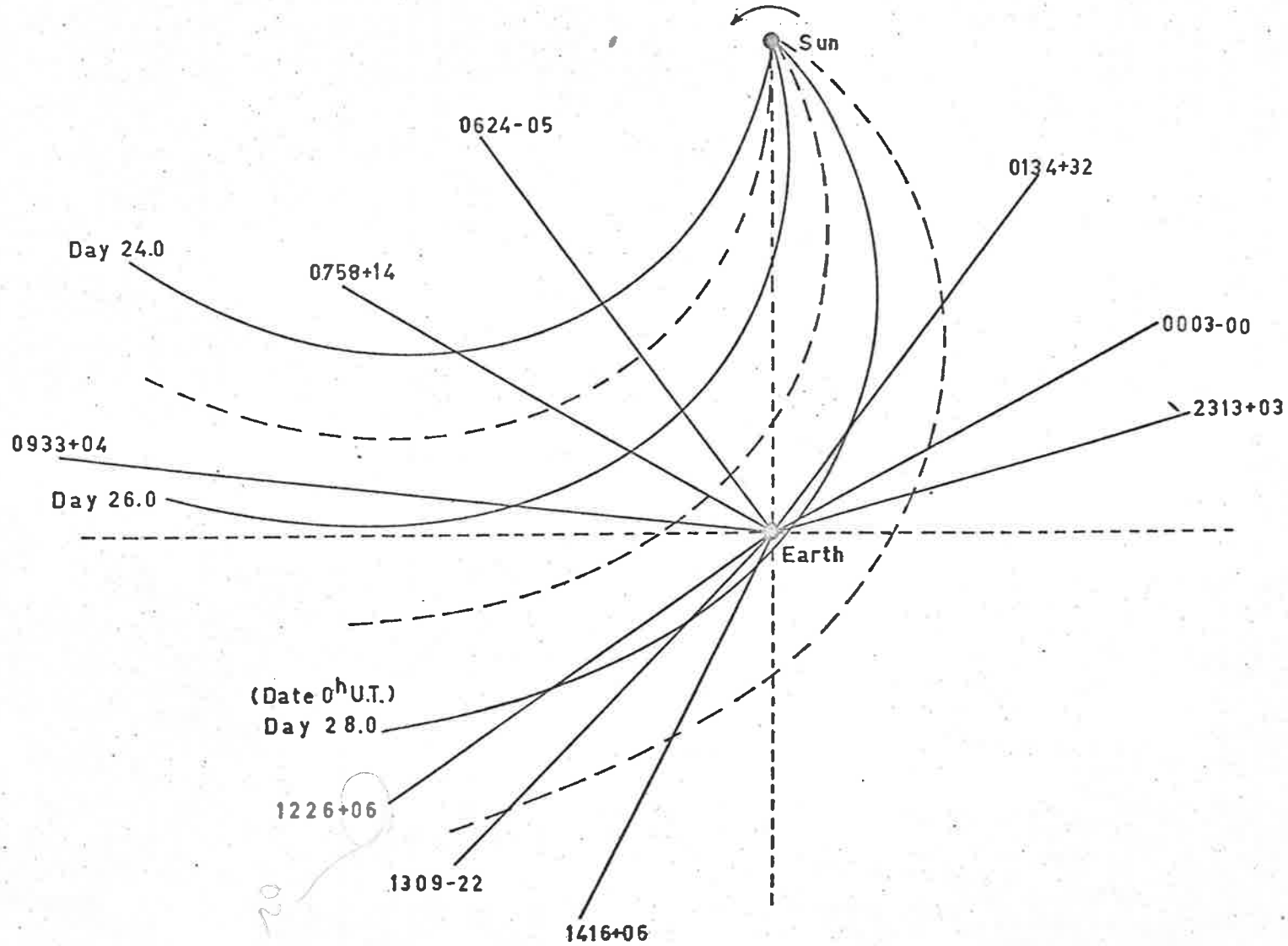

Figure 4.8 The leading edge of the proposed stream structure on consecutive days.

Figure 4.8 but the observations did allow a useful limit to be placed on this parameter. The duration of the enhanced scintillation for the sources 1226+02 and 1309-22 must be closely related to the width of the stream in the ecliptic plane. The observed duration of 2-3 days indicated a width of approximately 0.5 astronomical units at the orbit of the earth. It must be realised, however, that due to the curvature of the stream the far regions of the line of sight from the earth would still be affected by the stream after it has passed over those regions closer to the earth. This effect must be allowed for in any estimate of the stream width. Readhead (1971), has calculated the contribution to the scintillation index of different parts of the interplanetary medium along the line of sight from a monochromatic point source. These are reproduced in Figure 4.9 for various values of the solar elongation, ε. For 1226+02 and 1309-22 ($\varepsilon > 135^{\circ}$) it can be seen that 70% of the contribution to the scintillation index occurs over a distance of only 0.6 A.U. from the earth, so that the effect of far regions of the line of sight is comparatively small in this case and can be neglected. Thus our estimate of the stream width is probably correct to within 20%.

Having fixed the time at which the stream met the earth we now consider the remaining sources to examine their agreement with the model so far defined. The source 0758+14 showed enhanced scintillation up to May 25 and then a decrease by a factor of 2 on May 26 (from 0.30 to 0.16). The index remained low on succeeding days even though the line of sight to the earth still intercepted the stream until May 28. This is to

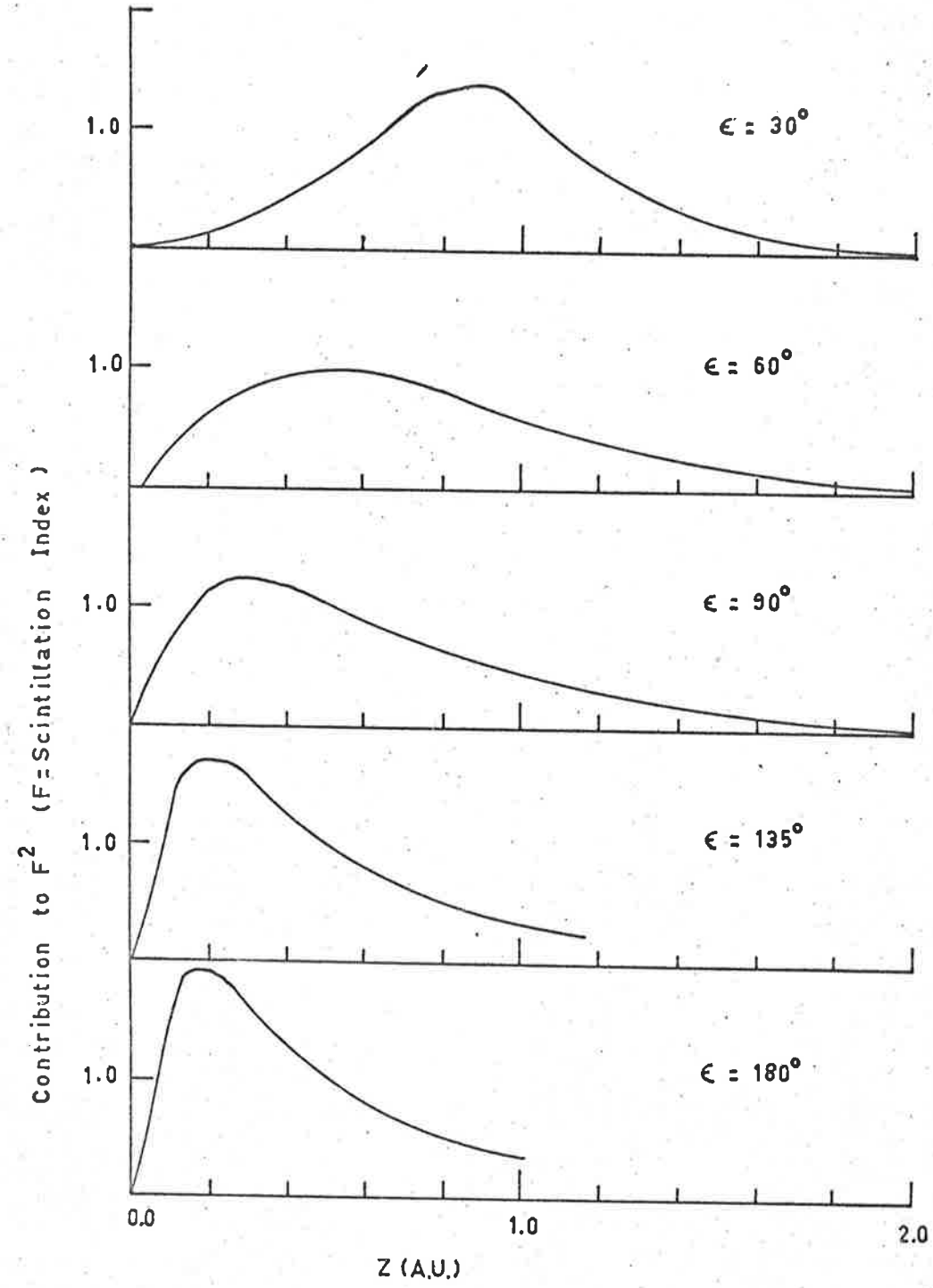

Figure 4.9 The contribution to the scintillation index squared of different parts of the interplanetary medium along the line of sight from a monochromatic point source (after Readhead, 1971).

be expected if the stream was of finite width, as we have suggested. It can be seen from Figure 4.8 that a stream of width 2 days would have intersected the line of sight to 0758+14 over the region 0.5 - 2.5 A.U. on May 25. However, on May 26 only the region between 0.3 and 0.7 A.U. on the line of sight would have been affected. Thus the effective enhanced scattering region was considerably reduced from one day (25) to the next (26) due to the stream geometry. The source 0933+04 was observed and recorded on only two days due to interference from severe solar noise storms. On May 25-26 the index increased by 100% in agreement with the proposed stream location for those days. No major changes in scintillation index were observed for 0624-05 although moderate scintillation was apparent during the whole of the observing period. A slight enhancement on May 26 and 27 was barely significant. A possible reason for this is the comparatively small region of the line of sight to the earth which was affected by the stream. However, if we consider this slight increase in index within the context of our model there appears at first sight to be a discrepancy, in that the enhancement of 0624-05 occurred one day later than the increase in index of 0758+14. This apparent anomaly is removed when the ecliptic latitude of the sources are considered. The line of sight to 0624-05 is 28 degrees below the ecliptic plane so that unless the stream was of indefinite extent perpendicular to the ecliptic, the source would not have been affected until the stream moved closer to the earth. A sketch of a possible stream configuration perpendicular to the ecliptic plane

is shown in Figure 4.10. This sketch is purely qualitative and is included to indicate that a more complete grid of radio sources out of the ecliptic plane should allow more quantitative limits to be placed on stream geometry outside the ecliptic.

4.5 Scintillation Power Spectra

The greatest uncertainty in the model discussed so far is the location of the predominant scattering region along the line of sight. In principle, the form of the scintillation power spectrum can provide additional information about the distance, z, from the scattering region to the observer.

When a plane monochromatic wave is incident upon a thin scattering region of phase-changing irregularities (the 'screen'), the emergent wave can be represented (Ratcliffe, 1956) as the sum of a specular (unscattered) plane wave of nearly unit amplitude and a number of plane waves of various amplitudes travelling at different angles with respect to the specular component. This is referred to as the angular spectrum of the emergent wave. Close to the screen the scattered wave amplitudes are in phase quadrature with the unscattered component and the resultant wave field has constant amplitude but random fluctuations in phase. Moving away from the screen the successive side waves of the angular spectrum produce their own components of amplitude modulation in succession; the wide angle components corresponding to the small spatial periods within the screen producing their full effects close to

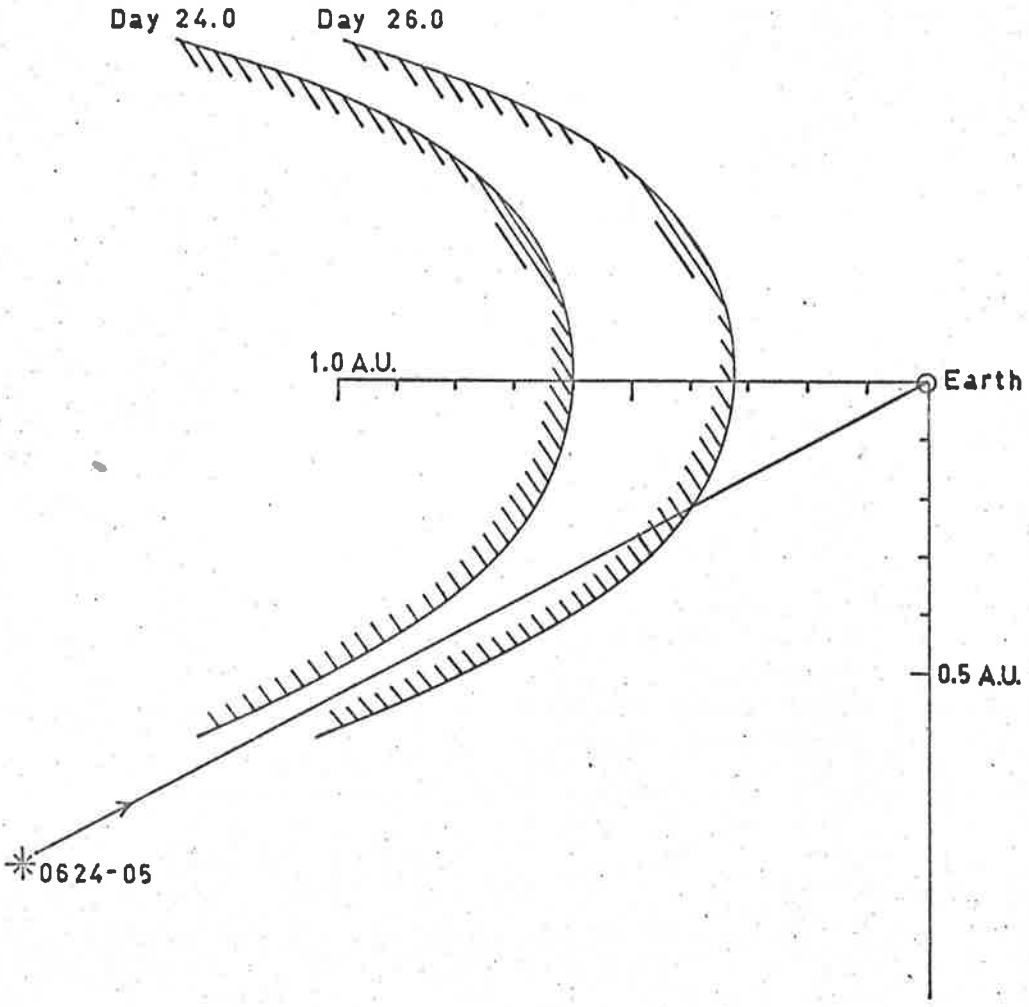

Figure 4.10 A possible stream configuration perpendicular to the ecliptic plane.

the screen and the small angle components corresponding to the larger spatial periods producing their effects further away. Thus the power spectrum of the intensity fluctuations close to the screen will show a deficiency of power at low frequencies which will become less significant and disappear as the distance from the screen increases.

The spectral analysis of scintillation records for this session was undertaken following the approach of Blackman and Tukey (1958). The magnetic tape data was a time series of discrete data points with a sampling interval of 1/32 sec. A low pass filter was applied to the data by use of a simple 3 point average, producing a new time series I(t) having a sampling interval of 3/32 sec. The mean value was computed and then subtracted from the data before the computation of the autocovariance function,

$$C(\tau) = \frac{1}{T - \tau} \sum_{t = 0}^{Tm} I(t)\, I(t + \tau) \qquad (4.6)$$

out to a maximum lag $\tau = T_m$. The autocorrelation function $C'(\tau)$ was formed by normalising the autocovariance function $C(\tau)$ with the sample variance, i.e. $C(0)$. Power spectral estimates were then computed from the finite cosine Fourier transform of the autocorrelation function,

$$P(f) = C'(0) + 2 \sum_{\tau = 1}^{m} C'(\tau)\, \mathrm{Cos}\, \frac{\pi f \tau}{m} + C'(m)\, \mathrm{Cos}\, (f \pi) \; . \qquad (4.7)$$

These estimates were found to exhibit some degree of instability and so the raw spectral data were convolved with a Hamming spectral window,

$$P_k(f) = 0.23\, P_{k-1}(f) + 0.54\, P_k(f) + 0.23\, P_{k+1}(f) \qquad (4.8)$$

which effectively reduced both the statistical variance of each

estimate and the leakage of power between adjacent spectral estimates. The Hamming spectral window was preferred to the more frequently used Hanning window since the highest side-lobe of the Hamming window in the time domain is only one-third of the highest side-lobe for the Hanning window. This advantage is offset slightly by the fact that the height of the side-lobes for the Hamming window do not fall off as rapidly as those for the Hanning window.

The spectra of the scintillations were finally obtained by subtracting the off-source (noise) spectrum from the on-source spectrum. Computations were carried out using the CDC 6400 computer at the University of Adelaide, a special program having been written to complete the analysis which we have discussed. Each 'block' of data was 90 sec in length and sampled at a frequency of 32 samples per second. After averaging over 3 points and removing the mean from the data the autocorrelation function was computed out to a maximum lag (T_m) of 50 points, i.e. 5% of the total data length. The spectrum resolution is given by,

$$\text{Res} = \frac{1}{2T_m} = 0.11 \text{ Hz} . \qquad (4.9)$$

On particular occasions the computed spectra were observed to show depressions at low frequencies. The data were in good agreement with the model we have proposed in that the depressions tended to occur on those occasions when the stream intercepted a limited region of a line of sight close to the earth. Some spectra from the source 0134+32 (the strongest

scintillator observed) are shown in Figure 4.11 for four days from 25-29 May. For each day four spectra are shown from independant blocks of data, to illustrate the changes which typically occur in the character of the scintillations over periods ∿ minutes. The shapes of the spectra can be seen to change considerably over the four days and those for May 28 show marked depressions at low frequencies, which is in good agreement with the position of the stream deduced from the observed changes in scintillation indices. The undisturbed spectra (May 25 for example) were often close to Gaussian. On May 29 the spectra did not exhibit any noticeable low frequency depression which was possibly due to the blurring effect of the extended scattered region in which the line of sight was immersed.

The significance of the low frequency dips in the spectra is determined by the statistical variability of the individual spectral estimates. It has been shown (Blackman and Tukey, 1958) that the variance of a spectral estimate is given by,

$$\text{Var} = \frac{T_m}{T} P^2(w) \cdot \frac{1}{1.3} \qquad (4.10)$$

where T_m is the maximum lag of the autocovariance function, T is the effective length of data and P(w) is the value of the spectral estimate. The factor 1.3 accounts for the effect of the Hamming spectral window. Applying this to our present data we obtain,

$$\text{Var} = 0.04\ P^2(w)$$

$$\text{i.e.} \qquad \text{rms error} = 0.2\ P(w)\ . \qquad (4.11)$$

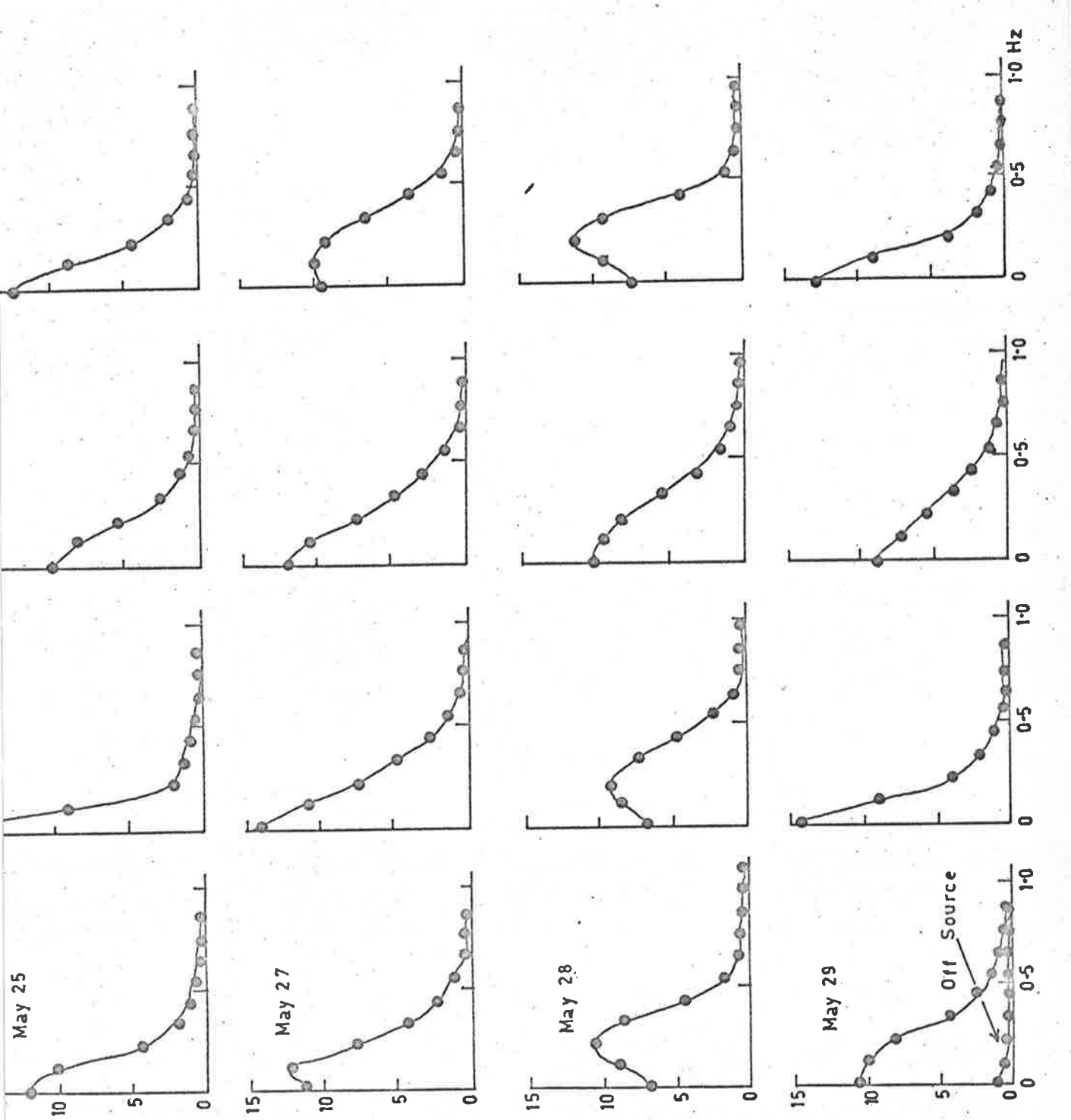

Figure 4.11 Power spectra of the interplanetary scintillations of the source 0134+32.

Thus the rms error in a spectral estimate is 20% of its value. One of the spectra of Figure 4.11 exhibiting a low frequency depression has been redrawn in Figure 4.12 showing the errors associated with each point. It can be seen that the depression is a real effect and not due to statistical variability.

Bowhill (1961) has shown quantitatively how the spectrum due to scattering from a thin phase screen with rms phase deviation $\phi_o < 1$ radian changes with distance, z, from the screen. The power spectrum of the intensity fluctuations observed at distance, z, is given by

$$V(X, Y) = P(X, Y) \sin^2 \left(\pi z \lambda (X^2 + Y^2) \right) , \qquad (4.12)$$

where P(X, Y) is the two-dimensional power spectrum of the phase fluctuations at the screen, and X and Y are spatial frequencies in the x and y directions parallel to the screen. It is clear that V(X, Y) has zeros at,

$$X^2 + Y^2 = \frac{n}{\lambda z} \qquad n = 0, 1, 2 \ldots \qquad (4.13)$$

where λ is the radio wavelength. There is also a zero at the origin since X = Y = 0 at n = 0. This is the low frequency depression which we have just discussed. Other zeros in V(X, Y) correspond to components of the angular spectrum which are converted first to amplitude and then back to pure phase variations (Ratcliffe, 1956) as the screen-observer distance increases. Parkin (1967) has considered the case where the spectrum of phase fluctuations at the screen has a Gaussian profile with scale size r_o and axial ratio β,

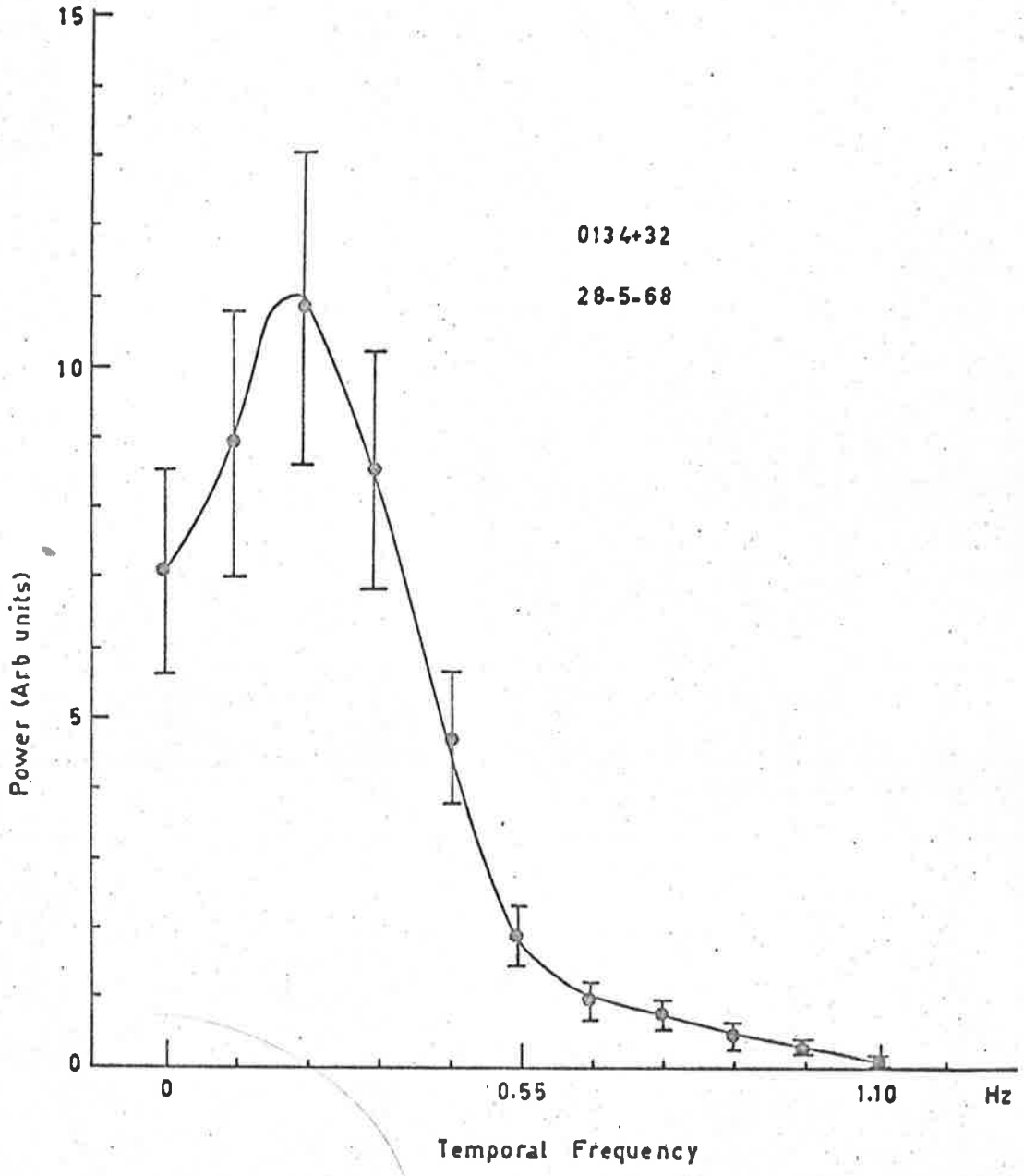

Figure 4.12 Power spectrum of source 0134+32 exhibiting a low frequency depression (20% error bars are shown).

$$P(X, Y) = \exp \left(-\pi^2 \left(r_o^2 X^2 + \beta^2 r_o^2 Y^2 \right) \right) . \qquad (4.14)$$

For the special case in which the pattern is drifting in the x direction and observed at a single receiver, the spectrum has the form,

$$W(X) = \int V(X, Y)\, dY , \qquad (4.15)$$

where $V(X,Y) = \exp \left(-\pi^2 r_o^2 (X^2 + \beta^2 Y^2)\right) \mathrm{Sin}^2 (\pi z \lambda (X^2 + Y^2))$. (4.16)

To compare the experimental power spectra with those predicted on a theoretical basis, the integral, W(X), has been calculated numerically for various values of r_o and z, at a frequency of 80 MHz (λ = 3.75 m). Since the theoretical spectra are referred to spatial frequency, it was necessary to estimate the velocity of the diffraction pattern in order to convert the experimental spectra to temporal frequency before direct comparisons could be made. For this purpose a velocity of 330 km/sec was used as measured by the Explorer 33 and 35 satellites between May 26-29 at geocentric distances of less than 80 earth radii. In addition the theoretical spectra were smoothed using the same spectral window as in the experimental case.

Figure 4.13 illustrates the variation in the shape of the theoretical spectra for a range of r_o and z. For convenience the axial ratio, β, was taken as 1.0; it probably lies in the range 1.0 - 2.0 (Dennison, 1969). A feature of these spectra which appears unusual at first sight, is the relative insensitivity of the size of the low-frequency dip to changes in z, the distance to the screen. This is in fact due to the low spatial frequency of the $\sin^2$ function with respect

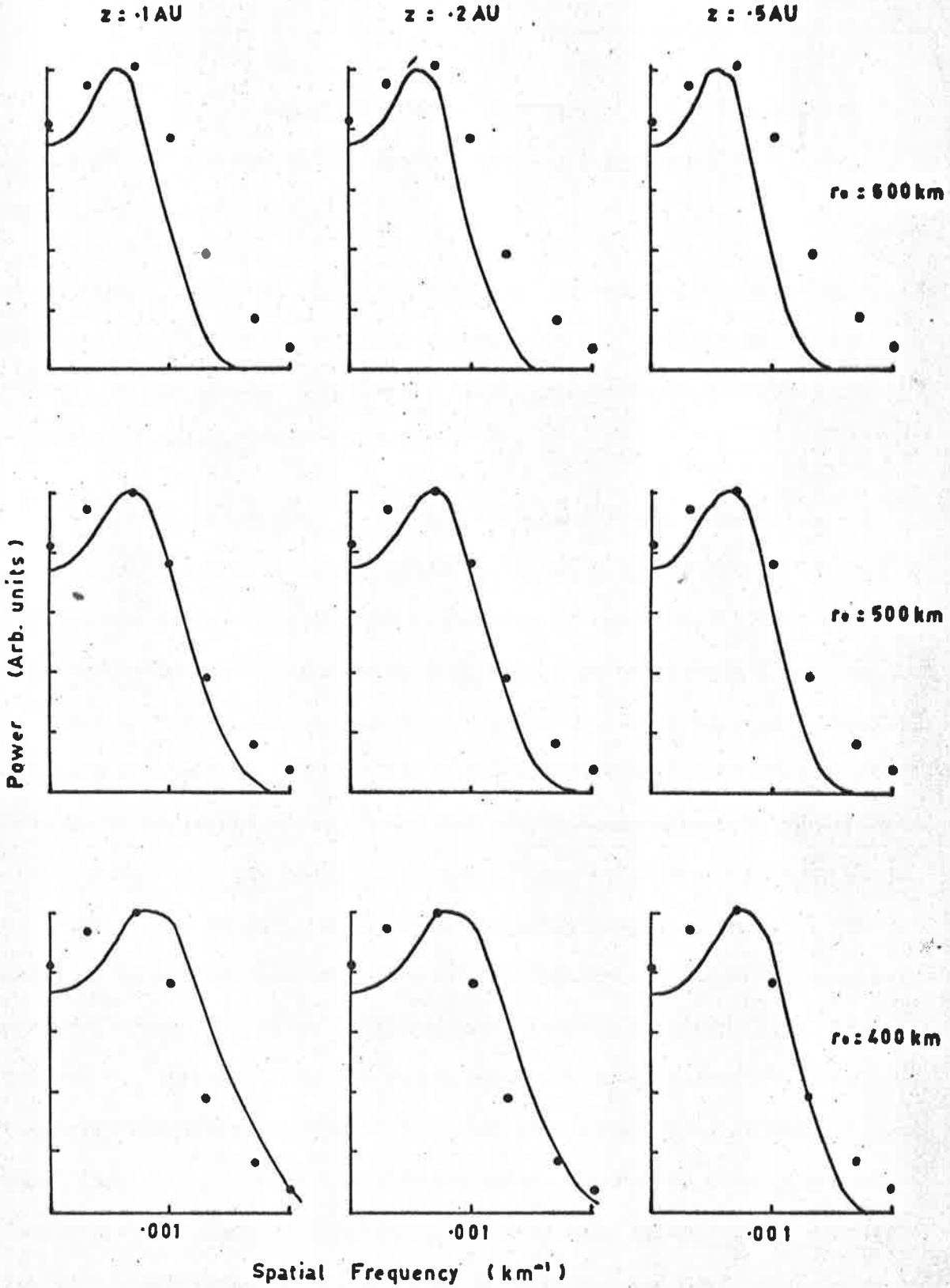

Figure 4.13 The variation in the shape of theoretical spectra for a range of r_o (scale) and z (screen-observer distance).

to the decay of the exponential term in equation 4.16. For smaller values of r_o, the dip at low frequencies would disappear much more rapidly with increasing z.

Using a numerical 'least-squares fit' technique, the best-fit theoretical spectrum to the average experimental spectrum of source 0134+32 on May 28 was calculated. This is shown in Figure 4.14, for values r_o = 500 km and z = 0.2 A.U.

From the persistence of the low-frequency depressions of the theoretical spectra at large distances it would appear that this feature should be observed more frequently in experimental spectra. Blesing (1972) has examined this aspect in some detail and has shown that in general fringes will not be observed for two basic reasons. Firstly, the line of sight to a particular radio source will generally encounter a velocity differential as it samples the various regions of the solar wind through which it passes. This will tend to blur any fringes which might have been produced by a single velocity region. Secondly, the model we have used assumed a thin scattering screen, whereas in general the scattering will occur in an extended layer. Salpeter (1967) has derived an expression for the two-dimensional power spectrum of the intensity fluctuations from an extended scattering layer of width L, and shown that the minima in the spectra become smeared as L is increased. Some practical examples of this effect have been calculated by Ward et al. (1972) and their discussion will not be repeated here.

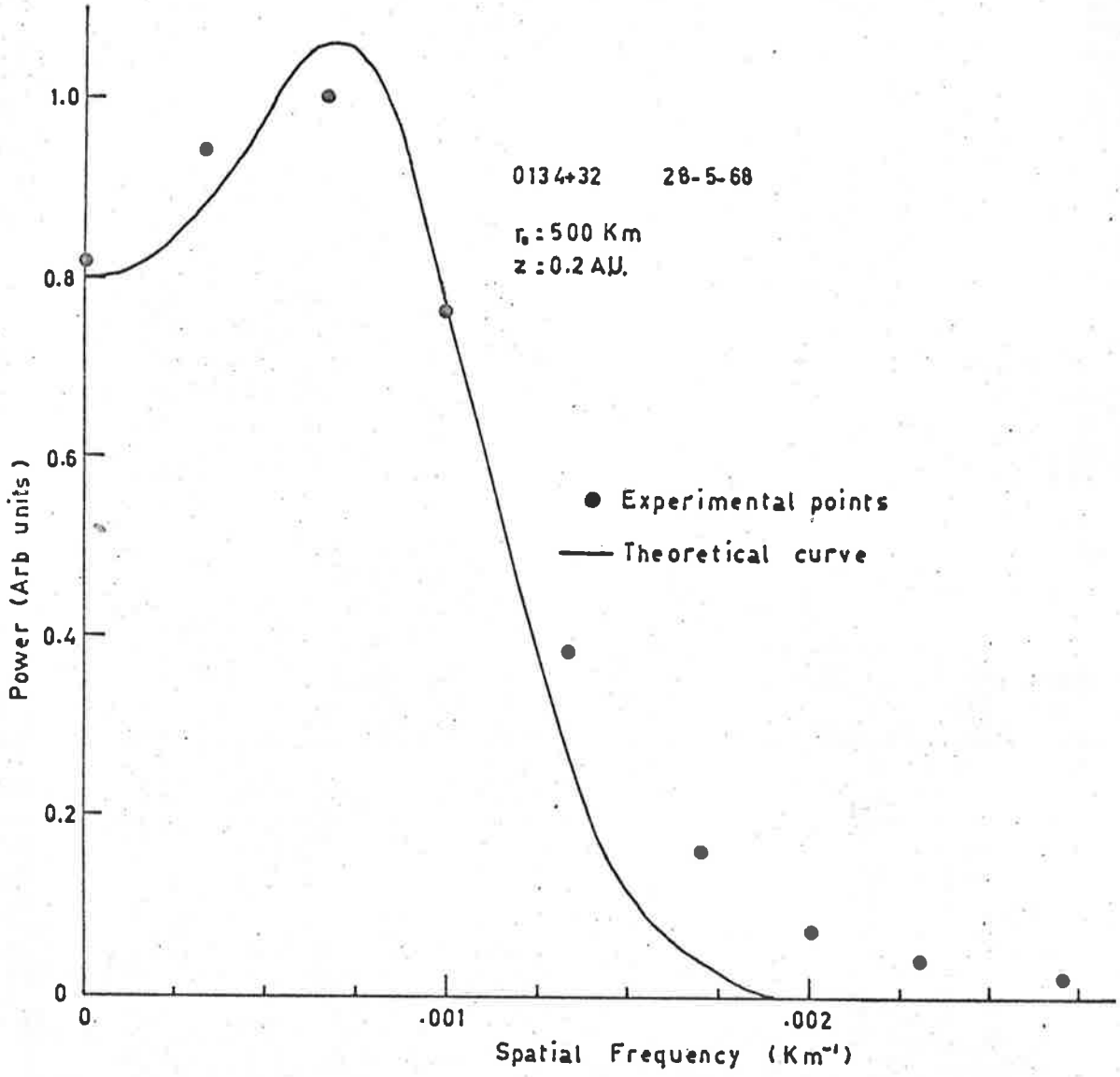

Figure 4.14 The best fit theoretical spectrum (---) to the average experiment spectrum (●) of source 0134+32 on May 28.

Thus the observation of a low-frequency depression in the experimental spectra is an indication of the existence of a well defined, thin scattering region situated at $\sim$ 0.2 A.U. from the earth on May 28. This is confirmed by spacecraft observations of the interplanetary electron density, which will be described in the following section.

The best fit theoretical spectrum of Figure 4.14 required a scale r_o = 500 km. This is very much greater than the scale derived from a correlation analysis of three-station scintillation observations. Dennison (1969) obtained values of r_o $\sim$ 150 km, at 1 A.U. from the sun, from extended observations of the source 3C48. The scale of the irregularities is normally defined as the e^{-1} point of the spatial autocorrelation function of the scintillation. When the screen is close to the earth, however, this method leads to values which are smaller than the actual scale, since the low frequency (large-scale) components still exist mainly as phase fluctuations and the small-scale components dominate the diffraction pattern. Bowhill (1961) has discussed this problem quantitatively, by defining the scale of the density fluctuations in terms of the Gaussian curve which is the best fit to the correlation function near the origin, and examining its dependence upon distance, z, from the screen. The general result is illustrated in Figure 4.15(a), and the measured scale, r, corresponding to a true scale, r_o, of 500 km is shown in Figure 4.15(b). Thus at z = 0.2 A.U. the observed scale will be $\sim$ 290 km, which is in better agreement with the scale size deduced by Dennison (1969), although still

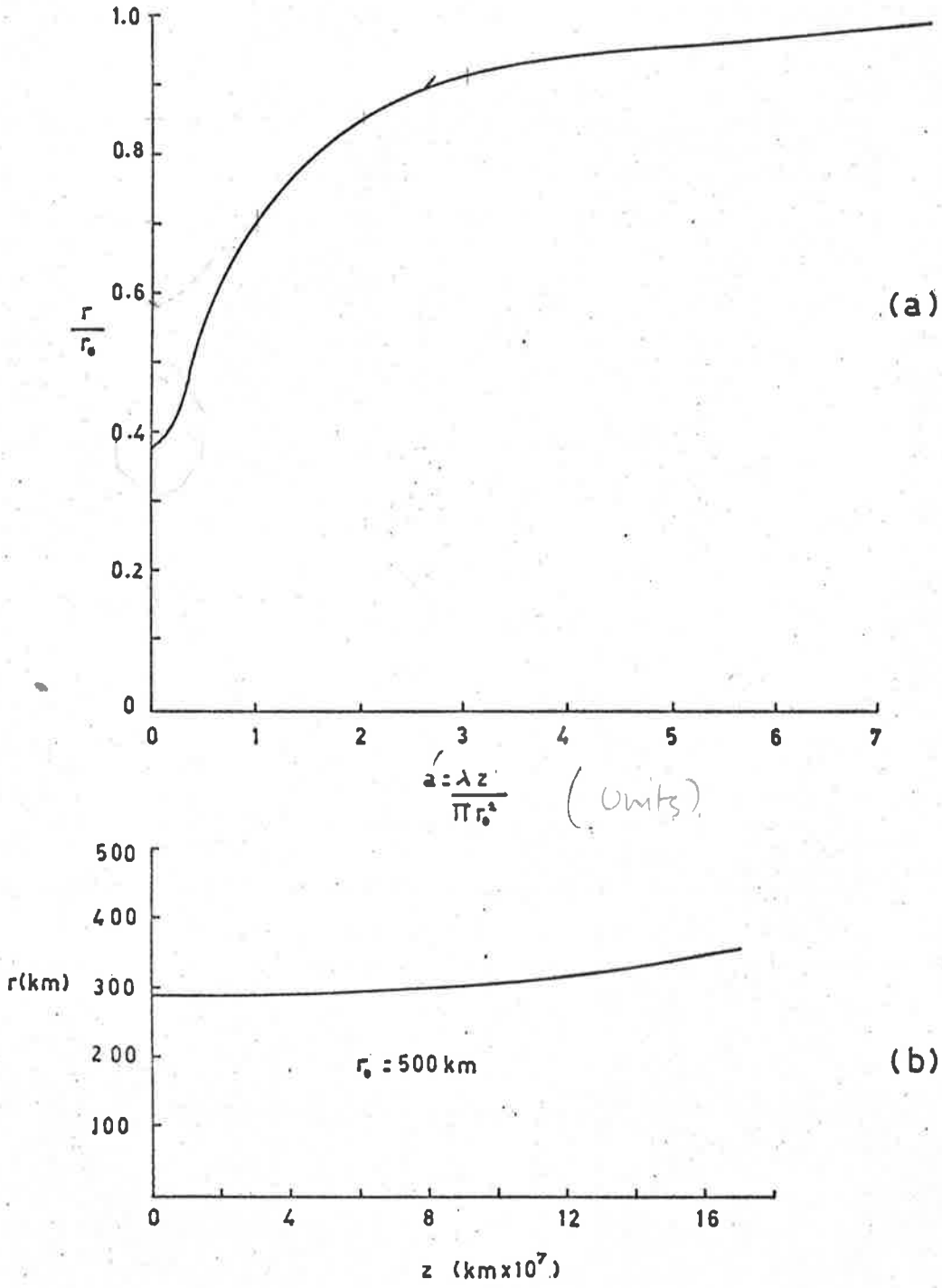

Figure 4.15 The measured (correlation analysis) scale, r, of the density fluctuations corresponding to a true scale, r_o, (after Bowhill, 1961).

see p. 102

significantly larger.

Further information may be gained from a comparison of the relative widths of the scintillation power spectra for a particular source on successive days. An increase in the width of a spectrum can be attributed to either an increase in the solar wind velocity, or a decrease in the characteristic scale of the electron density fluctuations in the medium. The large variations in velocity which are frequently observed by spacecraft in turbulent regions of plasma, might at first sight appear to support the former interpretation.

Figure 4.11 shows that the width of the frequency spectra did increase on May 27 and 28 during the proposed passage of the stream across the line of sight to 0134+32. The half-widths for each of the spectra shown in Figure 4.11 were measured after normalisation, and then an average half-width was calculated for each day,

Half-width (Hz)	May 1968
0.17	25
0.24	27
0.40	28
0.22	29

Thus the average spectrum width increased by a factor of 2.3 between May 25 and 28, during the passage of the stream. The significance of this result will be discussed in the following section in relation to changes in the solar wind parameters measured by spacecraft near the

earth.

4.6 Discussion

Various solar and geophysical parameters made available in the Solar Terrestrial Activity Chart† (1968) were examined in the light of the proposed corotating stream model. Figure 4.16 shows the variation of these parameters during May 1968. Figure 4.16 shows the hourly average values of solar wind velocity, density and interplanetary magnetic field data from Explorer 33 and 35 satellites at geocentric distances of less than 80 earth radii. B = total field intensity, θ = solar ecliptic latitude, northward positive, and ϕ = solar ecliptic longitude with nominal spiral angles 135° (outward) and 315° (inward) being indicated by horizontal lines.

The arrival of the stream at the earth on May 28 can be seen in the sudden increase in the solar wind density (labelled S in the diagram). Several peaks of enhanced density show the complex structure associated with such streams, and one or more of these enhancements were probably the source of the low-frequency depressions observed in the power spectra of 0134+32 on May 28. When only one distinct density enhancement had passed the earth, the conditions for spectral depression would be satisfied. Soon after, the line of sight to 0134+32 would have intercepted a number of these enhancements and the depression would be

† The Solar Terrestrial Activity Chart (STAC-B for January-June 1968) was issued by the Interdisciplinary Analysis Centre for Solar Terrestrial Activity, National Committee on Solar Terrestrial Physics, Science Council of Japan.

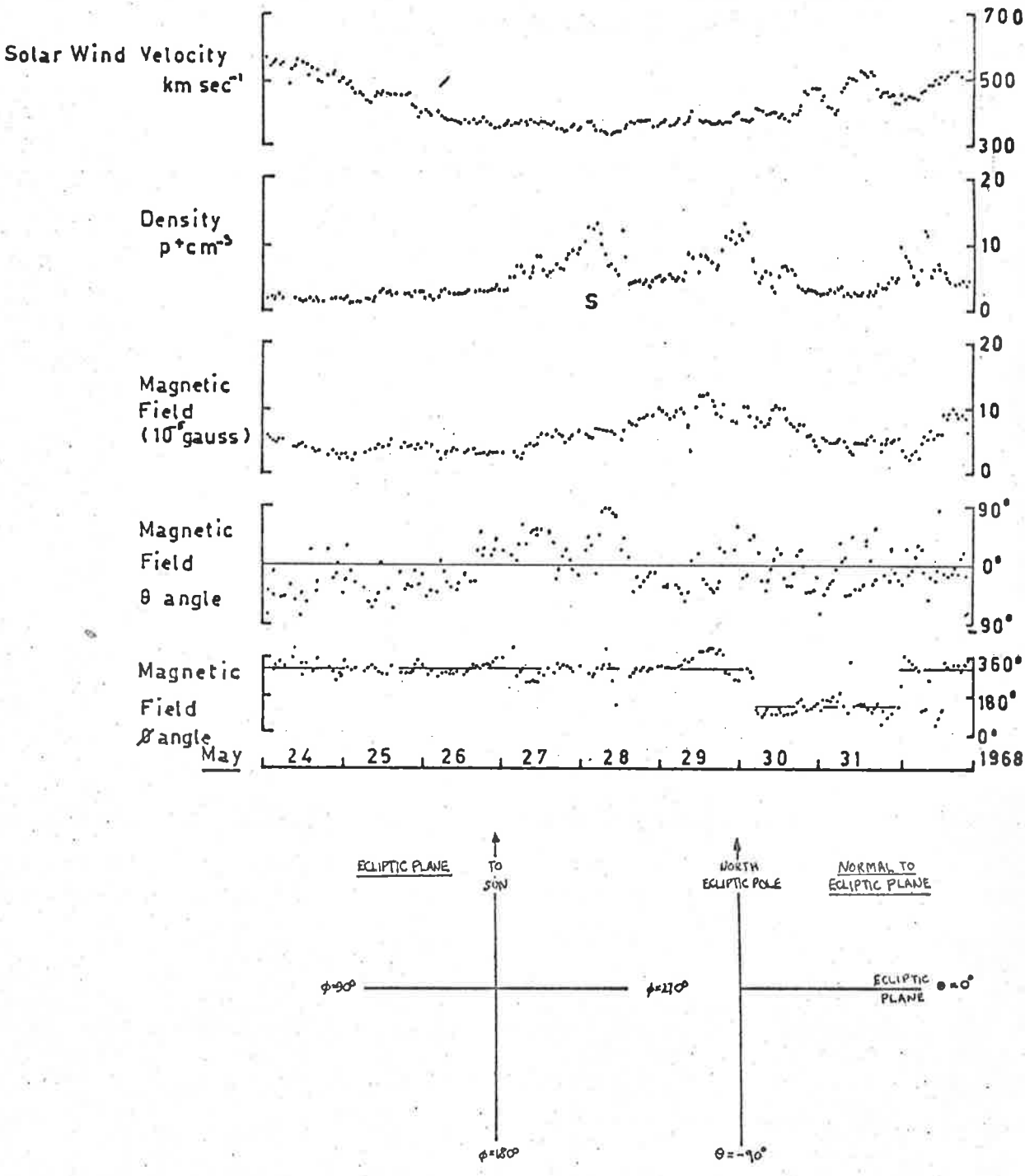

Figure 4.16 The hourly average values of solar wind velocity, density and interplanetary magnetic field data from Explorer 33 and 35 earth satellites.

blurred out.

The solar wind velocity showed no major variations during the period of our observations, but two significant increases occurred three days after the arrival of the stream at the earth. Thus at the time of the scintillation enhancements and increases in the widths of the power spectra, the velocity remained relatively constant. We therefore conclude that a significant decrease in the scale of the electron density irregularities must have been associated with the stream structure in the interplanetary medium. It is significant that the magnitude of the interplanetary magnetic field increased by a factor of 2-3 with the arrival of the stream, and this coincided with the increase in spectrum width (a factor of 2.3) on source 0134+32.

The experimental observations therefore suggest an inverse relation between the scale of the irregularities in the medium, and the magnitude of the interplanetary magnetic field. Such a relation would be expected if the irregularities originated from plasma instability and their scales were related to the ion gyro-radius in the medium. It has in fact been noted by other authors (see discussion in Chapter 2) that the scales derived from scintillation observations are not much larger than the expected ion gyro-radius in the medium.

Our observations then, strongly support this suggestion and imply that the measured scale from scintillation observations is not merely a diffraction limit, as inferred by Jokipii and Hollweg (1970), but

represents a real irregularity structure in the interplanetary medium probably caused by plasma instability.

The indices of geomagnetic activity (kp) in Figure 4.17 indicate that the effects of the stream on the earth varied considerably during successive solar rotations. Only a small increase was observed from May 27-30, but more pronounced effects were observed during the following two rotations. The kp indices also suggest that the stream may have been present during the previous six solar rotations.

From the plot of the solar ecliptic angle ϕ of the interplanetary magnetic field direction in Figure 4.16, it can be seen that the stream of enhanced electron density just preceded a sector boundary of the interplanetary field. This agrees with the distribution of density within the sectors of the interplanetary magnetic field as deduced by Wilcox and Ness (1965) and shown in Figure 1.8(c).

Our observed enhancements in scintillation during the passage of this preceding stream imply that the fluctuations in electron density increased at the same time as the average electron density. Although the velocity within this stream remained close to its ambient value, it can be seen from Figure 4.16 that the following sector boundary was 'driven' by a region of enhanced velocity and low, almost constant density. The interaction between these two different velocity streams presumably led to compression and enhancement of the magnetic field in front of the sector boundary, which was reflected in the change in ion

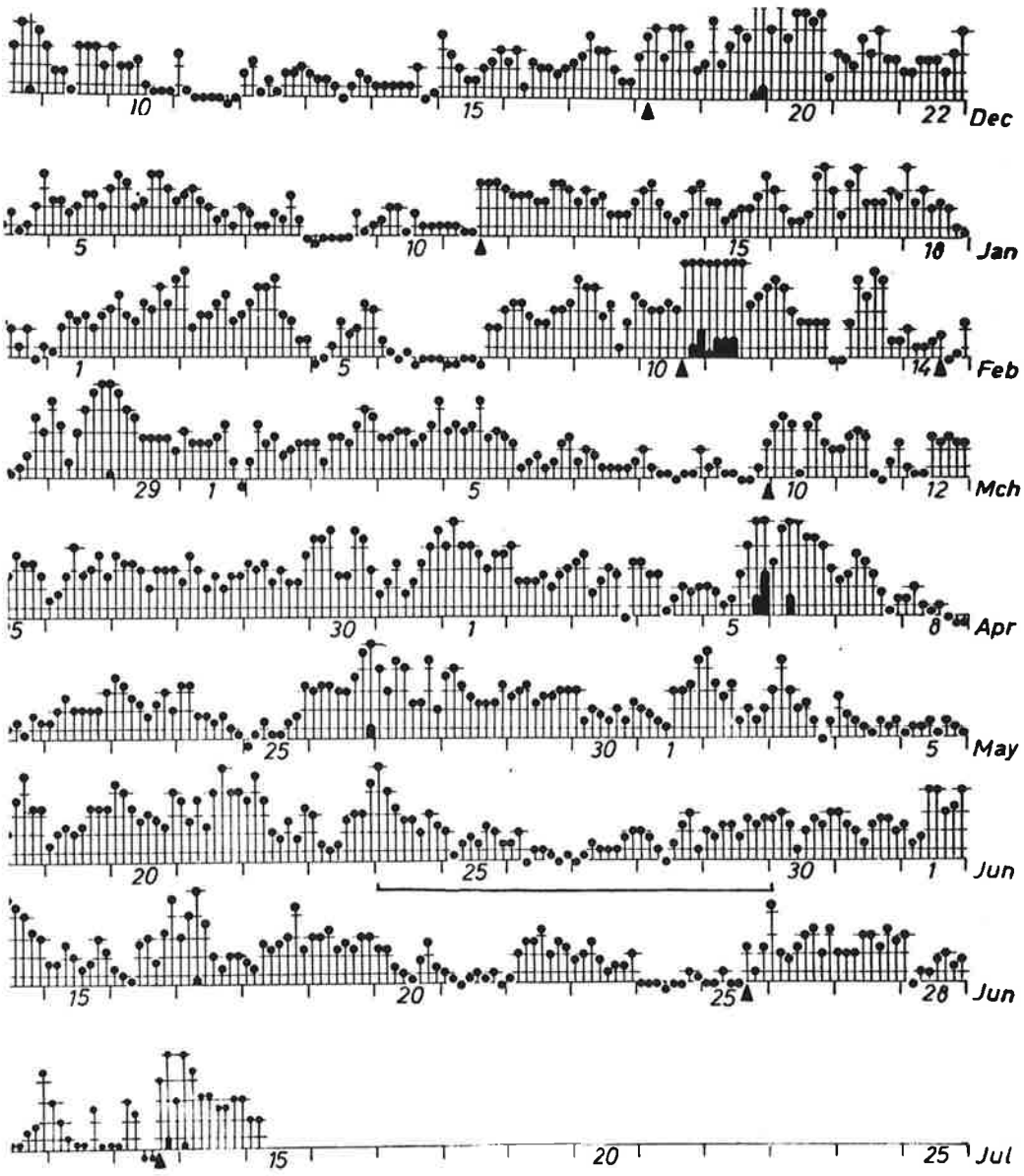

PLANETARY MAGNETIC
THREE-HOUR-RANGE INDICES
Kp (after Bartels)

Kp till 1968 June 30

Ks (from Wingst and Göttingen) till July 15

Figure 4.17

gyro-radius, and hence the widths of the scintillation power spectra. The observations suggest that scintillation studies can provide a powerful method for tracing the movement of such structures.

These preliminary results during May 1968 show the potential of interplanetary scintillation in the study of the development and movement of large scale features in the solar wind. The basic limitations of these results were the brevity of the observing session and the incomplete coverage of the interplanetary medium. These limitations were largely removed by observing over complete solar rotation intervals during 1969 and 1970. The analysis and results of these observations will be presented in the following chapters.

CHAPTER 5

METHODS OF ANALYSIS

Introduction

The large amounts of scintillation data recorded during June 1969 and June 1970 forced a re-appraisal of the analysis procedures previously used. Calculation of scintillation indices by hand was discarded as tedious and time consuming and some thought was given to computer programming for a complete analysis. A FORTRAN programme was eventually developed to calculate the power spectra, intensity probability distributions, autocorrelation functions, variances and scintillation indices for all the data.

In Section 5.1 we discuss the use of the Fast Fourier Transform in spectral analysis, and then describe its application to our particular problem in Section 5.3. Section 5.2 is a brief description of the acquisition of data.

5.1 The Fast Fourier Transform in Spectral Analysis

The basic criteria in the assessment of techniques for spectral analysis of time series, are maximum spectral resolution, minimum variance and minimum bias for each spectral estimate. The traditional approach to spectral analysis (Blackman and Tukey, 1958) via the cosine transform of the autocorrelation function has already been described in Chapter 4. Using this method, the resolution of the power spectrum is

determined by the maximum lag, T_m, of the autocorrelation function (ACF). The highest resolution possible would be obtained by computing the correlation function out to a maximum lag equal to the length of data, although in this case the correlation values would become increasingly unreliable at large lags due to the reduced effective length of data being used. However, in most practical cases the data length greatly exceeds the correlation length of the time series and so the effect is unimportant. Thus in most calculations the complete ACF (i.e. maximum lag = data length) is effectively multiplied by a rectangular window of unit height and of length $2\ T_m$. The cosine transform of this truncated ACF is thus the convolution of two functions $P(f) * H(f)$, where $P(f)$ is the Fourier transform of the extended ACF, and $H(f)$ is the Fourier transform of the rectangular truncation function. Hence each 'true' spectral estimate $P(f)$ is convolved with a function of the form,

$$H(f) = \frac{\text{Sin } (2\ \pi\ f\ Tm)}{(2\ \pi\ f\ Tm)} \qquad T_m << T, \tag{5.1}$$

which has zeros at,

$$f = \frac{n}{2\ T_m}\ . \qquad n = 1,\ 2\ \ldots.$$

The first side-lobe of $H(f)$ is as high as 20% of the main lobe amplitude so that significant leakage (spectral bias) occurs between adjacent spectral estimates, as illustrated in Figure 5.1. However, this leakage can be reduced by the application of a spectral window to the raw spectrum (see Chapter 4). This method of power spectrum estimation was found to be time consuming (and hence expensive) for a large number

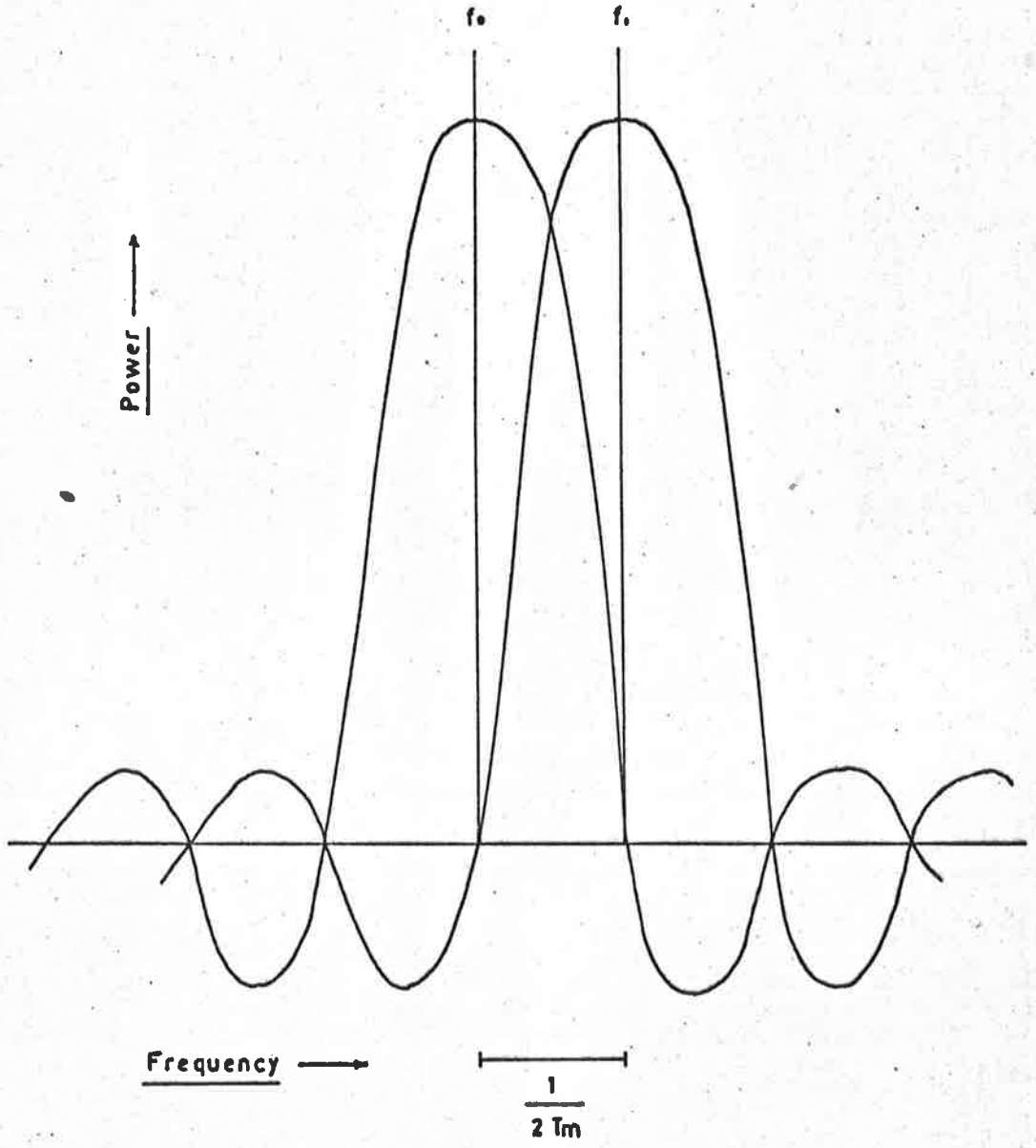

Figure 5.1 Adjacent estimates of the frequency power spectrum showing significant leakage.

of data points, and was therefore considered impractical for the large amount of data acquired during 1969 and 1970.

With the advent of the Fast Fourier Transform (FFT) algorithm (Cooley and Tukey, 1965) and its recent application to spectral analysis, it becomes computationally faster and more accurate to calculate the Fourier coefficients (and hence the spectral estimates) by a direct Fourier transform of the data, rather than by the transform of the autocorrelation function. The finite Fourier transform, C_n, of a sequence of N complex numbers, x_j ($j = 0, 1 \ldots\ldots N - 1$), is defined by the relation,

$$C_n = \frac{1}{N} \sum_{j=0}^{N-1} x_j \exp(-2\pi i j n/N), \qquad n = 0, 1 \ldots N - 1. \quad (5.2)$$

The reverse transform is similarly defined,

$$x_j = \sum_{n=0}^{N-1} C_n \exp(2\pi i j n/N), \qquad j = 0, 1 \ldots N - 1. \quad (5.3)$$

In a normal calculation of C_n from expression (5.2) there are $\sim N^2$ multiplications and additions required. However, by factoring N to ΠD_i, Cooley and Tukey (1965) produced an algorithm (FFT) which requires only $N \Sigma D_i$ operations. This represents a significant reduction in computing time; e.g. for N = 1024 there is a 50-fold decrease in computing time using this method.

We now consider a finite length, T seconds, of data sampled at time intervals Δt,

$$Y_j = Y(j \cdot \Delta t), \qquad j = 0, 1 \ldots N - 1 \quad (5.4)$$

The mean is removed in the usual way,

$$X_j = Y_j - \sum_{j=0}^{N-1} Y_j/N, \tag{5.5}$$

so that,

$$\sum_{j=0}^{N-1} X_j = 0. \tag{5.6}$$

The sample variance is then given by,

$$\overline{X^2} = \sum_{j=0}^{N-1} X_j \cdot X_j. \tag{5.7}$$

The squared modulus of the finite Fourier transform, properly normalised, gives N equally spaced samples of the periodogram,

$$P_K = \frac{1}{T} \left| \Delta t \sum_{j=0}^{N-1} X_j \exp (2 \pi i k j/N) \right|^2, \tag{5.8}$$

at discrete frequencies,

$$f = \frac{k}{T} = \frac{k}{N \Delta t}, \quad k = 0, 1 \ldots N - 1,$$

in units of power (X_j^2) per hertz. Because $P_K(f)$ is an even function, only $(\frac{N}{2} + 1)$ values are distinct, out to the Nyquist (folding) frequency, $f_N = 1/(2 \Delta t$. The 'true' power spectrum, S_K, of an infinite length of record, is related to the periodogram, P_K, by the convolution relation,

$$P_K = S_K * H_K, \tag{5.9}$$

where H_K is the spectral window through which S_K is 'seen,' due to the truncation of the data. Since the infinite length of data is effectively multiplied by a rectangular function, $W_K(t)$, of length T seconds and of unit amplitude, the true spectrum S_K is convolved with the squared modulus of the Fourier transform of W_K, which is,

$$H_K = \frac{1}{2\pi T} \frac{\mathrm{Sin}^2 (T \pi f)}{\mathrm{Sin}^2 (\pi f)} . \qquad (5.10)$$

This window has unit area, with a main peak at f = 0, of width 2/T. The first side-lobes occur near ± 3/2T and are ∿ 5% of the main peak amplitude. Thus an estimate at frequency f contains a 5% contribution from frequencies at $f \pm \frac{3T}{2}$. This spectral leakage is not a major problem for flat spectra, but it is difficult to correct for in spectra having steep slopes or containing sharp spikes (lines). The leakage can be reduced by varying the shape of the original window $W_K(t)$ so that the side-lobes of H_K are much smaller. Three important windows (Bartlett, Hanning and Hamming), are discussed in detail in Blackman and Tukey (1958).

The raw periodogram, P_K, is not a good estimate of the power spectrum, since the variance of the estimates do not converge to zero as N increases. The large-sample variance of the estimates is given (Cooley, Lewis and Welch, 1970) by,

$$\mathrm{Var}\ (P_K) \simeq P_K^2 .$$

This is only strictly true for Gaussian time series, but is a reasonable approximation in more general cases. The standard deviation of P_K is 100% of its mean value and is thus an unreliable estimate. To obtain a more meaningful estimate of the power spectrum for a given sample size N, the $\frac{1}{N \Delta t}$ resolution of the periodogram must be sacrificed for a reduction in the variance of the estimates. There are two methods of achieving this. In the first of these the N periodogram estimates are calculated from the whole record, and then blocks of L = N/m ordinates

are averaged to give $(\frac{N}{2L} + 1)$ estimates of the spectrum up to the folding frequency. This averaging produces the required reduction in variance by a factor of L. The average value

$$\overline{P_j} = \frac{1}{L} \sum_{\ell=0}^{L-1} P_{Lj+\ell}, \qquad j = 0, 1, 2 \ldots N/2L \tag{5.11}$$

is assigned to the centre of the averaged band,

$$f = j\ L + \frac{L - 1}{2}. \tag{5.12}$$

The second method is similar, but requires less computer storage for the calculation, and also has the advantage (Hinich and Clay, 1968) that the smoothing causes less bias in the spectral estimates if any peaks are present in the spectrum. The record is broken up into L non-overlapping segments of equal length R = N/L, and periodograms for each segment are computed separately. The estimate for each frequency is then formed as the average across L segments

$$P_K = \frac{1}{LT} \sum_{\ell=0}^{L-1} \left| \Delta t \sum_{j=0}^{R-1} X_{j\ell} \exp\ (2\ \pi\ i\ k\ j/R) \right|^2, \tag{5.13}$$

where RL Δt = T, and $X_{j\ell}$ is the j'th data value in the ℓ'th segment. Time series of indefinite length can be treated in this way with only modest storage requirements. The frequency resolution is,

$$\frac{L}{T} = \frac{1}{R\ \Delta t}, \tag{5.14}$$

and the variance of the estimates is reduced by a factor of L. The autocovariance function, $\rho(j)$, can then be computed as a direct Fourier transform of the power spectrum (Wiener-Khintchine theorem),

$$\rho(j) = \frac{1}{R\ \Delta t} \sum_{k=0}^{R-1} P_k \exp\ (2\ \pi\ i\ j\ k/R), \qquad j = 0, 1, \ldots R - 1 \quad (5.15)$$

where $\rho(j)$ is the value at a lag of $j\ .\ \Delta t$. Normalisation by the sample variance, $\overline{X^2} = \rho(0)$, yields the autocorrelation function. This method of calculating the ACF gives slightly different results when compared to the direct method, defined by,

$$\rho(j) = \frac{1}{N - j + 1} \sum_{\ell=1}^{N-j+1} X_\ell\ X_{\ell+j-1}. \quad (5.16)$$

The FFT method performs circular summation, i.e. with $X_K = X_{N+K}$, whereas the direct method performs linear summation with $X_K = 0$ for $0 > K > N - 1$. Thus using the FFT method the maximum lag of the ACF is reduced to T/2. This could be overcome by appending N zeros to P_K before transformation, but since we are usually only interested in cases where the data length, T, is very much greater than the correlation length of $\rho(j)$, the difference is unimportant.

5.2 Data Acquisition

The C.S.I.R.O. radioheliograph at Culgoora, N.S.W. produces 48 antenna beams spaced evenly in a north-south direction (see Chapter 4). The central six beams were displayed on two 3-channel pen recorders with time constants of 0.1 second, and the main on-source beam was also digitally recorded on magnetic tape (time constant 0.05 second) at 32 samples per second. The data on tape were recorded in 90 second blocks, each preceded by a header-label containing the block number. The recording unit produced block marker pulses which were displayed on the pen recorders to enable the chart and tape data to be correlated. An

extensive log-book was written, listing all the features associated with each block of data, and from this a set of punched cards was prepared containing the relative position of any interference (local, solar or instrumental), which could then be removed from the data during analysis.

5.3 Analysis

In Section 5.1 we discussed the role of the Fast Fourier Transform (FFT) in time series analysis: in this section we describe its application to our observational data.

Each 90 second block of data contained 2880 points written in a coded form determined by the particular digitiser used. Thus each block had to be decoded and written in a form compatible with the CDC 6400 computer on which the analysis was performed. Any isolated illegal (i.e. undefined) points encountered due to malfunction of the digitiser were rewritten with the previous point value, and a running total of these faults was stored and later printed out providing a 'quality indicator' for each block of data. Sections of data spoiled by solar noise bursts were then removed and the resultant data stored in an array X(I).

Electrical storm activity frequently produced lightning spikes on the records, and these were detected and removed by comparing the slope, X(I) - X(I - 1), between each pair of points with 5 times the average slope,

$$\frac{\sum_{i=1}^{63} (X(I) - X(I-1))}{63},$$

from the previous 2 seconds of data. Some sections of the data, especially during June 1969, suffered from mains supply contamination ($\sim$ 50.5 Hz), and a preliminary spectral analysis revealed a strong peak in the spectrum at the aliased frequency of 13.5 Hz. In order to remove the variation in the spectrum associated with this peak, a running-mean filter was applied to the data before Fourier transformation. The power transfer function (i.e. the factor by which the spectrum was multiplied due to application of the filter) was selected to have a zero value at or near the peak frequency. In the final analysis the data was treated with an 8-point running-mean filter,

$$X_K = \sum_{j=K}^{K+7} X_j \ /8,$$

of width 7/32 second. The effect of this in the frequency domain was to multiply the spectrum by the function,

$$H(f) = \frac{\mathrm{Sin}^2 \ (\pi \ f \ 7/32)}{(\pi \ f \ 7/32)^2} \ , \qquad (5.17)$$

which has zeros at,

$$f = 4\tfrac{4}{7},\ 9\tfrac{1}{7},\ 13\tfrac{5}{7},\ \ldots \text{ Hz}.$$

Thus the large peak at 13½ Hz was effectively removed. The effect of the window on the spectral region below 4 Hz was allowed for later in the analysis, but no correction could be applied beyond $4\frac{4}{7}$ Hz because of the zeros in H(f).

The Nyquist frequency was then set at 4 Hz by retaining only one in 4 of the averaged data, i.e.

$$X(1) = X(1), \quad X(2) = X(5), \quad X(3) = X(9), \quad \text{etc.}$$

Since consecutive blocks of data, X(I), were of various lengths after correction for interference, the spectra would have had varying resolution from block to block. To overcome this, each block of data was divided into two sub-arrays containing an equal number of real data points and being zero filled if necessary up to a complement of 384 points (i.e. 48 seconds of data). The arrays could then be transformed economically, two at a time, using a technique suggested by Cooley, Lewis and Welch (1969), and summarised as follows. If $X_1(j)$ and $X_2(j)$ are real arrays which transform to $A_1(n)$ and $A_2(n)$ respectively,

$$X_1(j) \leftrightarrow A_1(n), \qquad X_2(j) \leftrightarrow A_2(n),$$
$$j = 0, 1, \ldots N - 1, \qquad n = 0, 1, \ldots N - 1,$$

we form,

$$X(j) = X_1(j) + i\, X_2(j),$$

which transforms to A(n),

$$X(j) \leftrightarrow A(n).$$

Then from the linearity of the transform we have,

$$A(n) = A_1(n) + i\, A_2(n),$$

and it can easily be shown that,

$$A_1(n) = \frac{A(n) + \tilde{A}(N - n)}{2}, \tag{5.18}$$

and

$$A_2(n) = \frac{A(n) - \tilde{A}(N - n)}{2i},$$

where $\tilde{A}$ is the complex conjugate of A. Hence we obtain the transforms of both sub-arrays using only a single Fourier transformation and simple algebra. After subtracting the mean value for each sub-array the data was transformed to its Fourier coefficients, in groups of two as described. The coefficients were then divided by the function,

$$H(f) = \frac{\text{Sin } (\pi\ f\ 7/32)}{(\pi\ f\ 7/32)}, \tag{5.19}$$

to compensate for the effect of the running-mean filter. The periodogram estimates were formed for each sub-array A_i,

$$E_i(n) = \left| A_i(n) \right|^2, \tag{5.20}$$

and averaged over the K sub-arrays to yield the power spectrum estimates,

$$P(n) = \sum_{i=1}^{K} \left| A_i(n) \right|^2 . \tag{5.21}$$

The variance of each estimate (Welch, 1967) is given by,

$$\text{Var } (P(n)) = \frac{P^2(n)}{K} . \tag{5.22}$$

In most data blocks, K had the value 2, so that the rms deviation, $\sigma_p \sim 0.7\ P(n)$, was about 70% of the spectral estimate. Little significance could be attached to spectra having such large variances and so the periodogram was averaged over groups of four estimates,

$$P'(n) = \frac{1}{4} \sum_{j=0}^{3} P(4n + j), \qquad n = 0, 1, 2 \ldots \tag{5.23}$$

reducing the variance by a factor of 4. The spectral resolution was then 0.08 Hz.

Filtering of the spectrum was achieved simply by equating the

appropriate Fourier coefficients to zero. The limit of the (high pass) filter was set at 0.1 Hz to remove any power due to ionospheric scintillation or slow trends in the data caused by receiver gain drifts, and then the final filtered and averaged power spectrum for each data block was plotted out on the computer line printer. Where several blocks of data were taken for a particular source, a more reliable spectrum (reduced estimate variances) was computed as the average over those blocks.

The autocovariance function, $\rho(j)$, of each block of data at lags $j\,\Delta t$ was obtained by Fourier transformation of the power spectrum $P(n)$,

$$P(n) \leftrightarrow \rho(j).$$

The sample (i.e. data) variance, $\rho(0)$, is simply the total area under the frequency power spectrum. Normalisation of the autocovariance to $\rho(0) = 1$, yields the ACF at incremental time lags of 1/8 second. This function was also plotted on the line-printer. A parameter of particular importance in the interpretation of our results, was the scintillation index, F, which was obtained directly from a knowledge of $\rho(0)$,

$$F = \frac{(\text{signal variance - noise variance})^{\frac{1}{2}}}{\text{source height}}.$$

The index for each data block was calculated and then an average value produced for each source on each day of observation.

CHAPTER 6

RESULTS II - June 1969

Introduction

In Chapter 4 we have discussed a method for mapping the movement and geometry of large-scale features of the solar wind by observation of the interplanetary scintillation (IPS) of a grid of discrete radio sources. Using this method, the origin and development of both corotating streams and interplanetary blast-waves were observed during June 1969. In this chapter we describe the analysis and interpretation of these observations. We are able to show that both plasma blast waves and corotating streams can be primary agents in the onset of geomagnetic storms, and that IPS is a powerful method for investigating the structure of such phenomena. The relationship between the observed streams and the position of magnetic field sector boundaries is also discussed.

6.1 Observations

The present work was carried out from May 31 - June 26, 1969 using the C.S.I.R.O. Radioheliograph at Culgoora, N.S.W. The observing procedure was essentially the same as that described in Chapter 4. A grid of radio sources, spaced as evenly as possible about the celestial sphere, were observed every day, and a representative sample of their scintillation was recorded on magnetic tape for computer analysis. The signals were also displayed on two 3-channel pen-recorders, to provide visual interpretation of the magnetic tape data.

The analysis procedure which was applied to the present results was described in detail in the previous chapter. In the interpretation of our results we have assumed that the dominant scattering region for radiation from a particular source was normally located around the point of closest approach to the sun by the line of sight to the source.

6.2 Solar Activity in June 1969

Two major regions of activity dominated the solar disc during June 1969. Region A, which had central meridian passage (CMP) on June 9 and 10, was extremely flare active with large associated radio flux at 21 cm, 43 cm, and particularly at 10.7 cm where the flux exceeded ten times the estimated quiet sun level (Figure 6.1).

The flare activity on the sun during 1969 is conveniently summarized in the flare plot of Figure 6.2. This diagram was produced by separately counting the number of flares occurring in the northern and southern solar hemispheres in an area of solar surface defined by two heliographic longitudes, one day of rotation apart. The total number of flares occurring in these areas during their passage across the disc was plotted against the date of central meridian passage, and peaks on the graph then indicate the presence of solar active regions. In Figure 6.2, shaded areas indicate the presence of class 2 and 3 flares, and the unshaded portions represent class 1 flares.

Figure 6.2 shows that region A was prominently flare active for four solar rotations prior to June, and may also have been connected with

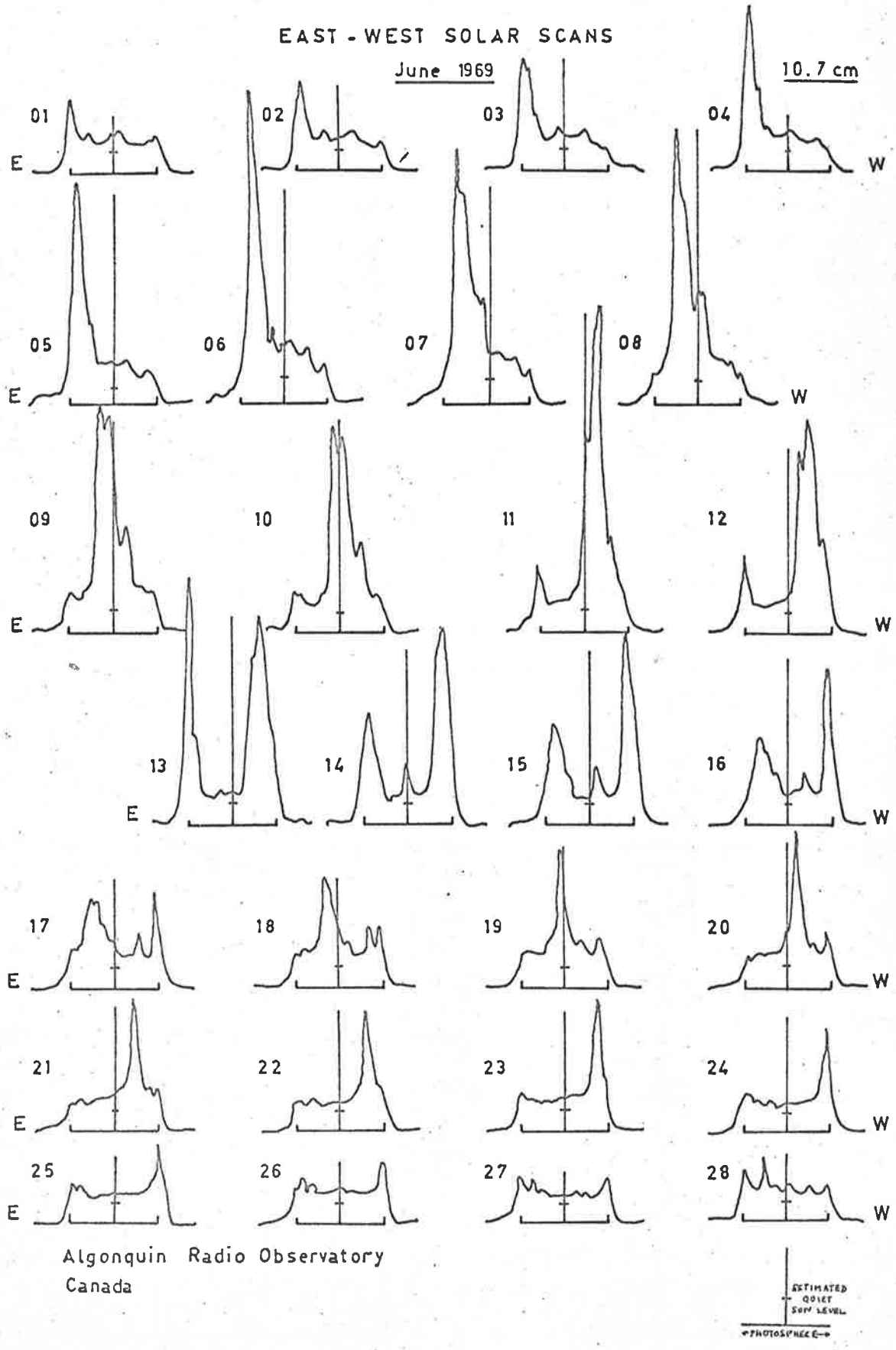

Figure 6.1 Measures of the radio flux in east-west scans across the solar disc at 10.7 cm.

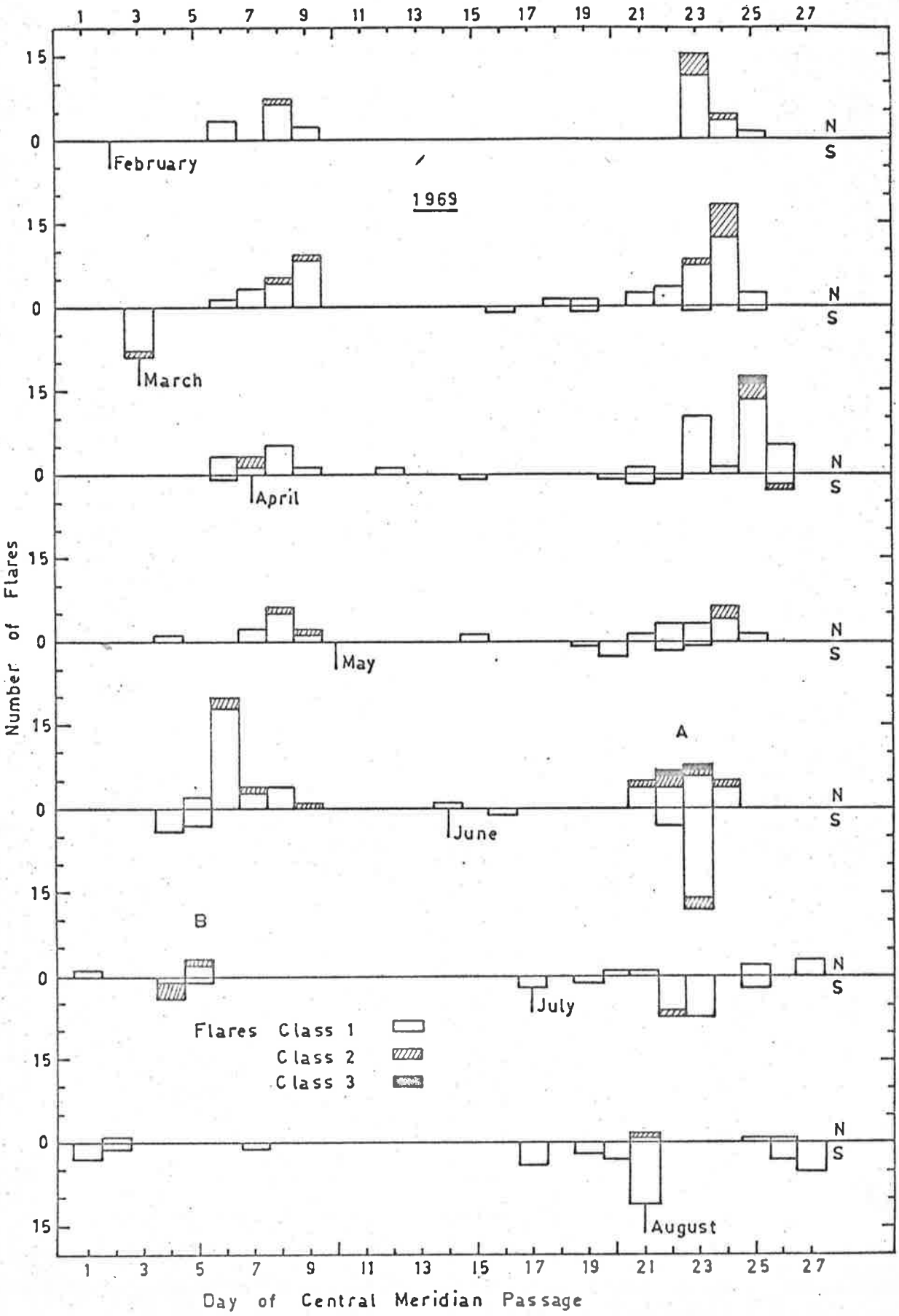

Figure 6.2 Solar flare activity in the interval February-August 1969.

the development of a southern active region (latitude 15° S) at the same longitude during June and July. (Solar data is from the Solar Geophysical Data Bulletins, Department of Commerce, U.S.A.). The activity of region A was dominated during the observing session by several very strong flares on June 5 at N10° E60° from 1000-1700 hours U.T. Two flares of class 3B were recorded with duration from between one and two hours, accompanied by two class 2B, two class 2N and two class 2F flares of duration from 10 minutes to 2 hours.

A second active region, B, at N10° with CMP on June 19, was extremely flare active during May (Figure 6.2) but subsided to moderate activity in the space of one solar rotation. The region appears to have been well defined for at least four rotations prior to May, and during June strong radio flux at 10.7 cm, 21 cm and 43 cm was associated with the activity in this region. Region B faded and lost its identity during the following rotation (July).

Photographs of the sun in Hα for June 10 and 18 are shown in Figures 6.3 and 6.4†. In Figure 6.3 region A is at central meridian passage and forms part of an extended flare group in the northern solar hemisphere. The southern active centre also at central meridian on June 10 was much weaker than region A, displaying a large number of class 1 and subflares, and only a single class 2 flare on June 6.

---

† Courtesy of Dr R. G. Giovanelli, C.S.I.R.O. Division of Physics.

S

W

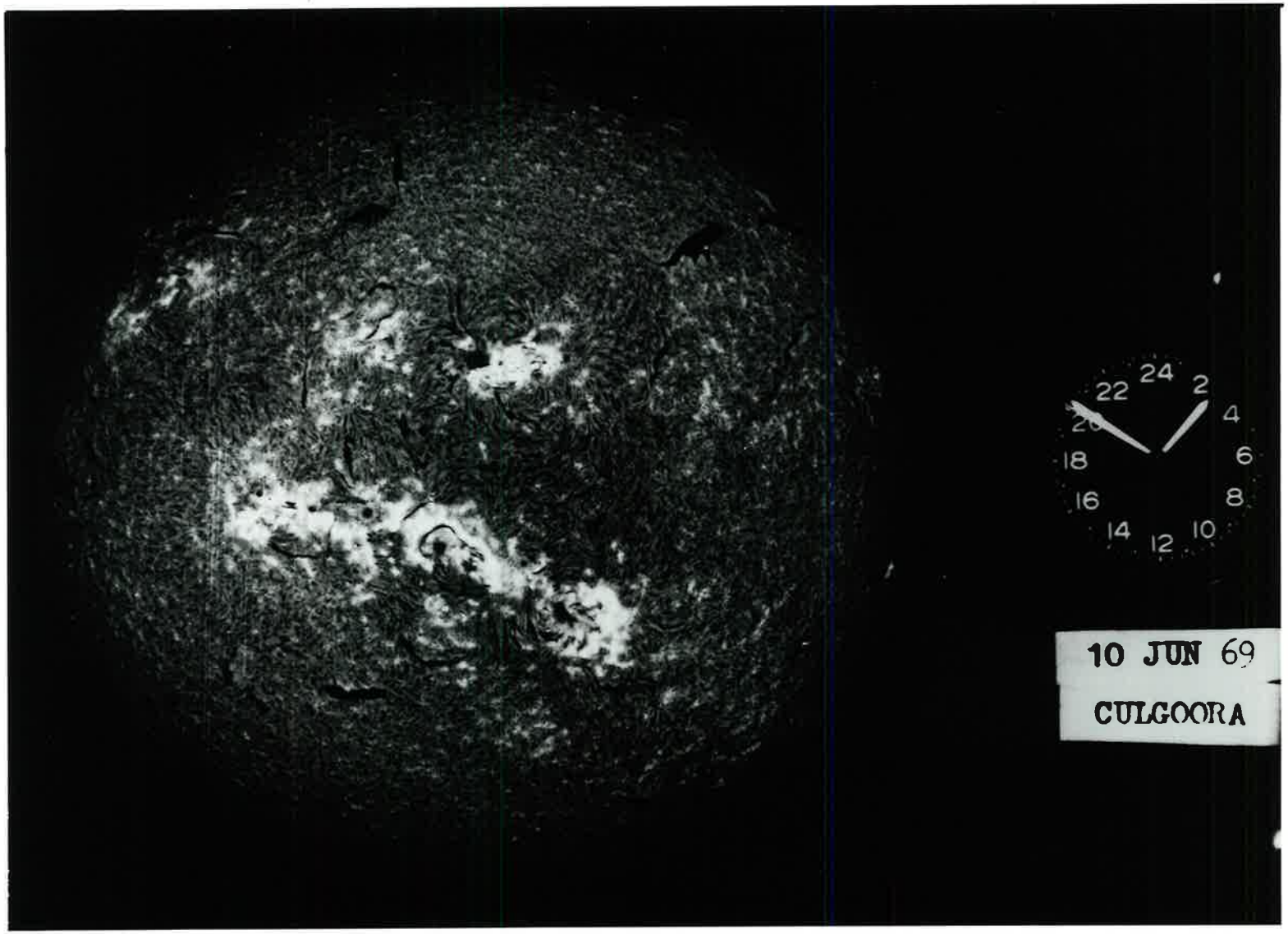

E

N

Figure 6.3

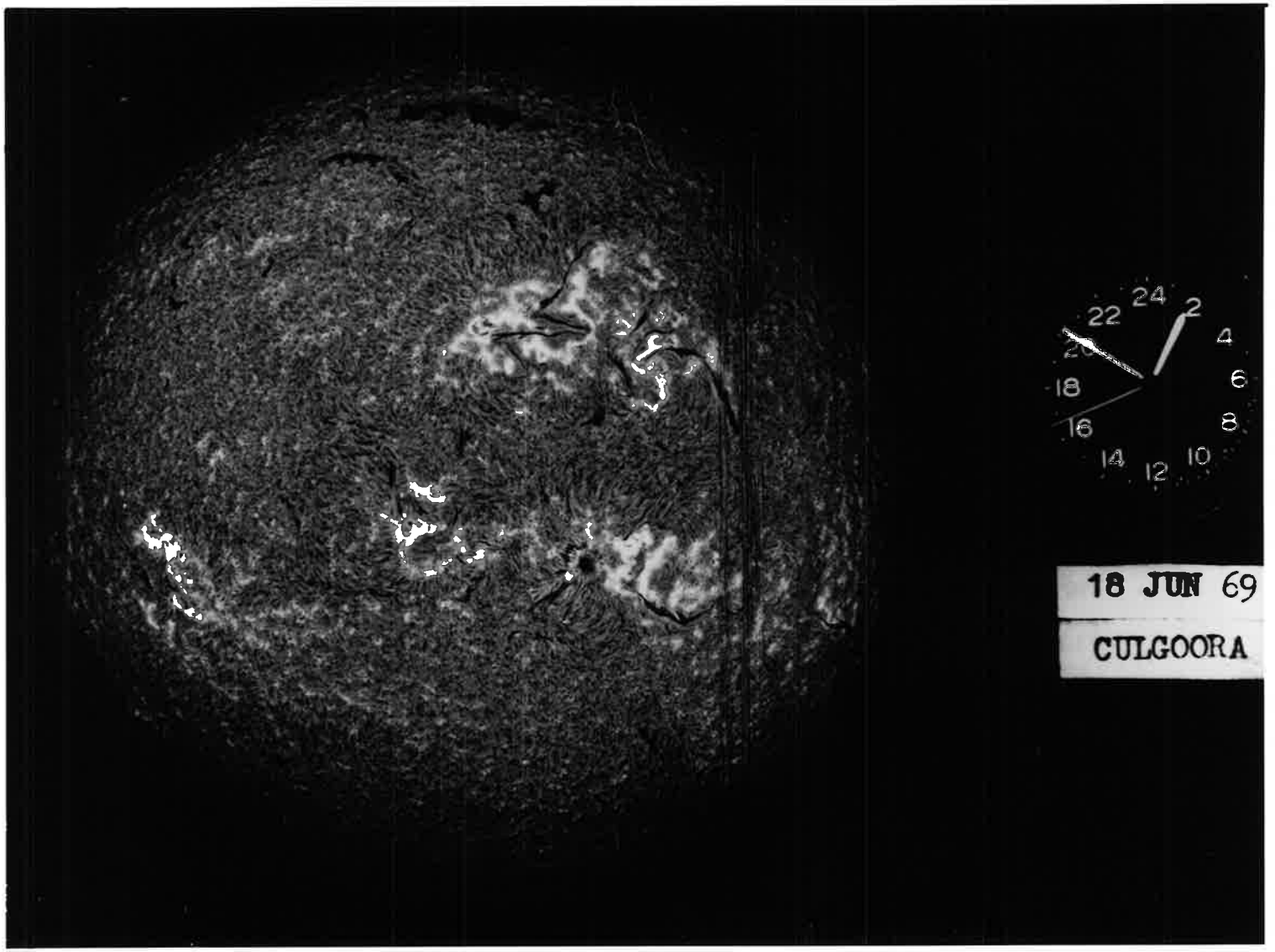

Figure 6.4

Figure 6.4 shows region B near central meridian passage in the northern solar hemisphere on June 18 (unfortunately photographs for June 19 were not available). As the activity in region B declined from May to June a southern region showed some activity on June 13 at S24^0. This region was also near central meridian passage on June 19, and can be seen in Figure 6.4.

6.3 Results and Discussion

In Figure 6.5 the scintillation indices for fourteen sources over the 27 day period of observation are shown, and the ecliptic latitude of each source is shown beside each graph. The most significant feature of this figure is the large increase in scintillation shown by most sources between June 7-8. Sources 0933+04, 0939+14, 1005+07, 1116-02, 1309-22, 1328+25 and 0134+32 showed more than 200% increases in their scintillation indices, while sources 0802+10, 0850+14, 0949+00, 1226+02, and 1416+06 showed more moderate increases. The position of these sources projected onto the ecliptic plane is shown in Figure 6.6 for June 1969. The absence of a major time sequence in the changes of the indices suggests that the increases were produced by a radial blast of turbulent plasma moving out from the sun. The observations exclude the alternative possibility of a corotating structure in the solar wind, which would have required from 3-5 days to move from source 0802+10 to source 1416+06. The fact that flare region A on the sun's eastern limb was extremely active only a short time before (June 5) strongly suggests a causal connection between the blast and the flare region on the sun.

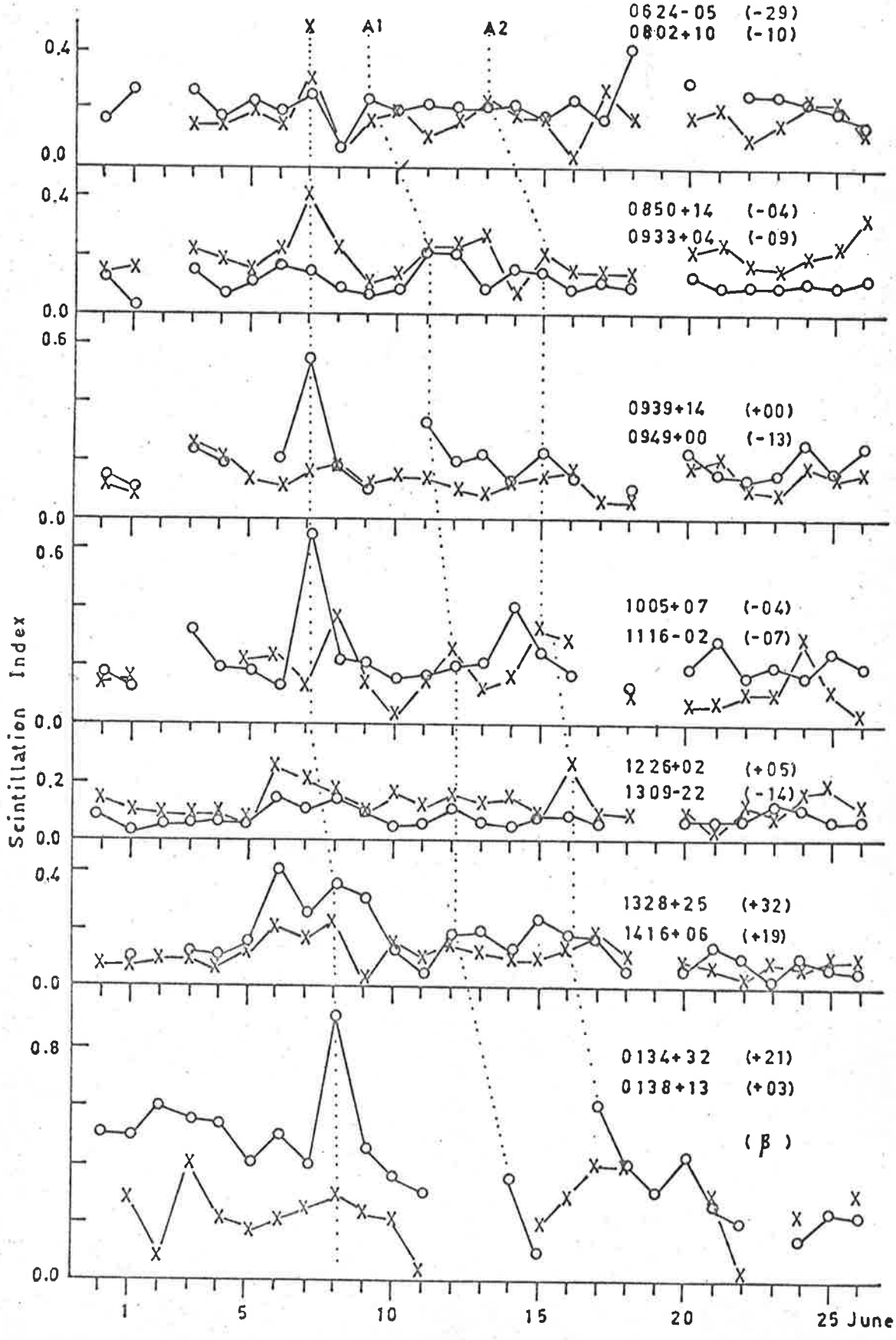

Figure 6.5 Scintillation indices for the fourteen sources observed during June 1969.

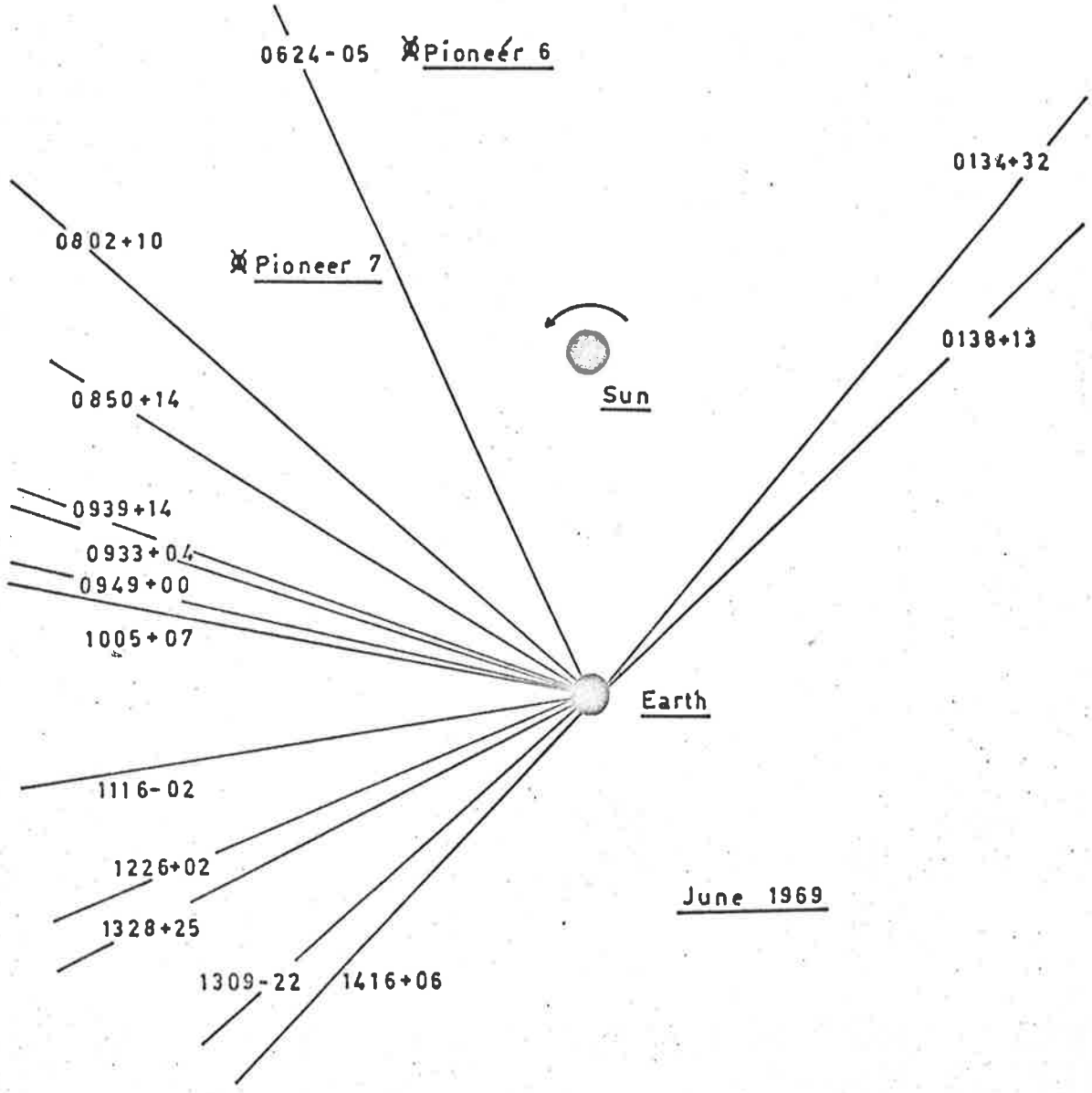

Figure 6.6 The ecliptic projection of the lines of sight to the observed radio sources, June 1969.

The time of arrival of the blast at the earth (June 8) could be estimated from the scintillation enhancement of sources lying in the anti-solar direction (e.g. 1416+06), since their points of closest approach to the sun along the lines of sight occurred near the earth. Source 0134+32 also showed a 200% increase in scintillation index on June 8, even though its point of closest approach was $\sim 50^{\circ}$ west of the earth-sun line. A sudden-commencement geomagnetic storm, also on June 8, was accompanied by a 3% Forbush decrease recorded at the Deep River neutron monitor.

An important feature of the blast wave was its velocity profile in the ecliptic plane. Graphs of the measured solar wind velocity from the Pioneer 6, Pioneer 7 and Vela 3 and 4 spacecraft are shown in Figures 6.7, 6.8 and 6.9. A sharp increase in velocity from 576 km/sec to 714 km/sec was observed on Pioneer 6 between 1800 U.T. on June 6 and 1400 U.T. on June 7. A similar range of velocities was observed on Pioneer 7, from 537 km/sec at 0200 U.T. to 653 km/sec at 1900 U.T. on June 7. This increase was preceded by two earlier velocity peaks on June 3 and 5, but in these cases there was no significant solar activity for a period of 10 days before the velocity events (Figure 6.2), and they must be attributed to some quasi-stable feature in the ambient solar wind which would have been swept past the spacecraft in its corotation with the sun. This velocity feature would corotate to the earth on June 11-12, and will be shown to coincide with stream A1, to be discussed later in this chapter.

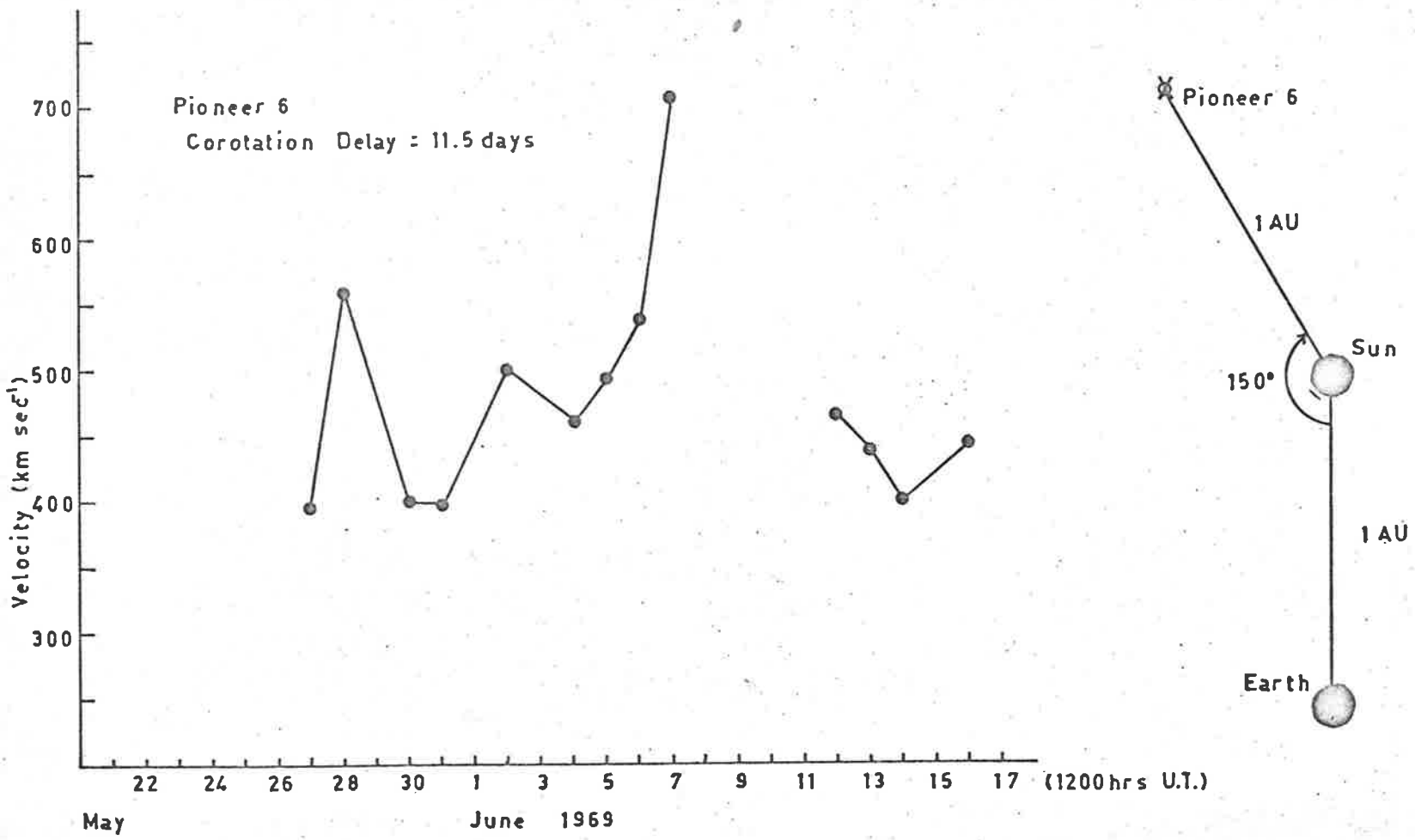

Figure 6.7 The measured solar wind velocity from Pioneer 6 during June 1969.

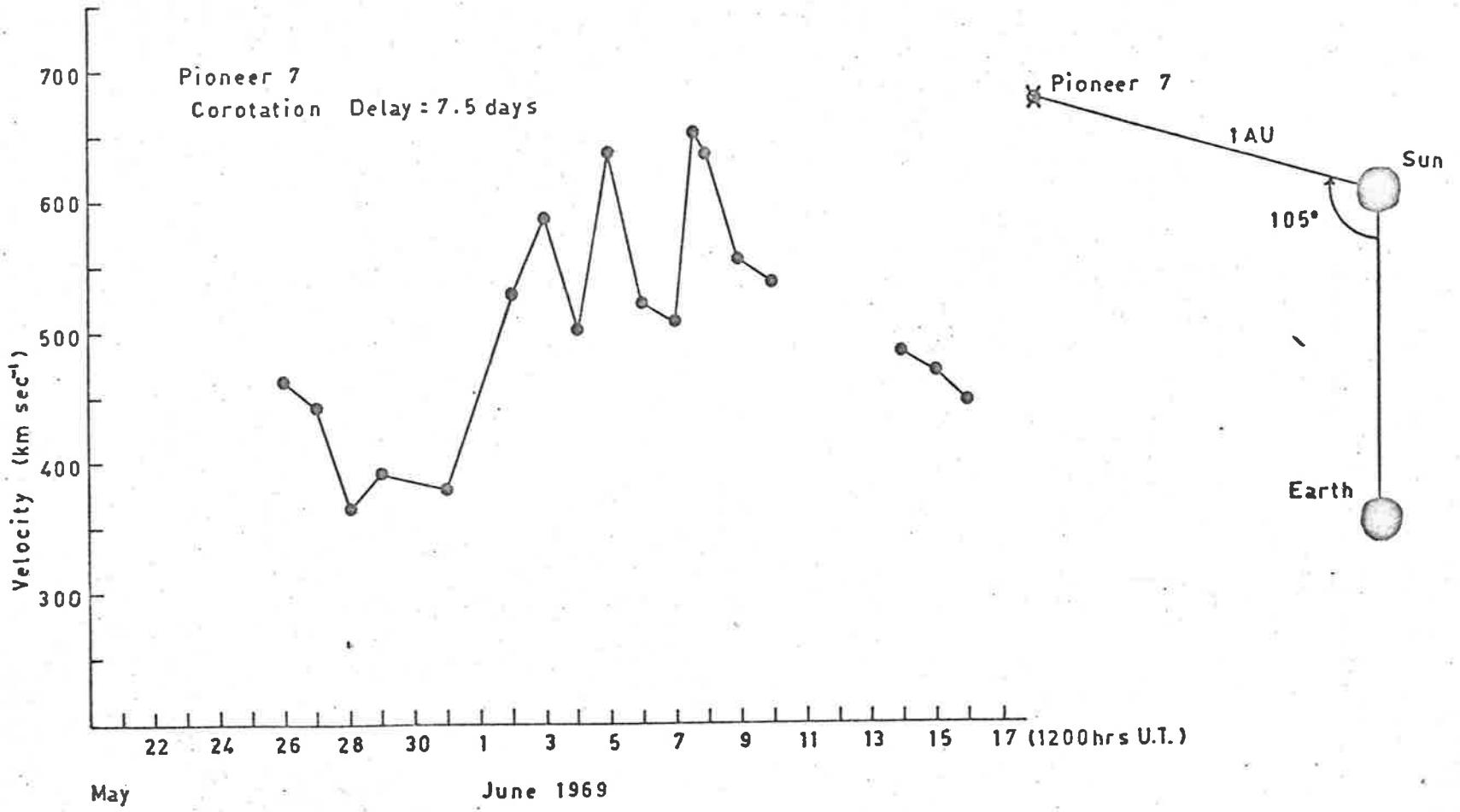

Figure 6.8 The measured solar wind velocity from Pioneer 7 during June 1969.

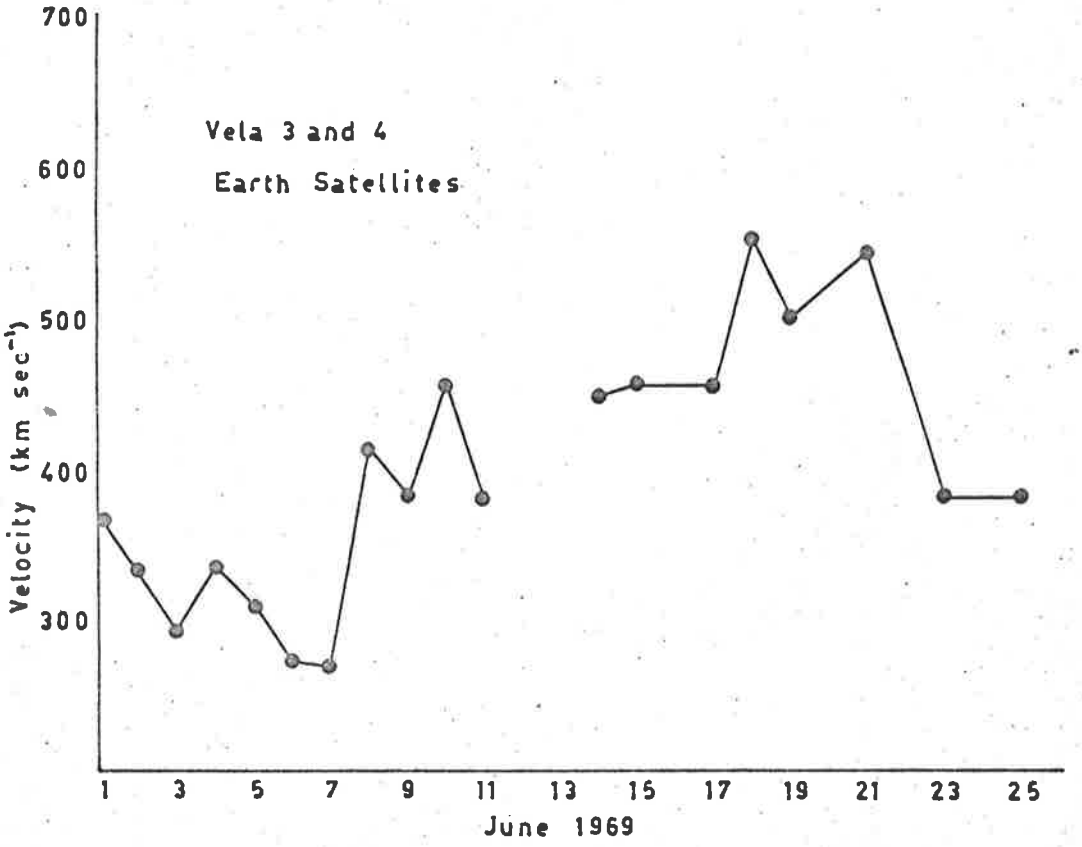

Figure 6.9 The measured solar wind velocity from Vela 3 and 4 during June 1969.

The velocities measured aboard Pioneer 6 and 7 on June 7 were in marked contrast with the observations from the Vela 3 and 4 spacecraft situated near the earth, where the velocity increased from 268 km/sec to 449 km/sec between 1100 U.T. on June 7 and 0700 U.T. on June 8. The positions of Pioneer 6 and 7 relative to the earth and the sun are shown in Figures 6.7 and 6.8 respectively. The delay of almost one day in the arrival of the enhanced plasma velocity at the earth compared with the arrival at Pioneer 6 and 7 (which are also at 1 A.U. from the sun) demonstrates a marked anisotropy in the structure of the blast wave.

This velocity anisotropy may be either inherent in the original blast structure or caused by the interaction of the blast with the ambient interplanetary plasma and magnetic field. If we assume that the flare activity in region A between 1000-1700 U.T. on June 5 was the source of the blast, then the measured propagation speed at the earth (450 km/sec) is lower than the minimum calculated mean transit velocity (600 km/sec), which implies a deceleration of the blast after its formation at the sun. There are two possible mechanisms involved. The deceleration may be due to the interaction of the ionized plasma with the ambient-flow magnetic field structure, or to the deceleration of the blast due to purely hydrodynamic flow considerations. The latter case has been treated by Hundhausen and Gentry (1969) and De Young and Hundhausen (1971) using numerical methods to simulate the observed conditions associated with such blasts. They have shown that as the duration of the initial disturbance, τ, is lowered, the energy of the

blast wave decreases and the wave is more strongly decelerated in transit. Blast waves which propagate from the sun to 1 A.U. in $\sim$ 60 hours, as in the present case, have energies near 10^{31} erg.

The source region, A, on June 5 was at E60° from central meridian, and hence 90° from the sun - Pioneer 6 line and 45° from the sun - Pioneer 7 line. Observation of the blast at these widely separated positions and also at the earth show that the structure developed on a very broad front, but with some departure from spherical symmetry, as indicated by the velocity anisotropy. The spacecraft and scintillation data allow some limits to be placed on the shape of the shock front in the ecliptic plane. Both Pioneer spacecraft measured maximum velocities between 1400 and 2300 U.T. on June 7, whereas Vela 3, 4 were not affected until $\sim$ 18 hours later on June 8. Similarly, sources 0624-05 to 1005+07 showed enhanced scintillation on June 7 whereas the remaining sources, at greater elongations east from the sun, were not affected until June 8. A possible shock profile is sketched in Figure 6.11(b) on the basis of these observations.

From the shape of the scintillation index enhancements we can also obtain a good estimate of the duration of the blast, or at least of the turbulence in electron density which was associated with it. All of the sources exhibited a sharp increase in scintillation for one day, except 1328+25 which showed an increase over 2 days. This extended width may have been due to a variation in the blast structure away from the

ecliptic plane, since 1328+25 is 32° north of the ecliptic. However, within the ecliptic plane the blast wave appears to have had a duration of one day, and this value was used in Figure 6.11.

The effect of the blast wave on sources in the anti-solar direction was partially confused by increases in scintillation index occurring on June 6. It is thought that these increases were associated with a corotating region of plasma affecting 1005+07 on June 3, 1116-02 on June 5 and then sources 1226+02, 1309-22, 1328+25 and 1416+06 on June 6. Unfortunately a lack of data early in June prevented a complete analysis of this event.

Following the effects of the blast-wave, there is evidence that a continuing flux of plasma from the same active region on the sun gave rise to a complex stream structure which corotated with the sun during the rest of the month, causing sequential increases in the scintillation indices over the grid of observed sources. In a preliminary analysis this stream structure was interpreted in terms of its gross overall appearance (Wiseman and Dennison, 1972). However more detailed study, especially with reference to the scintillation power spectra, showed that the stream had considerable substructure, and could in fact be considered as two distinct streams corotating a few days apart. These streams will be referred to as A1 and A2, in the following discussion, with A1 preceding A2. Although the overall model to be proposed is not based solely on changes in scintillation indices, but also on power spectra,

the events will be initially described in terms of their effects on the degree of scintillation of the observed sources. It will be useful during the following discussion if the reader refers to Figures 6.11 (a-d), where the positions of the various plasma events are shown. Streams A1 and A2 are both assumed to originate from region A on the sun, and B1 and B2 from region B, in the following discussion.

The time at which A1 reached the earth may be estimated from its effects on 1226+02, 1328+25 and 1416+06 since their lines of sight were closest to the sun near the earth. All three sources showed increases in their indices on June 12 followed by an apparent increase for 0134+32 on June 14. (The general enhancement of the indices for 0134+32 before June 8 will be discussed later in relation to a corotating stream configuration associated with region B). The effects of the stream can be seen earlier on 0624-05 on June 9, 0802+10 on June 9 and 10, 0850+14 on June 11 and 12, 0933+04 on June 11-13, 0939+14 on June 11 and 1116-02 on June 12.

The variation in the level of enhancement observed on different sources as the stream intercepted their lines of sight was caused, in part, by a reduction of the scintillation indices due to the finite angular diameters of the various sources (see Chapter 2). Table II lists those sources for which angular diameter information is available (Little and Hewish 1968, Cohen et al. 1967) and shows that there is some variation between sources. This variation does not directly affect

TABLE II

Source	Diameter (seconds of arc)	
	(Little and Hewish)	(Cohen et al.)
0802+10	<0.2	0.3
0850+14	0.5	0.3
0933+04	0.3	0.2
0939+14	0.2	0.2
0949+00	0.4	0.2
1005+07	<0.2	0.2
1116-02	0.15	-
1226+02	0.15	0.04
1328+25	<0.8	0.2
1416+06	0.6	0.2
0134+32	0.35 x <0.2	0.1
0138+13	<0.2	0.1

our analysis, since we only compare the scintillation indices on each source with those observed on other days, and not with those of other sources. The variations in enhancement can also be attributed to changes in the corotating stream conditions due to the changing level of solar activity at the base of the stream. Figure 6.10 is a plot of the date of maximum phase of flares occurring in region A only, during June 1969, and some variation in the level of activity can be seen to occur during the course of the observations.

Sources with elongations between 90° - 180° east from the sun (see Figure 6.11), have their line of sight nearly parallel to the stream boundary, and hence should give some indication of the width of the stream at 1 A.U. from the duration of the scintillation enhancements. Source 1328+25, which is 32° north of the ecliptic, showed a distinct enhancement over 2 days. However, the increases in index for 1226+02, 1309-22 and 1416+06 were not so well defined, and the durations could not be accurately determined. An upper limit of 2 days yields a width of $\sim$ 0.5 A.U. for a solar wind velocity of 400 km/sec.

The arrival of stream A2 at the earth can be estimated from the change of scintillation indices of sources lying in the anti-solar direction. 1309-22 and 1416+06 showed enhancements on June 16 while 1328+25 was affected one day earlier on June 15. A sudden-commencement geomagnetic storm on June 16 accompanied the arrival of the stream at the earth. By June 17 the earth was embedded in the stream, and the

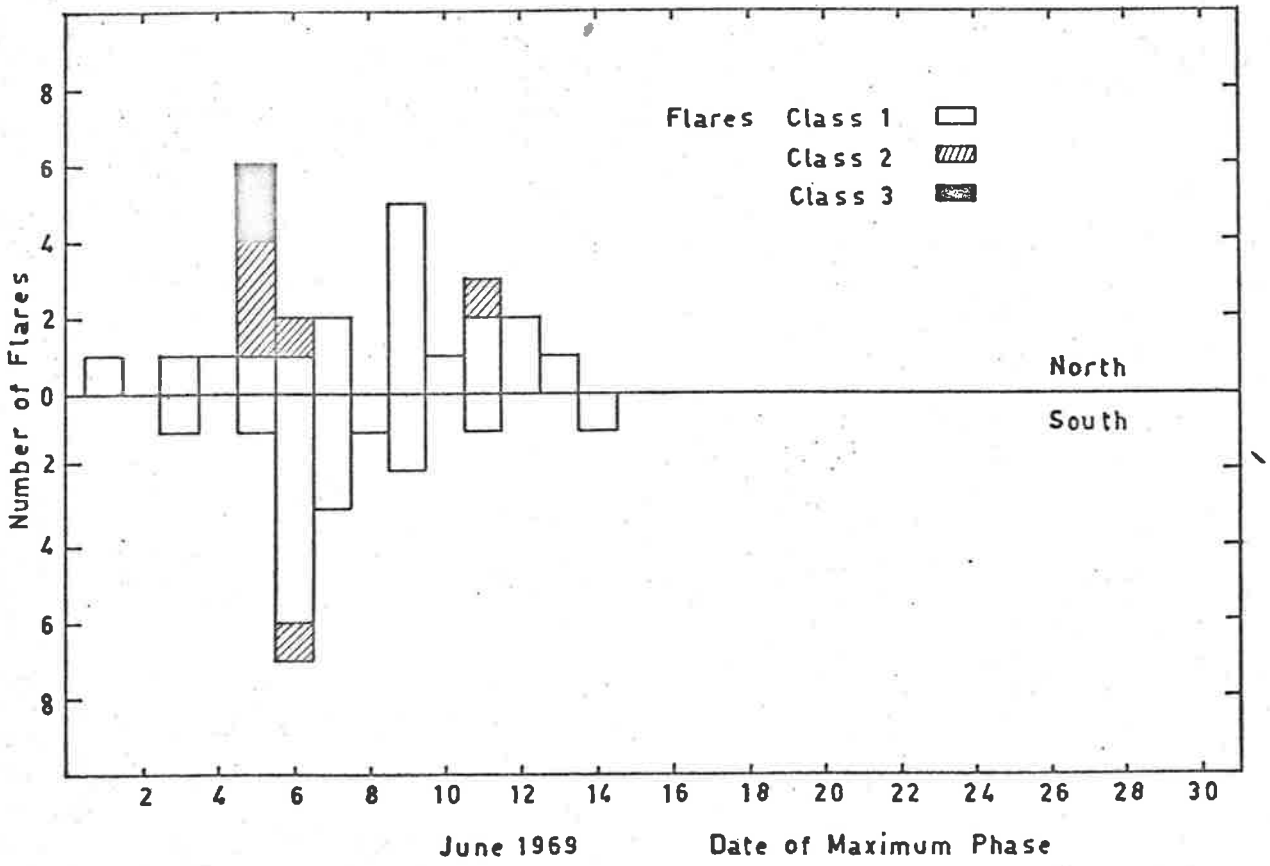

Figure 6.10 The date of maximum phase of flares occurring in region A only, during June 1969.

lines of sight to 0134+32 and 0138+13 intercepted the leading edge of the stream, causing a 200% increase in their scintillation indices. The corotation of the stream can be seen in the changes in the indices of the sources lying to the east of the sun; 0802+10 on June 13, followed by 0850+14 on June 14, and 0933+04, 0939+14, 0949+00 and 1116-02 on June 15. Figures 6.11(a-d) show the estimated position of the streams and blast wave during this period, assuming an average solar wind velocity of 400 km/sec and a stream width $\sim$ 1 day.

The second region of interest on the solar disc during June was the flare group at latitude 8° N having CMP date June 19 (region B). In May this region was extremely flare active (see Figure 6.2), but produced only moderate activity during June. There was evidence of an associated weak plasma structure corotating with the sun over the period of observation.

As in the case of the stream from region A, the stream structure associated with region B consisted of two streams, though not so clearly defined as A1 and A2. The earth satellites Vela 3 and 4 recorded an increase in the solar wind velocity from 300 - 450 km/sec on May 29-30, apparently associated with a 2-3% Forbush decrease on May 28-29. The continuing effect of the stream structure was seen in the enhanced scintillation of 0134+32 from June 2-4, and on 0138+13 on June 3.

Half a solar revolution later on June 18, 0624-05 exhibited a

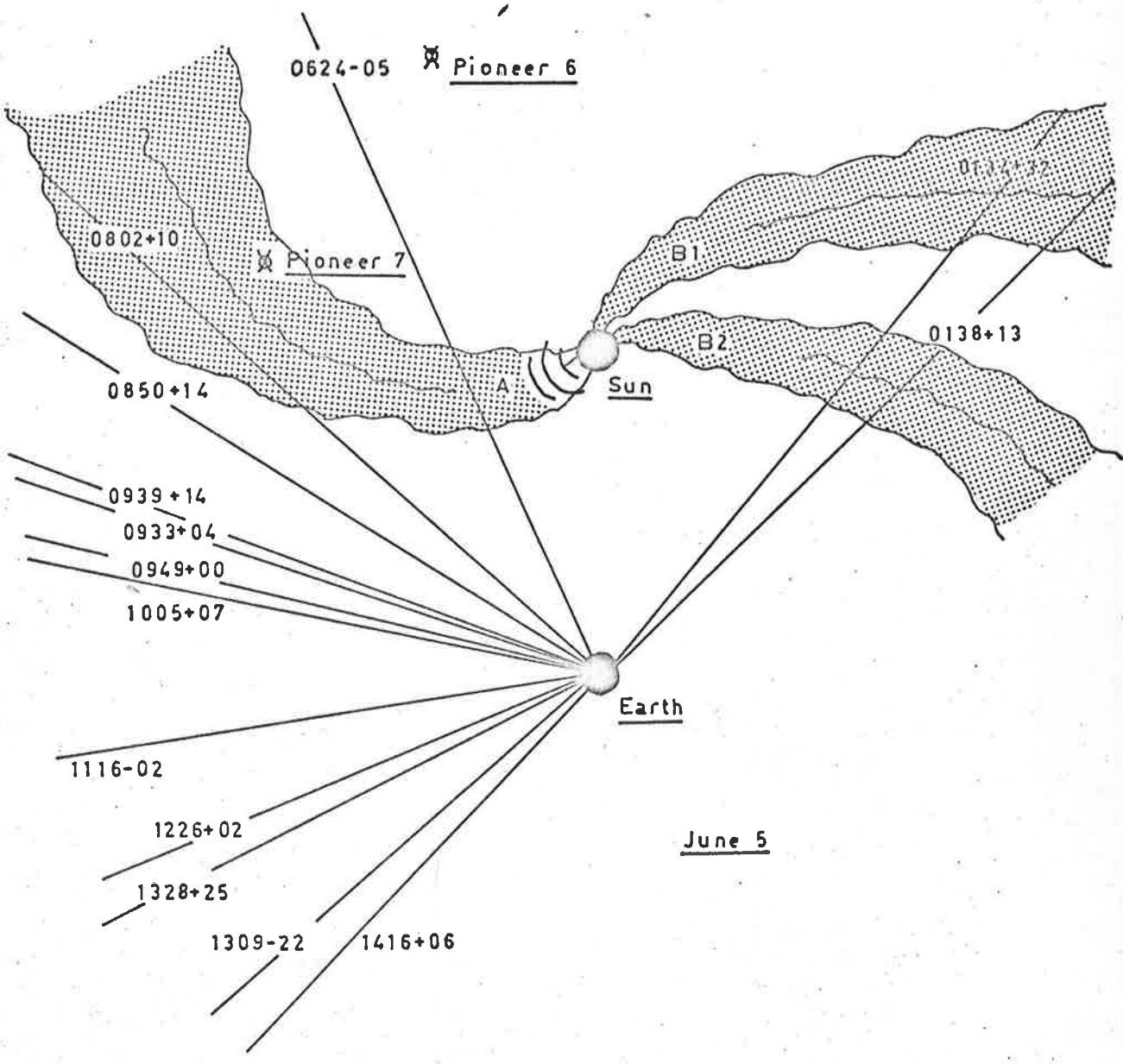

Figure 6.11(a) Estimated positions of the blast wave and corotating streams on June 5, 1969.

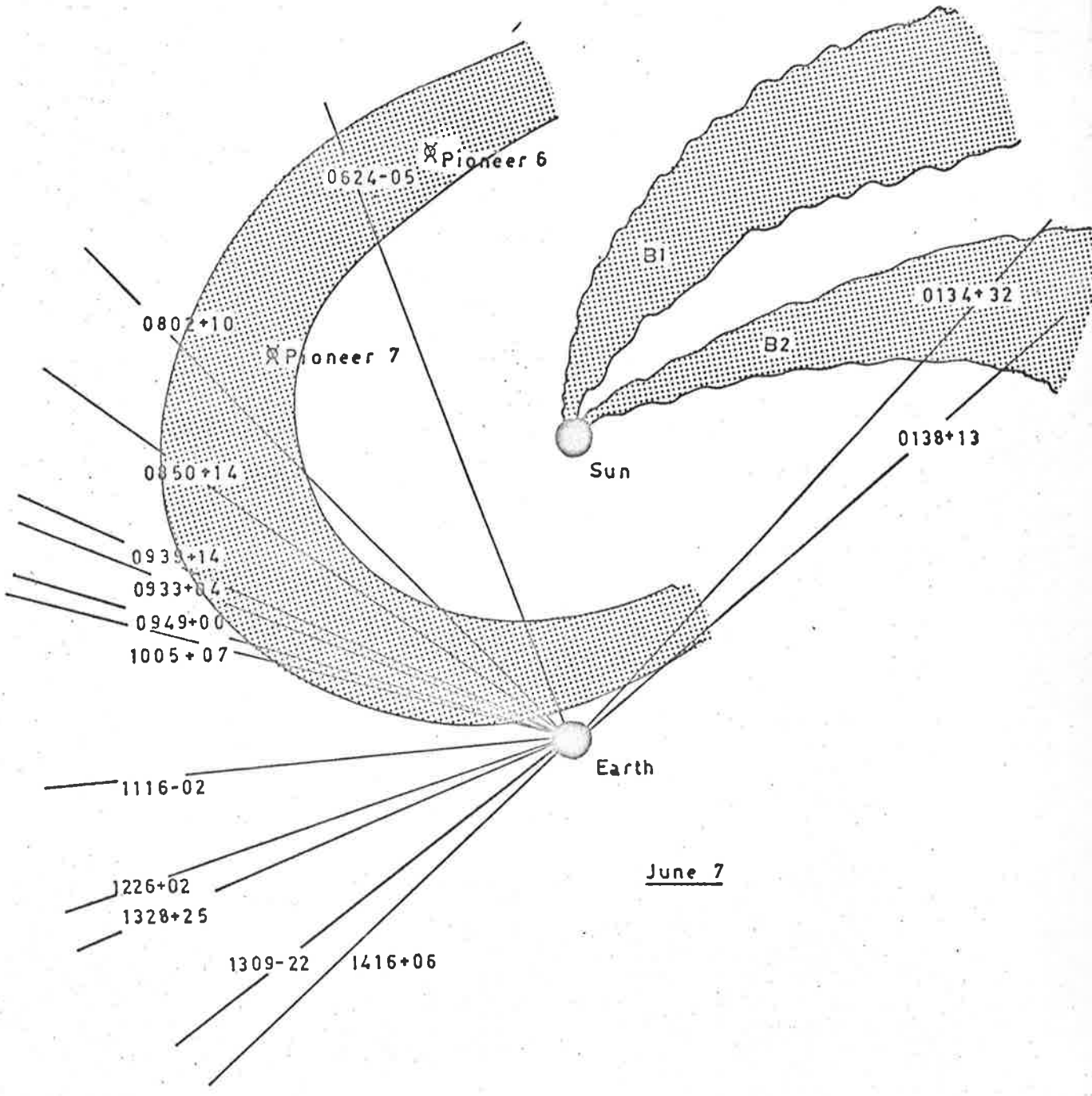

Figure 6.11(b) Estimated positions of the blast wave and corotating streams on June 7, 1969.

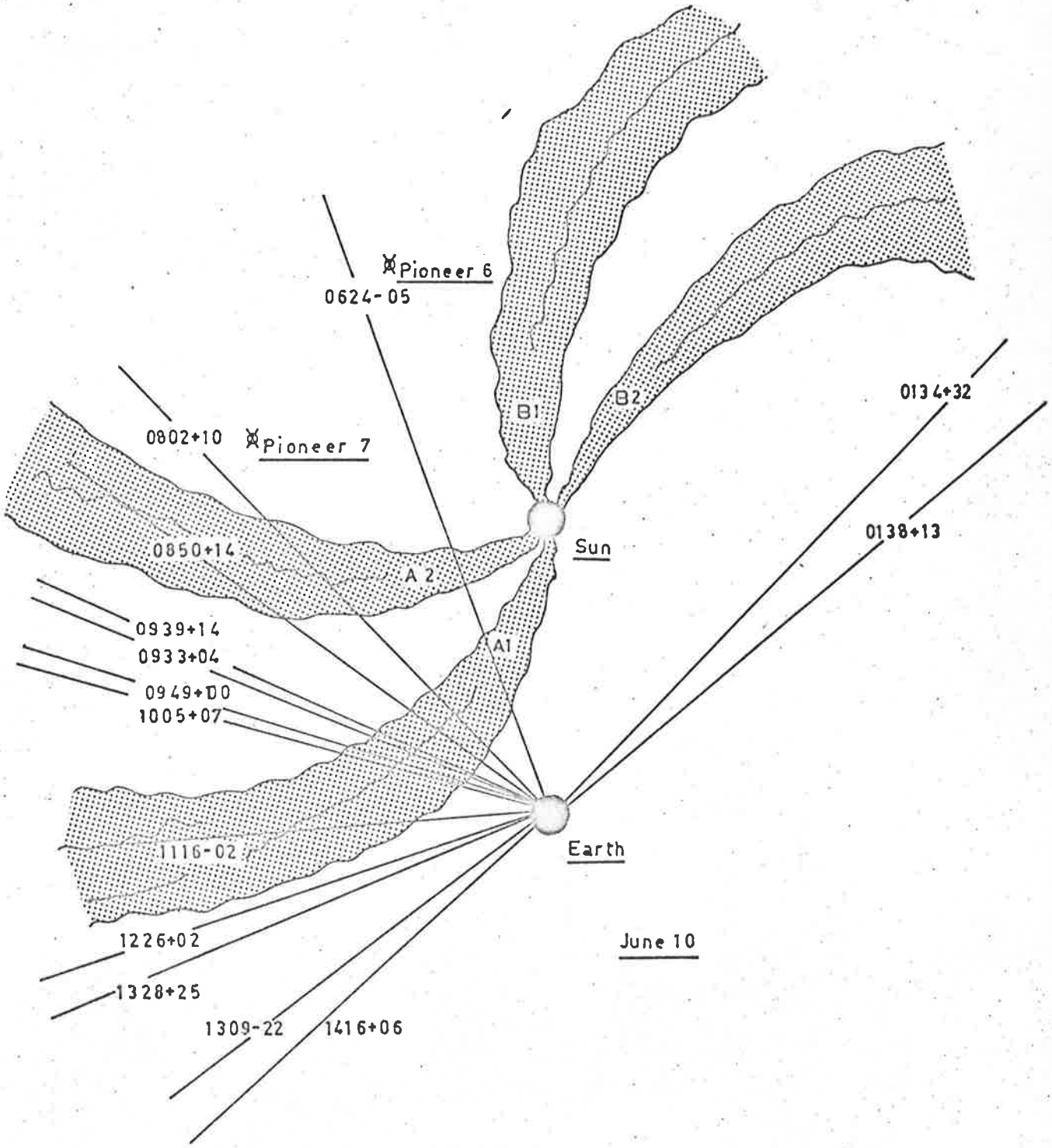

Figure 6.11(c) Estimated positions of the corotating streams on June 10, 1969.

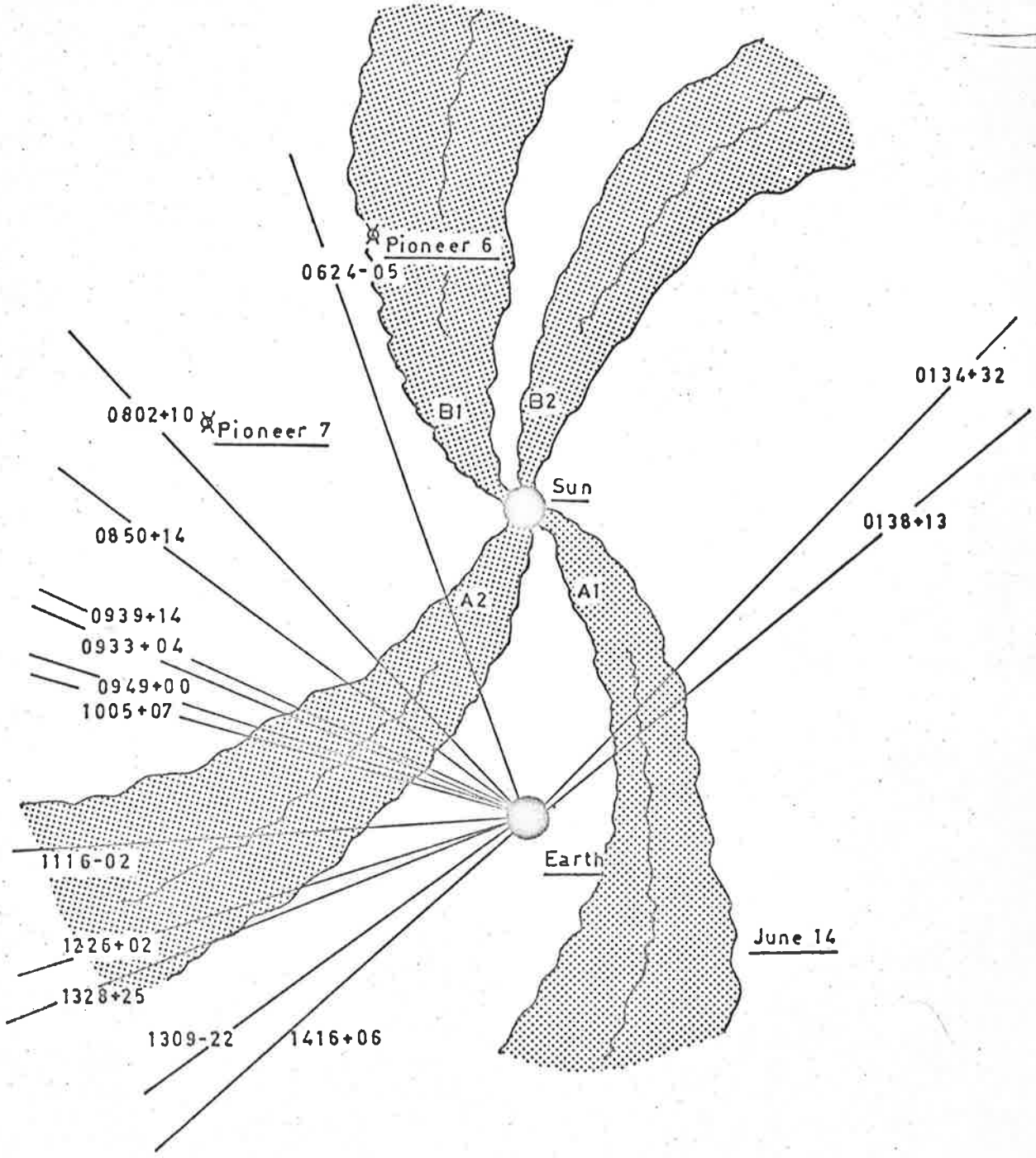

Figure 6.11(d) Estimated positions of the corotating streams on June 14, 1969.

200% increase in its index, with the arrival of stream B1, the first part of the substructure from region B. An enhancement was then observed to move sequentially through the sources whose lines of sight lay to the east of the sun; 0802+10 on June 17, 0850+14 on June 20, 0933+04 on June 20-21, 0939+14 on June 20, 0949+00, 1005+07, 1328+25 and 1416+06 on June 21. The relatively small changes in the scintillation indices on these sources emphasize the weakness of the disturbance.

In a similar fashion the movement of stream B2 through the medium can be traced, reaching the earth on June 24-25, 3 days after B1. Changes in scintillation index were observed on 0624-05 on June 20-21, 0802+10 on June 21, 0933+04 on June 24, 1116-02 on June 24, and 1309-22 on June 25. The estimated positions of these streams during June are outlined in Figures 6.11(a-d).

6.4 Scintillation Power Spectra

The method of spectral analysis applied to the present results has been described in Chapter 5. The spectral resolution was 0.08 Hz and the variances of the spectral estimates, P_n, were

$$\text{Var}\,(P_n) = P_n^2/8$$

i.e.

$$\sigma_{P_n} = P_n/\sqrt{8} = 35\% \cdot P_n \,,$$

where σ_{P_n} is the rms deviation of the spectral estimates. The spectra shown in Figure 6.12 are averages over several blocks of data, and so the variance of P_n is considerably reduced,

$$\text{Var } (P_n) = P_n^2/8K \ ,$$

where K is the number of blocks averaged. Typically K = 3 and then,

$$\text{Var } (P_n) = P_n^2/24 \ ,$$

and,

$$\sigma_{P_n} = 20\% \ P_n \ .$$

In the data analysis the mean value was subtracted from the original data, so that the first elementary frequency band of the spectrum has zero power. A further five elementary bands were set to zero to filter out any power due to ionospheric scintillation or drifts in receiver gain. Thus the first averaged point in the spectrum has zero power. The spectra formed in this way were smoothed using a Hanning spectral window (Blackman and Tukey, 1958), and hence the second point in each of the averaged spectra is contaminated by the unreal zero power in the first point, and the error bar for the second point will therefore be slightly greater than the standard 20% error bars shown in Figure 6.12. (Note: the first point of the power spectrum at zero frequency is not plotted in the diagram).

During the period of observation the computed scintillation power spectra exhibited significant dips at low frequency on four occasions. These spectra are drawn in Figure 6.12 on a logarithmic scale with the 20% error bars shown, and it can be seen that the dips have real significance and are not due to statistical variability.

On June 11 the stream A1 was inferred to be close to the earth

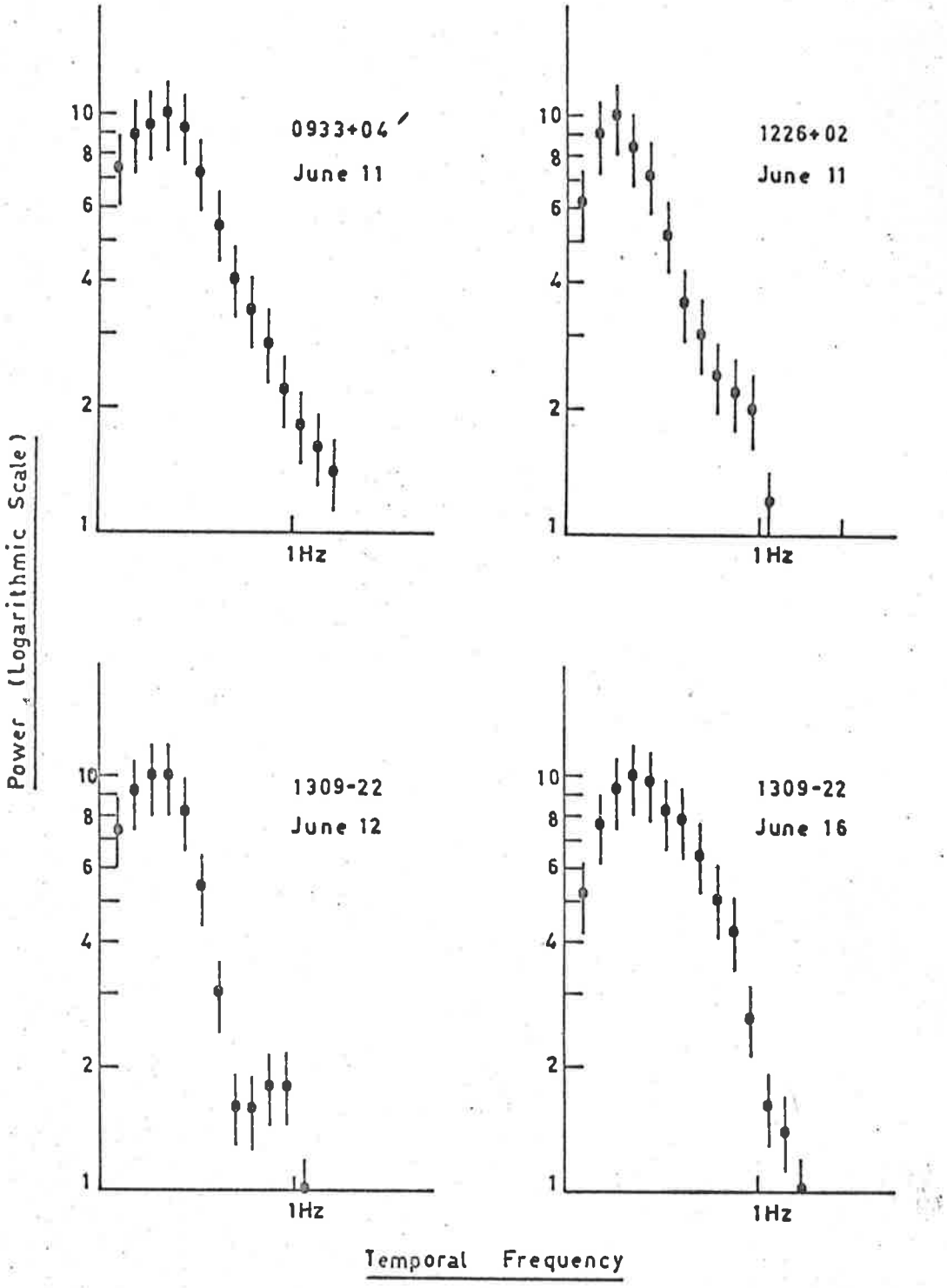

Figure 6.12 Scintillation power spectra exhibiting significant dips at low frequency (June 1969).

from consideration of the scintillation indices, and this conclusion is supported by the appearance of low frequency dips in the spectra of 0933+04 and 1226+02 on June 11 and 1309-22 on June 12. Each of these spectra were averaged over three blocks of data. A similar situation occurred on June 16 when stream A2 reached the earth, and source 1309-22 showed a low frequency depression in its power spectrum. The appearance of the depressions indicated the existence of a thin scattering region of well-defined velocity lying close to the earth, so that the earth was within the Fresnel region where the amplitude diffraction pattern was not fully developed.

Following the approach described in Chapter 4, a set of theoretical spectra were computed for various values of r_o, the scale size, and z, the screen-observer distance. To compare the experimental spectra with those computed theoretically, some measure of the solar wind velocity was required to convert the experimental spectra to a spatial frequency scale. The velocity, on the days in question was estimated from the Vela 3 and 4 satellite measurements shown in Figure 6.9. Unfortunately velocity data were not available on two of the days of interest (June 12 and 16) and interpolated values had to be used for those days. The components of these velocities perpendicular to the line of sight to the sources under consideration were then used to convert the experimental spectra. The best-fit theoretical spectra are shown in Figures 6.13 - 6.16, together with the limits of r_o and z for which reasonable fits could be obtained.

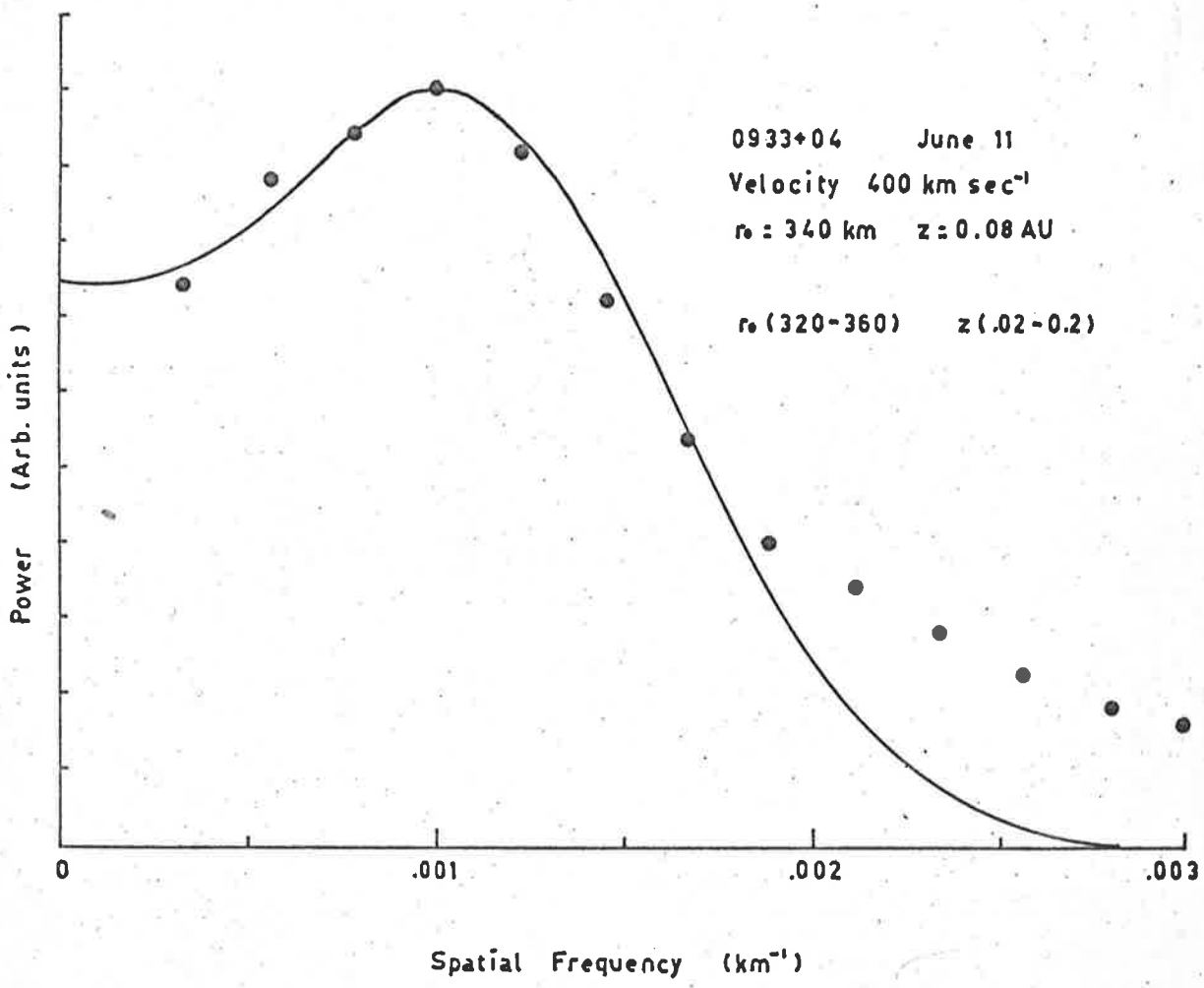

Figure 6.13 Best fit theoretical (---) spectrum to the experimental (●) spectrum of source 0933+04 on June 11, 1969.

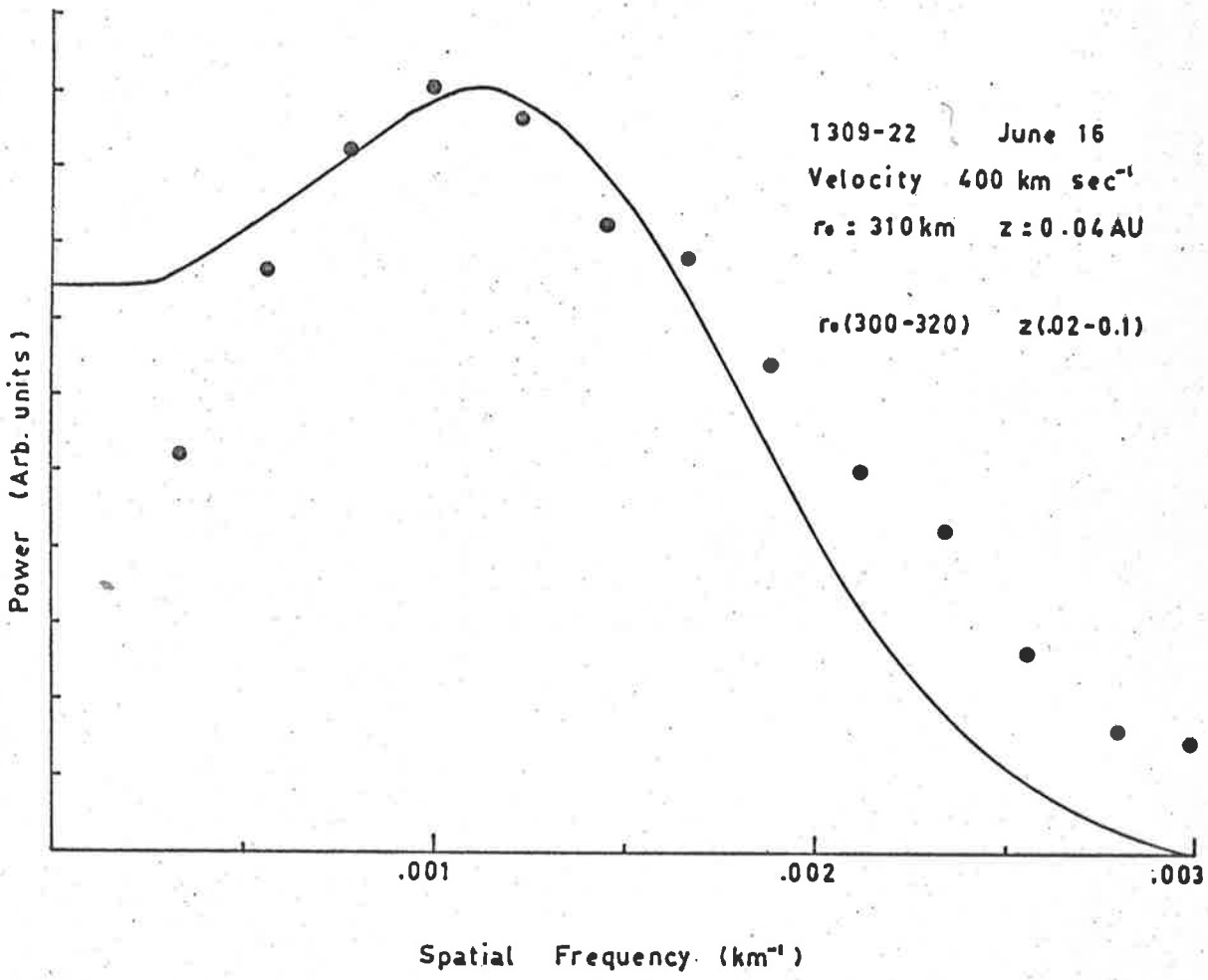

Figure 6.14 Best fit theoretical (---) spectrum to the experimental (●) spectrum of 1226+02 on June 11, 1969.

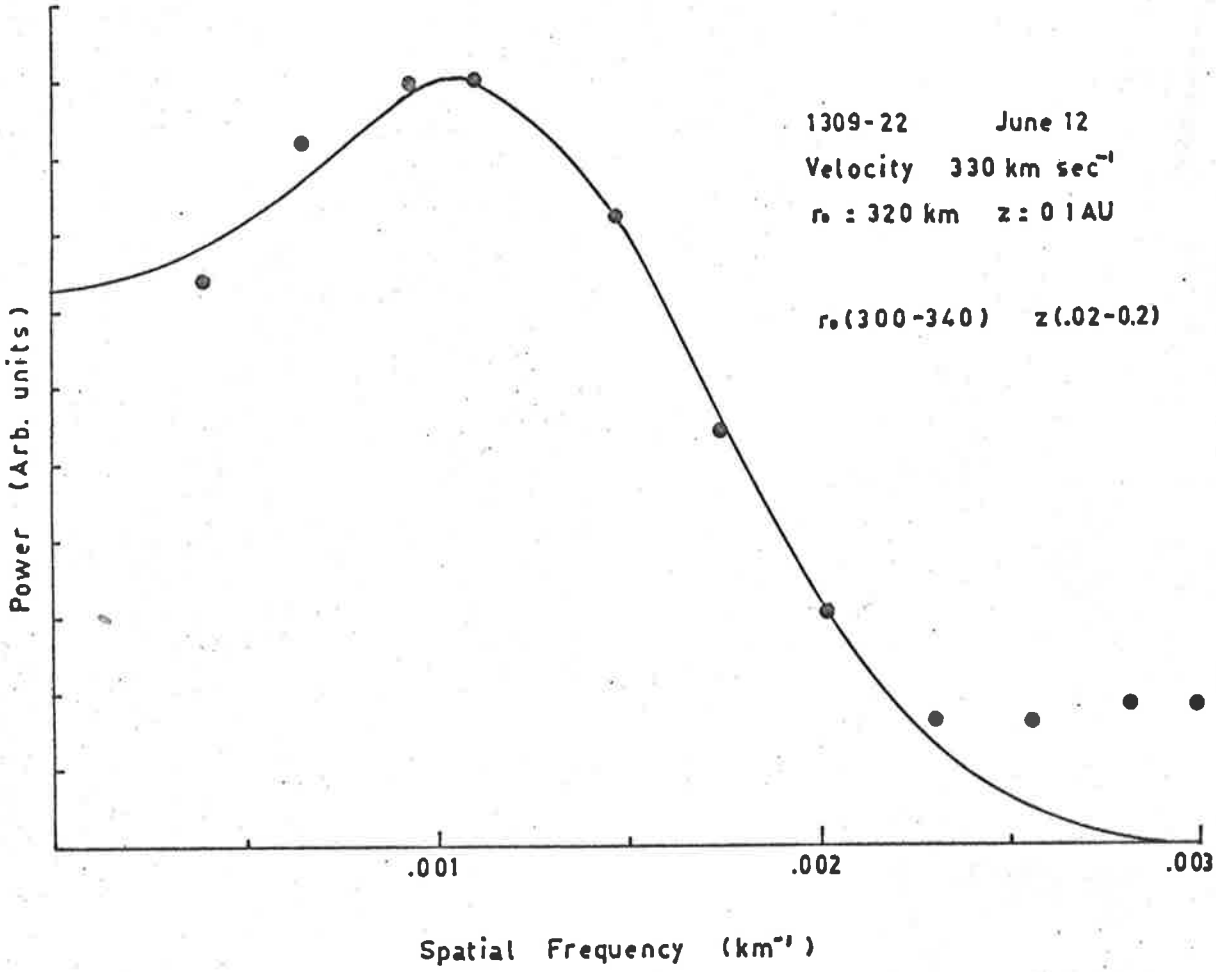

Figure 6.15 Best fit theoretical (---) spectrum to the experimental (●) spectrum of 1309-22 on June 12, 1969.

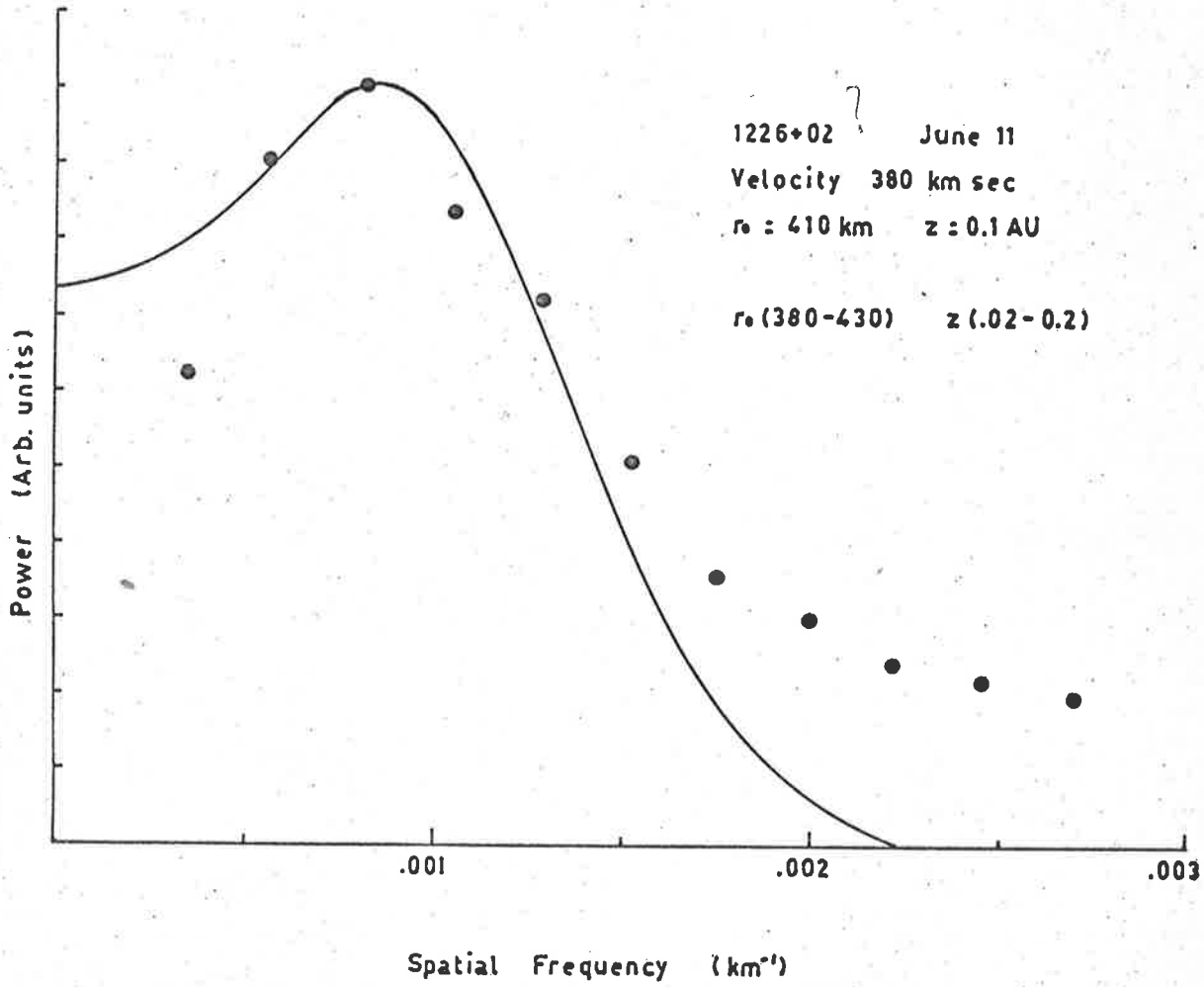

Figure 6.16 Best fit theoretical (---) spectrum to the experimental (●) spectrum of 1309-22 on June 16, 1969.

The non-Gaussian 'tails' on the experimental spectra require some explanation. As described in Chapter 5, each fundamental spectral estimate is convolved with the window,

$$H_K = \frac{1}{2\pi} \frac{\mathrm{Sin}^2 (T \pi f)}{T \, \mathrm{Sin}^2 (\pi f)} ,$$

which has major side-lobes at $f \pm 3/2T$, with height equal to 4% of the main peak amplitude. Thus there is a 4% contribution to the power at frequency, f, from the frequencies at $f \pm 3/2T$. This is known as spectral leakage, and the non-Gaussian tails on the experimental spectra can be explained in terms of this. Eventually the Gaussian spectrum falls off faster than any power of the frequency, and the side-lobes of the estimates begin to dominate the spectrum, thus producing a tail at higher frequencies. The situation can be improved by the application of a spectral window, as has been done with the present examples, but the tail cannot be completely removed.

Taking this factor into account, the theoretical spectra of Figures 6.13 to 6.16 can be seen to fit the experimental points quite well. The scale sizes, r_o, derived from the theoretical spectra are 340, 410, 320 and 310 km on the four occasions when low frequency depressions were observed. These are reasonably consistent within the accuracy of the method of estimation, and yield an average value of 350 km.

As in Chapter 4 we compare this actual scale with the scale which would be deduced from a correlation analysis of IPS. Using the

expression derived by Bowhill (1961),

$$r = r_o \left(\frac{1 + a^2}{3 + a^2} \right)^{\frac{1}{2}} ,$$

where

$$a = \frac{\lambda z}{\pi r_o^2} ,$$

the scale, r, measured by correlation analysis would be $\sim$ 200 km for r_o = 350 km. As a cross-check on this, the 1/e point of the spectrum in Figure 6.13 for r_o = 340 km, was measured ($\sim$ .0018 km^{-1}) and the scale r derived,

$$r = \frac{1}{\pi\ (.0018)}\ km$$

$$\simeq 180\ km,$$

which is consistent with the above value from Bowhill's expression, and in agreement with other independent measurements of the scale of irregularities in the solar wind, as summarized by Readhead (1971).

Another feature of the spectra which is relevant to our discussion are the changes in the widths of the power spectra on successive days of observation. In Figure 6.17(a, b) the relative half-widths of the normalised spectra are plotted for a number of sources. When compared with the scintillation enhancements of Figure 6.5, Figure 6.17 shows a strong correlation between increases in spectrum width and scintillation index. The features which are evident in Figure 6.17 have been labelled according to the positions of the blast wave (X) and corotating streams (A1, A2, B1, B2) which have been deduced from our analysis of the scintillation indices.

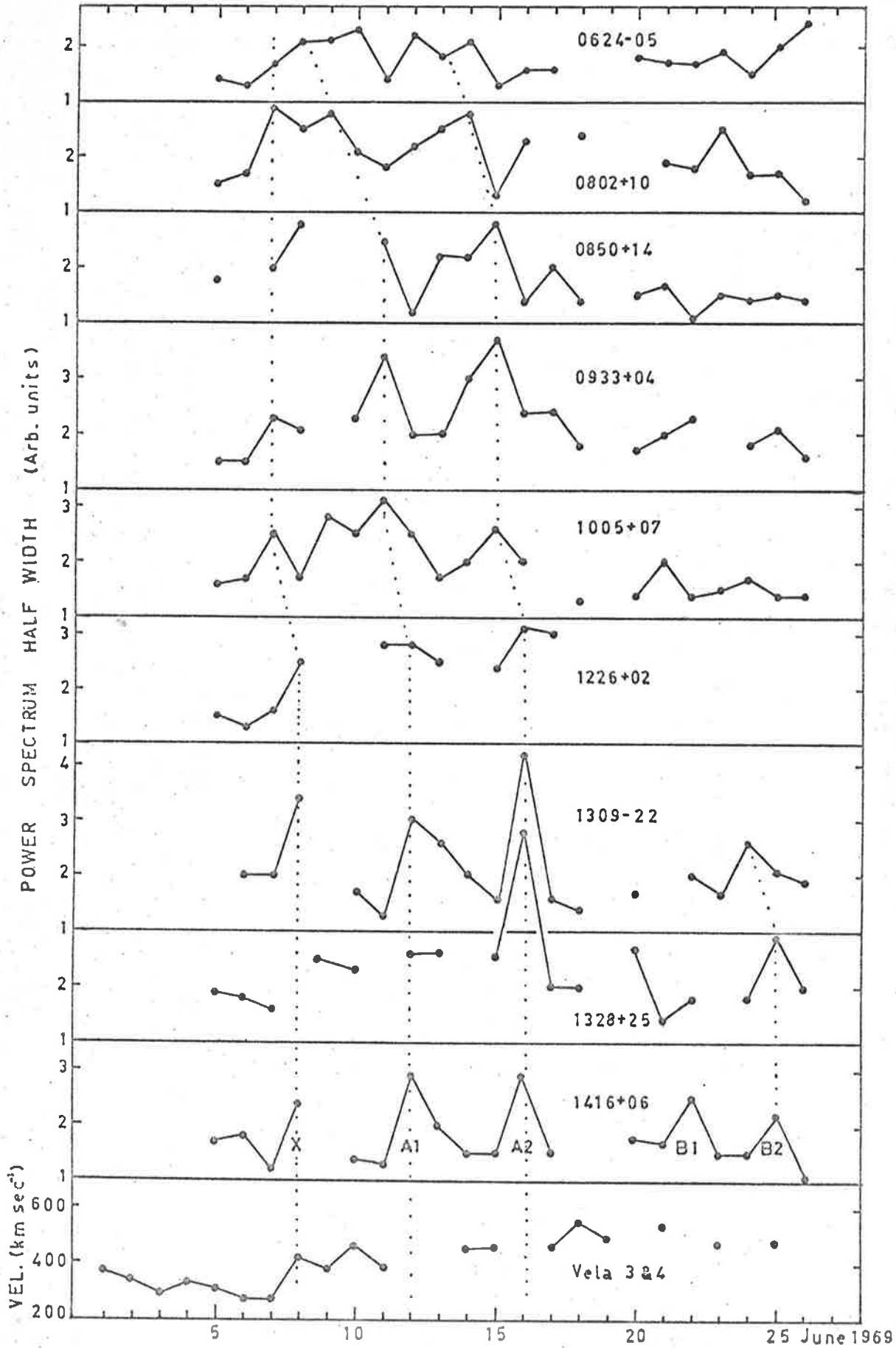

Figure 6.17 The half-widths of the scintillation power spectra for sources observed in June 1969.

Where sources lie nearly parallel to a possible stream boundary (between elongations 90° and 180° east of the earth-sun line), the passage of the streams showed quite markedly in the changes in spectrum width. Source 1416+06 is a particularly good example of this, showing the passage of the blast wave, and all four streams quite distinctly. Since the line of sight to 1416+06 was nearly parallel to the stream boundaries, the duration of the enhancements in spectral width is a good indication of the extent of the streams at 1 A.U. from the sun. Streams A2, B1 and B2 each had a width $\sim$ 1 day, while stream A1 showed a distinctly greater duration $\sim$ 2 days.

The lines of sight to sources which are between 0° and 90° east of the sun, intercept the streams for nearly one quarter of a solar rotation, and although the greatest contribution to the scintillation will occur when the stream intercepts the line of sight at its point of closest approach to the sun, there will be a significant contribution while the stream is a short distance on either side of this point. Hence the duration of the enhancements in spectral width on such sources would be extended, and this was in fact observed in Figure 6.17a. Thus the relative changes in the width of scintillation spectra is an extremely sensitive indicator of the presence of disturbed regions in the solar wind, and provides a valuable confirmation of the scintillation index analysis.

To determine whether the observed changes in spectral width were

associated with either variations in the scale of the irregularities in the interplanetary medium or variations in the plasma velocity, we have plotted the velocity measurements from the Vela 3 and 4 earth satellites beneath the spectral information in Figure 6.17(b). Unfortunately there was no velocity information available for June 12 and 16 during the arrival of the streams A1 and A2 at the earth, and it is therefore not possible to distinguish the source of the spectral width increases on those days. However, from Figure 6.18, which is a plot of the interplanetary magnetic field strength (Antonucci et al. 1971) from Pioneer 8 situated near the earth (Figure 6.21), there is clearly an increase in field strength associated with streams A1 and A2, on June 12 and 16.

If, as the results in Chapter 4 indicated, the scale of irregularities in the solar wind is closely linked to the ion gyro-radius in the medium, then the observed increases in field strength by a factor ~ 2, would produce a decrease in scale, and hence an increase in spectral width by the same factor. From Figure 6.17 it can be seen that the increases associated with A1 and A2 are indeed of this order. This relationship is only valid while the solar wind velocity remains constant, and for the events of June 1969 the result must await confirmation from spacecraft measurements of the velocity. Analysis of streams B1 and B2 face a similar restriction in the lack of continuous velocity data.

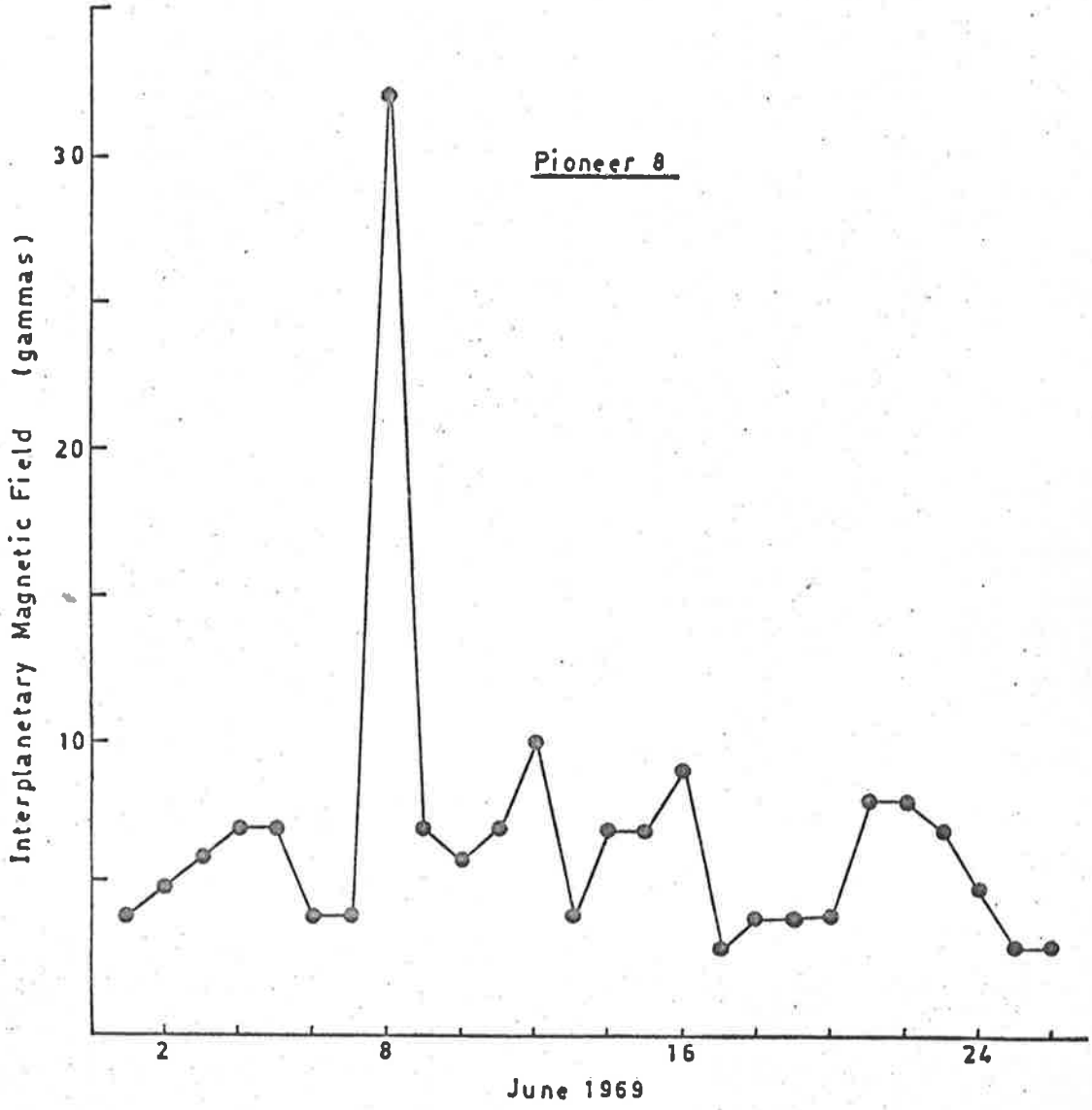

Figure 6.18 The strength of the interplanetary magnetic field during June 1969 measured by Pioneer 8.

The blast wave from region A on the sun, which arrived at the earth on June 8, was accompanied by an increase both in the velocity of the solar wind and the strength of the magnetic field at Pioneer 8. The spectral widths from a number of sources on June 8 increased by factors of 1.5 - 2.0, and this corresponded to the increase in solar wind velocity by a factor $\sim$ 1.6 from June 7-8. However, the magnetic field strength increased by a factor of $\sim$ 3.5 for a short period on June 8, and a change of this magnitude was not apparent in the variations in spectral width. One would expect a compression of the magnetic field along the leading edge of the blast wave and this was probably the source of the high field conditions observed on Pioneer 8. However, this enhancement would be localised at the shock front and of only limited extent, and thus the contribution to changes in spectral width would probably be negligible.

6.5 Discussion

A recent paper by Wilcox and Colburn (1971) presented the positions of the quiet-sun magnetic field sector boundaries observed near the earth during 1969, and their results lend strong support to our interpretation of the scintillation data presented in the previous section. The sector boundary crossings for 1969 have been reproduced in Figure 6.19, where dark shading represents field polarity toward the sun, and light shading field polarity away from the sun. The hatched shading indicates regions of ambiguous polarity, and the blank intervals indicate no available spacecraft observations of the interplanetary

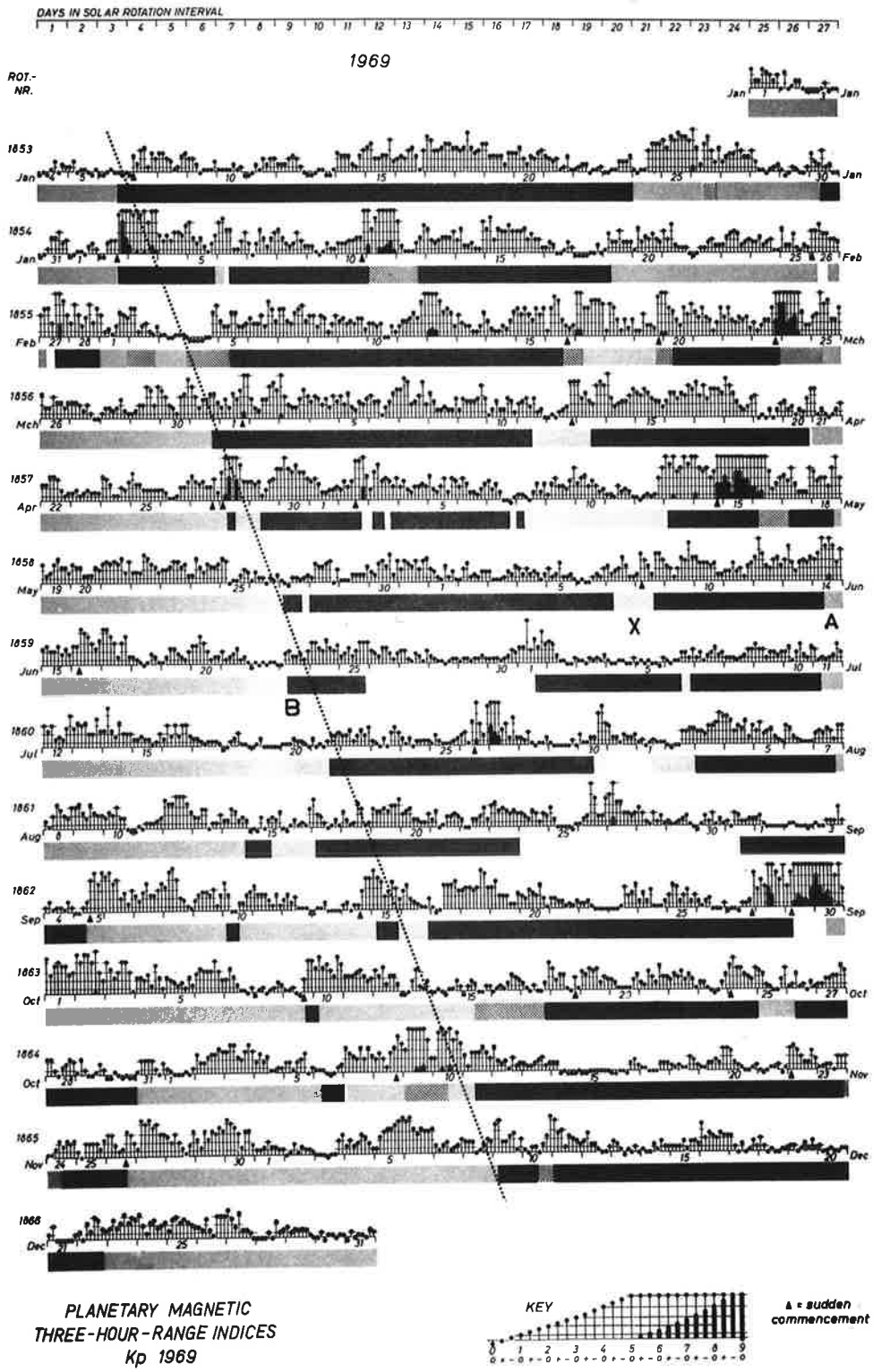

Figure 6.19 The interplanetary magnetic field sector boundaries.

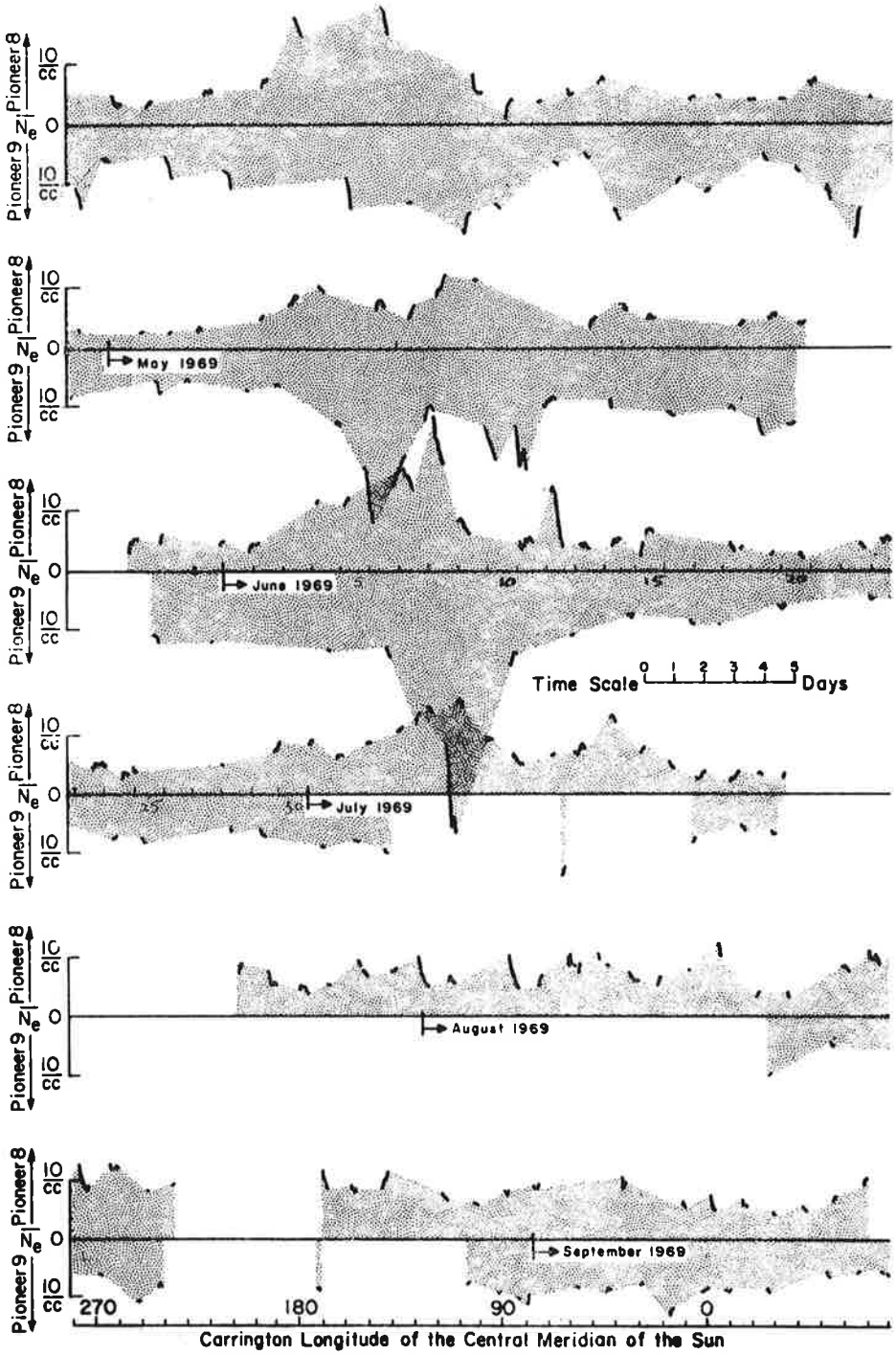

Comparison of the average solar wind density along the lines of sight to Pioneer 8 (plotted upward) and to Pioneer 9 (plotted downward) during twelve turns of the sun in 1969–1970

Figure 6.20

field. The events to be discussed here are marked X, A and B on June 8, 14 and 23.

The reversal of the dominant field polarity during June 7 and 8 coincided exactly with the arrival of the blast wave at the earth which we have deduced from scintillation observations. The duration of the field reversal in Figure 6.19 (1 day) agrees excellently with our estimate of the width of the blast in the ecliptic plane.

Following the blast, the continuing flux of plasma from region A on the sun which formed the complex stream structure A1 and A2, was also associated with a reversal of the dominant magnetic field direction, which in this case was the boundary between two sectors of opposite polarity. Stream A1 reached the earth on June 12 two days before the arrival of the sector boundary on June 14, and stream A2 followed two days later on June 16. Thus the two streams appear to have been spaced evenly $\sim$ 2 days on either side of the sector boundary crossing.

It is worth noting that stream A2 was much more turbulent than A1, as evidenced by the larger scintillation indices and the fact that the arrival of A2 at the earth was accompanied by a sudden-commencement geomagnetic storm, whereas A1 was not. This difference in activity between the trailing edge of one sector and the leading edge of the following sector, was therefore compared with the distribution of electron density within a sector, obtained by spacecraft measurements in the medium itself. The graph (Figure 1.8(c)) shows a sharp increase in

the electron density about 1-2 days after a sector boundary crossing, and this coincides with the estimated position of stream A2. Thus, it appears that the sharp increase in the total electron density is also accompanied by an increase in the fluctuations of the density responsible for interplanetary scintillation. The sharp increase in density associated with A2 was probably connected with the sudden-commencement geomagnetic storm on June 16. There is also a more gradual increase in electron density occurring in the trailing portion of a sector, and this corresponded roughly to the position of stream A1.

A comparison of the arrival times of streams B1 and B2 at the earth with the arrival of the magnetic field sector boundary late in June, showed a similar symmetry. The sector boundary reached the earth on June 23, and stream B1 arrived on June 21-22, and stream B2 on June 24-25. Thus, the structure associated with a sector boundary appears to have a typical width of 3-4 days, with regions of turbulence on either side of the boundary associated with the interaction of the two sectors.

Croft (1971) has obtained intermittent measurements of the average electron number density in the interplanetary medium along the signal path from Pioneer 6, 7, 8 and 9, and Mariner 5 to earth, and some of his results for 1969 are shown in Figure 6.20. Some caution must be exercised in the interpretation of these graphs since the short line segments are the real measured values, whereas the shading interpolated between these is 'an aid for the perception of continuity' (Croft, 1971).

However, a feature which clearly dominates the graphs is the large increases in electron density observed on June 8 on the paths between earth and Pioneer 8 and 9, the positions of which are shown in Figure 6.21. This feature corresponds to the suggested blast-wave structure which was initiated on the sun on June 5, and the fact that it was observed even on Pioneer 9 is an indication of the wide-angle nature of the blast.

A smaller, but still significant, increase in electron number density on June 12 along the propagation path to Pioneer 8 coincides with the arrival of stream A1 at the earth, but any effects possibly associated with the other streams are obscured by the poor time coverage of the data.

An interesting feature of the present scintillation study is the apparent source of sudden-commencement geomagnetic storms. We note that the arrival at the earth of both the blast-wave on June 8 and the stream A2 on June 16, were associated with storm sudden-commencements (ssc). This observation shows that ssc's can be caused by both propagating discontinuities in the interplanetary medium, and by streams of enhanced plasma which are convected past the earth by the expansion of the solar corona and the rotation of the sun.

In this chapter we have shown that IPS of a grid of radio sources is a particularly useful method for tracing the origin and development of interplanetary streams, plasma blast waves, and the magnetic field

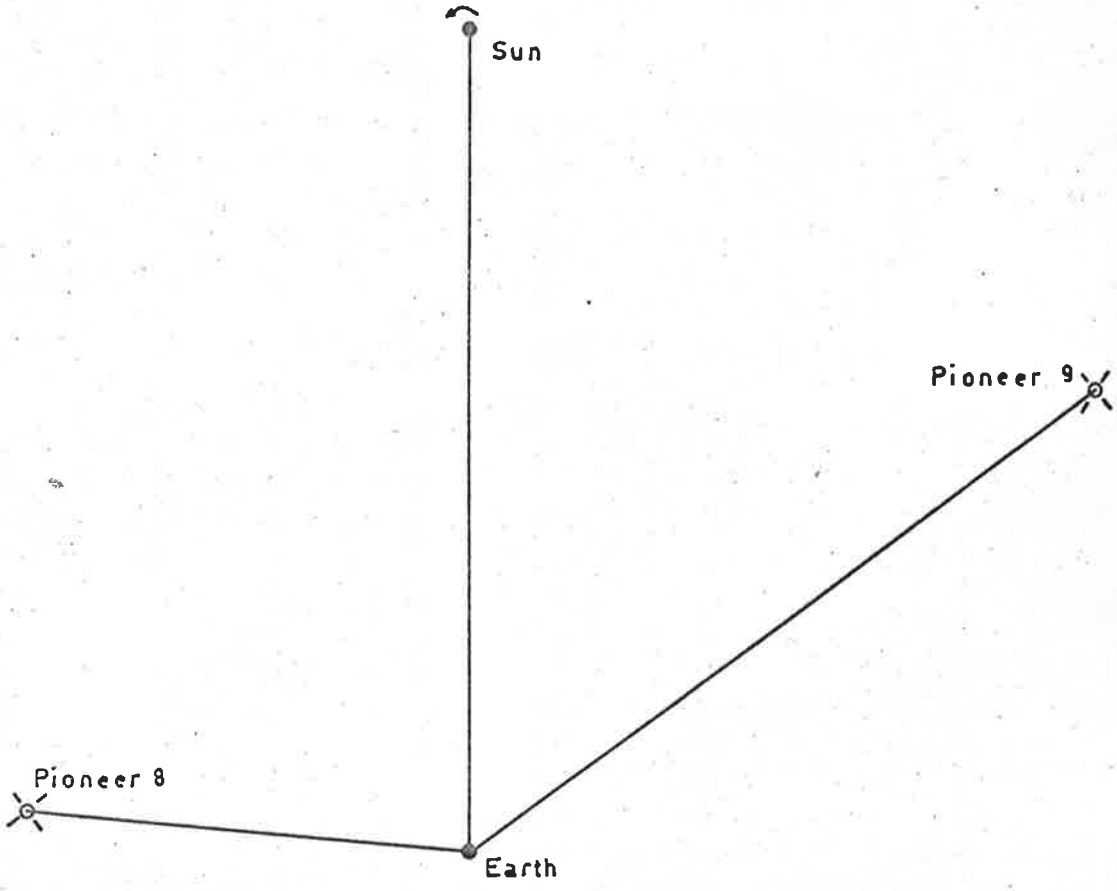

Figure 6.21 Positions of the Pioneer 8 and 9 spacecraft in June 1969.

sector boundaries in the solar wind. There is strong evidence that events such as these can be related to the presence of flare-active regions on the solar surface.

CHAPTER 7

RESULTS III - JUNE 1970

Introduction

A further observing period of one month during June 1970 was used to extend the previous work on the mapping of the movement and geometry of large scale features in the solar wind from single station scintillation observations. The work to be described was carried out between May 30 and June 24, 1970, again using the radioheliograph at Culgoora, N.S.W. The observing and analysis procedures have already been fully described in the preceding chapters and will not be repeated here.

7.1 Results and Discussion

A plot of the scintillation indices for fourteen sources observed during June 1970 (Figure 7.1) displayed three distinct features, which were consistent with the existence of three streams of disturbed plasma corotating with the sun over the period of observation. The results to be presented here will be described in terms of this model, and reference to Figure 7.2(a-f) showing the estimated positions of these events on a number of days will clarify the discussion to follow.

The effect of stream A was first seen clearly on source 0933+04 on June 5, causing a 300% increase in its scintillation index. Enhancements were then observed to occur sequentially for 0939+14 on

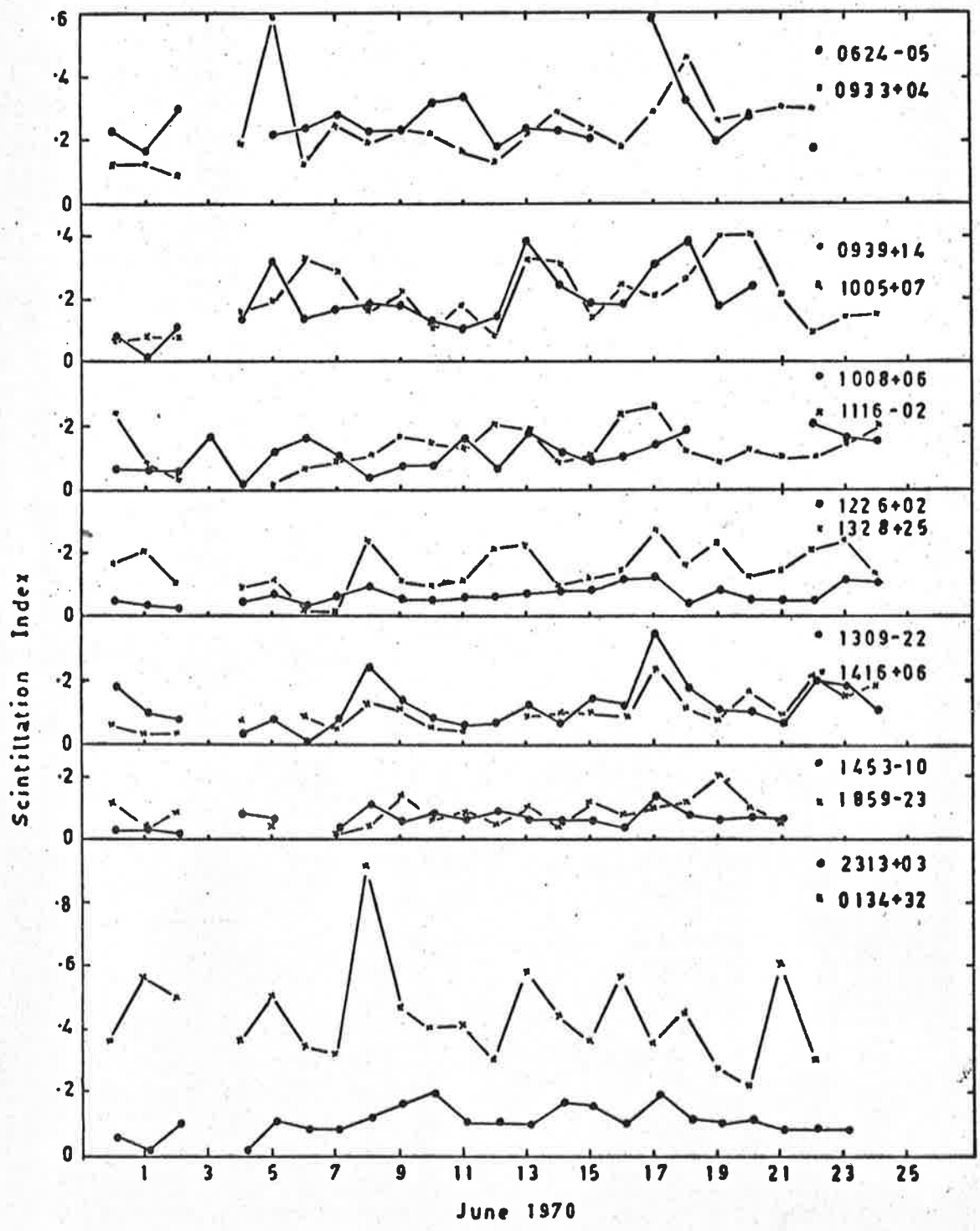

Figure 7.1 Scintillation indices for fourteen sources observed during June 1970.

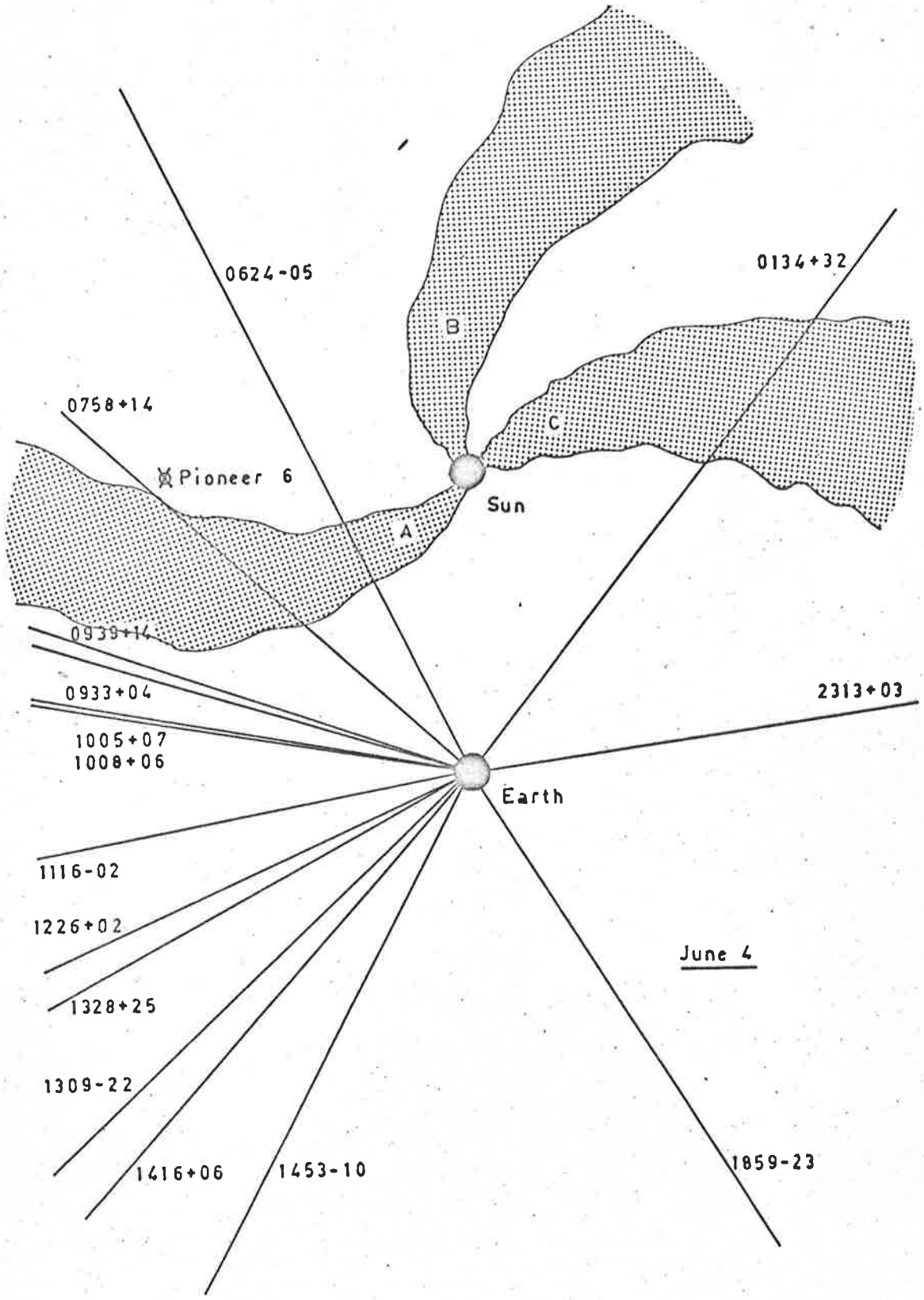

Figure 7.2(a) The estimated positions of the corotating streams during June 1970.

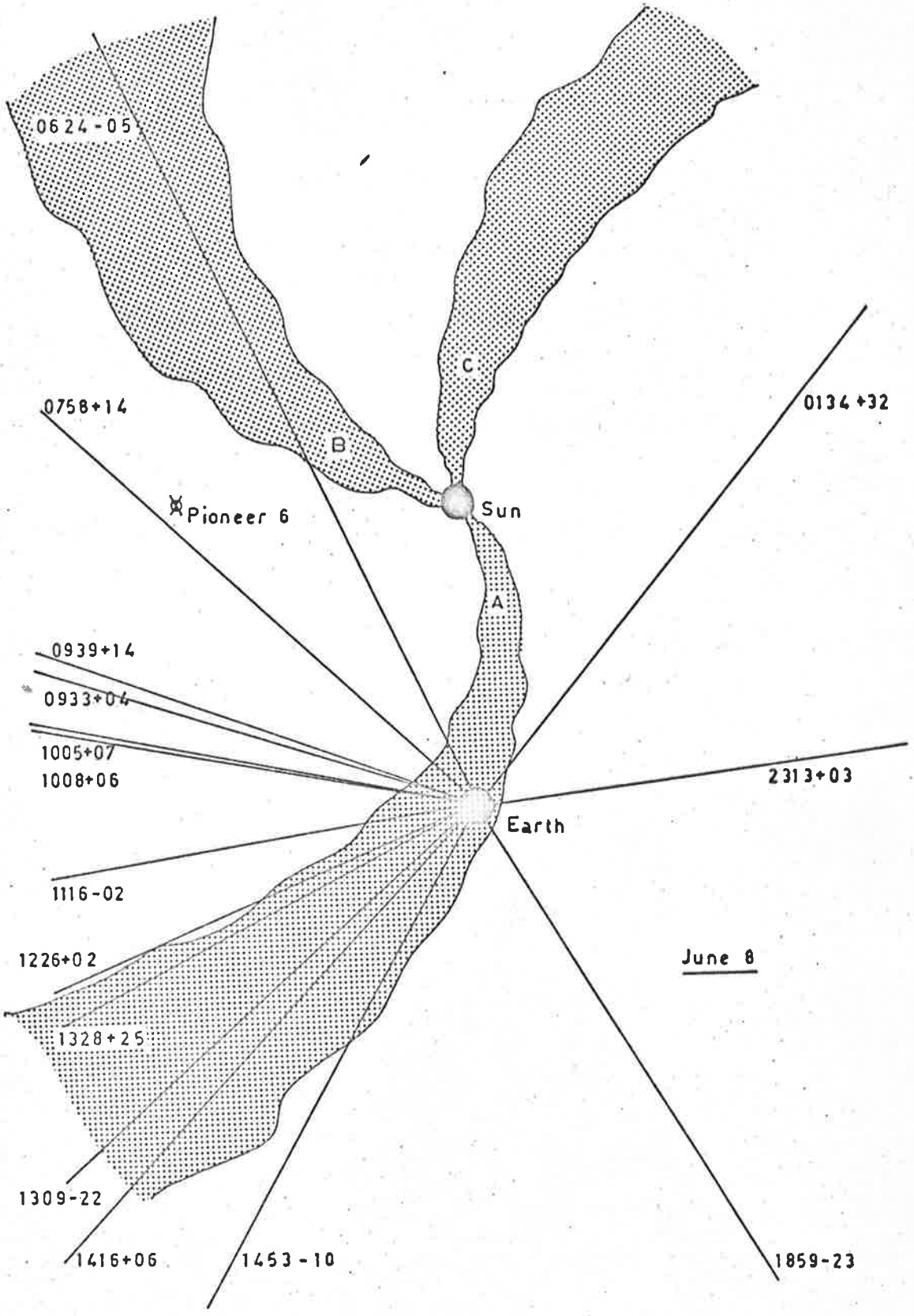

Figure 7.2(b) The estimated positions of the corotating streams during June 1970.

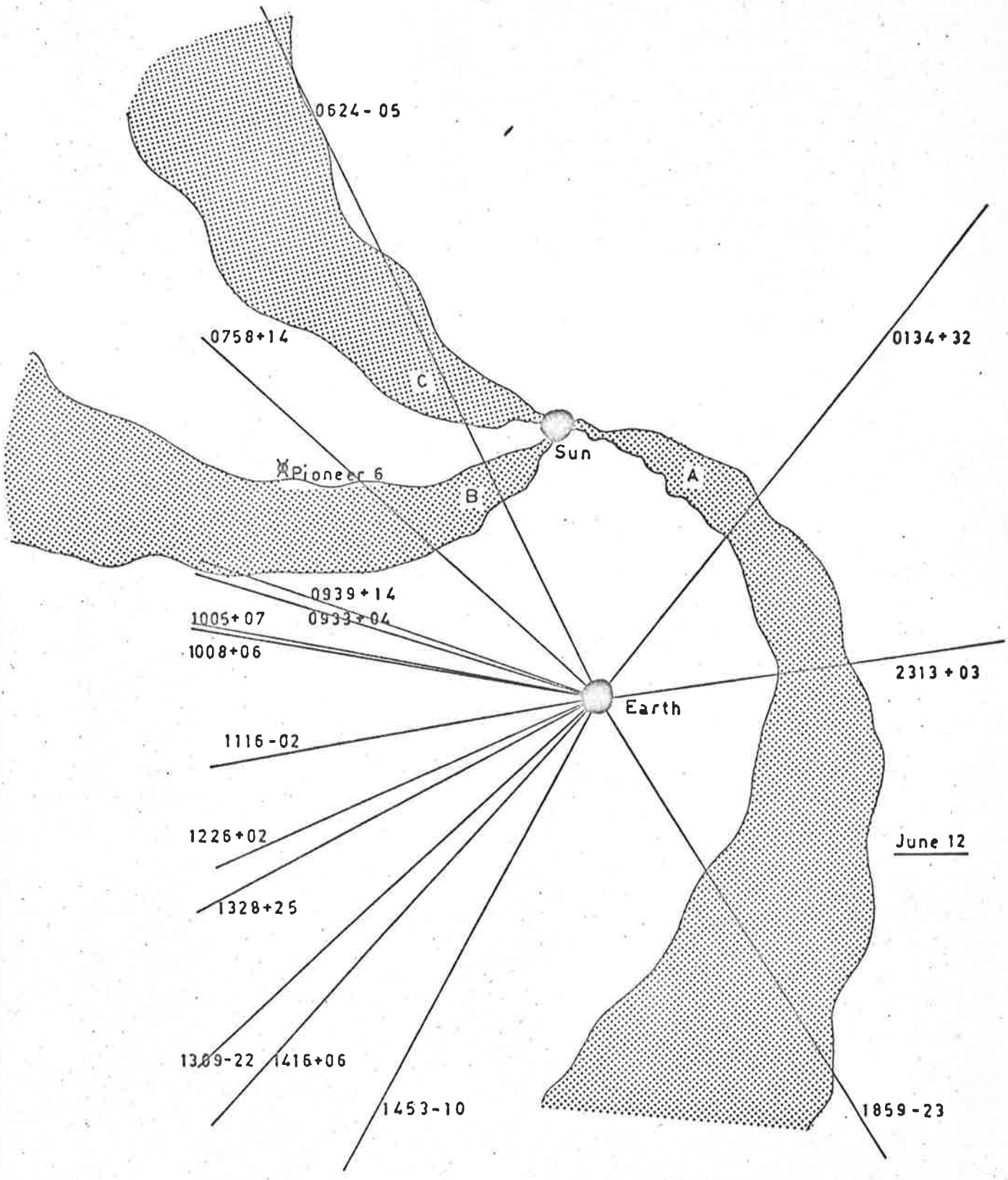

Figure 7.2(c) The estimated positions of the corotating streams during June 1970.

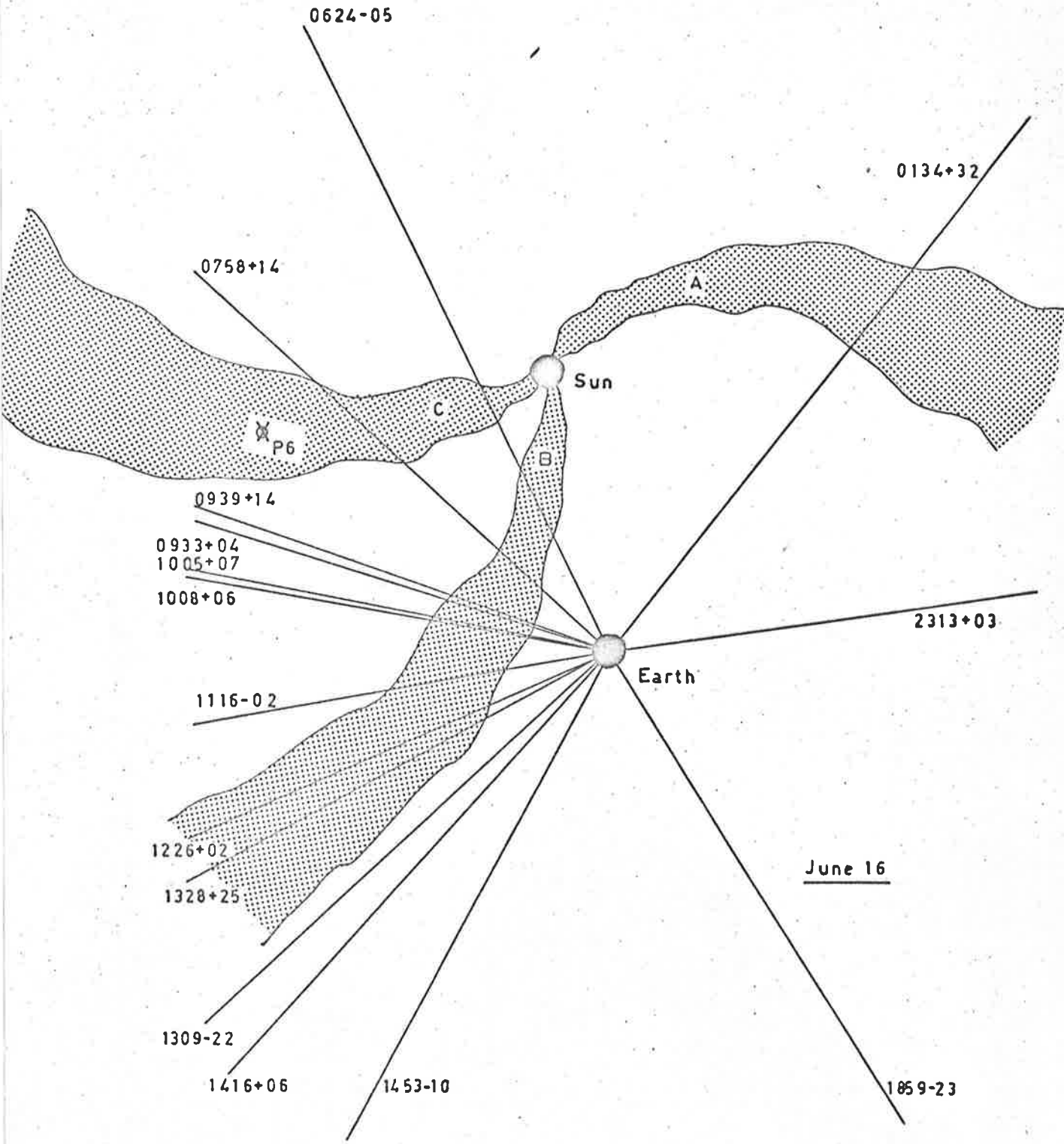

Figure 7.2(d) The estimated positions of the corotating streams during June 1970.

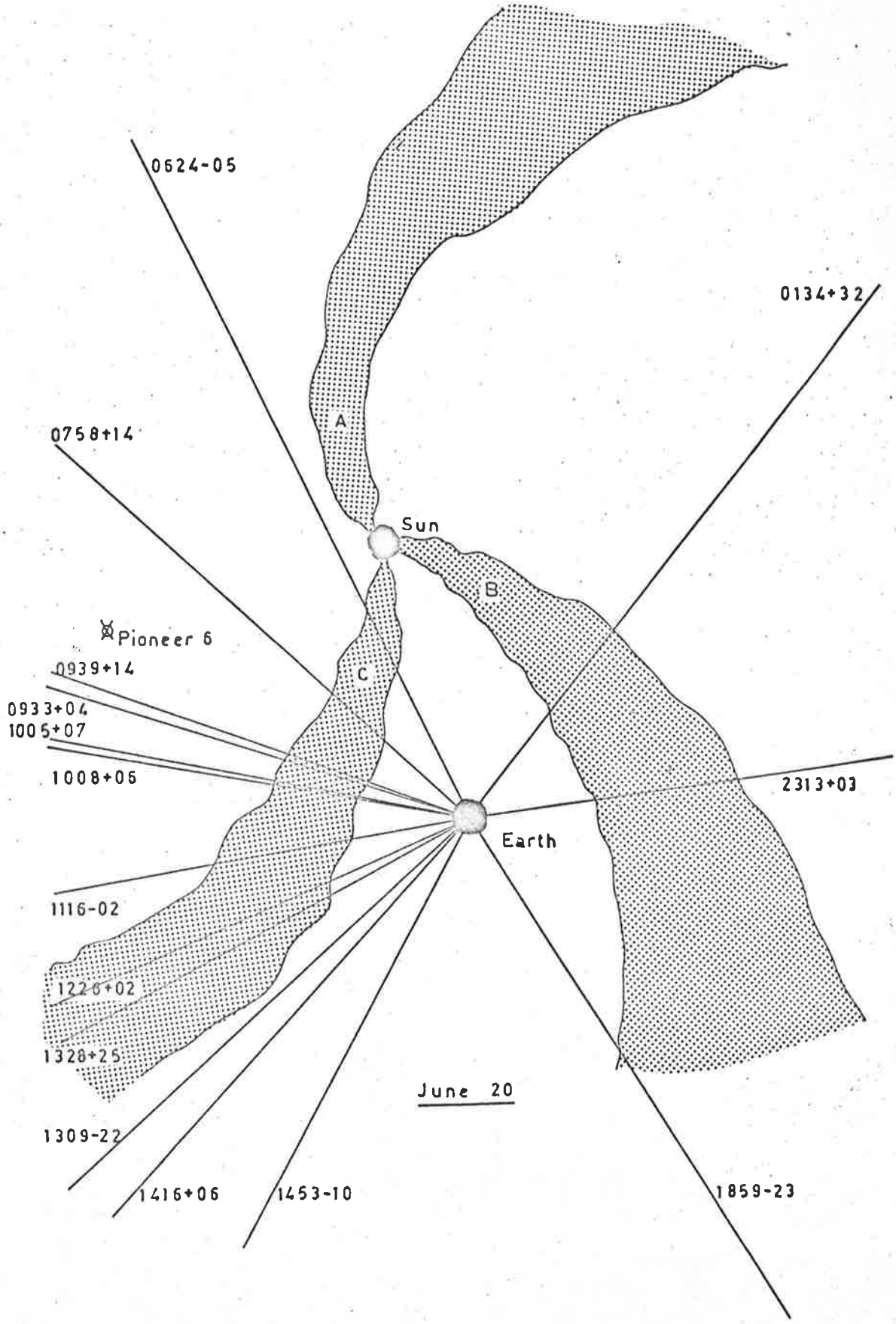

Figure 7.2(e) The estimated positions of the corotating streams during June 1970.

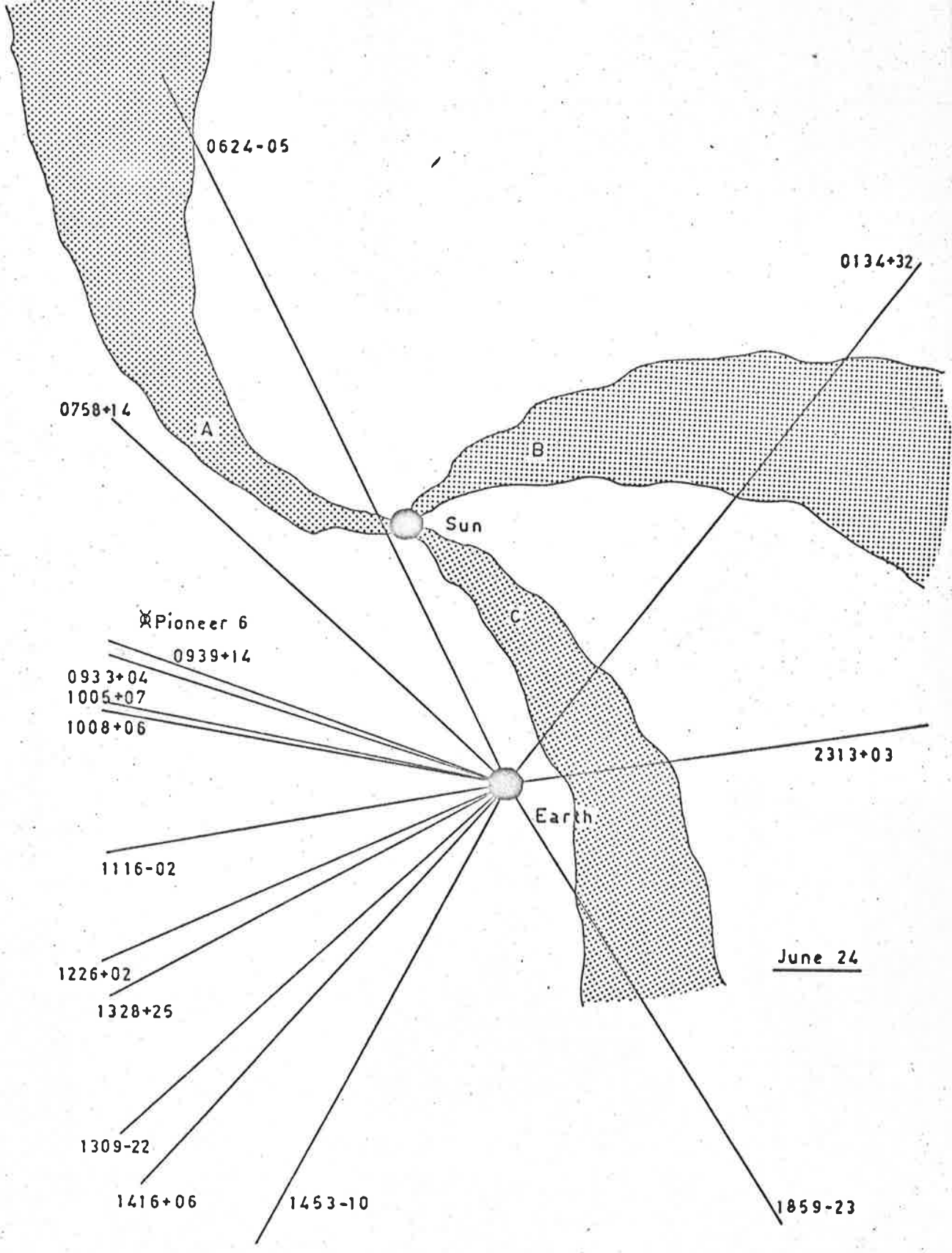

Figure 7.2(f) The estimated positions of the corotating streams during June 1970.

June 5 and 1005+07 on June 6. The arrival of the stream at the earth was determined, as in previous analyses, from the scintillation enhancement on sources with elongations in the range 90° to 180° east of the sun, since the lines of sight to these sources have their points of closest approach to the sun near the earth. Sources 1226+02, 1309-22, 1328+25 and 1416+06 all showed marked increases in scintillation on June 8, thus defining the leading edge of the stream at the earth. 0134+32 also showed enhanced scintillation on June 8, when the stream first intercepted the line of sight to the source, even though this was not at the closest approach to the sun.

As in previous analyses, the sequence of enhancements on these sources allowed some limits to be placed on the curvature of the stream in the ecliptic, and hence on the radial velocity of the solar wind associated with the stream (see in particular Chapter 4, P.59). Since the stream affected 0134+32 and also 1226+02, 1309-22 and 1328+25 on the same day, the curvature of the leading edge of the stream is well defined. The scintillation on sources 1859-23 and 2313+03 showed enhancements one day later, as the thickness of the scattering region for these sources increased with the movement of the stream. From the sequence of these events a velocity in the range 300 - 400 km/sec was estimated for this stream.

In order to identify possible source regions for stream A on the surface of the sun, a graph of the flare productivity of active regions

against their date of central meridian passage was plotted (similar to that described in Chapter 6). This is shown in Figure 7.3, where the shaded portions represent class 2 flares and the unshaded portions represent class 1 flares. Subflares are not shown on this graph, and no class 3 flares were observed during the period shown.

From the arrival of stream A at the earth on June 8, and the measured solar wind velocity on that day (350 km/sec from Vela 5B), the CMP date of the source region for this stream was estimated to be on $\sim$ June 3. Reference to Figure 7.3 shows that there was no activity above the level of subflares on that particular day, and the days on either side were equally inactive. However, on the following rotation a moderately active region did appear in this position (CMP June 30), only to fade again on the following rotation.

The shape of the scintillation enhancements on sources (1226+02, 1309-22, 1328+25, 1416+06) whose lines of sight were approximately parallel to the boundary of stream A allowed some useful limits to be placed on the width of the stream, and also on its extent perpendicular to the ecliptic plane. These sources indicated a stream width of $\sim$ 1 day which is equivalent to $\sim$ 0.25 A.U. at the orbit of the earth. The stream appeared to have affected both 1309-22 (14°S of the ecliptic plane) and 1328+25 (32°N of the ecliptic plane) in much the same way, indicating that the stream was of considerable extent perpendicular to the ecliptic plane.

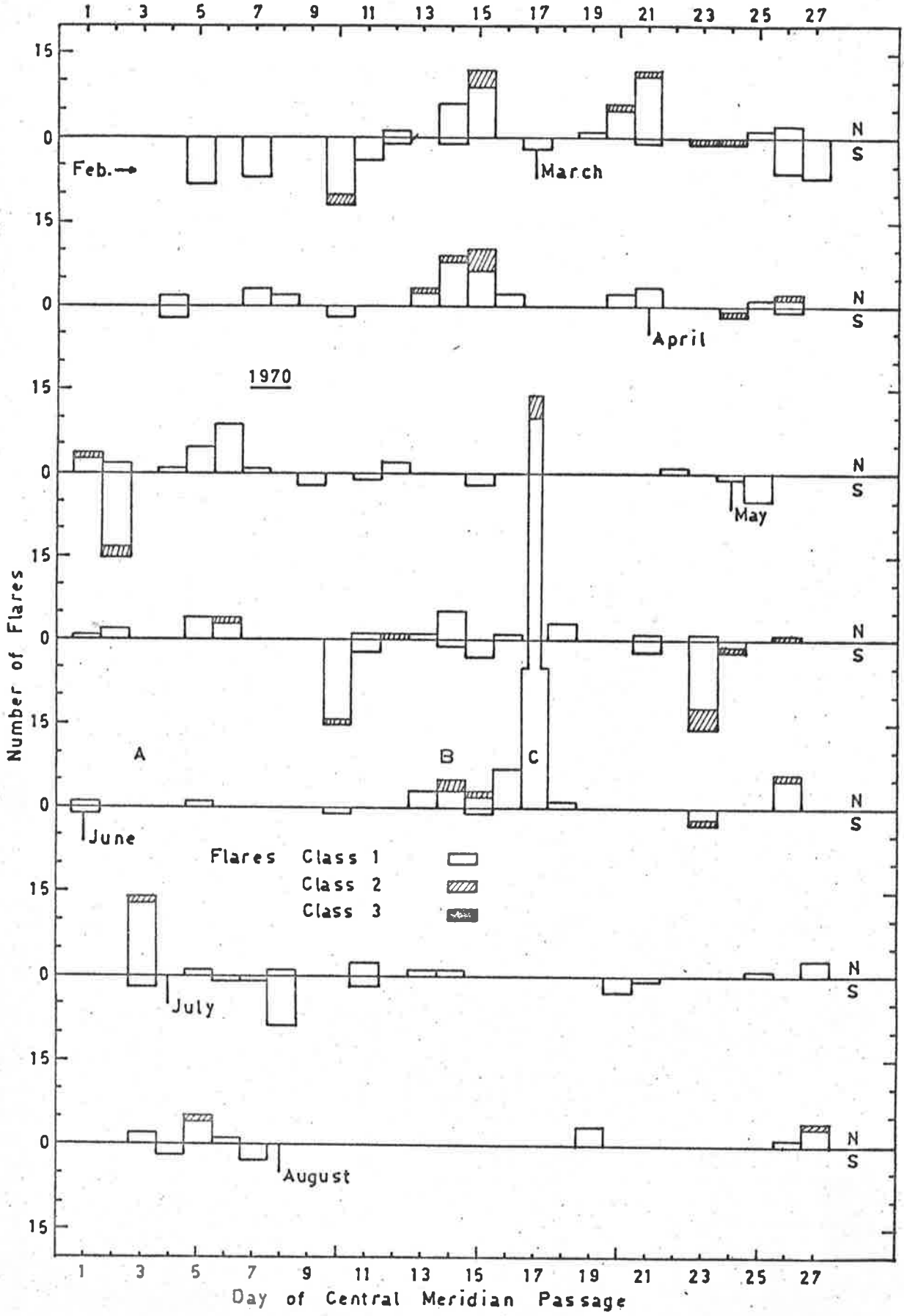

Figure 7.3 Solar flare activity from February to August, 1970.

The second feature of interest in Figure 7.1, which also appeared to move sequentially across the sources lying to the east of the sun, was stream B which intercepted the earth on June 17. Sources 1226+02, 1309-22, 1328+25 and 1416+06 all showed significant increases in scintillation index on that day. The region first appeared strongly in the enhancement of source 0624-05 on June 10-11, and then swept across the lines of sight to 0933+04 on June 13-14, 0939+14 on June 13, 1005+07 on June 13-14 and 1226+02 on June 16-17, and was associated with two sudden commencement geomagnetic storms on arrival at the earth on June 17 and 18. The enhancement on source 0134+32 on June 21, was identified with stream B from the changes in the widths of the power spectra for this source from day to day (see Section 7.2). This late arrival of the stream at 0134+32 compared with the arrival at sources 1309-22, 1328+25 and 1416+06 on June 17 (which is in contrast with the sequence of events observed for stream A), again allowed some limits to be placed on the velocity of the solar wind associated with the stream. The estimated velocity of the stream was in the range 400 - 550 km/sec (which is higher than that observed for stream A), and was confirmed by measurements aboard Vela 5B where a velocity of 450 km/sec was observed.

From the time of arrival of the stream at the earth and the measured solar wind velocity, the source region for stream B on the surface of the sun would have had CMP date on June 13-14. Figure 7.3 shows that an active region, producing several class 2 flares, was associated with this source-region on June 14, CMP. The region was

extremely weak on the two previous solar rotations, but appeared as a stronger well-defined region during February and March. As in the case of stream A, the stream had a duration of approximately 0.25 A.U. and appeared to have a considerable extent perpendicular to the ecliptic plane.

Stream C, the third feature of interest in Figure 7.1, appeared to be associated with the dominant solar activity occurring during June. The active region ("C" in Figure 7.3) was at central meridian passage on June 17 and is the most striking event on the figure. A plot of the date of maximum phase of flares occurring in source region C (with CMP between June 16 and 18) is shown in Figure 7.4. The region exhibited a peak of activity on June 14, when four class 2 flares and numerous class 1 and subflares were observed at N20° E43°. There was no evidence of the region having existed prior to June (Figure 7.3), and the activity faded and lost its identity in the rotation following June.

From Figure 7.1 the corotation of the stream can be seen in the movement of the enhancement 'C' across sources lying to the east of the sun; 0624-05 on June 17, 0933+04 and 0939+14 on June 18, 1005+07 on June 19-20, and then on sources with elongations greater than 90° east of the sun, 1226+02, 1309-22, 1328+25 and 1416+06 on June 22-24. The stream had a duration of $\sim$ 2 days (i.e. 0.5 A.U.) at the orbit of the earth, and was also observed at widely differing ecliptic latitudes. Its arrival at the earth was not associated with any significant

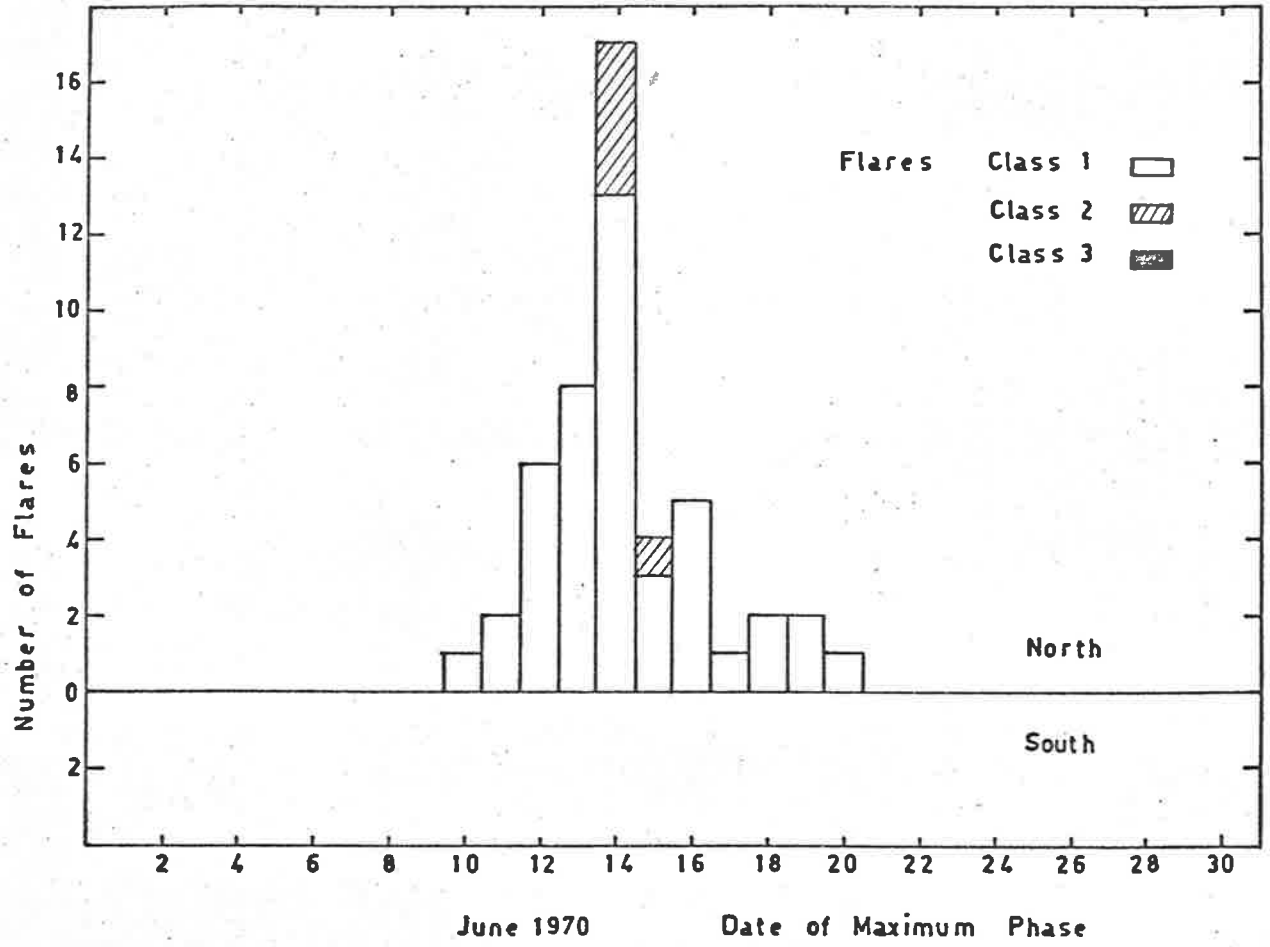

Figure 7.4 Date of maximum phase of flares occurring in region C during June 1970.

geomagnetic activity, and reference to Figure 7.4 shows that the source region C had been fairly quiet over the preceding five days.

The deduced positions of the three streams A, B and C are sketched in Figure 7.2(a-f) over the period of observation. The positions of the lines of sight to the sources are the ecliptic projections of their true right-ascension and declination for June 1970, and the stream geometries shown are for an average solar wind velocity of 400 km/sec with a duration of 1 day.

7.2 Power Spectra

The power spectral analysis of scintillation records was fully described in Chapter 5, and the present results have been computed following this same method. The shapes of most of the experimental spectra obtained during this observing session were close to Gaussian, as was the case in the 1968 and 1969 data. Typical spectra have been presented in Chapter 4, and we shall proceed directly to a discussion of the special features of the present spectra.

The spectra for source 1226+02 exhibited low-frequency depressions on two occasions, June 8 and 17, and these spectra are presented in Figure 7.5 on a logarithmic scale. The spectra for June 8 and 17 were averages over 7 and 10 blocks of data respectively, and the rms deviations of the spectral estimates were 13% and 11%. It can be seen that the dips in the spectra were real effects and not due to statistical variability, though the first point shown on each spectrum

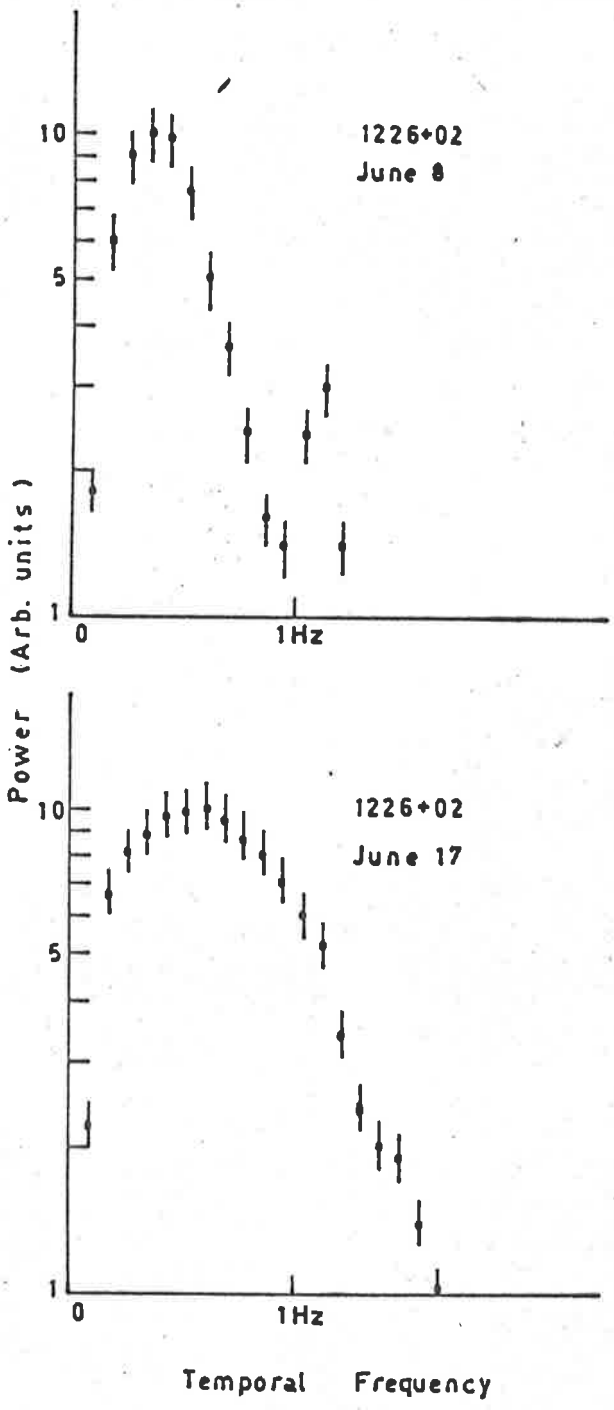

Figure 7.5 Experimental spectra for source 1226+02 observed on June 8 and 17, exhibited depressions at low frequency. Error bars are 13% and 11% respectively.

must not be given undue significance, since it is contaminated by the unreal zero power of the point at zero frequency.

The two dips observed in the spectra coincided with the arrival of streams A and B at the earth on June 8 and 17 respectively, and from the discussion in Chapter 4, we can imply the existence of a well defined thin scattering region lying close to the earth on those days. To examine the properties of this scattering region, an attempt was made to fit theoretical spectra to those observed, using the expression given in Chapter 4 for the observed spatial power spectrum of the scintillations,

$$W(X) = \int \exp\left(-\pi^2 r_o^2 \left(X^2 + \beta^2 Y^2\right)\right) \mathrm{Sin}^2\left(\pi \lambda z \left(X^2 + Y^2\right)\right) dY \ .$$

Before comparisons could be made, the theoretical spectra were smoothed using a Hanning spectral window, as for the experimental spectra, and the temporal frequency of the experimental spectra were converted to spatial frequency from a knowledge of the solar wind velocity. Figure 7.6 presents a plot of the solar wind proton velocity measured aboard the Vela 5B earth satellite and the heliocentric Pioneer 6 spacecraft. The data from Pioneer 6 have been corrected for the appropriate (7½ day) corotation time delay to give velocities at the position of the earth. Resolving the measured Vela 5B velocities in a direction perpendicular to the line of sight to 1226+02 yields 380 km/sec and 400 km/sec on June 8 and 17 respectively.

The theoretical spectra and experimental points are shown in

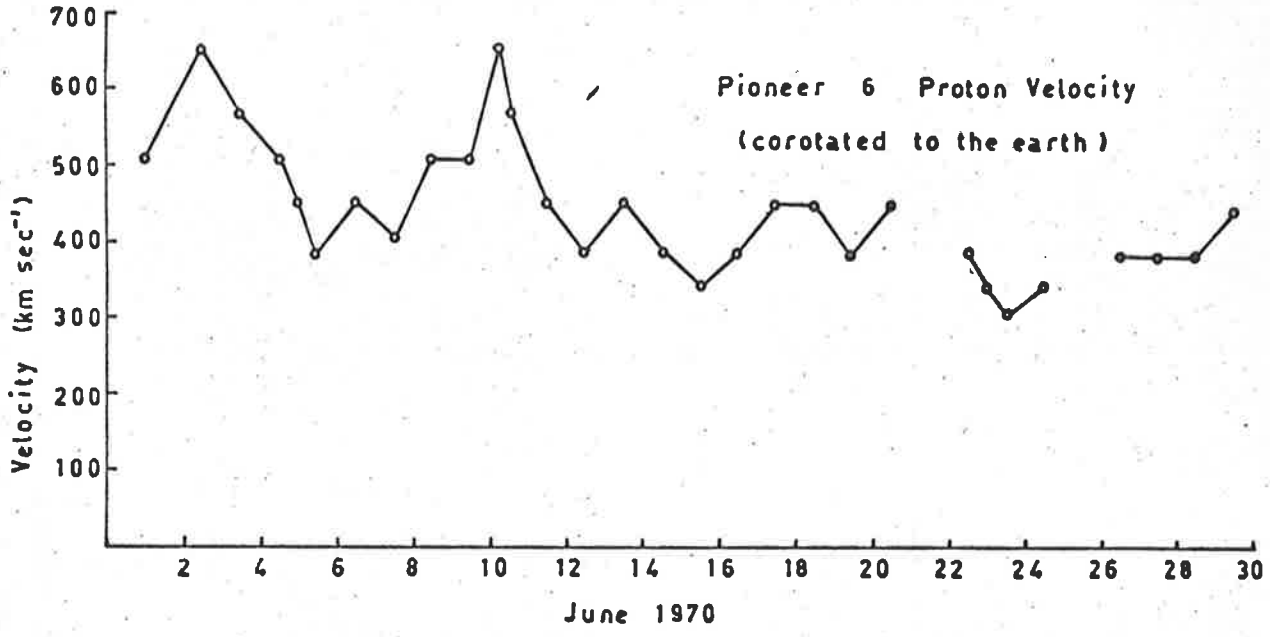

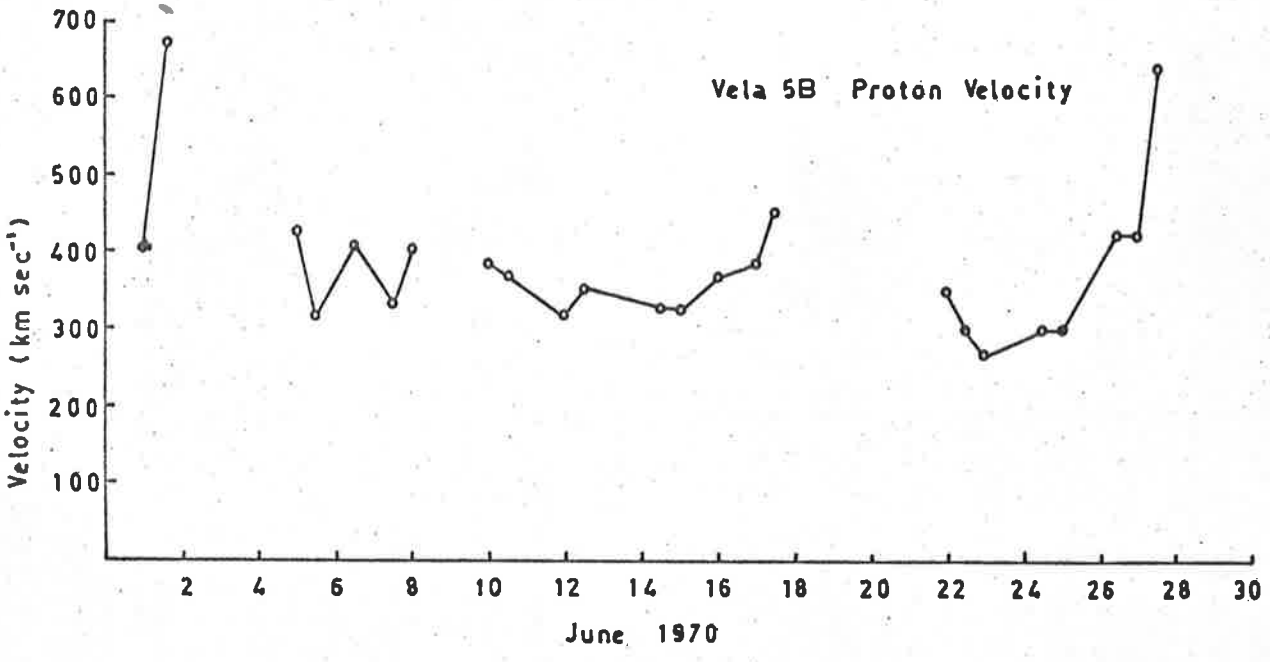

Figure 7.6 Solar wind proton velocity measured aboard the Vela 5B and Pioneer 6 spacecraft during June 1970. The data for Pioneer 6 are adjusted for the corotation delay from spacecraft to earth.

Figures 7.7 and 7.8, for the labelled values of r_o, the scale of the irregularities in the screen, and z, the screen-observer separation. (The peak at $\sim$ 1 Hz in the spectrum for June 8 is due to switching noise in the radioheliograph system which could not be suppressed). The scale of 330 km on June 8 is similar to the values obtained during 1969 from a similar analysis, but on June 17 a much lower scale, r_o = 220 km, was indicated. Unfortunately no interplanetary magnetic field data is yet available for 1970 at the time of writing, and it is not possible to ascertain whether this decrease in scale was associated with an increase in the field strength, and hence whether the scale was linked to the ion-gyro radius in the medium.

The relative widths of the normalised power spectra on successive days during June provided additional support for the proposed corotating stream model. Figure 7.9 presents a plot of the spectral widths for a number of sources which were not excessively contaminated with the 1 Hz switching peak mentioned earlier. No magnetic tape records were made after June 22, and so any possible enhancements associated with stream C were not recorded. Streams A and B, however, were both associated with increases in spectral width, and these are labelled in Figure 7.9 from the positions of the streams deduced from scintillation indices. The solar wind velocity measured aboard the Vela 5B satellite is also plotted on Figure 7.9 for comparison.

Both streams A and B were associated with spectral width increases

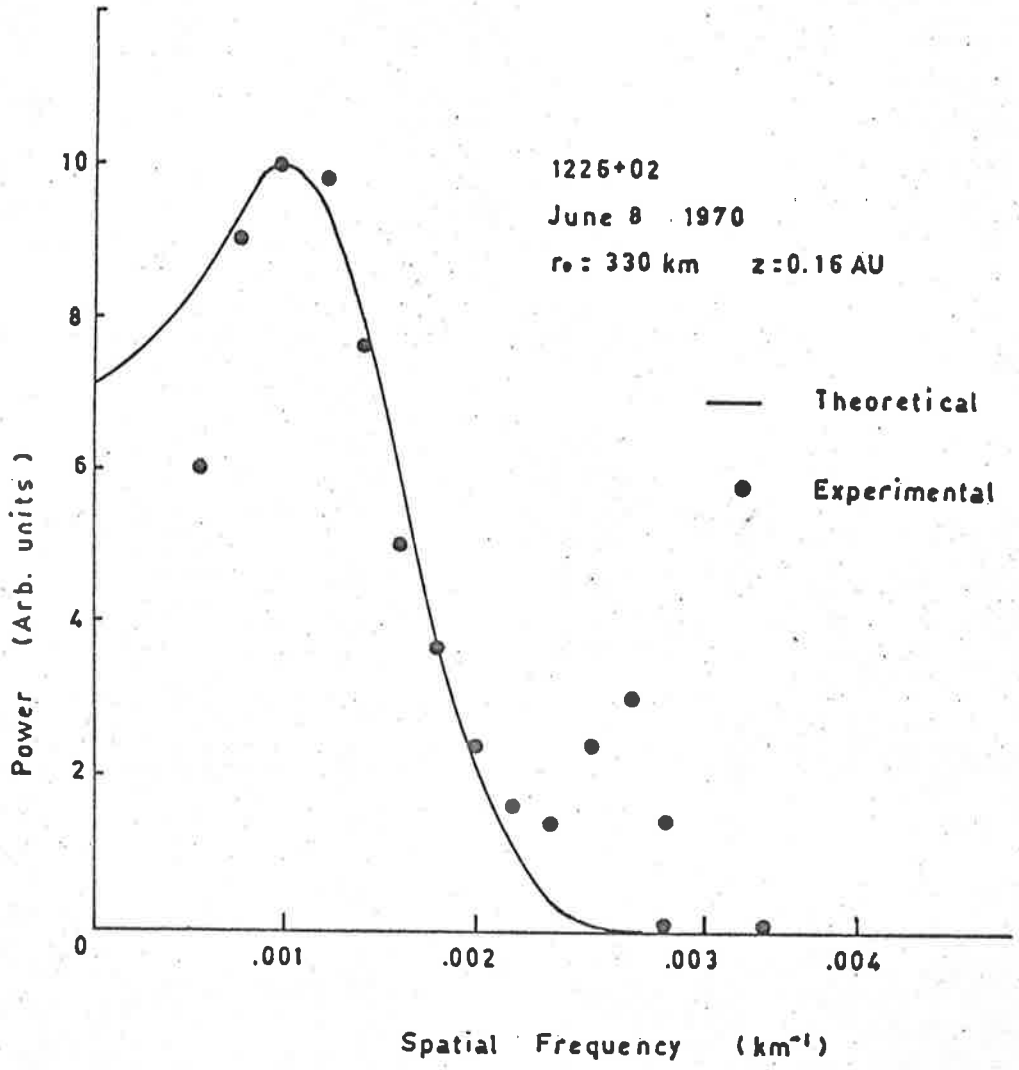

Figure 7.7 Theoretical (——) and experimental (●) spectra for source 1226+02 on June 8, 1970.

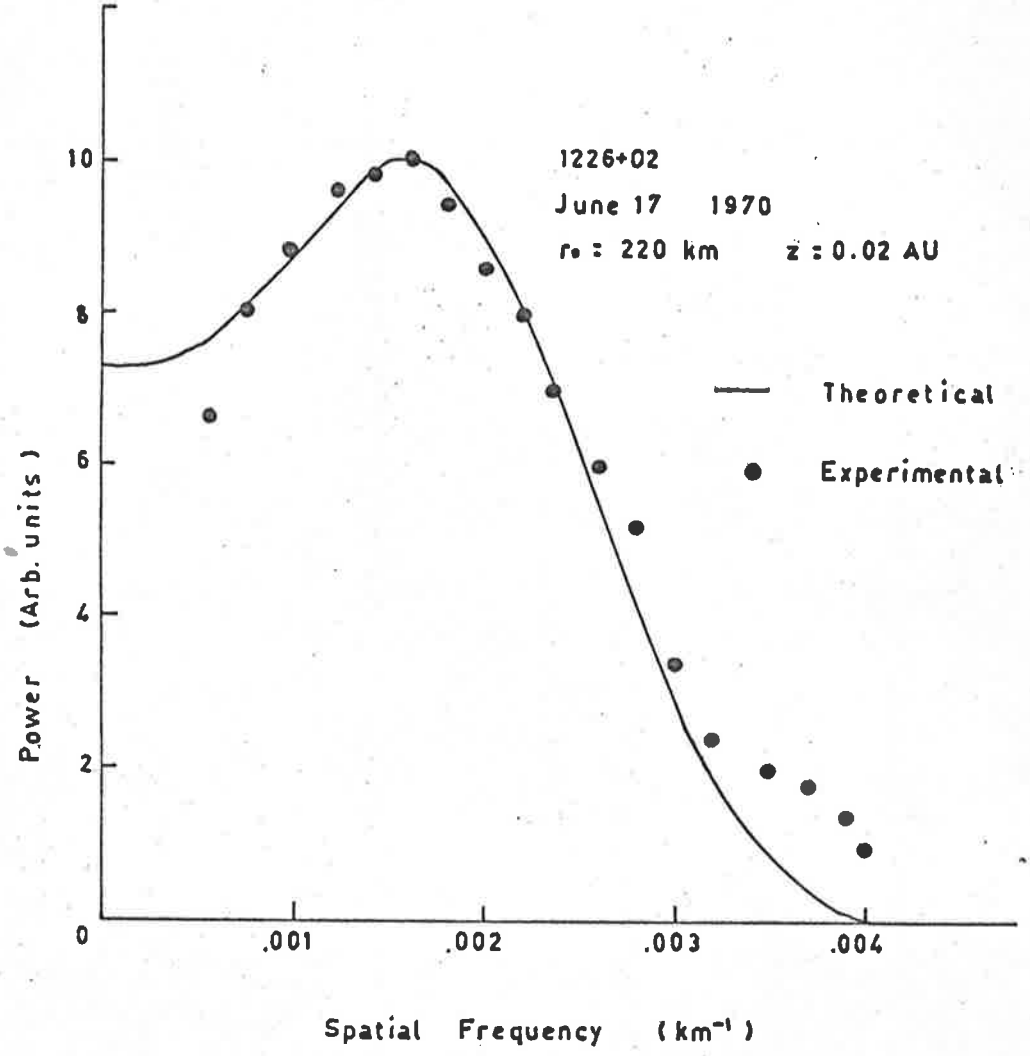

Figure 7.8 Theoretical (---) and experimental (●) spectra for source 1226+02 on June 17, 1970.

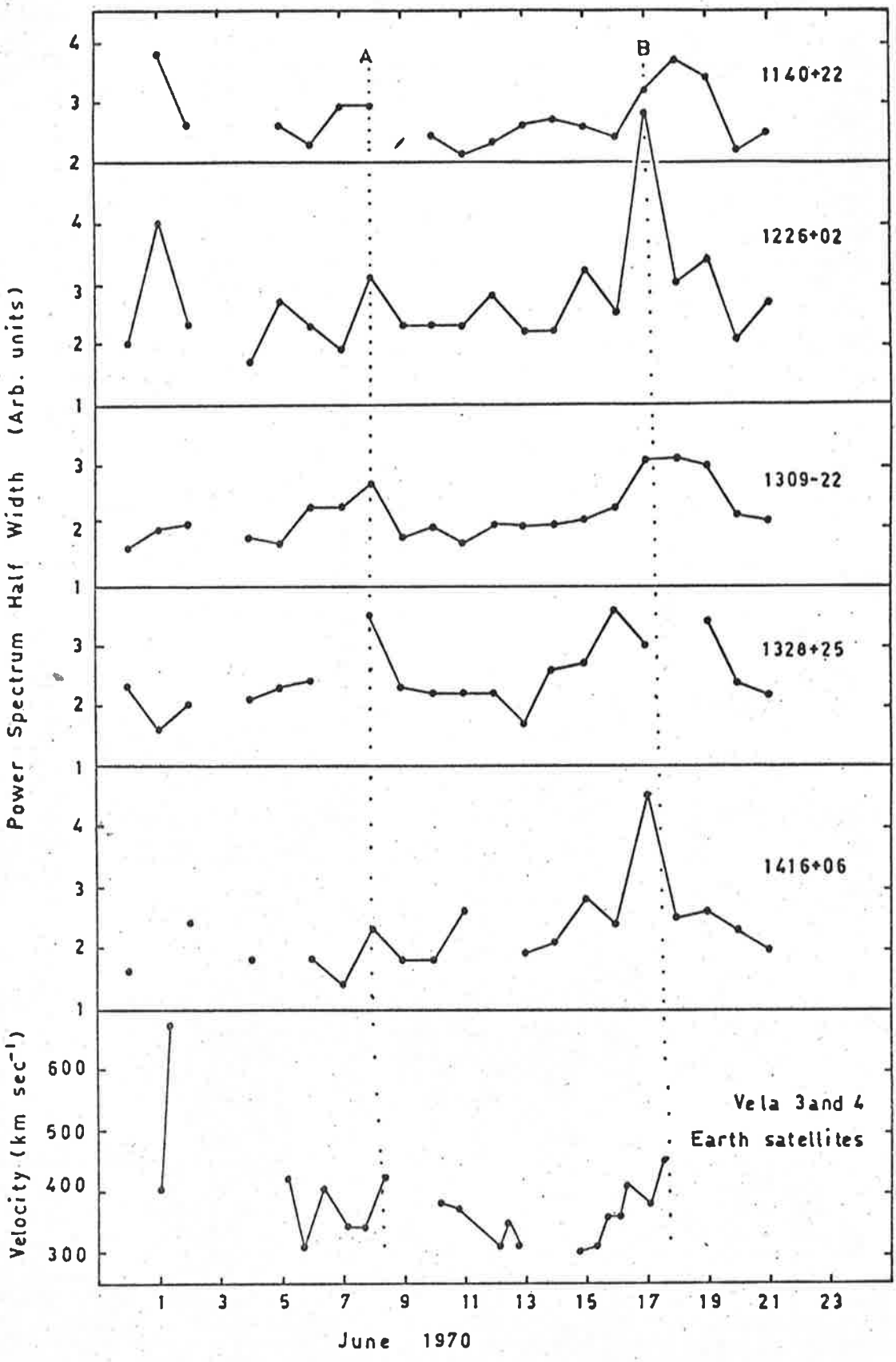

Figure 7.9 The half-widths of the scintillation power spectra for sources observed during June 1970.

by factors of about 1.5, and were also accompanied by velocity increases of approximately the same order. However, without information on the state of the interplanetary magnetic field during this period, we cannot determine the relative contributions of velocity and field strength to the increases in spectral width, assuming of course, that the scale is linked to the ion-gyro radius in the medium. The plot of spectral widths indicates that stream B had a complex configuration, extending over a number of days, with a main peak of duration $\sim$ 2 days. Stream A was not so well defined, but the increases in width which occurred were in agreement with the positions of the stream deduced from scintillation indices.

In 1968 and 1969 we have shown that the stream structures observed using IPS were closely identified with the sector boundaries of the interplanetary magnetic field. This close correlation suggests that the present stream structures will also indicate the position of sector boundaries in the field, but this point must await confirmation from published magnetic field data for 1970.

CHAPTER 8

THE ADELAIDE RADIO-ASTRONOMY ARRAY

Introduction

The scintillation studies described in the preceding chapters have been limited by the fact that observations were made at only a single receiving site. Two basic functions derived from such observations were the scintillation index and the scintillation power spectrum, which yield only limited information about the structure of the solar wind. Measurements of the speed, direction of flow, scale and anisotropy of the interplanetary plasma require observations to be made simultaneously from spaced receiving sites.

Previous work on the source 3C48 using a spaced receiver technique (Hewish et al., 1966; Dennison and Hewish, 1967; Hewish and Dennison, 1967) has established typical values for these parameters to within 0.35 A.U. of the sun, and indicated the existence of a flow anisotropy between polar and equatorial regions.

The solar wind models described in Chapter 1 have generally assumed spherical symmetry about the sun, and so experimental determination of the dependence of flow parameters on heliocentric distance and latitude is important for the development of further theoretical models.

Therefore, to extend the scope of previous work and to gain a better understanding of the nature of the scattering process in the

interplanetary medium, it was proposed to set up a dual-frequency spaced receiver project near Adelaide.

Although the role played by the author was mainly constructional, the project provided practical experience in the design and construction of a radio-astronomy array and associated receivers, and is therefore described here.

8.1 Specification and Design

The analysis of a drifting radio diffraction pattern using spaced receiver observations has been fully developed by Briggs et al. (1950), Phillips and Spencer (1955) and Briggs (1968). From measurements of the time displacement and correlation between scintillations recorded at three spaced receivers, information on the velocity and scale of the electron density irregularities in the solar wind can be obtained. The correlation between observations at two sites decreases with increasing separation of the receivers, and at the same time the observed time-delay becomes greater and hence more easily measured. Since the auto-correlation function (ACF) of the scintillations is approximately Gaussian, accurate values for the scale can be derived providing both too high and too low values of cross-correlation are avoided (Golley and Rossiter, 1970). Thus an important parameter in the establishment of such a receiver network is the spacing between the sites.

Previous work using spaced receivers (Dennison and Hewish, 1967 and Hewish and Dennison, 1967) established typical values for the scale,

ℓ, (100 - 200 km to the e^{-1} point of the ACF) and for the velocity, V, (300 - 500 km/sec) of irregularities in the solar wind. The expected correlations and time-delays for these ranges of ℓ and V are plotted in Figure 8.1 for various site separations. The optimum distance appears to be $\sim$ 100 km, corresponding to time-delays $\sim$ 0.2 - 0.3 sec and a correlation $\sim$ 0.5.

The base-station was established at Buckland Park, 26 miles north-west of Adelaide, on the site of a large aerial array already in use for research into ionospheric physics (Briggs et al., 1969). The two outstations were constructed at Burra in the north of South Australia, and at Kadina on Yorke Peninsula, being 110 km and 95 km respectively from Buckland Park. Figure 8.2 shows the location of the three sites on a map of South Australia.

8.2 Observing Frequencies

The choice of a suitable observing frequency for interplanetary scintillation is determined by the nature of the scattering process. This depends fundamentally on ϕ_o, the rms phase deviation across a wavefront traversing the interplanetary medium. For ϕ_o less than 1 radian the observed properties of the diffraction pattern can be related simply and directly to those of the solar wind. When ϕ_o is greater than 1 radian, the effect of multiple scattering becomes important, and the relation between the diffraction pattern and solar wind parameters involves a direct knowledge of ϕ_o. It is therefore desirable to work in

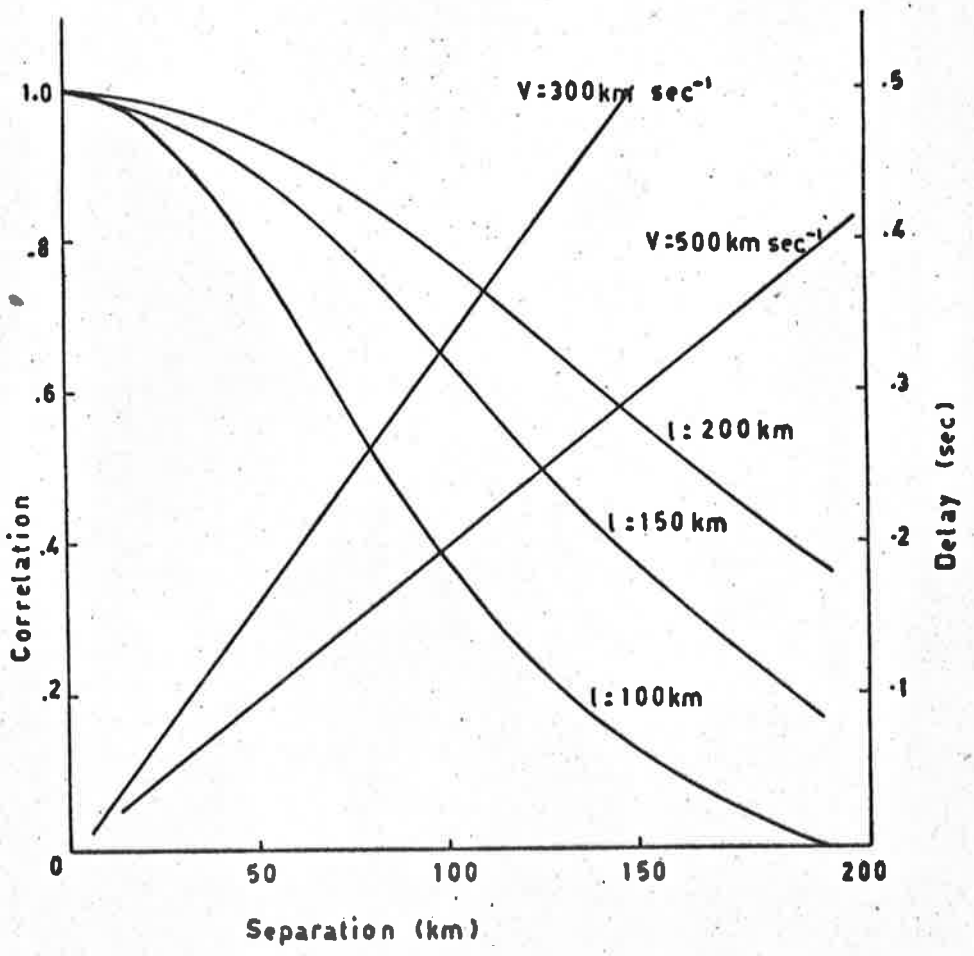

Figure 8.1 The optimum site separation for spaced receiver scintillation studies.

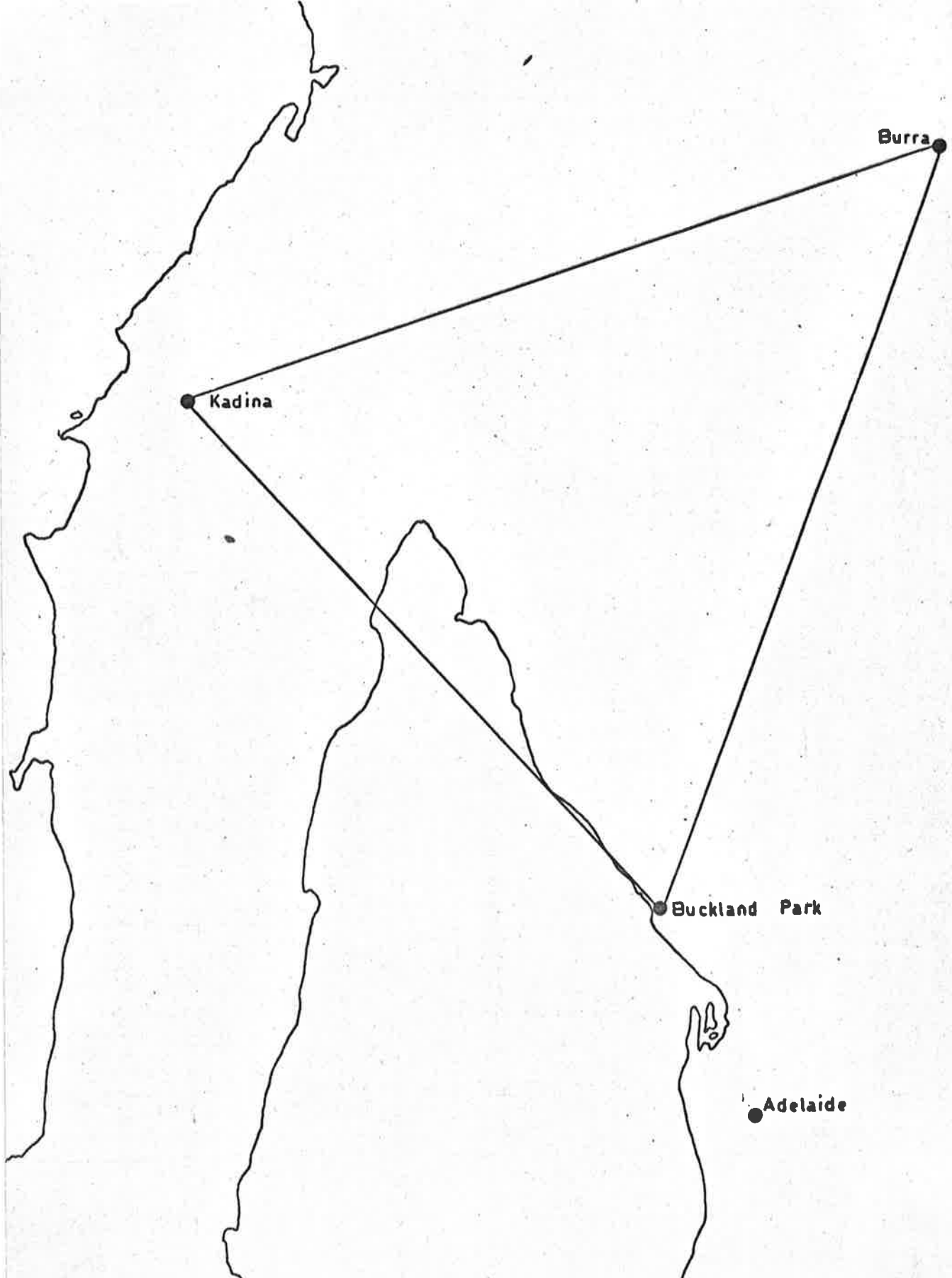

Figure 8.2 The location of the spaced receivers of the Adelaide radioastronomy array.

the weak scattering regime ($\phi_o < 1$) over as large a range of radial distance as possible.

Both ϕ_o and the scintillation index, F, vary inversely with the frequency of observation and decrease with radial distance from the sun. Thus there are two conflicting requirements; high frequencies are preferred so that the plasma close to the sun can be studied while still in the weak scattering regime, but too high a frequency would restrict observations to only those regions close to the sun because of the reduction in scintillation index with increasing radial distance.

At 80 MHz (λ = 3.75 metre) the transition from weak to strong scattering occurs at a radial distance of 0.3 A.U. (Hewish et al., 1966; Hewish and Symonds, 1969), and to investigate the properties of the solar wind in the range 0.1 - 1.0 A.U. it appears that observations at metre wavelengths would be ideal.

In the light of these considerations it was decided to provide for the system to operate simultaneously at two frequencies in the range 100 - 300 MHz, thus increasing the flexibility of the project and allowing for observations over a wider range of radial distance. An important advantage of two-frequency operation is the ability to determine directly the value of ϕ_o, the rms phase deviation, from a comparison of the scales of the diffraction patterns at the two frequencies. In the strong scattering regime the scale, a, of the pattern is identical to the scale, ℓ, of the electron density

irregularities in the scattering layer, while in the weak scattering regime, $\ell \sim a/\sqrt{2}\ \phi_o$. Thus when the scattering is weak at the higher frequency and strong at the lower frequency, ϕ_o can be estimated directly. The nature of the scattering can be further examined from the degree of correlation of scintillations and also from the ratio of the scintillation indices at the two frequencies (Dennison, 1967).

To guard against interference from commercial communication bands, the final choice of frequencies was made after consultation with the Commonwealth Postmaster-General's Department. The two frequencies finally allocated were 111.5 MHz and 235.9 MHz with bandwidths of 1 MHz and 2 MHz respectively.

8.3 Sensitivity and Noise Temperature

The sensitivity of a radio astronomy receiver is defined in terms of the minimum detectable change, $(\Delta T)_{min}$, in the input noise power, expressed as a temperature. It is usual to define the sensitivity, $(\Delta T)_{min}$, as some multiple of the rms noise fluctuations, typically $5\ (\Delta T)_{rms}$ (Christiansen and Högbom, 1969),

$$(\Delta T)_{min} = \frac{5M\ T_{sys}}{(\Delta\nu\ .\ \Delta t)^{\frac{1}{2}}} \qquad (8.1)$$

where $\Delta\nu$ is the predetection bandwidth, Δt the post-detection integration time and T_{sys} is the system noise due to the joint contributions of receiver noise and galactic sky background. The constant, M, has the value 2 for a phase-switched interferometer, and $\Delta t = 2\ t_{RC}$ for a

receiver using an RC filter in the post-detection stage, where t_{RC} is the RC time constant.

At 111.5 MHz the sky background temperature is typically (Kraus, 1966) 600 ^{o}K in the direction of the galactic pole and $\sim$ 6000 ^{o}K toward the galactic centre. Corresponding values at 236 MHz are 100 ^{o}K to 1000 ^{o}K respectively. The major scintillating sources lie well away from the galactic centre and so we assume a sky background temperature of 600 ^{o}K at 111.5 MHz. We shall use a figure of 300 ^{o}K as a reasonable receiver noise temperature, giving a total system noise temperature of $\sim$ 900 ^{o}K.

We now wish to calculate the antenna collecting area required to record at least two or three of the strongest scintillating sources. Based on observations at Culgoora at 80 MHz, Table III lists the strongest scintillating sources available, and it is seen that a number of these have fluxes at 111.5 MHz, $S_{111.5} > 50$ f.u. (1 f.u. = 10^{-26} watt m^{-2} Hz^{-1}).

The antenna temperature produced by a source of flux, S, is given by,

$$T_A = \frac{S \cdot A}{2k} , \qquad (8.2)$$

where k is Boltzmann's constant and A is the effective collecting area of the antenna. The factor of 2 arises from the fact that only one plane of polarization is recorded. Thus from Equations 8.1 and 8.2, the

TABLE III

Source	Flux at 111.5 MHz
0624-05	100
0758+14	25
1226+02	80
1309-22	45
1416+06	65
1938-15	25
2313+03	30

required collecting area to detect a source of flux S with a signal to noise of 5:1, is given by,

$$A = \frac{5 \cdot M \cdot k \cdot T_{sys} \cdot 2}{(\Delta\nu \cdot \Delta t)^{\frac{1}{2}} \cdot S} . \qquad (8.3)$$

At 111.5 MHz, for $\Delta\nu$ = 1 MHz, t_{RC} = 0.1 sec and T_{sys} = 900 ^{o}K, the required collecting area to detect a 50 f.u. source with a signal to noise ratio of 5:1 is A ≃ 1100 m^2. Assuming an average spectral index of - 0.75 for a non-thermal source (Kraus, 1966), the same source would have a flux density of 29 f.u. at 236 MHz. Thus the collecting area at 236 MHz, for $\Delta\nu$ = 2 MHz, t_{RC} = 0.1 sec, T_{sys} = 400 ^{o}K, and a signal to noise ratio of 5:1, is A ≃ 600 m^2.

8.4 Antenna Design

To achieve a reasonable collecting area within the limits of available finance, a necessary choice was a transit instrument. East-west corner reflectors were chosen in preference to flat-screen dipole arrays in order to obtain an improved declination response. Within each corner we proposed to construct two colinear dipole arrays to operate simultaneously at the two observing frequencies.

The design parameters for these corner reflectors were calculated from the empirical studies of Cottony and Wilson (1958) and Wilson and Cottony (1960) to obtain minimum side lobe response in declination, together with maximum gain. The configuration which was finally adopted is illustrated in Figure 8.3.

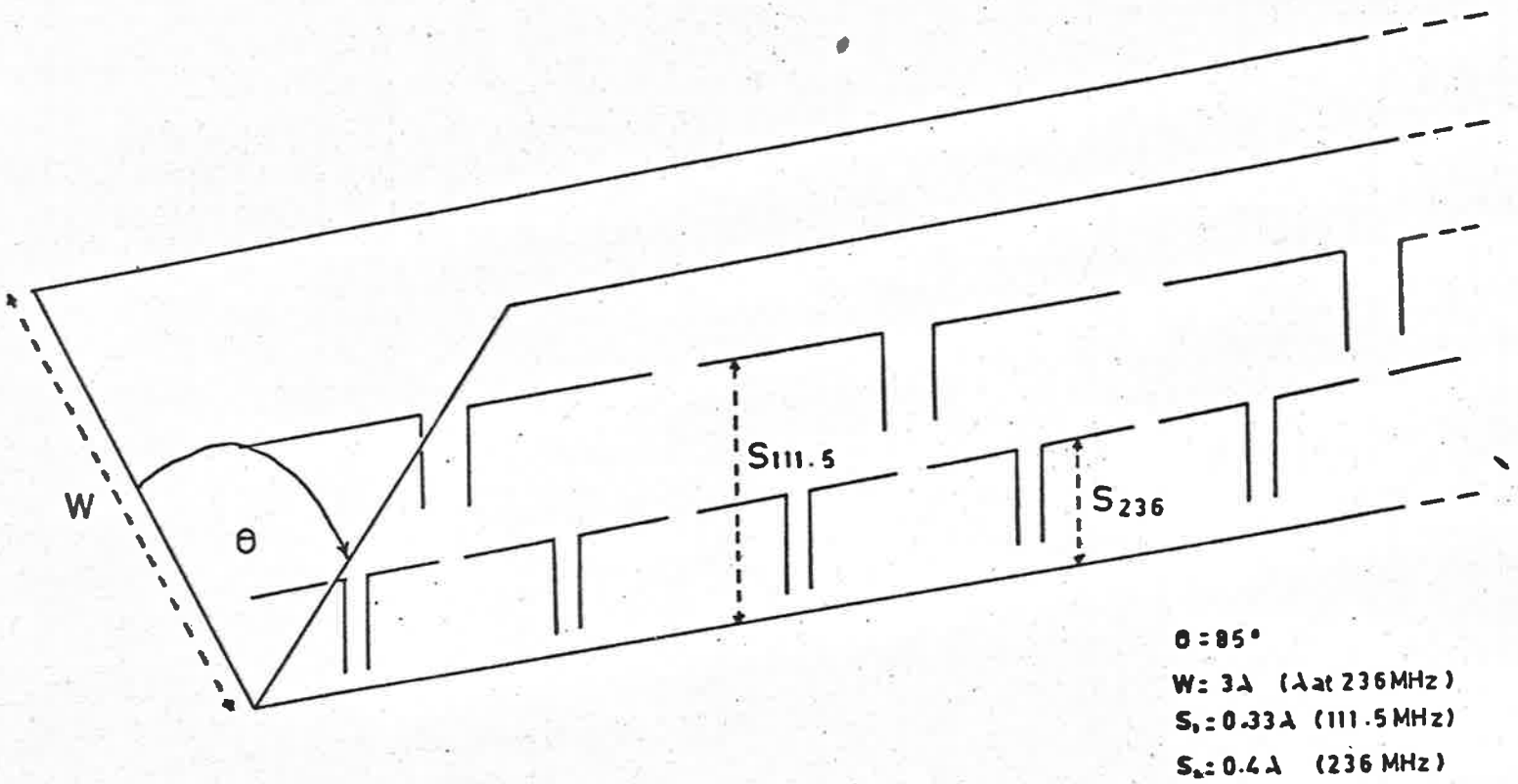

Figure 8.3 Specification of the corner reflector and dipole array.

Each corner reflector was chosen to be 250 metres in length to give a physical collecting area of $\sim$ 1300 m^2. Since construction began in 1969, four corner reflectors have been erected at Buckland Park, and a further four at the outstations, two at Burra and two at Kadina. A photograph of the array at Buckland Park is included on the following page.

Each corner reflector is separated from its neighbour by 3λ at 111.5 MHz. The reflector screen wires were separated by $\lambda/20$ at the highest observing frequency (236 MHz), to obtain efficient reflection properties with a front-to-back ratio > 20 dB (Wilson and Cottony, 1960).

Because of their high impedance, full-wave dipoles were used within the corner reflectors, allowing groups of 10 dipoles to be fed in parallel through an open-wire 300Ω copper line. Each group of ten was isolated from neighbouring groups using $\lambda/4$ shorts on the 300Ω line.

To ensure that each group of dipoles had an equal electrical path-length to the receiver, a 'christmas tree' feed arrangement was adopted (Figure 8.4). The impedance at the feed point for each group of dipoles was measured using a General Radio bridge and then transformed to match the 300Ω feeder using a shorted stub. A typical value for the impedance of a group before transformation was $(70 + j\ 70)\Omega$, the large reactive component being due to the interaction of the two different frequency dipole arrays within each corner. The stub matching limited the bandwidth of the arrays, but direct measurements showed a standing

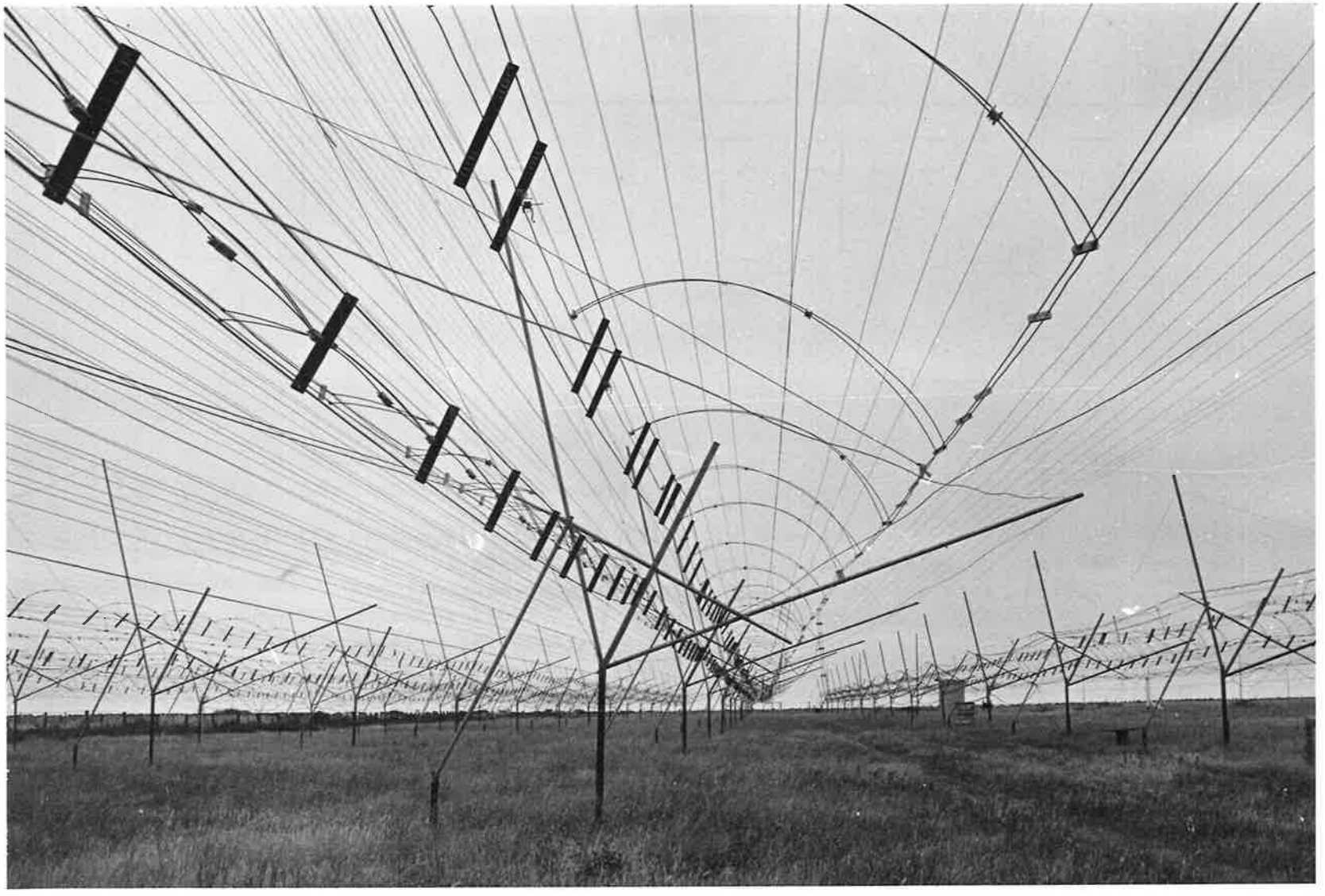

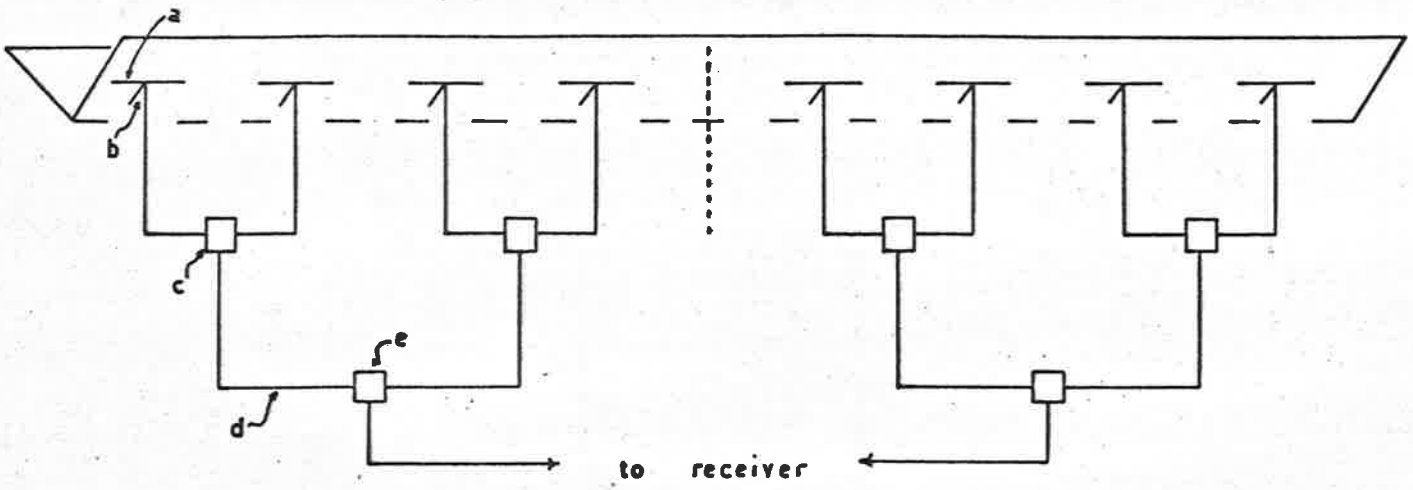

Figure 8.4 The feed system for the 111.5 MHz dipoles.
a – Group of 10 or 12 dipoles coupled in parallel to open 300 ohm feed and isolated from adjacent group by quarter wave shorts.
b – Matching stub.
c – Quarter wave matching transformer.
d – 300 ohm open line feeder.
e – Balance–unbalance transformer.

wave ratio of less than 2 over a 1% bandwidth about each of the observing frequencies, and this was considered satisfactory.

The signals from each half of the aerial were returned to the receiver along 50 ohm coaxial cable via balance-unbalance transformers, and then the two halves were phase-switched against each other to remove the noise contribution from the galaxy (Ryle, 1952). The aerial polar diagram in the east-west direction is illustrated by a typical source transit record in Figure 8.5.

Each corner reflector had a beam-width of 40° FWHP (full-width, half-power) in declination, which was centred on 0° declination by tilting each corner to an angle 35° north of zenith (Buckland Park latitude $\sim 35^{\circ}$ south), since most of the sources used for studies of IPS lie within declinations of $\pm 20^{\circ}$. An improved declination response was obtained by connecting the four corners together in phase, yielding responses spaced 20° in declination (at 111.5 MHz) and of width 5° FWHP. The beam positioning in declination was made even more flexible by combining the four aerials in different phase relationships, to produce a selection of beams spaced over the 40° envelope of each corner reflector. The phasing arrangement finally adopted was based on the use of hybrid-rings (Smith, 1961), and is shown in Figure 8.6(a). This arrangement produces four beam positions (Figure 8.6(b)) which can be recorded simultaneously. The same principle was followed in the design of phasing devices for 236 MHz operation.

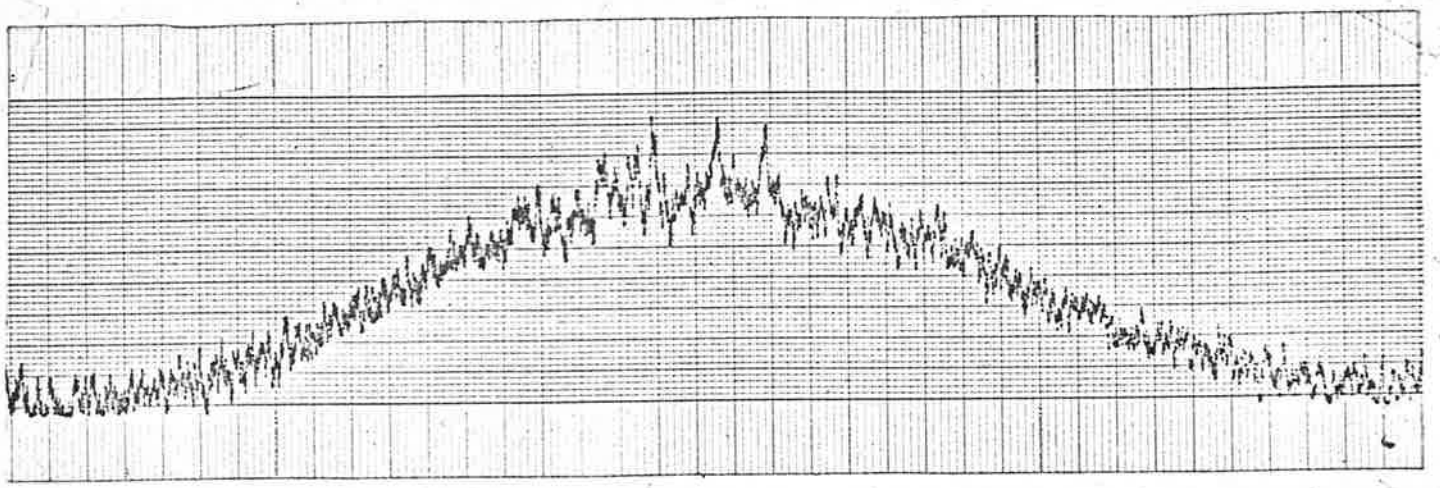

(a)

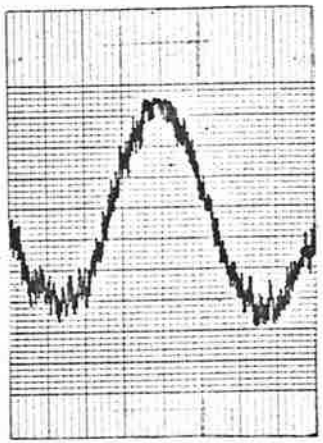

111.5 MHz

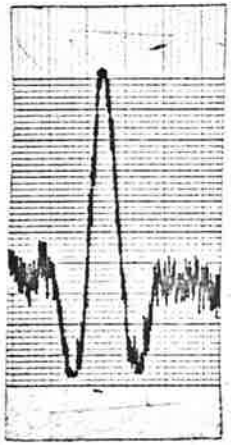

235.9 MHz

(b)

Figure 8.5 (a) Record of scintillation on 0624-05 at 111.5 MHz
(b) Source transits showing the shape of the polar diagrams

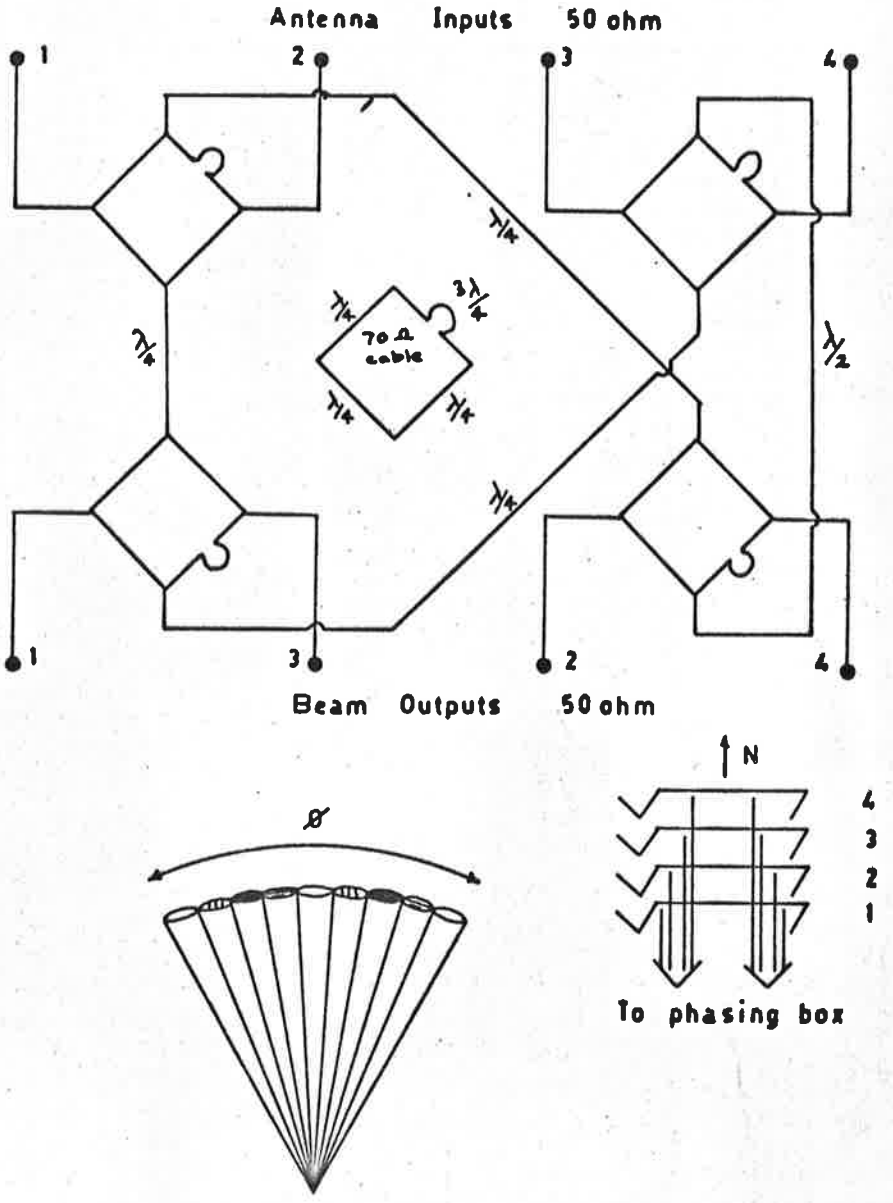

Figure 8.6 The beam configuration in declination at 111.5 Mhz from the phasing device shown.

Because of the difference in the longitude of the three observing stations, a particular radio source would transit at different times at each location. To obtain simultaneous recordings, the corner reflectors at the two outstations were offset from the horizontal by an appropriate amount, so that the three stations observed identical right ascensions.

8.5 Receiver Design

As mentioned earlier, each corner reflector was operated in the interferometer mode by phase-switching the east and west halves against each other. In this way the galactic background noise was removed, and only radiation from localised sources produced changes in the receiver output level. The principle of the phase-switched receiver is well known and is illustrated schematically in Figure 8.7.

The input from the two halves of the aerial (A and B) are combined in the input hybrid to produce independent in-phase (A + B) and out-of-phase (A - B) signals which are alternately switched to the mixer input at a frequency of $\sim$ 400 Hz. The switching is performed by diode switches driven by a square-wave generator. Any coherent source in the aerial beam will produce a square-wave component at the output of the square-law detector, and the demodulator then synchronously reverses the phase of the output square-wave to produce a d-c level which is directly proportional to the input signal strength from the source, and independent of the sky background temperature.

In the original development of the various units in the receiver,

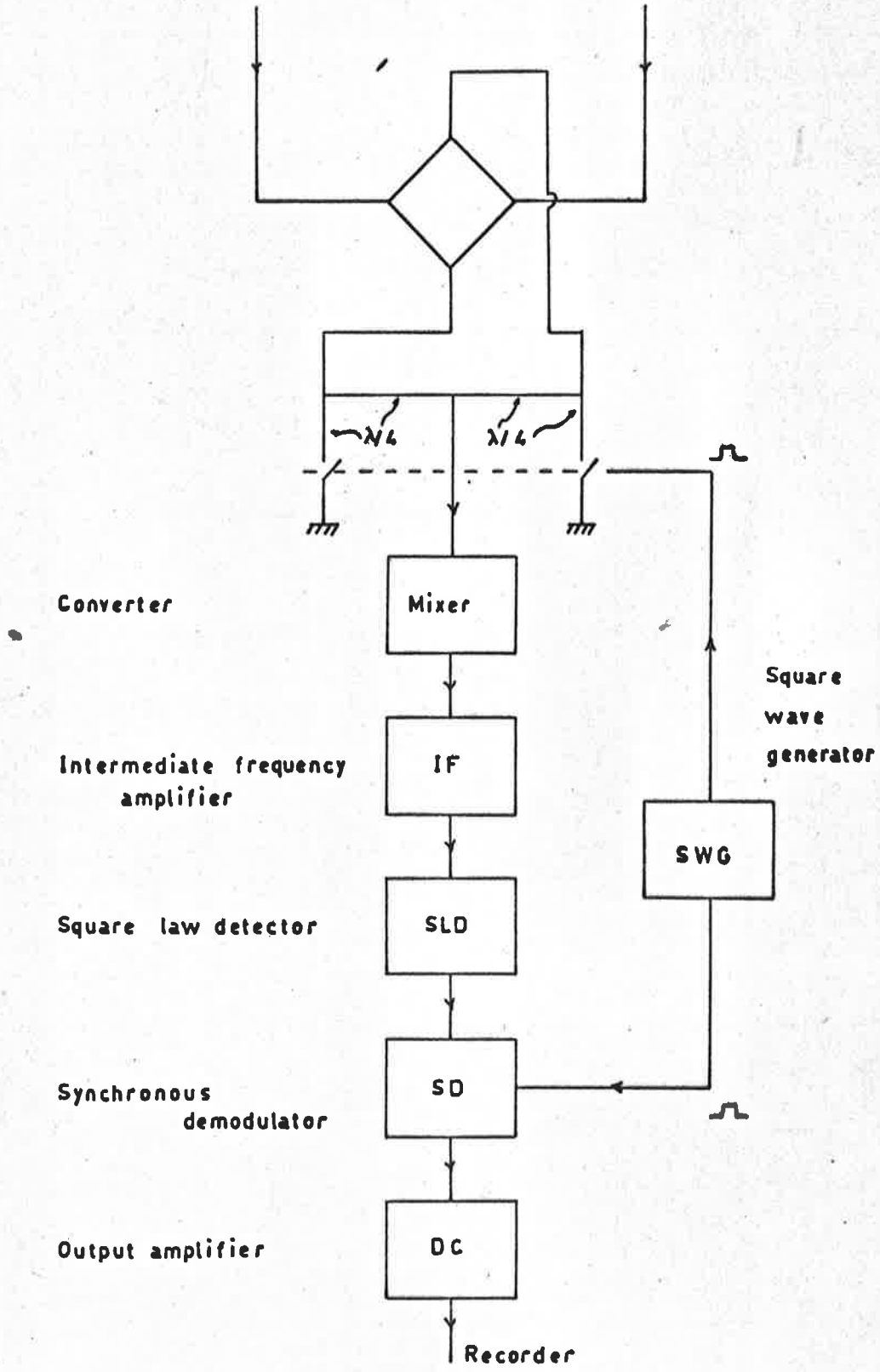

Figure 8.7 A block representation of a Phase Switched Receiver.

considerable assistance was received from the Department of Electrical Engineering at Sydney University. In particular the synchronous demodulator, which forms the heart of the receiver, follows closely a design of the Sydney Group (Frater, 1965). A particularly attractive feature of this demodulator is the provision for synchronous integration before demodulation, which produces a dynamic range which is largely independent of the noise level at the input. The circuit diagrams for the receiver are presented in Appendix B, and only a brief description of each unit will be given here.

The operation of the phase-switch was based on a principle which has been successfully applied up to frequencies in the gigahertz region (Landecker and Wielebinsky, 1970). Diode switches were used to alternately open and short one end of a quarter-wave length of coaxial cable, the other end of which was connected to the signal path (Figure 8.7). The original design incorporated gold-bonded germanium diodes (OA47), which gave a rejection ratio of $\sim$ 30 dB for non-correlated input signals. As a future development it is likely that P.I.N. diodes will be used to achieve a higher rejection ratio, especially at the higher observing frequency. A feature of the hybrid-ring is the high isolation between inputs from the two halves of the antenna.

The converter consisted of a moderately low noise pre-amplifier (noise temperature $\sim$ 1000 ^{o}K at 111.5 MHz), a crystal controlled local oscillator, and the mixer itself. The whole unit was assembled within a

single brass box, with special attention being given to shielding and rf bypassing of d-c supply lines. At 111.5 MHz the local oscillator frequency of 81.5 MHz was injected directly to produce the 30 MHz intermediate frequency (IF). For the 235.9 MHz receiver, the local oscillator frequency (68.63 MHz) was tripled to produce the required 205.9 MHz injection signal.

Following the converter, three stages of IF amplification were provided, in which the overall width and shape of the pass-band for the pre-detection stages of the receiver were determined. Each of the 3 stagger-tuned cascode pairs had adjustable damping so that an overall square response at 30 MHz with the required 3 dB bandwidth could be obtained.

The detector which followed the IF amplifier had a square-law characteristic so that the magnitude of the output square-wave voltage was directly proportional to the output noise power of the pre-detection section of the receiver. The signal was then demodulated synchronously with the phase-switch to produce a d-c output level.

Synchronous control of the phase-switch and demodulator was obtained from the square-wave generator, which was a simple multivibrator with an output frequency of 385 Hz, chosen to be well away from any harmonics of the 50 Hz mains supply. Following the synchronous demodulator, a single stage of amplification was provided to raise the d-c output level to $\sim$ 2 volts required to drive the pen-recorder.

To overcome losses in the cables, and to achieve the required low-noise characteristics, pre-amplifiers were placed at the feed points of each half of each aerial. They consisted of a simple cascode pair arrangement using GM290A germanium transistors, yielding noise figures of less than 500 ^{o}K at 111.5 MHz, and less than 700 ^{o}K at 235.9 MHz. These figures are higher than those specified in the original design, and work is currently under way to reduce the figures to $\sim$ 300 ^{o}K by using more recently developed transistors. The overall gain of the present preamplifiers is $\sim$ 10 dB (after allowing for cable losses), which is sufficient to make them the limiting factor in determining the overall receiver noise.

No provision was made for automatic gain control in the receiver design which was finally adopted. However, the dynamic range of the receiver was $\sim$ 30 dB, which was deemed sufficient for the present observations. In addition a variable attenuator was included at the input to the IF amplifier, providing from 3 to 33 dB attenuation in switched 3 dB steps.

Photographs of the complete receiver, IF amplifier and converter are included on the following pages.

8.6 Progress and Future Development

At the time of writing, the low frequency system at Buckland Park is operational and preliminary observations are being carried out. The high frequency system has been completed and final tests are being made

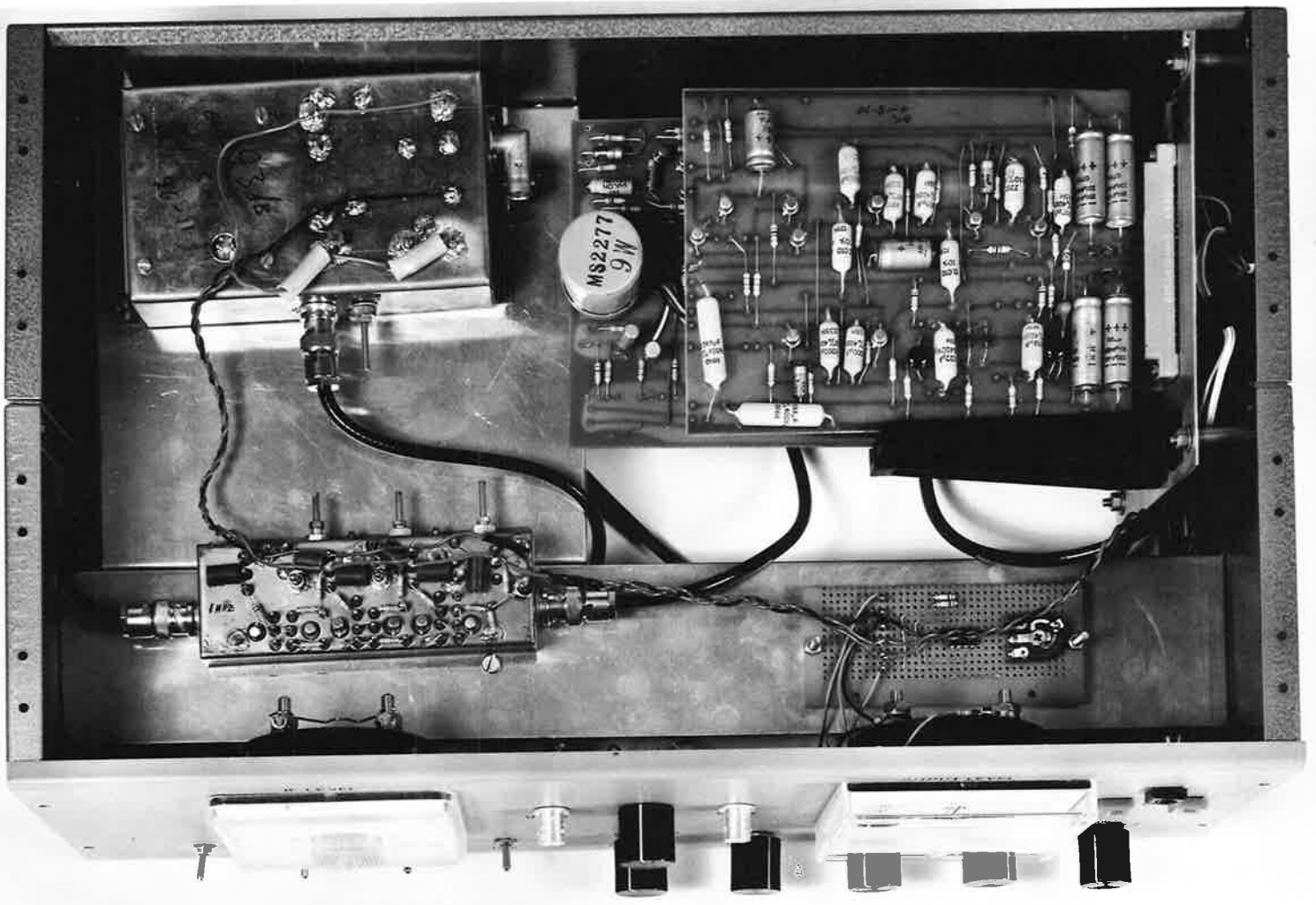

111·5 MHz RECEIVER

CONVERTER

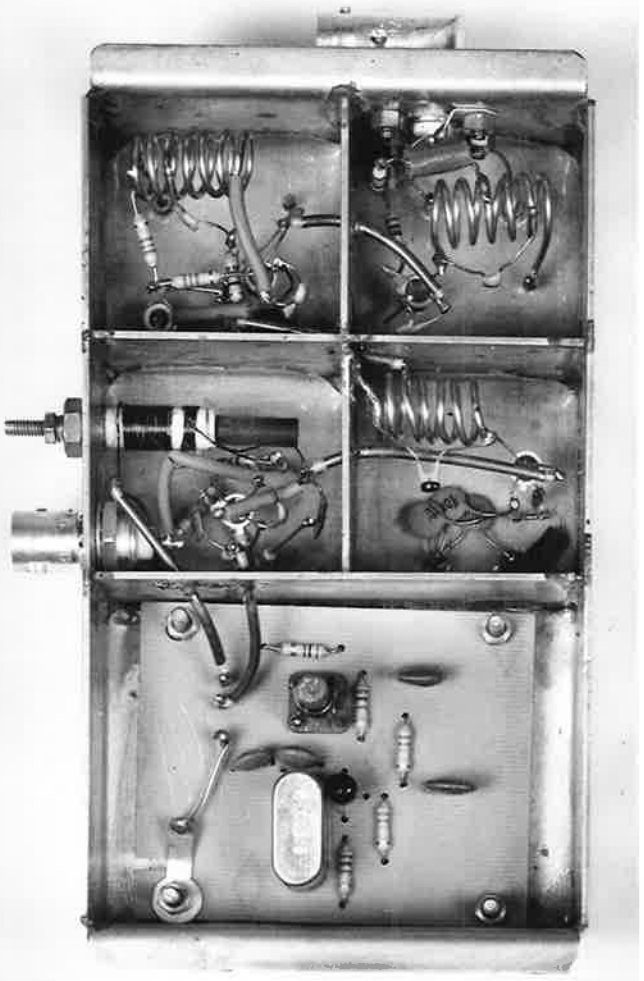

I.F. AMPLIFER

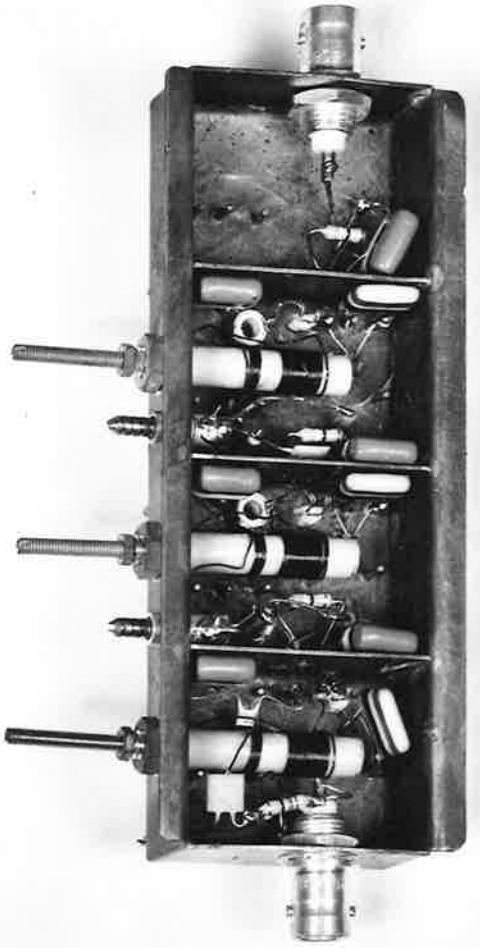

before the system is brought into operation. Constructional work at the outstations is complete, and only the feed systems remain to be installed.

The signals received at each outstation will be coded and then transmitted back to the base-station at Buckland Park using frequency-modulated (FM) radio links. To accomplish this, the author has designed a pulse-width modulation unit which time-multiplexes four channels of data. The present four channel unit is based on a design originally published by Fenelon and McDonald (1968). The variable width pulse train is used to frequency modulate the carrier of a standard communications FM radio link. A similar unit at the base station decodes the four data channels which can then be displayed simultaneously on a multiple-channel pen-recorder. A frequency multiplexing (proportional bandwidth) system is currently being designed and built by another member of the research group, and these two systems will be used in comparative tests before a final design is adopted.

The aerial arrays at the three stations will initially be used to study the properties of the solar wind by sampling the intensity of the radio source diffraction pattern at the earth, but it is intended to eventually develop the system to the stage where pairs of stations will be operated as long-baseline interferometers to obtain phase information about the diffraction pattern.

The fringe pattern generated by phase-switching between two

receivers separated by a distance, D, and operating at wavelength, λ, is given (Ryle, 1952) by,

$$A(\theta) \text{ Cos } (2 \pi D \theta/\lambda) ,$$

for small values of θ, the zenith angle of the radio source, where $A(\theta)$ is the aerial polar diagram, and the cosine modulation is due to the earth's rotation. At a frequency of 200 MHz and with a separation, D, of 100 km, the fringe frequency specified by the cosine function is $\sim$ 4.6 Hz; i.e. a fringe period of $\sim$ 0.2 sec. If the phase component of the diffraction pattern has roughly the same scale as the intensity pattern, then the fringe period will be significantly less than the typical time-scale of the phase diffraction pattern. Hence, the variation of the position of the observed fringes relative to the true (i.e. calculated) fringe positions should give a direct measure of the phase difference between the two receivers, caused by the changing diffraction pattern.

Only limited work on the observation of phase scintillations has been carried out in the past. Little et al., (1962) have applied this method to the investigation of ionospheric irregularities in the auroral zone, and Slee and Higgins (1968) have made estimates of the rms phase deviation of the IPS of Jupiter's radio emission. Further work in this field will provide a much fuller understanding of the nature of the basic scattering process in the interplanetary medium, both in the weak and strong scattering regimes.

CHAPTER 9

CONCLUSIONS

In Chapter 1 we have presented a review of the state of our present knowledge of the properties of the solar wind. We summarized the chemical composition, thermal properties, density and velocity distributions in the interplanetary medium, and considered their relation to the properties of the interplanetary magnetic field. A number of solar wind models were discussed to illustrate the development of current attempts to explain the observed solar wind properties on a theoretical basis.

The experimental work described in this thesis was based on a systematic study of the variations in the interplanetary scintillation of a grid of discrete radio sources, and Chapter 2 contains a brief summary of the relevant theoretical background. Following this, in Chapter 3, is a fairly detailed discussion of the properties of interplanetary blast waves and corotating plasma streams in the solar wind, which form the central topic of the thesis.

The experimental observations were carried out at Culgoora, N.S.W., using the C.S.I.R.O. 80 MHz radioheliograph during May 1968, June 1969 and June 1970. The observing procedure and preliminary scintillation index and spectral analyses have been described in Chapter 4, together with a discussion of the results obtained during May 1968. These latter

results were shown to be consistent with the existence of a stream of corotating plasma in the solar wind, with a width of $\sim$ 0.5 A.U. at the earth, and a stream velocity in the range 300 - 500 km/sec.

A consideration of the frequency power spectra of the scintillations was shown to provide additional information on the geometry and internal structure of the proposed stream. By comparison of the experimental spectra with those computed on a theoretical basis, the existence of an enhanced, relatively thin, single-velocity scattering region was inferred to be within 0.2 A.U. from the earth on May 28. The scale of the irregularities in electron density within the scattering region was also deduced from particular power spectra on May 28, and a value of 500 km was obtained. This scale is considerably larger than that measured from independent scintillation observations. However, the scale size normally deduced from a correlation analysis of IPS is considerably smaller than the real scale (which is measured in the present analysis), due to the Fresnel diffraction effect. When this effect was taken into account, the scale of 500 km was reduced to a 'correlation length' scale of 290 km. This value is in better agreement with the scale measured by other workers, though still significantly larger.

The changes in the width of the scintillation power spectra from day to day on a particular source have been shown to provide a valuable confirmation of the scintillation index analysis. When considered in

the light of the observed changes in the velocity of the solar wind and the strength of the magnetic field, strong evidence was found relating the scale of the electron density irregularities to the ion-gyro radius in the interplanetary medium.

It was observed that the stream structure deduced from the scintillation indices just preceded a sector boundary of the interplanetary magnetic field, and the position of the stream was observed to agree with the increase in the distribution of electron density which has been observed within such sectors by spacecraft. These preliminary results in May 1968 indicated the close correspondence between features of the interplanetary plasma and features of the interplanetary magnetic field, and showed the potential of systematic IPS surveys in investigating the nature of these features.

In Chapter 5 we presented a discussion of the methods of power spectrum analysis of IPS which have evolved with the advent of the Fast Fourier Transform algorithm of Cooley and Tukey (1965). The particular ease with which filtering of experimental data can be carried out using this approach was pointed out, and various techniques for producing more reliable power spectra by reducing the variance of the spectral estimates were discussed.

The preliminary observations of 1968 discussed in Chapter 4 were considerably extended by the more detailed studies during June 1969 and 1970, when observations were made over complete solar rotation intervals.

The results from these extended observations (Chapters 6 and 7) confirmed the existence of streams of disturbed plasma which corotated with the sun and maintained their identity over a full solar rotation. Supporting evidence from patterns of flare activity on the sun, indicated that two of the streams observed in 1969 had existed in the medium for as many as four solar rotations prior to June.

The scintillation analysis for 1969 and 1970 allowed useful limits to be placed on the width and spiral geometry of the streams in the ecliptic plane, and hence on the velocity of the solar wind within the streams. Our analysis showed that the streams extended over a wide range of heliocentric latitude at the orbit of the earth, and the possibility of mapping the stream structures in a direction perpendicular to the ecliptic plane was discussed in relation to the streams observed.

An event of particular importance was observed in June 1969, which demonstrated the power and flexibility of IPS as a method for probing the conditions occurring within the solar wind. On this occasion there is strong evidence that a blast of plasma was initiated by violent flare activity in a particular region on the sun. The blast wave was mapped (using IPS) as it propagated out through the interplanetary medium, and the extremely good coverage of this event allowed accurate limits to be placed on the duration and geometry of the blast in the ecliptic plane. The blast itself was shown to be significantly decelerated in transit,

and a combination of scintillation and published spacecraft observations enabled the full geometry of the blast to be mapped fairly accurately.

The power spectra of the scintillation activity associated with the blast and corotating streams in 1969 and 1970 provided valuable confirmation of our scintillation index analysis. By computing theoretical spectra for a best fit to those experimental spectra which exhibited depressions at low-frequencies, the average scale of the electron density irregularities in the scattering medium was deduced to be $\sim$ 350 km/sec, and the scattering screen was shown to lie close to the earth. This value of the scale, when adjusted for the Fresnel effect at small distances from the earth, yielded a correlation length (to the e^{-1} point of the spatial autocorrelation function) of $\sim$ 200 km, which is in good agreement with other independent measurements of the scale size at 1 A.U. The inferred position of the scattering region close to the earth on those days when dips appeared in the experimental spectra, agreed with the positions of the streams deduced from scintillation indices, and hence confirmed the consistency of our analysis.

As in the analysis of the 1968 results, the changes in the widths of the normalised power spectra for 1969 and 1970 also provided a valuable confirmation of the scintillation index analysis, since increases in spectral width were observed to show significant correlation with the increases in scintillation index. The passage of the blast wave through the interplanetary medium was accompanied by increases in

the spectral widths for a number of sources and by an increase in the velocity of the solar wind by approximately the same factor. The changes in spectral width were thus directly attributed to the increase in velocity. However, a very strong increase in the strength of the interplanetary magnetic field associated with the blast was not accompanied by a similar change in the power spectra, as might have been expected if the scale of irregularities in the medium was linked to the ion-gyro radius. This observed behaviour was explained in terms of the localised compression of the magnetic field along the leading edge of the blast wave, which would lead to high field conditions of only a limited extent, and thus the contribution to changes in spectral width would be negligible.

The stream structures observed in 1969 were shown to be directly associated with the occurrence of sector boundaries in the interplanetary magnetic field, and this strong association (together with that observed in 1968) leads us to predict that the stream structures observed in 1970 will also be found to coincide with sector boundaries, when the magnetic field data becomes available. The blast wave in 1969 was also directly associated with a reversal of the dominant magnetic field polarity for a period of one day, which agreed excellently with our estimate of the width of the blast from the scintillation analysis. The observed stream positions in 1969 corresponded closely to the distribution of electron density within the magnetic field sectors as measured by spacecraft, which implies that

the general increases in electron density were accompanied by increases in the electron density fluctuations responsible for IPS.

The blast wave and most of the streams observed during 1969 and 1970 appeared to be linked to the presence of active regions on the sun. This agrees with the general observation mentioned in Chapter 3, that solar active regions have preferred locations which tend to just follow magnetic field sector boundaries. In particular, the only class 3 flares occurring during the periods of observation were associated directly with a plasma blast wave moving out from the sun on a very broad front, and then followed by a continuing flux of plasma which formed an enhanced stream associated with a magnetic field sector boundary.

An interesting feature of the present study is the apparent interaction of features in the solar wind and the occurrence of sudden-commencement geomagnetic storms. Both the plasma blast wave and two of the streams observed using IPS were directly connected with the onset of such activity. The nature of this interaction could possibly be investigated by a comparative study using IPS and some dynamic measure of the geomagnetic perturbations of the earth's field. In the near future it is intended to co-operate in such an investigation using the present scintillation results and the sonagrams of the micropulsations in the earth's magnetic field which have been recorded by a research group at the University of Queensland. It is hoped that it will be

possible to relate the known characteristics and geometry of the blast wave observed in 1969 with the eigen-modes of the magnetosphere excited by this shock. With this type of comparative study it may become possible to distinguish between the magnetospheric excitations caused by propagating interplanetary shock waves and those caused by corotating streams.

The present study of IPS and its relation to solar and geomagnetic activity and the occurrence of plasma blast waves, corotating streams and interplanetary magnetic field sector boundaries, demonstrates the scope and flexibility of this technique, and suggests that further work in this field will provide a valuable tool for probing a whole range of solar and geomagnetic phenomena.

In Chapter 8 we have presented a description of the design and construction of the Adelaide radio-astronomy aerial array. This system is being developed as the basis of a current research project to extend the present IPS studies to measurements on two frequencies with full phase and amplitude information at three spaced receiving sites. When the system becomes fully operational these features will allow the parameters of the phase and amplitude diffraction patterns at the earth to be completely specified, and will thus provide a significant contribution to our present knowledge of the scattering of radio waves by electron density irregularities in the solar wind.

BIBLIOGRAPHY

Akasofu, S.I., and Yoshida, S.	1967a	Planet. Space Sci. 15, 39.
	1967b	Planet. Space Sci. 15, 942.
Altschuler, M.D., and Newkirk, G.	1969	Solar Phys. 9, 131.
Antonucci, E. et al.	1971	12th International Conference on Cosmic Rays, Hobart, Tasmania.
Axford, W.I.	1968	Space Sci. Rev. 8, 331.
Ballif, J.R., and Jones, D.E.	1967	Journ. Geophys. Res. 72, 5173.
	1969a	Journ. Geophys. Res. 74, 3499.
	1969b	Journ. Geophys. Res. 74, 3512.
Ballif, J.R. et al.	1971	Journ. Geophys. Res. 76, 8401.
Bame, S.J. et al.	1968a	Journ. Geophys. Res. 73, 5761.
	1968b	Phys. Rev. Lett. 20, 393.
Barnes, A.	1968	Astrophys. J. 154, 751.
	1969	Astrophys. J. 155, 311.
Bartley, W.C. et al.	1966	Journ. Geophys. Res. 71, 3297.
Bell, B.	1961	Smithsonian Contrib. Astrophys. 5, 69.
Biermann, L.	1951	Z. Astrophys. 29, 274.
Billings, D.E., and Roberts, W.O.	1964	Astrophys. Noweg. 9, 147.
Blackman, R.B., and Tukey, J.W.	1958	'The Measurement of Power Spectra'. Dover Press.
Blesing, R.G.	1972	Ph.D. Thesis, Univ. of Adelaide.
Bowhill, S.A.	1961	J. Res. Nat. Bur. Stand. 65D, 275.

Branley, E.N.	1967	J. At. Terr. Phys. 29, 1.
Bramley, E.N., and Young, M.	1967	Proc. Inst. Elec. Eng. 114, 553.
Briggs, B. H., et al.	1950	Proc. Phys. Soc. B, 63, 106.
Briggs, B.H.	1966	Radio Sci. 1, 1163.
	1968	J. At. Terr. Phys. 30, 1777.
Briggs, B.H., et al.	1969	Nature. 223, 1321.
Buckley, R.	1971	Planet. Space Sci. 19, 421.
	1971a	Aust. Journ. Phys. 24, 351.
	1971b	Aust. Journ. Phys. 24, 373.
Budden, K.G.	1965	J. At. Terr. Phys. 27, 883.
Bugoslavskaya, E.Y.	1949	Publ. Sternberg Inst. No. 19.
Bühler, F., et al.	1969	Science. 166, 1502.
Bumba, V., and Howard, R.	1965	Astrophys. J. 141, 1502.
Burlaga, L.F., and Ogilvie, K.W.	1969	Journ. Geophys. Res. 74, 2815.
	1970	Astrophys. J. 159, 659.
Burnell, S.J.	1969	Nature. 224, 356.
Carovillano, R.L., and Siscoe, G.L.	1969	Solar Phys. 8, 401.
Chapman, S.	1966	'The Solar Wind', R.J. Mackin and M. Neugebauer, ed. Pergamon Press.
Christiansen, W.N., and Hogbom, J.A.	1969	'Radiotelescopes', Camb. Univ. Press.
Clauser, F.H.	1960	Nuovo Cimento Suppl. 22, No. 1.
Cohen, M.H., et al.	1967	Astrophys. J. 150, 767.
Coleman, P.J.	1968	Astrophys. J. 153, 371.

Cooley, J.W. et al.	1969	IEEE Trans. Acoust. and Electraacoust. AU-17, 77.
	1970	J. Sound Vib. 12, 339.
Cooley, J.W., and Tukey, J.W.	1965	Maths Comput. 19, 297.
Coon, J.H.	1966	'Radiation Trapped in the Earth's Magnetic Field', D. Reidel Publ. Co.
Cottony, H.V., and Wilson, A.C.	1958	Trans. IRE. AP-6, 366.
Cowling, T.G.	1969	The Observatory. 89, 973.
Croft, T.A.	1971	Radio Sci. 6, 55.
Cuperman, S., and Harten, A.	1970	Astrophys. J. 162, 315.
Davis, L.	1965	'Stellar and Solar Magnetic Fields' North-Holland Publ. Co.
Davis, L. et al.	1966	'The Solar Wind', R.J. Mackin and M. Neugebauer, ed. Pergamon Press.
Dennison, P.A.	1967	Ph.D. Thesis, Univ. of Cambridge.
Dennison, P.A., and Hewish, A.	1967	Nature. 213, 343.
Dennison, P.A., and Wiseman, M.	1968	Proc. ASA. 1, 142.
Dennison, P.A.	1969	Planet. Space Sci. 17, 189.
Dessler, A.J.	1967	Reviews of Geophysics. 5, 1.
De Young, D.S., and Hundhausen, A.J.	1971	Journ. Geophys. Res. 76, 2245.
Dryer, M.	1967	8th International Space Science Symposium, 10th COSPAR Plenary Meeting, London.
Dryer, M., and Jones, D.L.	1968	Journ. Geophys. Res. 73, 4875.
Eviatar, A., and Shulz, M.	1970	Planet. Space Sci. 18, 321.

Fairfield, D.H., and Ness, N.F.	1967	Journ. Geophys. Res. 72, 2379.
Fan, C.Y. et al.	1966	Proc. International Conference on Cosmic Rays. London.
Fenelon, A.R., and McDonald, R.D.	1968	Electronic Engineering 40, 145.
Forslund, D.W.	1970	Journ. Geophys. Res. 75, 17.
Frater, R.H.	1965	Rev. Sci. Instr. 36, 634.
Gold, T.	1959	Journ. Geophys. Res. 64, 1665.
Goldstein, E., and Siscoe, G.L.	1971	Proc. of the Asilomar Conference on the Solar Wind.
Golley, M.G., and Rossiter, D.E.	1970	J. At. Terr. Phys. 32, 1215.
Gosling, J.T. et al.	1967	Journ. Geophys. Res. 72, 1813.
	1968	Journ. Geophys. Res. 73, 43.
Greenstadt, E.W. et al.	1970	Planet. Space Sci. 18, 333.
Griffel, D.H., and Davis, L.	1969	Planet. Space Sci. 17, 1009.
Gringauz, K.I. et al.	1966	Book of Abstracts, Inter-Union Symp. on Solar-Terrestrial Phys. Belgrade.
Hartle, R.E., and Sturrock, P.A.	1968	Astrophys. J. 151, 1155.
Hartle, R.E., and Barnes, A.	1970	Journ. Geophys. Res. 75, 6915.
Hewish, A. et al.	1964	Nature. 203, 1214.
	1966	Nature. 209, 1188.
Hewish, A., and Dennison, P.A.	1967	Journ. Geophys. Res. 72, 1977.
Hewish, A., and Symonds, M.D.	1969	Planet. Space Sci. 17, 313.
Hewish, A.	1971	Astrophys. J. 163, 645.
Hinich, M.J., and Clay, C.S.	1968	Reviews of Geophysics 6, 347.

Hirshberg, J.	1968	Planet. Space Sci. 16, 309.
	1969	Journ. Geophys. Res. 74, 5814.
Hirshberg, J. et al.	1970	Journ. Geophys. Res. 75, 1.
Hollweg, J.V.	1970	Journ. Geophys. Res. 75, 2403.
Hollweg, J.V., and Volk, H.J.	1970	Journ. Geophys. Res. 75, 5297.
Holzer, R.E. et al.	1966	Journ. Geophys. Res. 71, 1481.
Holzer, R.E., and Axford, W.I.	1970	Ann. Rev. Astron. Astrophys.
Houminer, Z.	1971	Nature Phys. Science. 231, 165.
Howard, R.	1959	Astrophys. J. 130, 193.
Hundhausen, A.J. et al.	1967a	Journ. Geophys. Res. 72, 87.
	1967b	Journ. Geophys. Res. 72, 1979.
	1967c	Journ. Geophys. Res. 72, 5265.
Hundhausen, A.J.	1968	Space Sci. Rev. 8, 690.
	1969	Journ. Geophys. Rev. 74, 5810.
Hundhausen, A.J., and Gentry, R.A.	1969	Journ. Geophys. Res. 74, 2908.
Hundhausen, A.J.	1970	Reviews of Geophysics and Space Physics. 8, 729.
Hundhausen, A.J. et al.	1970	Journ. Geophys. Res. 75, 4643.
Intriligator, D.S., and Wolfe, J.H.	1970	Astrophys. J. 162, L187.
Jokipii, J.R., and Coleman, P.J.	1968	Journ. Geophys. Res. 73, 5495.
Jokipii, J.R., and Hollweg, J.V.	1970	Astrophys. J. 160, 745.
Kennel, C.F., and Scarf, F.L.	1968	Journ. Geophys. Res. 73, 6149.
Kraus, J.D.	1966	'Radio Astronomy'. McGraw-Hill.
Landecker, T.L., and Wielebinsky, R.	1970	Proc. IREE (Aust). 31, 73.

Lazarus, A.J. et al.	1966	Journ. Geophys. Res. 71, 3787.
Lee, T.S., and Chen, T.	1968	Planet. Space Sci. 16, 1483.
Little, C.G. et al.	1962	Journ. Geophys. Res. 67, 1763.
Little, L.T., and Hewish, A.	1966	M.N.R.A.S. 134, 221.
	1968	M.N.R.A.S. 138, 393.
Lovelace, R.V.E. et al.	1970	Astrophys. J. 159, 1047.
McCracken, K.G., and Ness, N.F.	1966	Journ. Geophys. Res. 71, 3315.
McCracken, K.G. et al.	1967	Journ. Geophys. Res. 72, 4293.
Mercier, R.P.	1962	Proc. Camb. Phil. Soc. 58, 382.
Montgomery, M.D. et al.	1968a	Trans. Am. Geophys. Union. 49.
	1968b	Journ. Geophys. Res. 73, 4999.
Ness, N.F., and Wilcox, J.M.	1964	Phys. Rev. Lett. 13, 461.
	1966	Astrophys. J. 143, 23.
Ness, N.F.	1966	Journ. Geophys. Res. 71, 3319.
	1967	IQSY/COSPAR Symposium, London.
Ness, N.F., and Wilcox, J.M.	1967	Solar Phys. 2, 351.
Neugebauer, M., and Snyder, C.W.	1966	Journ. Geophys. Res. 71, 4469.
	1967	Journ. Geophys. Res. 72, 1823.
Newkirk, G.A.	1967	Ann. Rev. Astron. Astrophys. 5, 213.
Newkirk, G.A. et al.	1968	I.A.U. Symposium No. 35, D. Reidel Publ. Co.
	1970	Magnetic Fields and the Solar Corona III. Preprint.
Noble, L.M., and Scarf, F.L.	1963	Astrophys. J. 138, 1169.

Ogilvie, K.W. et al.	1968	Journ. Geophys. Res. 73, 6809.
Ogilvie, K.W., and Burlaga, L.F.	1969	Solar Phys. 8, 422.
Ogilvie, K.W., and Wilkerson, T.D.	1969	Solar Phys. 8, 435.
Orhaug, T.A.	1965	Trans. Chalmers Univ. Tech. 299.
Pai, G.L. et al.	1967	Trans. Am. Geophys. Union. 48, 176.
Parker, E.N.	1958	Astrophys. J. 128, 664.
	1963a	'The Solar Corona'. Academic Press.
	1963b	'Interplanetary Dynamical Processes'. Interscience Publ.
	1964	Astrophys. J. 139, 72.
	1964	Astrophys. J. 139, 93.
	1965	Space Sci. Rev. 4, 666.
	1969	Space Sci. Rev. 9, 325.
Parkin, I.A.	1967	Ph.D. Thesis, Univ. of Adelaide.
Phillips, G.J., and Spencer, M.	1955	Proc. Phys. Soc. B, 68, 481.
Pisareva, V.V.	1959	AJ. USSR. 36, 427.
Pneuman, G.W.	1966	Astrophys. J. 145, 242.
Rao, U.R. et al.	1967	Journ. Geophys. Res. 72, 4325.
Ratcliffe, J.A.	1956	Rep. Progr. Phys. 19, 188.
Readhead, A.C.S.	1971	M.N.R.A.S. 155, 185.
Rice, S.O.	1944	Bell System Tech. J. 23, 282.
Robbins, D.E. et al.	1970	Journ. Geophys. Res. 75, 1178.

Ryle, M.	1952	Proc. Roy. Soc. A 211, 351.
Salpeter, E.E.	1967	Astrophys. J. 147, 433.
Sarabhai, V.	1963	Journ. Geophys. Res. 68, 1555.
Scarf, F.L., and Noble, L.M.	1965	Astrophys. J. 141, 1479.
Scarf, F.L.	1970	Space Sci. Rev. 11, 234.
Schatten, K.H. et al.	1968	Solar Phys. 5, 240.
	1969	Solar Phys. 6, 422.
Schatten, K.H.	1970	Internal Report X-692-70-264 Preprint Goddard Space Flight Centre, Maryland.
Serbu, G.P., and Maier, E.J.R.	1966	Journ. Geophys. Res. 71, 3755.
Severny, A. et al.	1970	Solar Phys. 15, 3.
Sharp, L.E., and Harris, D.E.	1967	Nature. 213, 377.
Simon, M., and Axford, W.I.	1966	Planet. Space Sci. 14, 901.
Siscoe, G.L., and Finley, L.T.	1969	Solar Phys. 9, 452.
Siscoe, G.L. et al.	1969	Journ. Geophys. Res. 74, 1759.
Siscoe, G.L., and Finley, L.T.	1970	Journ. Geophys. Res. 75, 1817.
	1972	'Solar Wind Structure Determined by Corotating Coronal Inhomogeneities', Journ. Geophys. Res. In press.
Slee, O.B., and Higgins, C.S.	1968	Aust. J. Phys. 21, 341.
Smith, F.G.	1961	Proc. IEE. 108B, 201.
Sonnet, C.P. et al.	1964	Phys. Rev. Lett. 13, 153.
Strong, I.B. et al.	1966	Phys. Rev. Lett. 16, 631.
	1967a	Trans. Am. Geophys. Union. 48, 191.

	1967b	'Zodiacal Light and the Interplanetary Medium', NASA SP-150, ed. J. Weinberg.
Sturrock, P.H., and Hartle, R.E.	1966	Phys. Rev. Lett. 16, 628.
Taylor, H.E.	1969	Solar Phys. 6, 320.
Uscinski, B.J.	1966	J. At. Terr. Phys. 29, 641.
Ward, B.D. et al.	1972	Proc. ASA. 2, 82.
Weber, E.J., and Davis, L.	1967	Astrophys. J. 148, 217.
Whang, Y.C., and Chang, C.C.	1965	Journ. Geophys. Res. 70, 4175.
Whang, Y.C. et al.	1966	Astrophys. J. 145, 255.
Wilcox, J.M., and Ness, N.F.	1965	Journ. Geophys. Res. 70, 5793.
	1967	Solar Phys. 1, 437.
Wilcox, J.M.	1968	Space Sci. Rev. 8, 258.
	1969	Paper presented at the 3rd ESLAB/ESRIN Symposium Noordwijk, Holland.
Wilcox, J.M. et al.	1969	Nature. 224, 353.
Wilcox, J.M., and Colburn, D.S.	1969	Journ. Geophys. Res. 74, 2388.
	1970	Journ. Geophys. Res. 75, 6366.
	1971	Journ. Geophys. Res. in press.
Wild, J.P.	1967	Proc. IREE 28, 277.
Wilson, A.C., and Cottony, H.V.	1960	Trans. IRE. AP-8, 144.
Wiseman, M., and Dennison, P.A.	1972	Proc. ASA. 2, 79.
Wolfe, J.H. et al.	1966a	Journ. Geophys. Res. 71, 1319.
	1966b	Journ. Geophys. Res. 71, 3329.
Wolfe, J.H., and McKibbin, D.D.	1968	Planet. Space Sci. 16, 953.

Wolfe, J.H., and Intriligator, D.S. 1970 Space Sci. Rev. 10, 511.

Wolfe, J.H. 1971 Proc. Asilomar Conference on the Solar Wind.

APPENDIX A

APPENDIX A

Budden (1965) has derived an expression for the normalised correlation coefficient of the amplitude fluctuations of signals received simultaneously on two frequencies at a single fixed receiving point. He considers the case where the scattering region can be represented as a very thin, irregular phase-changing screen. Waves at two frequencies $f = f_1, f_2$ are represented by their free space wave numbers,

$$k_1 = \frac{2\pi f_1}{c}, \qquad k_2 = \frac{2\pi f_2}{c}$$

(where $f_2 > f_1$), and are obliquely incident on the layer with wave normals in a direction given by the polar angles (θ, ϕ). The receiver is assumed to be at the point where an incident ray through the origin (in the screen) meets the ground, so that its coordinates are $(z \tan\theta \cos\phi, z \tan\theta \sin\phi, z)$, where z is the vertical distance from the centre of the scattering layer to the ground. The resulting normalised correlation coefficient is then,

$$C(k_1, k_2) = \frac{R_e (E - F)}{(GH)^{\frac{1}{2}}}, \qquad (A.1)$$

where,

$$E = (T_1 T_2 \cos^4\theta - D^2 - i\beta D)^{-\frac{1}{2}},$$

$$F = (T_1 T_2 \cos^4\theta - S^2 + i\beta S)^{-\frac{1}{2}},$$

$$G = (T_1 T_2 \cos^4\theta)^{-\frac{1}{2}} - R_e (T_1 T_2 \cos^4\theta - 4/k_1^2 + 2i\beta/k_1)^{-\frac{1}{2}},$$

$$H = (T_1 T_2 \cos^4\theta)^{-\frac{1}{2}} - R_e (T_1 T_2 \cos^4\theta - 4/k_2^2 + 2i\beta/k_2)^{-\frac{1}{2}},$$

and,

$$T_1 = \tfrac{1}{2} R_1^2/z, \qquad T_2 = \tfrac{1}{2} R_2^2/z,$$

$$\beta = \left(T_1 (1 - \mathrm{Sin}^2\,\theta\,\mathrm{Cos}^2\,\phi) + T_2 (1 - \mathrm{Sin}^2\,\theta\,\mathrm{Sin}^2\,\phi)\right) \mathrm{Cos}\,\theta,$$

$$D = \frac{k_2 - k_1}{k_1\,k_2}, \qquad S = \frac{k_1 + k_2}{k_1\,k_2},$$

R_e = real part, amd

R_1, R_2 are the scale sizes of the irregularities in the screen.

In the simplest and probably most realistic case, where $R_1 = R_2$ (= R) and $\theta = \phi = 0$ (vertical incidence), expression (A.1) can be considerably simplified:

$$T_1 = T_2 = R^2/2z\ ,$$

$$\beta = T_1 + T_2 = 2T\ ,$$

$$E = (T_1\,T_2\,\mathrm{Cos}^4\,\theta - D^2 - i\,\beta\,D)^{-\frac{1}{2}}\ ,$$

$$= (T^2 - D^2 - i\,2\,T\,D)^{-\frac{1}{2}}$$

$$= \frac{T + i\,D}{T^2 + D^2}\ . \qquad \text{(A.2)}$$

Similarly,

$$F = \frac{T - i\,S}{T^2 + S^2}\ , \qquad \text{(A.3)}$$

hence

$$R_e\,(E - F) = \frac{T}{T^2 + D^2} - \frac{T}{T^2 + S^2}\ . \qquad \text{(A.4)}$$

Also,

$$G = (T_1\,T_2\,\mathrm{Cos}^4\,\theta)^{-\frac{1}{2}} - R_e\,(T_1\,T_2\,\mathrm{Cos}^4\,\theta - 4/k_1^2 + 2\,i\,\beta/k_1)^{-\frac{1}{2}}\ ,$$

$$= \frac{1}{T} - R_e\,(T^2 - 4/k_1^2 + 4\,i\,T/k_1)^{-\frac{1}{2}}$$

$$= \frac{1}{T} - R_e\,(T + 2\,i/k_1)^{-1}$$

$$= \frac{1}{T} - \frac{T}{T^2 + 4/k_1^2}\ . \qquad \text{(A.5)}$$

Similarly,

$$H = \frac{1}{T} - \frac{T}{T^2 + 4/k_2^2} \cdot \qquad (A.6)$$

If we now assume that

$$k_1 \sim k_2 \sim k = \frac{k_1 + k_2}{2} ,$$

then,

$$D \simeq \frac{k_2 - k_1}{k^2} , \qquad S \simeq \frac{2}{k} ,$$

and

$$C = \frac{T/(T^2 + D^2) - T/(T^2 + S^2)}{(1/T - T/(T^2 + 4/k^2))} ,$$

which, after rearrangement,

$$= \frac{T^2 (S^2 - D^2)}{S^2 (T^2 + D^2)} . \qquad (A.7)$$

Writing $Y = \frac{T}{S}$ and $B = \frac{D}{S}$ we have,

$$C = \frac{Y^2 (1 - B^2)}{Y^2 + B^2} ,$$

which yields

$$B = \frac{Y \sqrt{1 - C}}{\sqrt{Y^2 + C}} . \qquad (A.8)$$

With,

$$B = \frac{D}{S} = \frac{\Delta k}{k^2} \cdot \frac{k}{2} \qquad (k = k_2 - k_1)$$

$$= \frac{\Delta f}{2f} , \qquad \left(f = \frac{f_2 + f_1}{2}\right)$$

and

$$Y = \frac{T}{S} = \frac{k R^2}{4z}$$

$$= \frac{\pi R^2}{2 \lambda Z} ,$$

then after substituting and rearranging, we finally obtain

$$\frac{\Delta f}{f} = \frac{A\,X}{\sqrt{X^2 + B}}, \qquad (A.9)$$

where $A = 2\sqrt{1 - C}$,

$B = 4C/\pi^2$,

$X = \frac{R^2}{\lambda Z}$,

C = correlation coefficient

We can simplify this further for the case C = 0.5,

$$\frac{\Delta f}{f} = \frac{\sqrt{2}\,X}{\sqrt{X^2 + 2/\pi^2}}$$

Using typical values for R, λ, Z in the case of interplanetary scintillation,

$$\lambda = 3m$$

$$R = 200\ Km$$

$$Z = 0.5\ A.U.$$

then,

$$X \simeq 2 \times 10^{-2}$$

$$X^2 \simeq 4 \times 10^{-4}$$

compared with

$$2/\pi^2 \sim 0.2.$$

Thus,

$$\frac{\Delta f}{f} \simeq \frac{\sqrt{2}\,X}{\sqrt{2}/\pi} \qquad (2/\pi^2 >> X^2)$$

i.e.

$$\frac{\Delta f}{f} = \frac{\pi R^2}{\lambda Z} \qquad (A.10)$$

In Figure A1 we have plotted Equations A.1, A.9 and A.10 for a correlation coefficient C (k_1, k_2) of 0.5. It can be seen that for X << 0.1, which is the case for IPS, the approximate Equations A.9 and

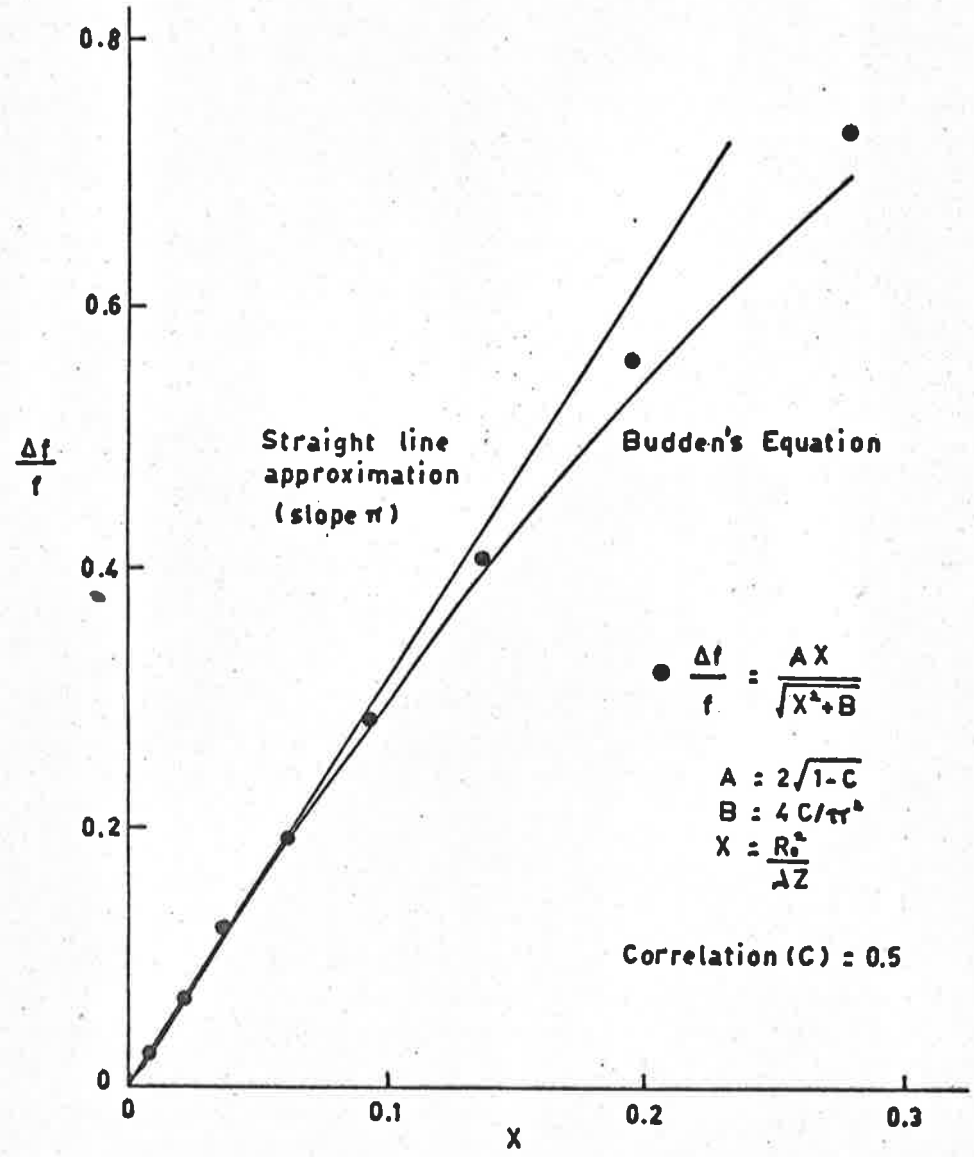

Figure A1 Approximations for the correlation of amplitude scintillations observed at two frequencies.

A.10 deviate by less than 10% from Budden's accurate result, Equation A.1.

APPENDIX B

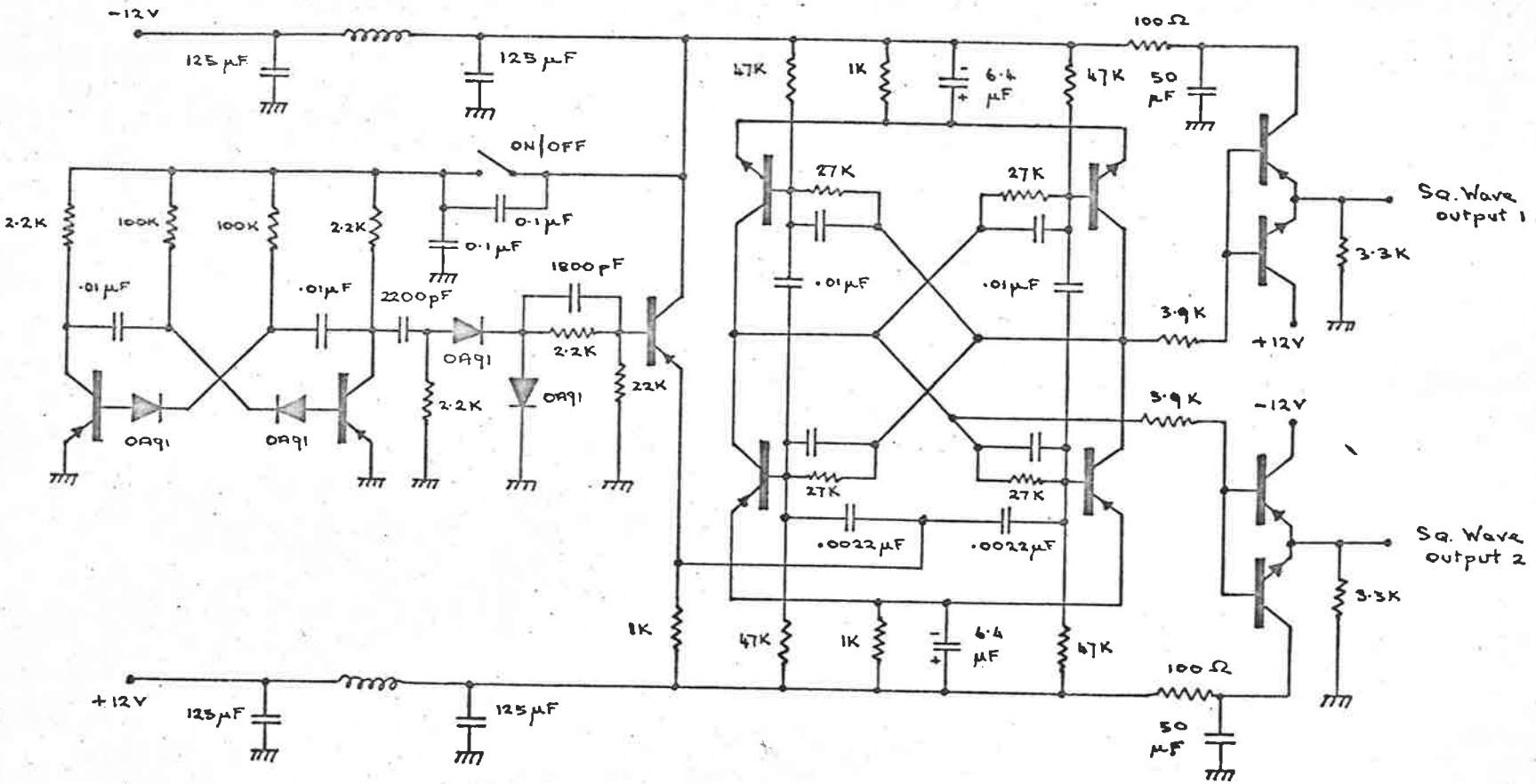

Transistors: NPN BC107
PNP BC177

SQUARE WAVE GENERATOR

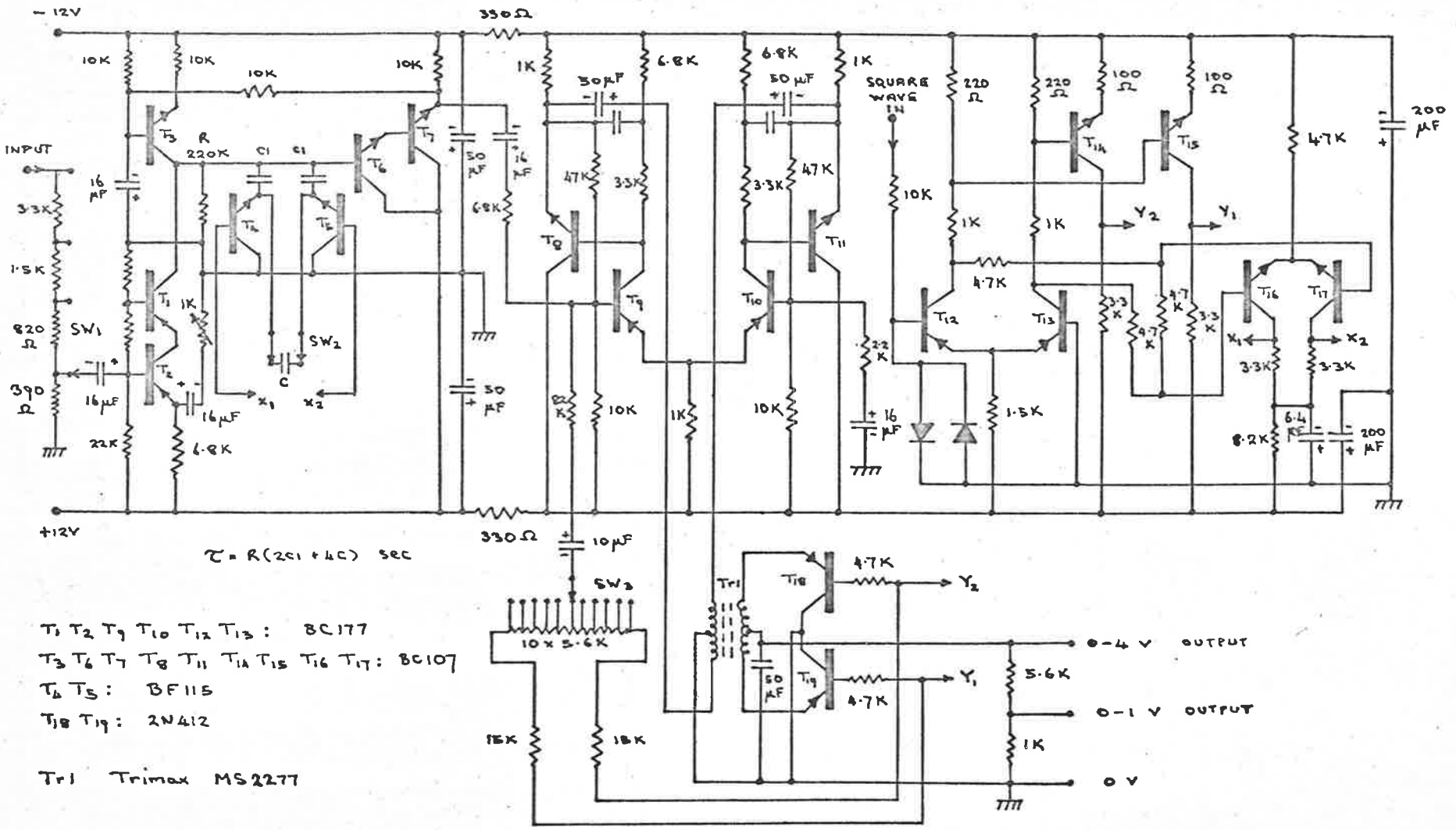

T_1 T_2 T_9 T_{10} T_{12} T_{13} : BC177

T_3 T_6 T_7 T_8 T_{11} T_{14} T_{15} T_{16} T_{17}: BC107

T_4 T_5 : BF115

T_{18} T_{19} : 2N412

Tr1 Trimax MS2277

SYNCHRONOUS INTEGRATOR-DEMODULATOR

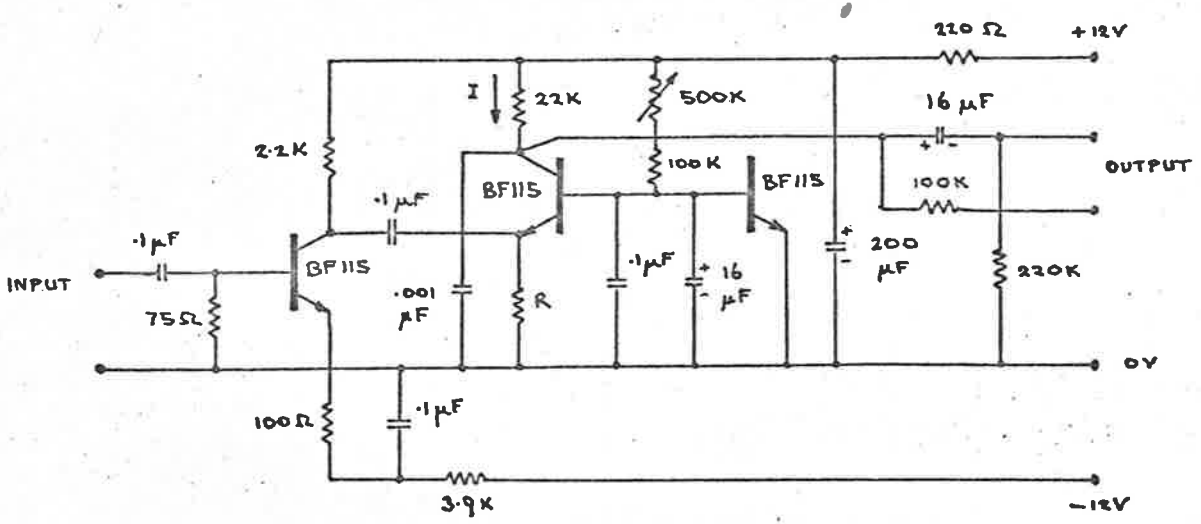

Adjust $I = 34\ \mu A$ for $R = 100\ \Omega$

SQUARE LAW DETECTOR

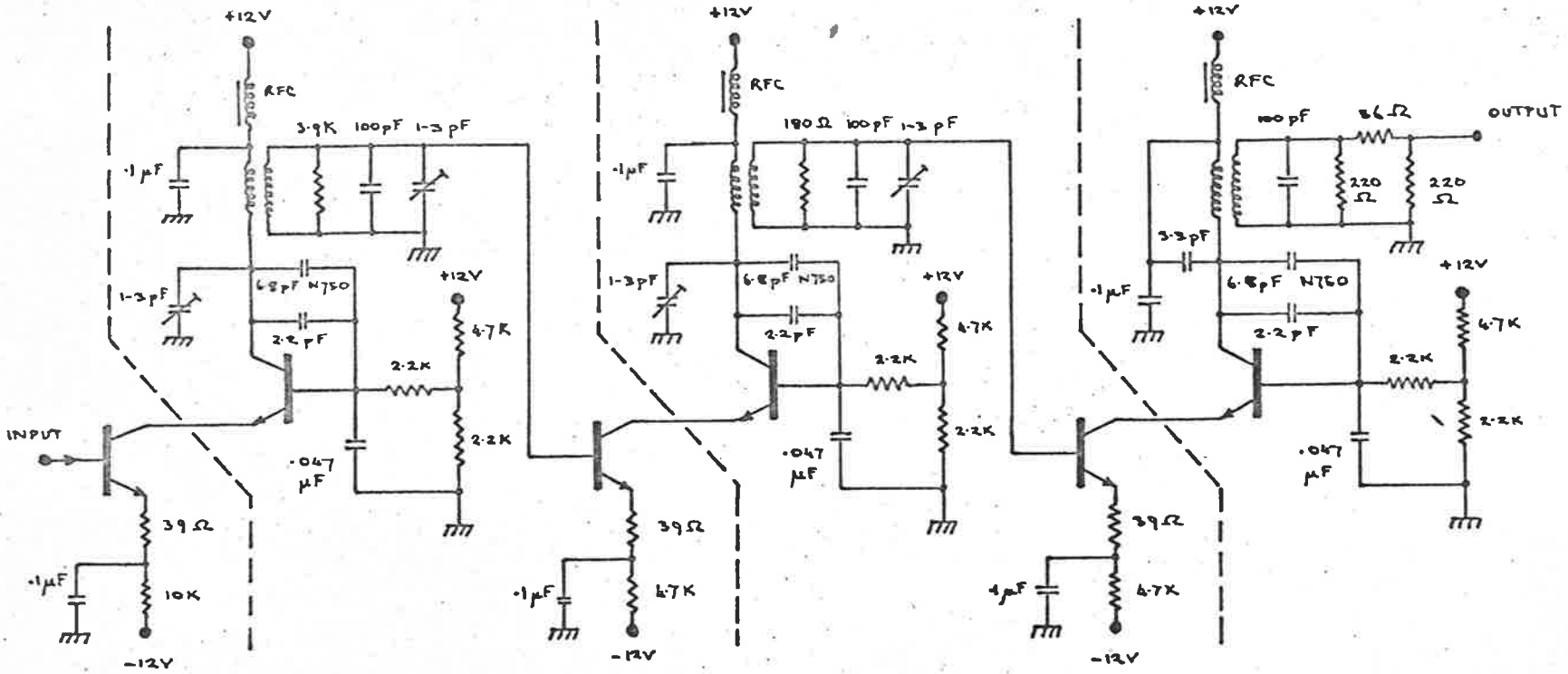

All Transistors : BF 115

I.F. Amplifier

Frequency	30 MHz
Bandwidth	1 MHz
Gain	60 db

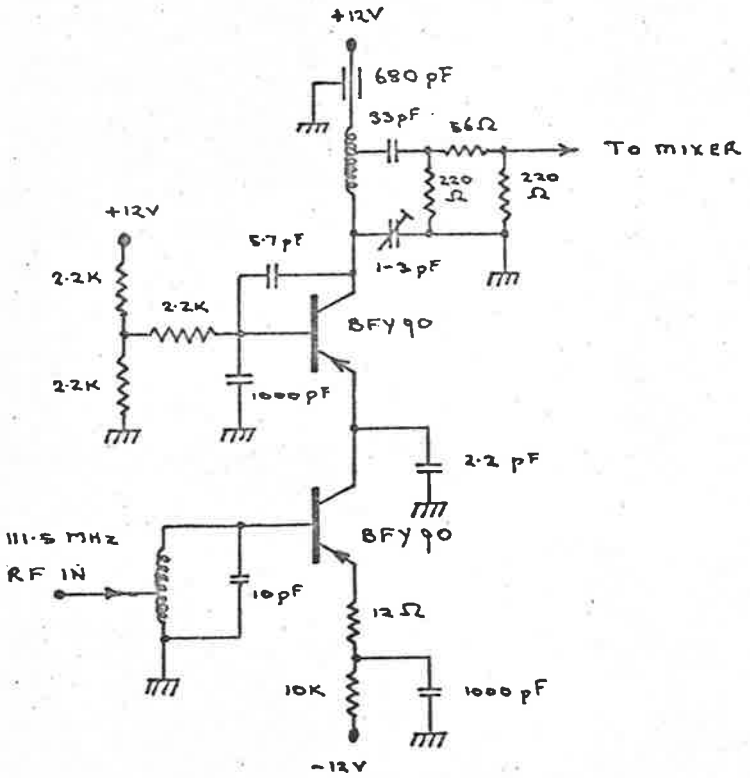

Preamplifier

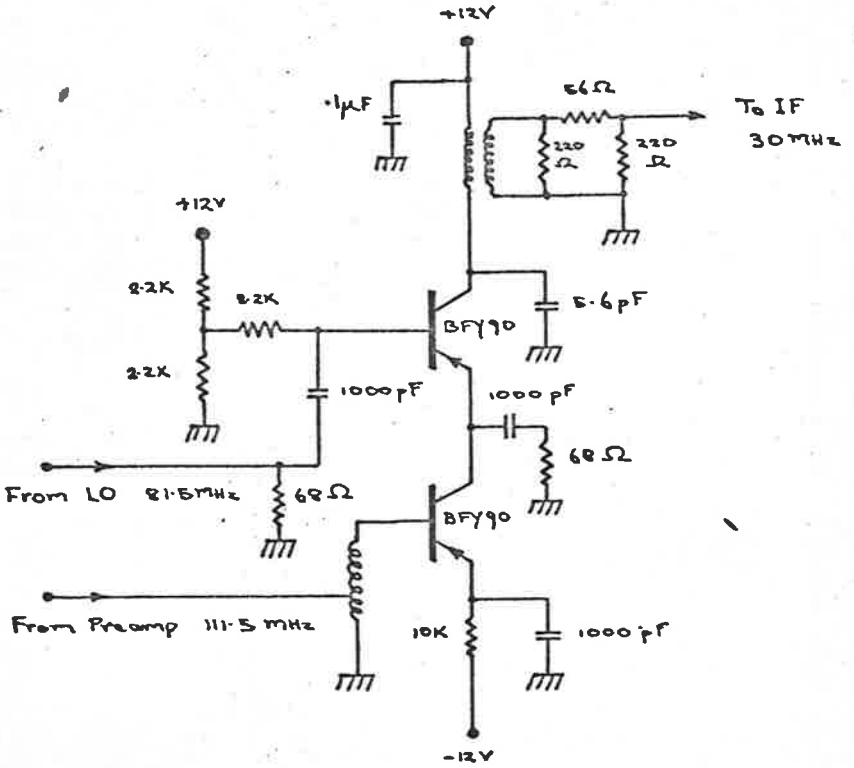

Mixer

Local Oscillator

PYE XL691

Converter Circuitry

(111·5 MHz)

Aerial Preamplifier

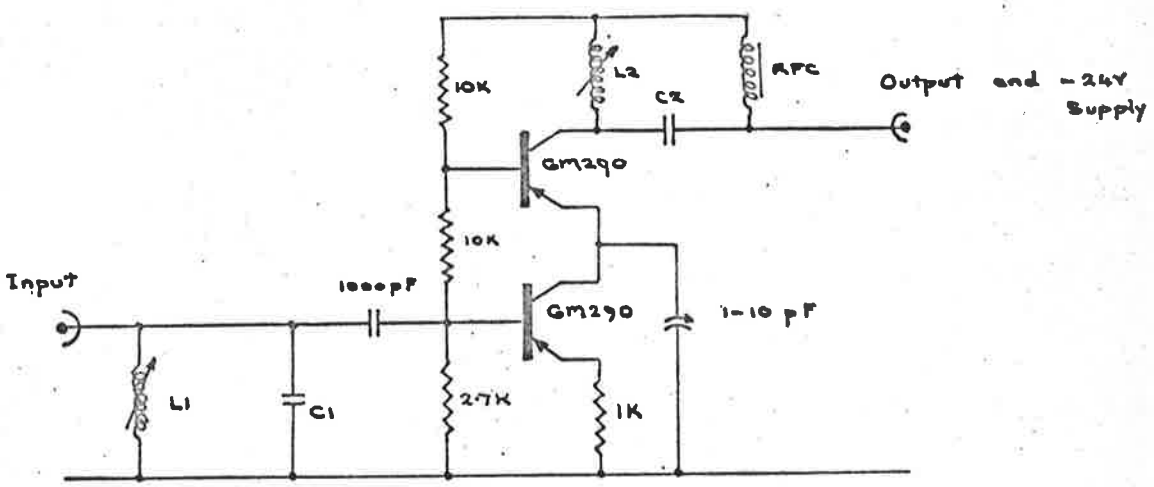

	111·5 MHz	235·9 MHz
L1 :	8 t Ferrite Slug	4 t Ferrite Slug
L2 :	13 t (22 swg) Brass Slug	6 t (22 SWG) Brass Slug
C1 :	3 pF	3pF
C2 :	5 pF	3pF

REPRINT:

'Preliminary Observations of the Effects of a Corotating stream on Interplanetary Scintillation.'

by

P. A. Dennison and M. Wiseman

Dennison, P. A., & Wiseman, M. (2016). Preliminary Observations of the Effects of a Corotating Stream on Interplanetary Scintillation. *Publications of the Astronomical Society of Australia, 1*(4), 142-145.

NOTE:
This publication is included in the print copy
of the thesis held in the University of Adelaide Library.

It is also available online to authorised users at:
https://doi.org/10.1017/S1323358000011103

REPRINT:

'Flare Induced Shocks and Corotating Streams in the Interplanetary Medium.'

by

M. Wiseman and P. A. Dennison

Wiseman, M., & Dennison, P. A. (2016). Flare Induced Shocks and Corotating Streams in the Interplanetary Medium. *Publications of the Astronomical Society of Australia, 2*(2), 79-82.

NOTE:
This publication is included in the print copy
of the thesis held in the University of Adelaide Library.

It is also available online to authorised users at:
https://doi.org/10.1017/S1323358000012923